



**HAL**  
open science

# Durability of reinforcement in low-carbon concretes (low clinker, alkali-activated slag, supersulfated cement)

Lola Doussang

## ► To cite this version:

Lola Doussang. Durability of reinforcement in low-carbon concretes (low clinker, alkali-activated slag, supersulfated cement). Civil Engineering. INSA de Toulouse, 2023. English. NNT : 2023ISAT0019 . tel-04327015

**HAL Id: tel-04327015**

**<https://theses.hal.science/tel-04327015>**

Submitted on 6 Dec 2023

**HAL** is a multi-disciplinary open access archive for the deposit and dissemination of scientific research documents, whether they are published or not. The documents may come from teaching and research institutions in France or abroad, or from public or private research centers.

L'archive ouverte pluridisciplinaire **HAL**, est destinée au dépôt et à la diffusion de documents scientifiques de niveau recherche, publiés ou non, émanant des établissements d'enseignement et de recherche français ou étrangers, des laboratoires publics ou privés.



# THÈSE

**En vue de l'obtention du  
DOCTORAT DE L'UNIVERSITÉ DE TOULOUSE**  
Délivré par l'Institut National des Sciences Appliquées de  
Toulouse

---

**Présentée et soutenue par  
Lola DOUSSANG**

Le 4 juillet 2023

**Durabilité des armatures dans des bétons bas carbone (bas  
clinker, laitier alcali-activé, ciment sursulfaté)**

---

Ecole doctorale : **MEGEP - Mécanique, Energétique, Génie civil, Procédés**

Spécialité : **Génie civil**

Unité de recherche :

**LMDC - Laboratoire Matériaux et Durabilité des Constructions de Toulouse**

Thèse dirigée par  
**Martin CYR et Gabriel SAMSON**

Jury

**M. Arnaud CASTEL**, Rapporteur  
**Mme Siham KAMALI-BERNARD**, Rapporteuse  
**Mme Véronique BAROGHEL-BOUNY**, Examinatrice  
**Mme Marijana SERDAR**, Examinatrice  
**M. Fabrice DEBY**, Examineur  
**M. Martin CYR**, Directeur de thèse  
**M. Gabriel SAMSON**, Co-directeur de thèse



## Acknowledgements

First, I would like to acknowledge the company Holcim for the financing of this thesis work and for giving me the chance to take part in it, as well as the Laboratory of Materials and Durability of Constructions (LMDC) and the INSA Toulouse for welcoming me during these three years.

Because this work is above all a team effort, I want to express my thank to my academic and industrial supervisors: Martin Cyr, Gabriel Samson, Fabrice Deby, Emmanuel Guillon and Bruno Huet, for the supervision of this work, the knowledge and ideas they have shared, their support, availability, guidance, advise, confidence and patience. I have learned a lot during these three years with you.

I would also like to express my gratitude to all the LMDC staff and colleagues for their participation, help and support to perform my many experiments. Carole Soula, Sylvain Dos Santos, Yann Bouaskeur, Frédéric Leclerc and David Dupiet for the mechanical service. Vanessa Mazars, Maud Schiettekatte, and Guillaume Lambaré for the chemistry service. Marc Bégué, David Guillouset, Laurent Boix and Fabien Nougarrowles for the physics service. Céline Berné and Ghislaine Dupouey for the administrative service. But also Jean-Phillipe Nougarrow from the mechanical department of INSA, for its kindness and its availability for the cutting of many steel rebars. Lionel Boudeville, from the mechanical department of IUT Paul Sabatier, for its reactivity and the machining of steel rebars. Finally, I address a special thanks to all the Ph.D. students, post-docs and Ecocem staff for the moments spent together.

My sincere thanks must also go to some members of the company Holcim. Emmanuel Guillon and Bruno Huet for their warm welcome to Holcim Innovation Centre for some experimental work and discussions. Florian Maurice and Yves Francomme for the regular expedition of materials and casting of concrete. Guillaume Pommier, Gabriel Pham and all other persons involved for the durability tests.

I would not forget all the external people who took the time to answer my questions and requests. The harbour of Saint-Cast and the CCI of Côtes d'Armor, for letting me use their tidal area for two years to perform my experiments. Robert Visser from Robesol, for his help with the sensors and the interface box for the O<sub>2</sub>/CO<sub>2</sub> cell. The company Corexco for the manufacture of the O<sub>2</sub>/CO<sub>2</sub> cell. Léo Granier for the program to record the data of the O<sub>2</sub>/CO<sub>2</sub> cell.

Last but not least, I deeply thank my friends and family because this work could never have been done without their positive energy and their presence by my side. Aurélie, Loïc, Jorge, Morgane, Léo, Marie, Sarah, Elisa, Olympe for allowing me to be so well surrounded. My parents and my brother for their unconditional support and love.

## **Abstract**

New concrete technologies with a reduced carbon footprint have been developed, to address current environmental challenges. However, as these technologies are recent, little information on their durability is available, which limits their use. In particular information related to corrosion of reinforcing steel is required, because it is one of the main causes for the failure of ordinary reinforced concrete structures.

The objective of this thesis is thus to evaluate the durability of rebars in three types of low-carbon concretes, of same strength class C25/30: low clinker content (LCK), alkali-activated slag with sodium carbonate (AAS) and supersulfated cement (SSC). These concretes allow a reduction of the carbon footprint ranging from 40% to 75%, compared to a traditional concrete made with CEM I. The objective is to characterize their behaviour against corrosion under different exposure conditions (exposure to chlorides or carbonation).

The first part of this work consists in characterizing and comparing the general transfer properties, the transport of chlorides and CO<sub>2</sub> in the three concretes studied, which will condition the initiation time of corrosion. This first part of the study also allows to identify the strengths and weaknesses of each low-carbon solution, as well as the environments in which they perform best. The results show that LCK concrete is characterized by very good transfer properties (low water porosity, gas permeability, water permeability and capillary absorption), but a high viscosity at fresh state and a high chloride permeability. AAS and SSC concretes have similar transfer properties, comparable to conventional C25/30 concretes, and are extremely resistant to chloride penetration. All three binders are quite sensitive to natural carbonation, especially for short curing times.

A second part is dedicated to the evaluation of corrosion kinetics, in the case of activation by chloride contamination or by natural carbonation. Little information is available on this subject in the literature, or a lack of consensus is reported for binders with a high slag content, for which classical electrochemical measurements lead to difficulties in the interpretation of the results obtained. This study proposes an original alternative approach to evaluate the corrosion kinetics, based on a galvanic current measurement combined with mass loss on the rebars. The results show that the galvanic current is significant in most of the cases tested (chlorides, carbonation) and should be taken into account in the evaluation of the corrosion currents, except for the SSC binder for which it remains low, whatever the conditions tested. Finally, the corrosion rates of the anodes activated by chlorides or carbonation are nevertheless high for the three low-carbon binders in the study, because the total current density is composed of the measured galvanic current, added to a high local current density at the anode. The corrosion rates on the carbonated anodes are however overestimated, as they were obtained on samples with an increased water/binder ratio, chosen to accelerate their natural carbonation.

Thus, a complete study of the corrosion risk is proposed, dealing with both the initiation and propagation phases, which are often dissociated. This experimental study also provides new perspectives to improve the use of these three low-carbon concretes, based on the evaluation of the durability of reinforcements in different environments (chlorides, carbonation). Finally, a method for the evaluation of corrosion kinetics applicable to other types of low-carbon concrete is proposed.

## **Keywords**

Durability, low-carbon concretes, electrochemical measurements, corrosion, alkali-activated materials, supersulfated cement.

## Résumé

De nouvelles technologies de béton avec une empreinte carbone réduite ont été développées, afin de répondre aux enjeux environnementaux actuels. Cependant, comme ces technologies sont récentes, peu d'informations sur leur durabilité sont disponibles, ce qui limite leur utilisation. En particulier des informations sur la résistance à la corrosion des armatures sont requises car il s'agit d'une des principales causes de dégradation des structures en béton armé ordinaires.

Cette thèse a donc pour objectif d'évaluer la durabilité des armatures dans trois types de bétons bas carbone, de même classe de résistance C25/30 : basse teneur en clinker (LCK), laitier alcali-activé au carbonate de sodium (AAS) et ciment sursulfaté (SSC). Ces bétons permettent une réduction de l'empreinte carbone allant de 40% à 75%, par rapport à un béton traditionnel à base de CEM I. L'objectif est de caractériser leur comportement vis-à-vis de la corrosion dans des conditions d'exposition différentes (exposition aux chlorures ou à la carbonatation).

Une première partie de ce travail consiste à caractériser et comparer les propriétés générales de transfert, le transport des chlorures et du CO<sub>2</sub> dans les trois bétons étudiés, qui vont conditionner le temps d'initiation de la corrosion dans ces derniers. Cette première partie de l'étude permet d'identifier les atouts et les limites de chaque solution bas carbone, ainsi que les environnements dans lesquels elles sont les plus performantes. Les résultats montrent que le béton LCK est caractérisé par de très bonnes propriétés de transfert (faible porosité à l'eau, perméabilité aux gaz, perméabilité à l'eau et absorption capillaire), mais une viscosité élevée à l'état frais et une perméabilité aux chlorures élevée. Les bétons AAS et SSC ont des propriétés de transfert similaires, comparables aux bétons classiques C25/30, et sont extrêmement résistants à la pénétration des chlorures. Les trois liants sont assez sensibles à la carbonatation naturelle, en particulier pour des courtes durées de cure.

Une seconde partie est dédiée à l'évaluation des cinétiques de corrosion, dans le cas d'une activation par contamination par les chlorures ou par carbonatation naturelle. En effet, peu d'information sont disponibles à ce sujet dans la littérature ou une absence de consensus est rapportée pour les liants à forte teneur en laitier, pour lesquels les mesures électrochimiques classiques entraînent des difficultés dans l'interprétation des résultats obtenus. Cette étude propose donc une approche alternative originale afin d'évaluer les cinétiques de corrosion, basée sur une mesure du courant galvanique combinée à de la perte de masse sur les armatures. Les résultats montrent que le courant galvanique est significatif dans la plupart des cas testés (chlorures, carbonatation) et devrait être pris en compte dans l'évaluation des courants de corrosion, excepté pour le liant SSC pour lequel il reste faible, peu importe les conditions testées. Finalement, les vitesses de corrosion des anodes activées par les chlorures ou par carbonatation sont néanmoins élevées pour les trois liants bas carbone de l'étude, car la densité de courant totale est composée du courant galvanique mesuré, auquel s'ajoute une densité de courant locale élevée au niveau de l'anode. Les vitesses sur les anodes carbonatées étant toutefois surestimées, car obtenues sur des échantillons avec un rapport eau/liant augmenté, choisi pour accélérer leur carbonatation naturelle.

Ainsi, une étude complète du risque de corrosion est proposée traitant à la fois les phases d'initiation et de propagation, qui sont souvent dissociées. Cette étude expérimentale permet aussi d'apporter de nouvelles perspectives pour améliorer l'utilisation de ces trois bétons bas carbone, basées sur l'évaluation de la durabilité des armatures dans différents environnements. Enfin, une méthode d'évaluation des cinétiques de corrosion applicable à d'autres types de béton bas carbone est proposée.

## Mots clés

Durabilité, béton bas carbone, mesures électrochimiques, corrosion, matériaux alcali-activés, ciment sursulfaté






# Table of Contents

<b>CHAPTER 1 - GENERAL INTRODUCTION.....</b>	<b>9</b>
<b>CHAPTER 2 – THEORETICAL BACKGROUND.....</b>	<b>17</b>
<b>CHAPTER 3 – ARTICLE A.....</b>	<b>39</b>
Durability (general transfer properties and chloride penetration resistance) of three low-carbon concretes (low clinker, alkali-activated slag and supersulfated cement)	
<b>CHAPTER 4 – ARTICLE B.....</b>	<b>93</b>
Resistance to carbonation of three low-carbon concretes (low clinker, alkali-activated slag and supersulfated cement) through natural and accelerated tests	
<b>CHAPTER 5 – ARTICLE C.....</b>	<b>147</b>
Chloride-induced corrosion of steel in three low-carbon concretes studied by galvanic current measurements	
<b>CHAPTER 6 – ARTICLE D.....</b>	<b>199</b>
Carbonation-induced corrosion of steel in three low-carbon concretes, with different saturation conditions, studied by galvanic current measurements	
<b>CHAPTER 7 – SYNTHESIS CHAPTER.....</b>	<b>261</b>
Durability of reinforcement in the three low-carbon concretes exposed to chlorides or carbonation	
<b>CHAPTER 8 – GENERAL CONCLUSION.....</b>	<b>275</b>







Chapter 1

# General Introduction



## 1 Context

The reduction of CO<sub>2</sub> emissions in the construction field is a big challenge nowadays in the fight against global warming. The stakes are high because concrete is the second most consumed material in the world after water (Scrivener, John, and Gartner 2018). Its manufacture from generally low-cost and widely available materials, as well as its convenience for different types of structures and environments, have made it an essential building material. The manufacture of Portland cement, which is traditionally used in its binder composition, is responsible for around 5-8% of greenhouse gas emissions worldwide (Olivier, Schure, and Peters 2017; Benhelal et al. 2013; Lakusic 2019). With the expansion of urbanization in the coming decades, the demand for cement and concrete is expected to increase, which requires the development of more sustainable concretes to limit their impact on the environment and to meet environmental requirements (Habert et al. 2020; Scrivener, John, and Gartner 2018).

In a concrete, approximately 90% of its carbon footprint is associated with the Ordinary Portland cement it contains, compared to 10% for the other components (aggregates, admixtures, etc.), the production of one ton of cement being equivalent to the production of about 800 kg of CO<sub>2</sub> (World Business Council for Sustainable Development 2014). One of the levers to reduce the carbon footprint of concrete, is therefore to reduce the amount of cement in the binder: either by reducing it to a more efficient use or by partially or entirely replacing it with other low-CO<sub>2</sub> supplementary cementitious materials (SCMs). These concretes are commonly referred to as low-carbon concretes, even if there is no official definition for such materials.

Different solutions of more eco-friendly concretes have been proposed, but as these materials are quite recent, the lack of information regarding their durability and particularly their compatibility with rebars and the associated risk of corrosion, still limits their use. Controlling the durability of structures is, indeed, a major issue in order to guarantee their safety and service life. This is even more true for corrosion, which is precisely one of the main causes of degradation leading to damage at the structural level (cracking, spalling, section loss of reinforcement) and significant repair costs. Moreover, corrosion of reinforcement can concern the majority of concrete structures, since it can be initiated by chloride ions (from marine environment or from de-icing salts for example), or by a drop in the pH of the pore solution (mainly caused by carbonation), in the presence of sufficient water and oxygen.

The service life of a reinforced concrete structure is generally divided into a corrosion initiation phase and a corrosion propagation phase. The initiation phase is the time needed for the aggressive agents (chlorides or CO<sub>2</sub>) to reach the rebar and potentially initiate corrosion, while the propagation phase is the active state of corrosion. Until now, most methods for lifetime prediction only considered the initiation phase, based on the diffusion rates of chlorides or the carbonation rates, which is a safe approach concerning the design of structures. Therefore, the great majority of the scientific literature also focuses on these phenomena and comparatively, a limited number of studies addressed the associated corrosion rates (Angst et al. 2020). Recently, several authors reported the importance to shift the focus in research to studying

corrosion of steel, without neglecting the initiation period of corrosion. It offers a great opportunity for the use of low-carbon concretes.

## **2 Objectives and challenges**

This thesis work, financed by the company Holcim, took place at the Laboratory of Materials and Durability of Constructions (LMDC - Toulouse), with some experimental tests carried out in parallel at Holcim Innovation Centre. The studies conducted focus on the durability of reinforcement in three technologies of low-carbon concretes: low clinker (LCK) concrete, alkali-activated slag with sodium carbonate (AAS) concrete and supersulfated cement (SSC) concrete. These three concretes are based on three different technologies and were chosen because they offer three different solutions for making low-carbon concretes (with at least 30% CO<sub>2</sub> footprint reduction). They have indeed different compositions, different carbon footprint and different performances, depending on the environments to which they are exposed. For the purpose of comparison in this work, the three concretes have been formulated to have the same strength class C25/30 and to be self-compacting. Higher strength classes are generally used for exposure to chlorides, but the approach here is to characterize the performance of C25/30 concretes, which are the most common in France. The measured performances on C25/30 concretes will be improved on concretes of a higher strength class. In the opposite case, improvement solutions will be proposed. The fact that they are self-compacting makes them easy to handle.

The main objective of this work is to characterize their behavior towards corrosion, in presence of chlorides or exposed to carbonation. In each case, the goal is to determine the time required for corrosion to initiate and the corrosion rates once the latter is initiated. Thus, it is expected to better understand the performance of each concrete in both environments and to provide a new insight to improve their use and to maximize their durability, based on the evaluation of their corrosion risks.

Another challenge, related to this first objective, is to use reliable and representative test methods, to characterize these concretes with different compositions and chemistry compared to Portland cement. The use of traditional protocols for durability tests or classical measurements for corrosion assessment, needs to be questioned before being applied to alternative low-carbon binders, to determine if metrology adaptations are required and to avoid misinterpretations of the results. Moreover, the corrosion phenomena being slow to develop in a reinforced concrete structure, actions must be taken to accelerate these phenomena in order to be able to study them over the duration of the thesis.

## **3 Organisation of the manuscript and research approach**

This manuscript has an original structure that is summarized as an organisation chart in Figure 1. It has been chosen to present the work done in four independent articles.

No bibliographic chapter was made, as it was replaced by a theoretical background chapter, and a literature review in the introductions of each article in order to give an efficient state of the

art of the topics addressed. The theoretical background proposes, on the one hand, a general presentation of the three concretes studied: composition, hydration mechanisms and associated hydration products. These characteristics allow a better understanding of the results obtained afterwards, as they are likely to influence the transfer properties of the three concretes, as well as their interaction with chlorides or CO<sub>2</sub> or even the corrosion process. On the other hand, the theoretical background described the classical corrosion mechanisms and a focus is made on the galvanic current.

Similarly, the materials and methods are not presented in a dedicated chapter, but are detailed at the beginning of each article.

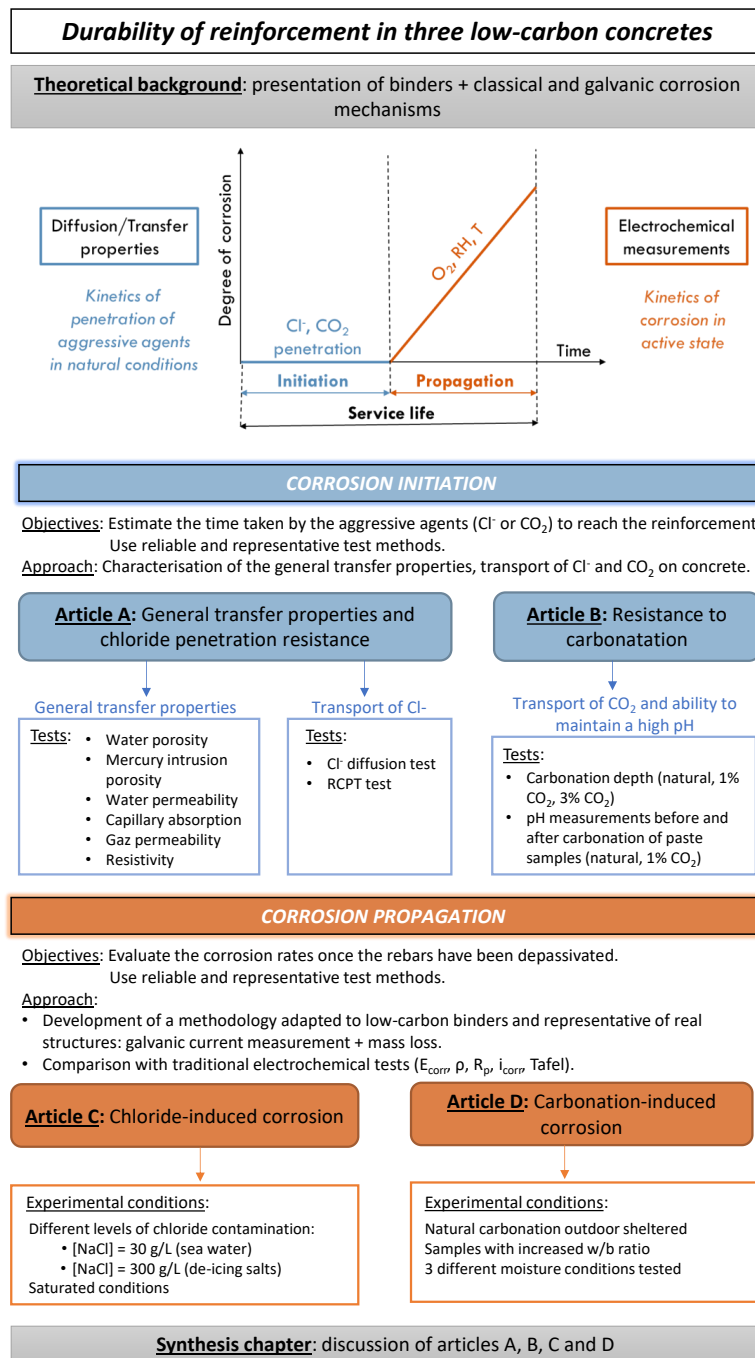


Figure 1: Organisation of the manuscript and research approach

## 4 Articles content

The approach chosen to study the durability of reinforcement can be explained from the Tuutti diagram, which decomposes the service life of reinforced concrete structures into two main time periods: a period of corrosion initiation and a period of propagation (Figure 1). An experimental work is proposed to answer the objectives. When possible, the tests are performed on concrete, in natural conditions, to remain as close as possible to real conditions.

**Articles A and B** focus on the initiation period. The main objective is to determine the time taken by the aggressive agents (chlorides or CO<sub>2</sub>) to penetrate through the concrete and to reach the rebar, causing a progressive rupture of the passive film on the steel surface. This initiation period depends mainly on the transfer and diffusion properties of the material, which must therefore be characterized. The properties of each concrete can also be compared to determine the strengths and weaknesses of each technology. The transition period from the time when the aggressive agents are at the steel concrete interface, to the time when steel depassivates and the corrosion starts, is not studied.

**Article A** studies the *general transfer properties* and *chloride* penetration resistance of the three concretes. General transfer properties are of primary importance, as the pore structure of the concrete is going to influence not only the corrosion initiation, but also the transport of water and oxygen at the steel concrete interface, necessary for the propagation period. Several durability indicators are evaluated. For the transport of chlorides, both natural and accelerated tests are performed, and the chloride binding capacity of each binder is discussed. The kinetics obtained are then extrapolated to deduce the time required for chlorides to reach the reinforcement. The properties of each concrete are compared with each other and to reference concretes from the literature. The use of durability tests that require a preconditioning phase is also questioned before being applied to low-carbon binders.

**Article B** is complementary to Article A, with a focus made on *carbonation* exposure. Article B compares the resistance to carbonation of the three concretes through natural and accelerated tests. The carbonation rates considering different curing periods are evaluated, and extrapolated to deduce the time required for the carbonation front to reach the reinforcement. The ability of LCK, AAS and SSC binders to maintain a high pH during the carbonation process is also investigated. Finally, the relevance of accelerated tests at 1 and 3% CO<sub>2</sub> to characterize the carbonation of low-carbon concretes is discussed.

**Articles C and D** focus on the propagation period, which corresponds to the active state of corrosion and is generally studied by electrochemical measurements. The objective is to evaluate the corrosion kinetics in each binder, once the rebars have been depassivated, either by chlorides (Article C), or by carbonation (Article D). As the literature reports difficulties to interpret the results obtained by classical electrochemical tests on slag-based binders, an original method (galvanic current) is proposed.

**Article C** focuses on the *corrosion rates in the presence of chlorides*. Corrosion is initiated by drying the samples, then immersing them in NaCl solutions. Two levels of chloride contamination are tested to evaluate the influence on the corrosion rates:  $[\text{NaCl}] = 30 \text{ g/L}$  (seawater), and  $[\text{NaCl}] = 300 \text{ g/L}$  (de-icing salts for example). Once the corrosion is initiated, the propagation period is studied by a galvanic current measurement combined with mass loss on the rebar. A comparison with classical electrochemical measurements (corrosion potential  $E_{\text{corr}}$ , polarization resistance  $R_p$ ) is also performed. Finally, recommendations are given for the use of each binder, in chloride-rich environments.

**Article D** focuses on the *corrosion rates due to carbonation*. Corrosion is initiated by natural carbonation on samples with an increased w/b ratio, to accelerate the initiation period. Three saturation conditions were tested to evaluate an interval of possible corrosion rates. Once the corrosion is initiated, the propagation period is studied by a galvanic current measurement combined with mass loss on the rebar. A comparison with classical electrochemical measurements (corrosion potential  $E_{\text{corr}}$ , polarization resistance  $R_p$ ) is also performed. As before, recommendations are given for the use of each binder, exposed to carbonation.

Finally, a synthetic chapter deals with the durability of the three low-carbon concretes exposed to chlorides or carbonation, from the point of view of corrosion. The behaviour of the low-carbon concretes compared to conventional concretes, is also discussed.

## 5 References

- Angst, Fabrizio Moro, Mette Geiker, Sylvia Kessler, Hans Beushausen, Carmen Andrade, Jukka Lahdensivu, et al. 2020. ‘Corrosion of Steel in Carbonated Concrete: Mechanisms, Practical Experience, and Research Priorities – a Critical Review by RILEM TC 281-CCC’. *RILEM Technical Letters* 5 (December): 85–100. <https://doi.org/10.21809/rilemtechlett.2020.127>.
- Benhelal, Emad, Gholamreza Zahedi, Ezzatollah Shamsaei, and Alireza Bahadori. 2013. ‘Global Strategies and Potentials to Curb CO<sub>2</sub> Emissions in Cement Industry’. *Journal of Cleaner Production* 51 (July): 142–61. <https://doi.org/10.1016/j.jclepro.2012.10.049>.
- Habert, G., S. A. Miller, V. M. John, J. L. Provis, A. Favier, A. Horvath, and K. L. Scrivener. 2020. ‘Environmental Impacts and Decarbonization Strategies in the Cement and Concrete Industries’. *Nature Reviews Earth & Environment* 1 (11): 559–73. <https://doi.org/10.1038/s43017-020-0093-3>.
- Lakusic, Stjepan. 2019. ‘Research Challenges for Broader Application of Alternative Binders in Concrete’. *Journal of the Croatian Association of Civil Engineers* 71 (10): 877–88. <https://doi.org/10.14256/JCE.2729.2019>.
- Olivier, J.G.J., K.M. Schure, and J.A.H.W. Peters. 2017. ‘Trends in Global CO<sub>2</sub> and Total Greenhouse Gas Emissions: 2017 Report’. Text. <https://www.pbl.nl/en/publications/trends-in-global-co2-and-total-greenhouse-gas-emissions-2017-report>.
- Scrivener, Karen L., Vanderley M. John, and Ellis M. Gartner. 2018. ‘Eco-Efficient Cements: Potential Economically Viable Solutions for a Low-CO<sub>2</sub> Cement-Based Materials Industry’. *Cement and Concrete Research* 114 (December): 2–26. <https://doi.org/10.1016/j.cemconres.2018.03.015>.
- World Business Council for Sustainable Development. 2014. ‘Cement Sustainability Initiative, Project Emissions Report 2014’. <http://www.gnr-project.org/>.





Chapter 2

# Theoretical Background

## Table of contents

<b>1</b>	<b>General presentation of the three low-carbon concretes studied .....</b>	<b>19</b>
1.1	Low clinker content (LCK) concrete.....	19
1.1.1	<i>General information .....</i>	<i>19</i>
1.1.2	<i>Hydration mechanisms and hydration products.....</i>	<i>20</i>
1.2	Alkali-activated slag (AAS) concrete.....	21
1.2.1	<i>General information .....</i>	<i>21</i>
1.2.2	<i>Hydration mechanisms .....</i>	<i>22</i>
1.2.3	<i>Hydration products.....</i>	<i>23</i>
1.3	Supersulfated cement (SSC) concrete .....	23
1.3.1	<i>General information .....</i>	<i>23</i>
1.3.2	<i>Hydration mechanisms and hydration products.....</i>	<i>24</i>
<b>2</b>	<b>Corrosion of steel rebars in reinforced concrete.....</b>	<b>26</b>
2.1	Corrosion process .....	26
2.1.1	<i>Passive film.....</i>	<i>26</i>
2.1.2	<i>Electrochemical background.....</i>	<i>27</i>
2.2	Uniform corrosion .....	28
2.3	Galvanic corrosion .....	29
<b>3</b>	<b>References.....</b>	<b>33</b>



## THEORETICAL BACKGROUND

The theoretical background is divided into two main parts. In section 1, a general presentation of the three concretes studied is proposed: composition, hydration mechanisms and associated hydration products. Then, in section 2, the classical corrosion mechanisms are presented and a focus is made on the galvanic current.

### 1 General presentation of the three low-carbon concretes studied

The thesis focuses on three types of low-carbon concretes: low clinker (LCK) concrete, alkali-activated slag with sodium carbonate ( $\text{Na}_2\text{CO}_3$ -AAS) concrete and supersulfated cement (SSC) concrete. In this section, a general presentation of the three concretes studied is proposed, dealing with their composition, hydration mechanisms and associated hydration products. These characteristics allow a better understanding of the results obtained in the research work, as they are likely to influence the transfer properties of the three concretes, as well as their interaction with chlorides or  $\text{CO}_2$  or even the corrosion process. Their main characteristics given by the literature are summarized in Table 1, and presented in more detail in the following sections.

*Table 1: Summary of main hydrates and  $\text{CO}_2$  footprint of LCK,  $\text{Na}_2\text{CO}_3$ -AAS and SSC concretes, from literature.*

	<b>LCK</b>	<b><math>\text{Na}_2\text{CO}_3</math>-AAS</b>	<b>SSC</b>
Binder composition	Ordinary Portland cement + limestone filler	Slag + $\text{Na}_2\text{CO}_3$ as activator	Slag + calcium sulfate + Portland cement
Main hydrates (Secondary hydrates)	C-S-H, $\text{Ca}(\text{OH})_2$ + ettringite, AFm	C-A-S-H + hydrotalcite, AFm	Ettringite, C-S-H + hydrotalcite
$\text{CO}_2$ footprint reduction / CEM I	↓ 15% for CEM II/A-L ↓ 27% for CEM II/B-L French values from SFIC (Syndicat Français de l'Industrie Cimentière) available on (ATILH 2022)	↓ 80% (Habert, d'Espinose de Lacaillerie, and Roussel 2011)	↓ 94% (Cyr et al. 2019)

#### 1.1 Low clinker content (LCK) concrete

##### 1.1.1 General information

LCK concrete is obtained by reducing the proportion of Portland cement in the binder, which is replaced by a large quantity of limestone filler. Its binder is also frequently called limestone blended cement or Portland limestone cement. In the thesis the LCK concrete considered has a higher binder volume made of 27% CEM I and 73% limestone filler.

The use of limestone filler as an addition in concrete was allowed for the first time in 1965 in Germany, then followed by different countries, and later in 2000 by the European Standard EN 197-1 as Portland limestone cements CEM II/A-L (6–20% limestone content) and CEM II/B-L (21–35% limestone content) (Elgalhud, Dhir, and Ghataora 2017). Portland limestone cements are now used worldwide, as calcium carbonate is a natural material widely available (Thenepalli et al. 2015), which makes it one of the most commonly used additions, compared to slag or fly ash for example.

The replacement of a part of the cement by a high amount of inert limestone fillers enables to reduce the amount of water needed while maintaining an acceptable rheology of concrete at fresh state, due to an optimized packing and admixture.. The fillers also have a filling function, to maintain acceptable mechanical resistances and durability performances. A decrease of durability performances is observed for more than 15% replacement by limestone fillers (Dhir et al. 2007; Hooton, Nokken, and Thomas 2007; Elgalhud, Dhir, and Ghataora 2017; 2018). They also act as a nucleation site, to accelerate hydration reactions.

In the literature, a limestone content up to 20% have been extensively studied because it corresponds to standard recommendations, as observed by the review of (Elgalhud, Dhir, and Ghataora 2017). In the same review, the authors report a limited number of studies investigating higher replacement levels by filler, up to 50%, which is still lower than the 73% filler content for the LCK concrete of this study.

### *1.1.2 Hydration mechanisms and hydration products*

Since LCK concrete is composed of CEM I and inert fillers, hydration mechanisms and products are similar to those of a traditional Portland cement-based concrete.

Anhydrous cement is composed of clinker and calcium sulfate (anhydrite or gypsum) in small quantities, acting as a setting regulator. By reacting with water, ordinary Portland cement, which is a hydraulic binder, will set and harden as a result of hydration reactions involving mechanisms of dissolution and precipitation. The hydration process has been widely described in the literature (Marchon and Flatt 2016; Bullard et al. 2011; E. M. Gartner and Gaidis 1989) and results in the formation of different hydration products presented below.

The main hydrates formed in a Portland cement-based concrete are C-S-H, portlandite, ettringite and AFm.

- **C-S-H** constitute 60 to 70% of an ordinary cement paste and provide the mechanical strength to the paste. They have a low solubility, a large specific surface and a layered structure.
- **Portlandite** ( $\text{Ca}(\text{OH})_2$ ) represents 20 to 25% of an ordinary cement paste. It is the most soluble hydrate and will therefore have an important impact on durability, because moving into solution it will increase porosity. Portlandite is also responsible for the very alkaline pH of the pore fluid solution.
- **Ettringite** and **AFm**. The proportion of ettringite and AFm formed depends on the initial amount of gypsum and aluminate. Ettringite often crystallizes in the form of

needles. It is stable at room temperature, but decomposes at 60 °C, which can impact the properties of the material for durability tests that require high drying temperatures. Literature reports that even if limestone fillers are inert compounds, their presence favour the formation of hemicarboaluminates and monocarboaluminates, instead of AFm (Lothenbach et al. 2008).

## **1.2 Alkali-activated slag (AAS) concrete**

### *1.2.1 General information*

Alkali-activated materials exist since the 1930s-1940s, but research around these materials really intensified in the 1990s, motivated by their low environmental impact compared to Portland cement as well as their good durability properties in aggressive environments, while offering mechanical performance superior or similar to some Portland cements (J. L. Provis and van Deventer 2014).

Alkali-activated materials are made of a precursor and an alkaline activator.

The **precursor** is a siliceous or silico-aluminous material, which is usually an industrial waste (slag, fly ash, glass powder, etc.) or a natural material having received a thermal treatment in the case of metakaolin. Depending on the precursor used, a system with a high calcium content (in the case of alkali-activated slag) or with a low calcium content (in the case of alkali-activated fly ash or metakaolin) is obtained.

The **alkaline activator** is a liquid or solid component whose alkaline source is an element from the group of alkali metals of the periodic table (except francium for its radioactive nature) and/or magnesium and/or calcium. The alkaline activator allows to provide a high pH to initiate the dissolution of the precursor and the setting process. The most commonly used alkaline activators studied in the literature for their availability and cost, are sodium silicate ( $\text{Na}_2\text{O} \cdot n\text{SiO}_2$ ), sodium hydroxide ( $\text{NaOH}$ ), sodium carbonate ( $\text{Na}_2\text{CO}_3$ ) and sodium sulfate ( $\text{Na}_2\text{SO}_4$ ) (Shi, Krivenko, and Roy 2006). Sodium carbonate activation is less often studied because it has a slower mechanical strength development (J. L. Provis and van Deventer 2014). However, sodium carbonate is in powder form with a lower risk of use than activations in alkaline solution form (S. Bernal 2016; Awoyera and Adesina 2019). Sodium carbonate has been the subject of new publications recently (Abdalqader, Jin, and Al-Tabbaa 2019; Ke et al. 2018) because it is less expensive and more environmentally friendly in its manufacturing process than sodium hydroxide or silicate. Thus, this state of the art will focus on the case of **AAS with sodium carbonate**.

The properties of AAS (hydration products, pore solution, structure of the porous network) are highly dependent on the slag composition and the type of alkaline activator.

### 1.2.2 Hydration mechanisms

The general mechanism of hydration of AAS and the reactions involved can be described as follows, according to (Ke 2017a; Mundra et al. 2020a; J. L. Provis and van Deventer 2014): (1) dissolution of the slag, i.e. destruction of Ca-O, Mg-O, Si-O-Si, Al-O-Al and Al-O-Si bonds; (2) exchange and rearrangement among the dissolved species from the slag and the activator; (3) formation of the hydration products; (4) solidification, hardening, and development of mechanical strengths.

A simplified diagram that summarizes the hydration process in the case of Na<sub>2</sub>CO<sub>3</sub>-AAS, is proposed on Figure 2, from (Ke, Bernal, and Provis 2016).

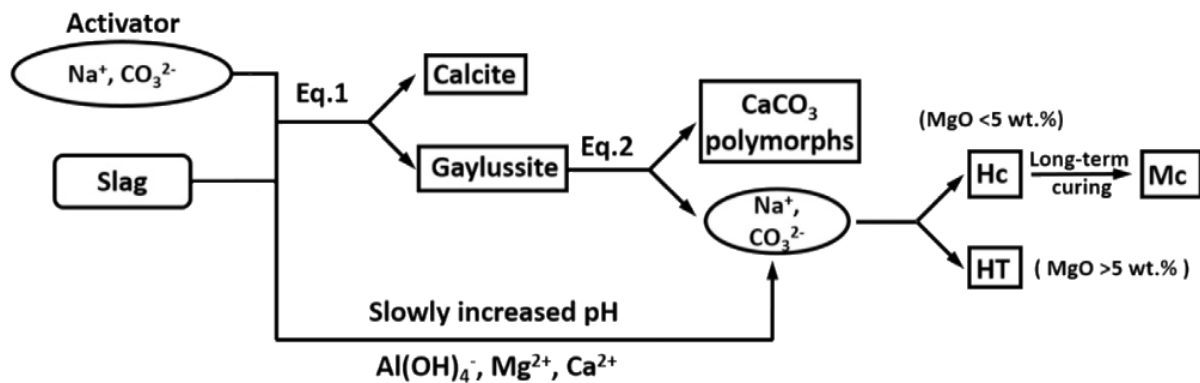
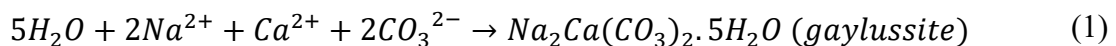
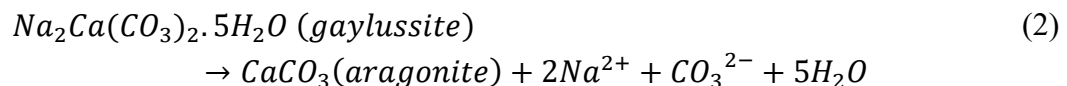


Figure 2: Simplified hydration mechanisms of alkali-activated slag with sodium carbonate. Hc: calcium hemicarboaluminates, Mc: calcium monocarboaluminates, HT: hydrotalcite. Adapted from (Ke, Bernal, and Provis 2016).

During hydration of Na<sub>2</sub>CO<sub>3</sub>-AAS, Ca<sup>2+</sup> ions released during slag dissolution, react with CO<sub>3</sub><sup>2-</sup> ions from the alkaline activator to form carbonate salts such as calcite (CaCO<sub>3</sub>) or gaylussite (Equation (1)). Gaylussite is often formed at a young age in Na<sub>2</sub>CO<sub>3</sub>-AAS, thanks to the high concentration of sodium brought by the activator (S. A. Bernal et al. 2015).



Then, when C-A-S-H (not represented on Figure 2) and secondary hydration products start to precipitate, gaylussite dissolves due to the decrease in CO<sub>3</sub><sup>2-</sup> concentration in the aqueous solution (S. A. Bernal et al. 2015). The carbonate ions then rapidly re-precipitate as CaCO<sub>3</sub> polymorphs (Equation (2)) (Bischoff, Herbst, and Rosenbauer 1991).



In addition to C-A-S-H, the calcium and aluminum remaining in solution will also precipitate to form AFm, as calcium hemicarboaluminates (Hc) which will become calcium monocarboaluminates (Mc) in the long term (after 28 days) (Ke, Bernal, and Provis 2016; C.

Li, Sun, and Li 2010). When magnesium is present in sufficient quantity, it will react with aluminum and carbonate ions to form hydrotalcite. The proportion of AFm and hydrotalcite depends directly on the chemical composition of the slag used and in particular on its magnesium content (Figure 2). For moderate MgO content, hydrotalcite and AFm are both formed (Ke, Bernal, and Provis 2016).

### 1.2.3 Hydration products

In the case of AAS with sodium carbonate, the main hydration product obtained is a gel-like C-A-S-H and two secondary hydration products are also formed (AFm and hydrotalcite) (J. L. Provis and Bernal 2014). AFm and hydrotalcite are both of type Double Lamellar Hydroxides (LDH): Ca-Al type for AFm and Mg-Al for hydrotalcite.

LDHs are groups of minerals that have a positively charged layer structure. This particular structure allows them to perform anion exchange with the pore solution in their intermediate layer, as with  $\text{OH}^-$  or  $\text{CO}_3^{2-}$  ions (Duan and Evans 2006; Mills et al. 2012; Matschei, Lothenbach, and Glasser 2007).

## 1.3 Supersulfated cement (SSC) concrete

### 1.3.1 General information

The activation of slag by sulfates was first described in 1909 by (Kühl 1908). The production of this cement began in 1914 in Germany, then in 1932 in France and Belgium and also spread to other European countries like Italy and the United Kingdom. One example is the use of supersulfated cement for the construction of the Palais de Chaillot in Paris in 1937 (Moranville-Regourd and Kamali-Bernard 2019). The realizations based on supersulfated cement developed particularly after the Second World War in Europe, during the period 1940-1960 (M. Papadakis, Venuat, and Vandamme 1970), because of a lack of Portland cement, leading to the standardization of this binder in several countries such as Germany or the United Kingdom. Later supersulfated cement disappeared from the market. The main reason given in the literature refers to changes in the chemical composition of granulated blast furnace slag (low  $\text{Al}_2\text{O}_3$  content) due to the raw materials used and the steelmaking processes, resulting in a less reactive slag, which could no longer be used with the former supersulfated cement formulations. The market then moved to the use of slag in slag-cement mixes (M.C.G. Juenger et al. 2011).

The composition of the supersulfated cement is defined by the European standard EN 15743 (AFNOR 2010). It is a mix of:

- **Slag** (>75%),
- **Calcium sulfate** (5-20%),  
*Calcium sulfate can be gypsum ( $\text{CaSO}_4 \cdot 2\text{H}_2\text{O}$ ), hemihydrate ( $\text{CaSO}_4 \cdot \frac{1}{2}\text{H}_2\text{O}$ ), or anhydrite ( $\text{CaSO}_4$ ) or a mixture of these three (AFNOR 2010).*
- **Portland cement** as alkaline activator (0-5%) to obtain a sufficient reactivity.



Other alkaline activators such as potassium hydroxide (KOH), calcium hydroxide ( $\text{Ca}(\text{OH})_2$ ) or sodium carbonate ( $\text{Na}_2\text{CO}_3$ ) have also been used (M.C.G. Juenger et al. 2011), but the most common is Portland cement.

- **Secondary constituents** such as lime, can also be added up to 5%, to improve the reactivity or physical properties of the cement (workability, water retention) (AFNOR 2010).

Nowadays, supersulfated cement is used for its low environmental impact, its low heat of hydration and its very good durability properties in chemically aggressive environments (particularly against sulfates or seawater), favouring its use for seaside constructions or underground structures (Ioannou 2012; Moranville-Regourd and Kamali-Bernard 2019; Novak and Sommer 2002; Cerib 2022). It is also worth noting the existence of commercially developed supersulfated cement, such as the Austrian Slagstar® (Woltron 2009).

### 1.3.2 Hydration mechanisms and hydration products

The hydration mechanisms of supersulfated cement were studied by several authors in the literature (A. Gruskovnjak et al. 2008; Astrid Gruskovnjak et al. 2011; Jacquemot 2014; Moranville-Regourd and Kamali-Bernard 2019).

Figure 3 shows an example of phase composition obtained for a supersulfated cement **activated by KOH**, from thermodynamic calculations (A. Gruskovnjak et al. 2008). In general, the alkaline environment of the pore solution promotes slag dissolution, allowing aluminum, calcium, and silicon from the slag to pass into solution. These ions can then react with calcium sulfate to form ettringite ( $\text{C}_3\text{A} \cdot 3\text{CaSO}_4 \cdot 32\text{H}_2\text{O}$ ) and C-S-H (with a different  $\text{CaO}/\text{SiO}_2$  ratio than Portland cement), which are the primary hydration products of supersulfated cements. Compared to Portland cement, a large amount of ettringite is formed during the first 7 days of hydration and is responsible for the setting and strength development at young age. This primary ettringite, formed during cement hydration, is not expansive and therefore does not lead to cracking (Portland Cement Association 2001). Secondary hydration products can also be formed such as hydrotalcite, by consuming magnesium and part of the aluminum. Traces of FeS complex are also observed due to the presence of sulfur in the slag. The reaction kinetics depend strongly on the slag chemistry, its fineness and the activator used.

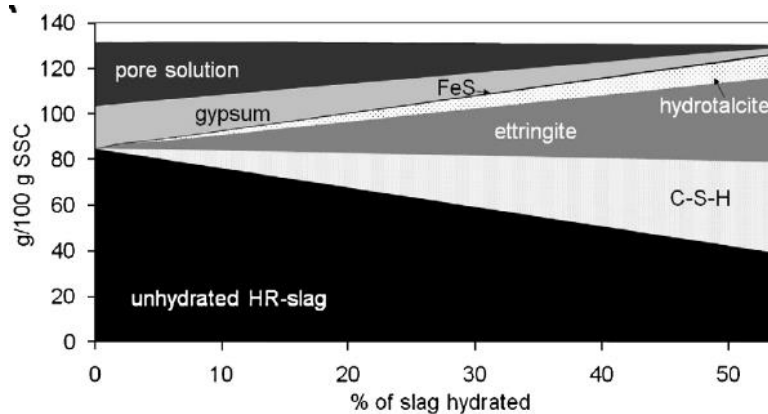


Figure 3: Hydration products formed in a supersulfated cement (composed by 85% reactive slag, 15% anhydrite and 0.5% KOH), according to the degree of hydration of the slag, obtained by thermodynamic calculations (A. Gruskovnjak et al. 2008).

For supersulfated cements **activated by Portland cement**, initially the Portland cement will hydrate to form C-S-H and portlandite ( $\text{Ca}(\text{OH})_2$ ). The portlandite will provide a highly alkaline solution to promote the dissolution of the slag (K. S. Nguyen et al. 2018), hence the role of alkaline activator. Then, in a second step the slag will react with calcium sulfate and portlandite released from the cement, to produce ettringite and C-S-H as described previously (Hegazy et al. 2019). The portlandite is completely consumed during hydration which makes the supersulfated cement vulnerable to carbonation (lack of  $\text{Ca}(\text{OH})_2$  to act as a pH buffer), but also particularly resistant to aggressive agents, because the very soluble portlandite is generally the first hydrate to pass into solution.

To summarize, the main hydration products of supersulfated cements are ettringite (the majority phase of the microstructure) and C-S-H, as well as a small amount of hydrotalcite as a secondary hydration product (Divet and Le Roy 2013; A. Gruskovnjak et al. 2008; Hegazy et al. 2019; M.C.G. Juenger et al. 2011; K. S. Nguyen et al. 2018). The chemical composition of the slag used to make supersulfated cement, strongly influences the amount of hydrates formed as well as the volume of reacted slag (A. Gruskovnjak et al. 2008).

## 2 Corrosion of steel rebars in reinforced concrete

In civil engineering, the corrosion of reinforced concrete is one of the main causes of the degradation of structures, resulting in a loss of adhesion between the rebar and the concrete, cracking in the case of expansive corrosion products, spalling and finally a loss of section of the rebars and thus of the mechanical resistances. Understanding the corrosion process and being able to quantify the associated kinetics, is therefore of great importance to anticipate these degradations.

In this section, the theoretical concepts relative to uniform corrosion or galvanic corrosion are introduced (Laurens et al. 2016; Broomfield 1997; C. Andrade et al. 1992; Raupach 1996; Luca Bertolini et al. 2013; Poursaee 2016; Zhou et al. 2015). The general mechanisms presented are those occurring in traditional Portland cement based-concretes.

### 2.1 Corrosion process

#### 2.1.1 Passive film

Steel in concrete is initially in a passive state, due to the very high pH of the pore solution ( $\text{pH} \approx 13$ ), which leads to the spontaneous formation of a protective layer of iron oxides on the rebar, called the passive film. The formation the passive film is thermodynamically possible in concrete, as illustrated by the potential-pH Pourbaix diagram of Fe/H<sub>2</sub>O system (Figure 4).

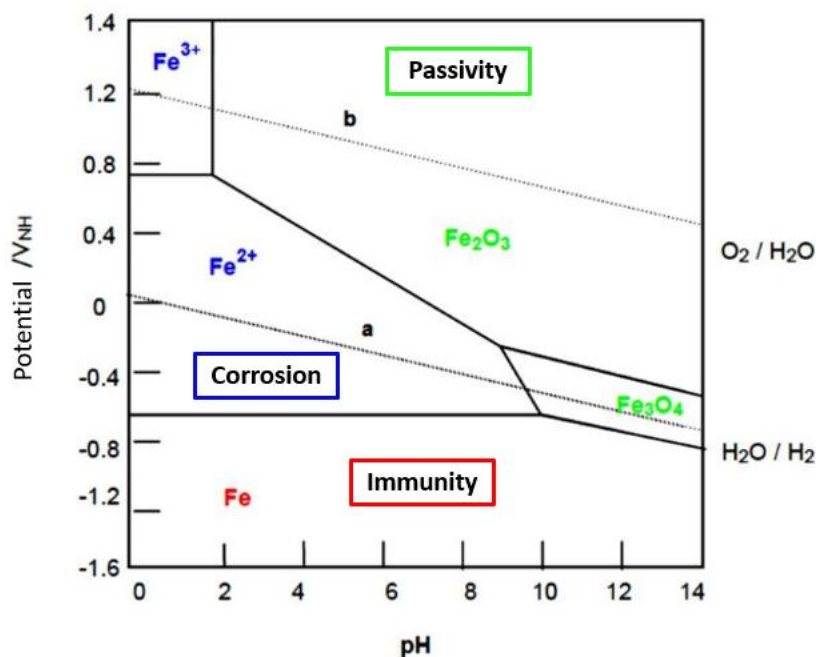


Figure 4: Simplified Pourbaix diagram of the Fe/H<sub>2</sub>O system, at 25 °C and 1 atm (for  $[\text{Fe}^{2+}] = [\text{Fe}^{3+}] = 10^{-6} \text{ mol/L}$ ), adapted from (Pourbaix and de Zoubov 1963).

In reinforced concrete the depassivation of the steel, i.e. the rupture of its passive film, can lead to corrosion. There are two main causes able to lead to steel depassivation:

- The contamination of concrete by **chloride ions** (from sea water, sea air or de-icing salts). The ingress of chloride ions in concrete may lead to a local breakdown of the passive film when a high concentration is reached at the steel/concrete interface, and corrosion can be initiated.
- The concrete **carbonation**, as the carbonation reactions lead to a pH drop in the concrete pore solution. For a pH less than 9 the passive film becomes unstable and steel depassivation can occur, leading to a corrosion initiation.

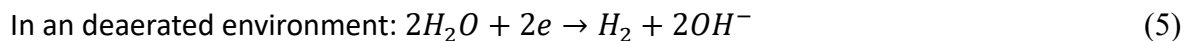
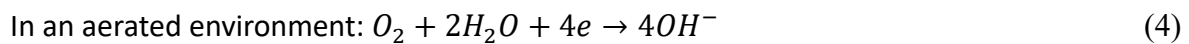
### 2.1.2 Electrochemical background

Once the steel is locally depassivated, the following four conditions are required for stable corrosion to develop in reinforced concrete:

- **1 anodic reaction:** oxidation of iron, producing electrons (Equation (3)).

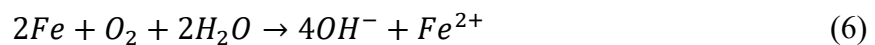


- **1 cathodic reaction:** oxygen reduction consuming electrons (Equations (4) or (5)).



- **1 ionic conductor or electrolyte:** concrete.
- **1 electronic conductor** transporting electrons from the anode to the cathode: the rebar.

To summarize, corrosion reactions are oxidation-reduction reactions that take place at the steel/concrete interface and involve the  $Fe^{2+}/Fe$  and  $O_2/H_2O$  redox couples. Corrosion is an electrochemical process that involves the anodic dissolution of iron which will provide electrons for the cathodic reduction of oxygen, through the redox reaction (Equation (6)):



The rebar acts as an electrical connection to transfer electrons from the anode to the cathode, while the concrete pore solution acts as an electrolyte allowing the transport of ionic species, as shown in Figure 5.

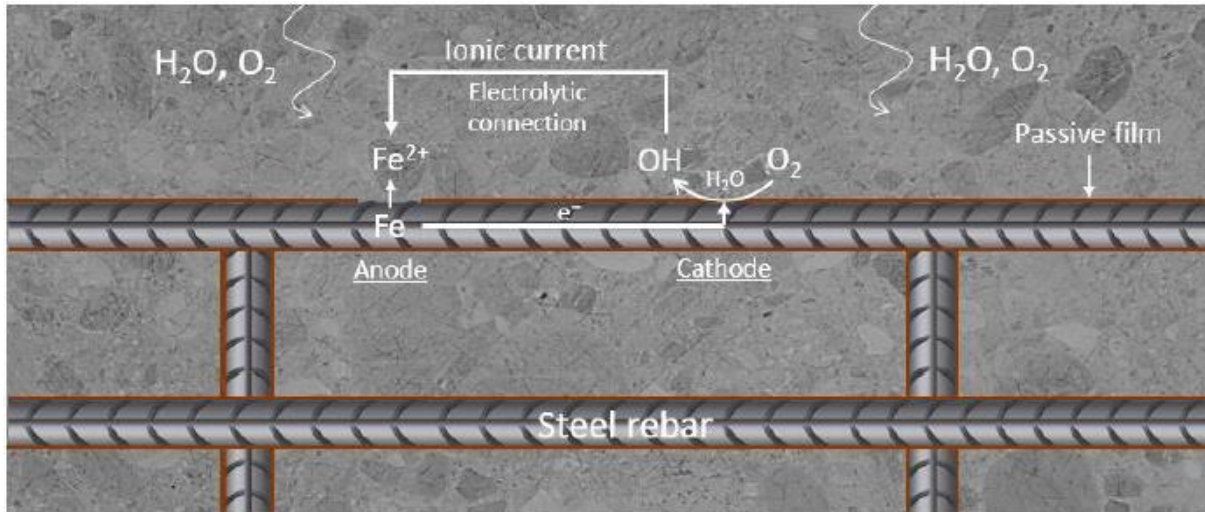


Figure 5: Corrosion process of steel in concrete from (Rodrigues et al. 2020).

Depending on the spatial location of the anodic and cathodic reactions, two main types of corrosion can be distinguished in steel reinforced concrete: **uniform corrosion** and **galvanic corrosion**.

## 2.2 Uniform corrosion

In the case of uniform corrosion (also called microcell corrosion), the sites of the cathodic and anodic reactions are not spatially dissociated on the macroscopic scale. Therefore, there is no electrical resistance between the anode and cathode, and each electron produced by the anodic reaction is locally consumed by the cathodic reaction.

Steel rebars have a uniform electrochemical state (active or passive) and therefore there is no current flowing in the concrete volume. The reciprocal polarization of the two redox systems and the negligible electrolyte resistivity, leads to a single potential and a uniform corrosion rate.

The passive steel can also be considered as a uniform corrosion system, associated to a very low corrosion rate and considered negligible compared to the lifetime of the structure.

The electrochemical behaviour of a uniform corrosion system can be described by the Butler-Volmer equation (Equation (7)), which is composed of a cathodic part (corresponding to the reduction of oxygen) and an anodic part (corresponding to the oxidation of iron), as illustrated in Figure 6. The equilibrium corrosion potential ( $E_{corr}$ ) corresponds to the value at which anodic current is balanced by cathodic current (Figure 6).

$$i = i_{corr} \left( \exp \left( \ln (10) \frac{E - E_{corr}}{\beta_a} \right) - \exp \left( \ln (10) \frac{E - E_{corr}}{\beta_c} \right) \right) \quad (7)$$

With:

$E_{corr}$  = potential of the uniform corrosion system at equilibrium (V/ref.)

$i$  = net current density ( $A/m^2$ ) flowing through the metal-electrolyte interface of the uniform system forced at potential  $E$  (involving a polarization with respect to the equilibrium potential  $E_{corr}$ )

$i_{\text{corr}}$  = corrosion current density ( $\text{A}/\text{m}^2$ ), corresponding to the exchange current density of the uniform corrosion system

$\beta_a$  and  $\beta_c$  = anodic and cathodic Tafel slopes ( $\text{V}/\text{dec}$ ) of the electrochemical system, respectively

The **polarization curves** (current-potential curve) corresponding to the electrochemical behaviour of either an active uniform corrosion system (referred by “a” indices) or a passive uniform corrosion system (referred by “p” indices), are presented in Figure 6. They are described by the Butler-Volmer model (Equation (7)).

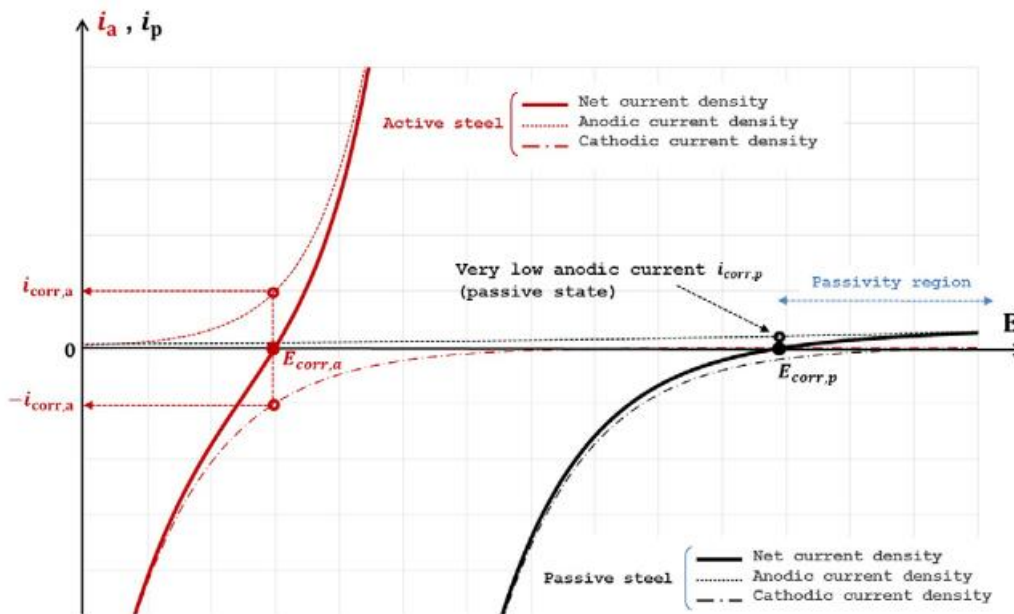


Figure 6: Polarization curves of active (in red) and passive (in black) uniform corrosion systems, from (Laurens et al. 2016).

### 2.3 Galvanic corrosion

In the case of galvanic corrosion (also called macrocell or localized corrosion), the anodic and cathodic reactions are spatially dissociated on a macroscopic scale (as opposed to the uniform corrosion presented before). This results in the existence of an electrical resistance between the anode and cathode (electrical resistivity of the concrete between active and passive sites is not negligible).

Steel rebars have no more a uniform electrochemical state. On the contrary, local differences in the steel electrochemical state are induced by partial carbonation of the concrete, or contamination by chloride ions, resulting in a local depassivation of the steel. In this configuration (galvanic corrosion system), electrons produced by the anodic reaction can be consumed by the cathodic reaction taking place on a distant site on the rebar network (the rebar network being electrically connected).

Therefore, as the electrical resistivity of concrete is not negligible, there is a non-uniform potential field and a galvanic current exchanged through the rebar network, combined with a ionic current flowing in the concrete volume between the anodic and cathodic sites. The concrete resistivity is an important parameter, because it strongly influences the galvanic ionic current exchanged.

As proposed by (Laurens et al. 2016), a galvanic corrosion system “may be defined as the electrical coupling of active and passive uniform corrosion systems, making it possible for the two systems to exchange electrons through a metallic connection”, as represented on Figure 7. Consequently, there is a mutual polarisation of anode and cathode, as the passive steel is subjected to a cathodic polarisation ( $E_{corr,p}$  towards  $E_p$ ), while active steel is subjected to an anodic polarisation ( $E_{corr,a}$  towards  $E_a$ ) (Figure 7). Due to concrete resistivity, there is no a single potential and the passive cathodic potential ( $E_p$ ) remains higher than the active anodic potential ( $E_a$ ), as illustrated on Figure 7.

According to Ohm’s law, the ohmic drop between active ( $E_a$ ) and passive ( $E_p$ ) potentials can be related to the galvanic current ( $I_m$ ) and the concrete resistance ( $R_e$ ) (Equation (8)).

$$E_p - E_a = R_e - I_m \quad (8)$$

At the equilibrium of the galvanic system, the anodic current produced by the anodic area ( $I_a$ ) is balanced by the cathodic current produced by the cathodic area ( $I_p$ ), resulting in the galvanic current ( $I_m$ ) (Equation (9)).

$$I_a = -I_p = I_m \quad (9)$$

As illustrated on Figure 7, in addition to the galvanic corrosion ( $I_m$ ), a uniform corrosion on the active steel area can still occur ( $I_{micro}$ ). The total corrosion rate ( $I_{corr}$ ) is therefore the sum of the two, as described by Equation (10).

$$I_{corr} = I_m + I_{micro} \quad (10)$$

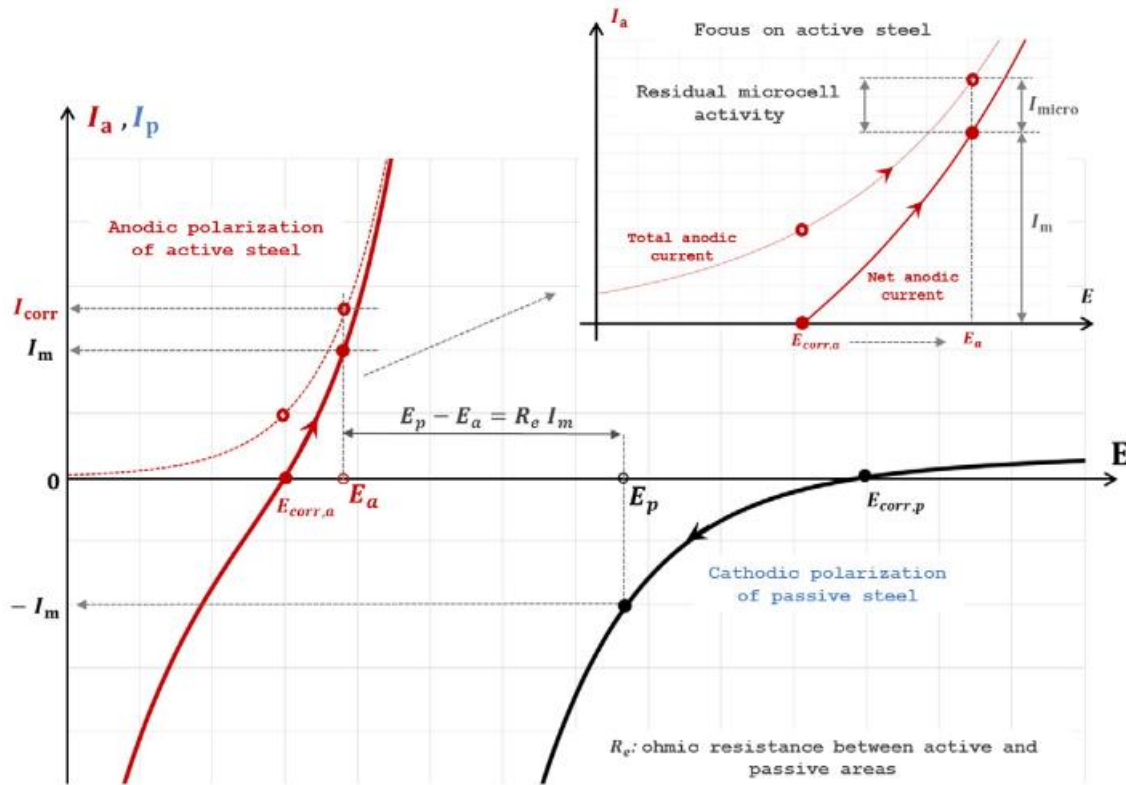


Figure 7: Mutual polarization of active (in red) and passive (in black) areas in a galvanic corrosion system, from (Laurens et al. 2016).

In a real structure, the penetration of chlorides into the concrete is not uniform due to the heterogeneity of the material, which results in a localized corrosion. The locally activated areas, are then coupled with the rest of the passive rebar network, generating a galvanic current, as shown in Figure 8. These localized attacks of the rebar network are generally characterized by corrosion spots.

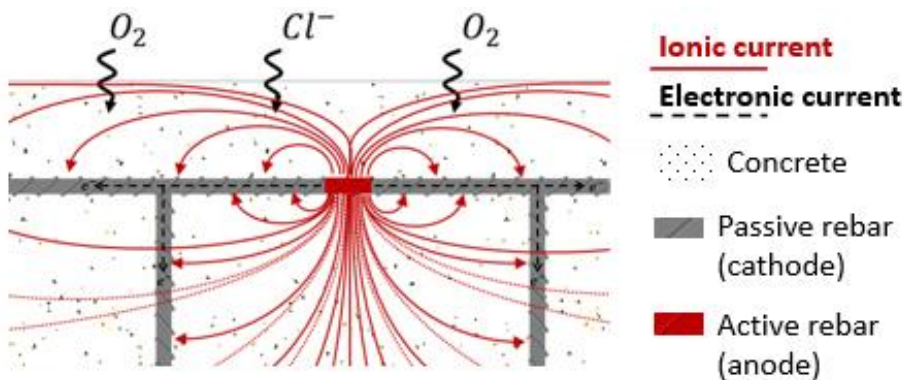


Figure 8: Representation of the galvanic corrosion due to chloride contamination of concrete (Deby and Laurens 2017).

Similarly, in a real structure exposed to carbonation, the carbonation front is rarely uniform due to the heterogeneous nature of the concrete. As for chlorides, the depassivation of a local area or of the first bed of rebar, will generate a galvanic current with the rest of the passive network, as shown in Figure 9.



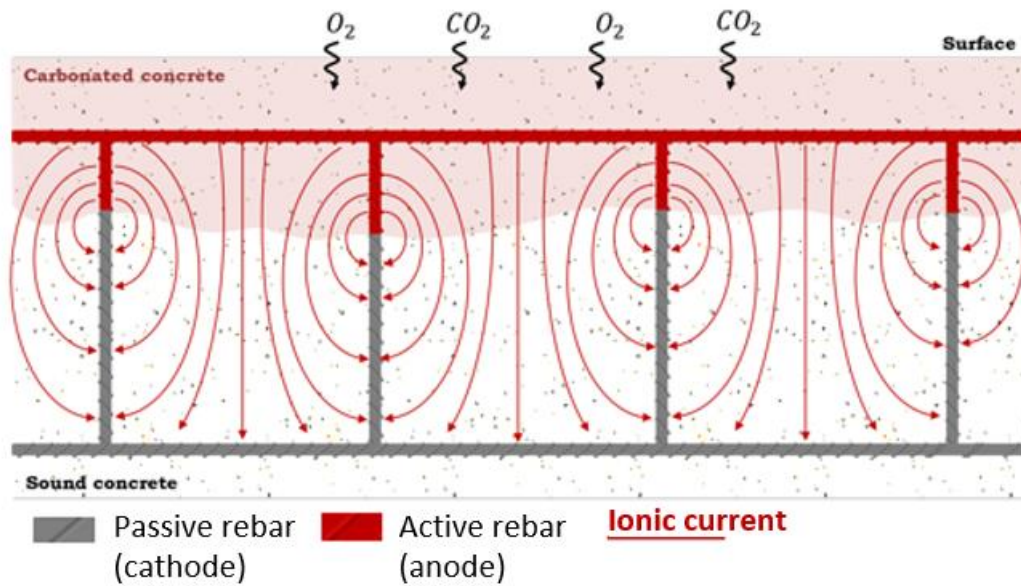


Figure 9: Representation of the galvanic corrosion due to concrete carbonation (Deby and Laurens 2017).

Finally, the surface ratio between cathode and anode ( $C/A$ ) is also an important parameter which will condition the level of galvanic current exchanged and the corrosion kinetics. The higher the  $C/A$  ratio, the higher the dissolution rate of the anodic zone. Different  $C/A$  ratios can be expected in the case of chloride contamination (small active steel surface) and in the case of carbonation (higher active steel surface), as shown in Figure 8 and Figure 9. These ratios are not fixed and will evolve over time as the active steel zones get larger and larger.

### 3 References

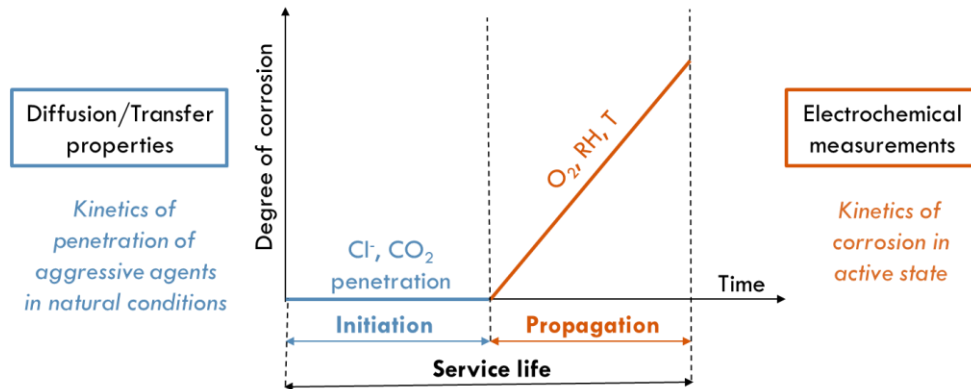
- Abdalqader, Ahmed, Fei Jin, and Abir Al-Tabbaa. 2019. 'Performance of Magnesia-Modified Sodium Carbonate-Activated Slag/Fly Ash Concrete'. *Cement and Concrete Composites* 103 (October): 160–74. <https://doi.org/10.1016/j.cemconcomp.2019.05.007>.
- AFNOR. 2010. 'NF EN 15743 : Ciment Sursulfaté - Composition, Spécifications et Critères de Conformité'.
- Andrade, C., I.R. Maribona, S. Feliu, J.A. González, and S. Feliu. 1992. 'The Effect of Macrocells between Active and Passive Areas of Steel Reinforcements'. *Corrosion Science* 33 (2): 237–49. [https://doi.org/10.1016/0010-938X\(92\)90148-V](https://doi.org/10.1016/0010-938X(92)90148-V).
- ATILH. 2022. 'Ciments et LHR : Analyse et Inventaire Du Cycle de Vie (ACV/ICV), Déclaration Environnementale Produit (DEP)'. Infociments. June 2022. <https://www.infociments.fr/ciments/ciments-declaration-environnementale-inventaire-analyse-du-cycle-de-vie>.
- Awoyera, Paul, and Adeyemi Adesina. 2019. 'A Critical Review on Application of Alkali Activated Slag as a Sustainable Composite Binder'. *Case Studies in Construction Materials* 11 (December): e00268. <https://doi.org/10.1016/j.cscm.2019.e00268>.
- Bernal, Susan. 2016. 'Advances in Near-Neutral Salts Activation of Blast Furnace Slags'. *RILEM Technical Letters* 1 (June): 39. <https://doi.org/10.21809/rilemtechlett.2016.8>.
- Bernal, Susan A., John L. Provis, Rupert J. Myers, Rackel San Nicolas, and Jannie S. J. van Deventer. 2015. 'Role of Carbonates in the Chemical Evolution of Sodium Carbonate-Activated Slag Binders'. *Materials and Structures* 48 (3): 517–29. <https://doi.org/10.1617/s11527-014-0412-6>.
- Bischoff, James L., David B. Herbst, and Robert J. Rosenbauer. 1991. 'Gaylussite Formation at Mono Lake, California'. *Geochimica et Cosmochimica Acta* 55 (6): 1743–47. [https://doi.org/10.1016/0016-7037\(91\)90144-T](https://doi.org/10.1016/0016-7037(91)90144-T).
- Broomfield, J.P. 1997. *Corrosion of Steel in Concrete*. E&FN Spon. London, UK.
- Bullard, Jeffrey W., Hamlin M. Jennings, Richard A. Livingston, Andre Nonat, George W. Scherer, Jeffrey S. Schweitzer, Karen L. Scrivener, and Jeffrey J. Thomas. 2011. 'Mechanisms of Cement Hydration'. *Cement and Concrete Research, Conferences Special: Cement Hydration Kinetics and Modeling, Quebec City, 2009 & CONMOD10, Lausanne, 2010*, 41 (12): 1208–23. <https://doi.org/10.1016/j.cemconres.2010.09.011>.
- Cerib. 2022. 'Impact Carbone Des Laitiers de Haut Fourneau Utilisés Dans Les Ciments'. July 2022. <https://www.cerib.com/impact-carbone-des-laitiers-de-haut-fourneau-utilises-dans-les-ciments/>.
- Cyr, Martin, Ludovic André, Mailys Ruau, Nicolas Musikas, and Laurent Frouin. 2019. 'Durability of Supersulfated Cement with Improved Early Strength'. *15th International Congress on the Chemistry of Cement, Prague, Czech Republic*.
- Deby, Fabrice, and Stéphane Laurens. 2017. 'Théorie Générale de La Corrosion, Cas de l'acier Dans Le Béton'. Cours de master 2 IDRIMS, INSA Toulouse, Université Toulouse III.
- Dhir, R. K., M. C. Limbachiya, M. J. McCarthy, and A. Chaipanich. 2007. 'Evaluation of Portland Limestone Cements for Use in Concrete Construction'. *Materials and Structures* 40 (5): 459–73. <https://doi.org/10.1617/s11527-006-9143-7>.
- Divet, Loïc, and Robert Le Roy. 2013. 'Étude de La Durabilité Vis-à-Vis de La Corrosion Des Armatures Des Bétons Formulés Avec Des Ciments à Forte Teneur En Laitier de Haut Fourneau'. *BLPC*, no. 280–281 (November).
- Duan, Xue, and David G. Evans. 2006. *Layered Double Hydroxides*. Springer Science & Business Media.
- Elgalhud, Abdurrahman A., Ravindra K. Dhir, and Gurmel Ghataora. 2018. 'Chloride Ingress in Concrete: Limestone Addition Effects'. *Magazine of Concrete Research* 70 (6): 292–313. <https://doi.org/10.1680/jmacr.17.00177>.
- Elgalhud, Abdurrahman A., Ravindra K. Dhir, and Gurmel S. Ghataora. 2017. 'Carbonation Resistance of Concrete: Limestone Addition Effect'. *Magazine of Concrete Research* 69 (2): 84–106. <https://doi.org/10.1680/jmacr.16.00371>.
- Gartner, E.M., and J.M. Gaidis. 1989. 'Hydration Mechanisms'. *Materials Science of Concrete, The American Ceramic Society*, 99–125.

- Gruskovnjak, A., B. Lothenbach, F. Winnefeld, R. Figi, S.-C. Ko, M. Adler, and U. Mäder. 2008. 'Hydration Mechanisms of Super Sulphated Slag Cement'. *Cement and Concrete Research* 38 (7): 983–92. <https://doi.org/10.1016/j.cemconres.2008.03.004>.
- Gruskovnjak, Astrid, Barbara Lothenbach, Frank Winnefeld, Beat Münch, Renato Figi, Suz-Chung Ko, Michael Adler, and Urs Mäder. 2011. 'Quantification of Hydration Phases in Supersulfated Cements: Review and New Approaches'. *Advances in Cement Research* 23 (6): 265–75. <https://doi.org/10.1680/adcr.2011.23.6.265>.
- Habert, G., J.B. d'Espinose de Lacaillerie, and N. Roussel. 2011. 'An Environmental Evaluation of Geopolymer Based Concrete Production: Reviewing Current Research Trends'. *Journal of Cleaner Production* 19 (11): 1229–38. <https://doi.org/10.1016/j.jclepro.2011.03.012>.
- Hegazy, A., A. Khalil, E. El-Alfi, and M. El-Shahat. 2019. 'Durability of Supersulphated Cement Pastes Activated with Portland Cement in Magnesium Chloride Solution'. *Egyptian Journal of Chemistry* 62 (6): 1145–55. <https://doi.org/10.21608/ejchem.2019.6563.1579>.
- Hooton, Doug, Michelle Nokken, and M. Thomas. 2007. 'Portland-Limestone Cement: State-of-the-Art Report and Gap Analysis For CSA A 3000'. *SN3053*, January.
- Ioannou, Socrates. 2012. 'An Assessment of the Performance of Calcium Sulfoaluminate and Supersulfated Cements for Use in Concrete'. PhD, UK: University of Bath.
- Jacquemot, François. 2014. 'Accélération Du Durcissement Des Liants à Base de Laitier de Haut Fourneau Pour Les Produits Préfabriqués En Béton'. Mines de Douai.
- Juenger, M.C.G., F. Winnefeld, J.L. Provis, and J.H. Ideker. 2011. 'Advances in Alternative Cementitious Binders'. *Cement and Concrete Research* 41 (12): 1232–43. <https://doi.org/10.1016/j.cemconres.2010.11.012>.
- Ke, Xinyuan. 2017. 'Improved Durability and Sustainability of Alkali-Activated Slag Cements'. PhD, University of Sheffield. <http://etheses.whiterose.ac.uk/17557/>.
- Ke, Xinyuan, Susan A. Bernal, and John L. Provis. 2016. 'Controlling the Reaction Kinetics of Sodium Carbonate-Activated Slag Cements Using Calcined Layered Double Hydroxides'. *Cement and Concrete Research* 81 (March): 24–37. <https://doi.org/10.1016/j.cemconres.2015.11.012>.
- Ke, Xinyuan, Maria Criado, John L. Provis, and Susan A. Bernal. 2018. 'Slag-Based Cements That Resist Damage Induced by Carbon Dioxide'. *ACS Sustainable Chemistry & Engineering* 6 (4): 5067–75. <https://doi.org/10.1021/acssuschemeng.7b04730>.
- Kühl, H. 1908. Verfahren zur Herstellung von Zement aus Hochofenschlacke. German Patent No. 237777, issued 1908.
- Laurens, S., P. Hénoq, N. Rouleau, F. Deby, E. Samson, J. Marchand, and B. Bissonnette. 2016. 'Steady-State Polarization Response of Chloride-Induced Macrocell Corrosion Systems in Steel Reinforced Concrete — Numerical and Experimental Investigations'. *Cement and Concrete Research* 79 (January): 272–90. <https://doi.org/10.1016/j.cemconres.2015.09.021>.
- Li, Chao, Henghu Sun, and Longtu Li. 2010. 'A Review: The Comparison between Alkali-Activated Slag (Si+Ca) and Metakaolin (Si+Al) Cements'. *Cement and Concrete Research* 40 (9): 1341–49. <https://doi.org/10.1016/j.cemconres.2010.03.020>.
- Lothenbach, Barbara, Gwenn Le Saout, Emmanuel Gallucci, and Karen Scrivener. 2008. 'Influence of Limestone on the Hydration of Portland Cements'. *Cement and Concrete Research*, 848–60. <https://doi.org/10.1016/j.cemconres.2008.01.002>.
- Marchon, D., and R. J. Flatt. 2016. '8 - Mechanisms of Cement Hydration'. In *Science and Technology of Concrete Admixtures*, edited by Pierre-Claude Aïtcin and Robert J Flatt, 129–45. Woodhead Publishing. <https://doi.org/10.1016/B978-0-08-100693-1.00008-4>.
- Matschei, T., B. Lothenbach, and F.P. Glasser. 2007. 'The AFm Phase in Portland Cement'. *Cement and Concrete Research* 37 (2): 118–30. <https://doi.org/10.1016/j.cemconres.2006.10.010>.
- Mills, S. J., A. G. Christy, J.-M. R. Génin, T. Kameda, and F. Colombo. 2012. 'Nomenclature of the Hydrotalcite Supergroup: Natural Layered Double Hydroxides'. *Mineralogical Magazine* 76 (5): 1289–1336. <https://doi.org/10.1180/minmag.2012.076.5.10>.
- Moranville-Regourd, Micheline, and Siham Kamali-Bernard. 2019. 'Cements Made From Blastfurnace Slag'. In *Lea's Chemistry of Cement and Concrete*, 469–507. Elsevier. <https://doi.org/10.1016/B978-0-08-100773-0.00010-1>.

- Mundra, Shishir, Dale P. Prentice, Susan A. Bernal, and John L. Provis. 2020. ‘Modelling Chloride Transport in Alkali-Activated Slags’. *Cement and Concrete Research* 130 (April): 106011. <https://doi.org/10.1016/j.cemconres.2020.106011>.
- Nguyen, Khanh Son, Anh Toan Nguyen-Phung, Hong Thai Le, Thanh Tri Ho, Tri Huynh Nguyen-Ngoc, Soon Poh Yap, Nobuhiro Chijiwa, and Nobuaki Otsuki. 2018. ‘Chloride Binding Ability and Anti-Corrosion Properties of Supersulfated Cement in Seawater/Sand Mixing Concrete’. In *Proceedings of the 4th Congrès International de Géotechnique - Ouvrages -Structures*, edited by Hoang-Hung Tran-Nguyen, Henry Wong, Frederic Ragueneau, and Cuong Ha-Minh, 8:367–76. Singapore: Springer Singapore. [https://doi.org/10.1007/978-981-10-6713-6\\_36](https://doi.org/10.1007/978-981-10-6713-6_36).
- Novak, D, and H Sommer. 2002. ‘A New Low-Heat Sulfate Resistant Binder for Mass Concrete, HPC and SCC’. *Proceedings of the International Conference Held at the University of Dundee, Scotland, Challenges of Concrete Construction*, 5 (September): 213–22. <https://doi.org/10.1680/scc.31777>.
- Papadakis, M., M. Venuat, and J. Vandamme. 1970. *Industrie de La Chaux, Du Ciment et Du Plâtre*. Dunod. Paris.
- Portland Cement Association. *Ettringite Formation and the Performance of Concrete*. Portland Cement Association, 2001.
- Pourbaix, M.J.N., and N. de Zoubov. 1963. *Atlas d’équilibres Electrochimiques*. Gauthier-Villars. Paris.
- Provis, John L., and Susan A. Bernal. 2014. ‘Geopolymers and Related Alkali-Activated Materials’. *Annual Review of Materials Research* 44 (1): 299–327. <https://doi.org/10.1146/annurev-matsci-070813-113515>.
- Provis, John L., and Jannie S. J. van Deventer, eds. 2014. *Alkali Activated Materials*. Vol. 13. RILEM State-of-the-Art Reports. Dordrecht: Springer Netherlands. <https://doi.org/10.1007/978-94-007-7672-2>.
- Raupach, M. 1996. ‘Chloride-Induced Macrocell Corrosion of Steel in Concrete—Theoretical Background and Practical Consequences’. *Construction and Building Materials, Durability of Reinforced Concrete Structures*, 10 (5): 329–38. [https://doi.org/10.1016/0950-0618\(95\)00018-6](https://doi.org/10.1016/0950-0618(95)00018-6).
- Rodrigues, Romain, Stéphane Gaboreau, Julien Gance, Ioannis Ignatiadis, and Stéphanie Betelu. 2020. ‘Corrosion of Carbon Steel in Concrete: Current Knowledge of Corrosion Mechanisms and Non-Destructive Testing of Corrosion Rates’.
- Shi, Caijun, Pavel V. Krivenko, and Della M. Roy. 2006. *Alkali-Activated Cements and Concretes*. New York: Taylor & Francis.
- Thenepalli, Thriveni, Ahn Young Jun, Choon Han, Chilakala Ramakrishna, and Ji-whan Ahn. 2015. ‘A strategy of precipitated calcium carbonate (CaCO<sub>3</sub>) fillers for enhancing the mechanical properties of polypropylene polymers’. *Korean Journal of Chemical Engineering* 32 (6): 1009–22. <https://doi.org/10.1007/s11814-015-0057-3>.
- Woltron, Günter. 2009. ‘The Utilisation of GGBFS for Advanced Supersulfated Cements’. *World Cement Magazine*, 157–62.

## Durability of reinforcement in three low-carbon concretes

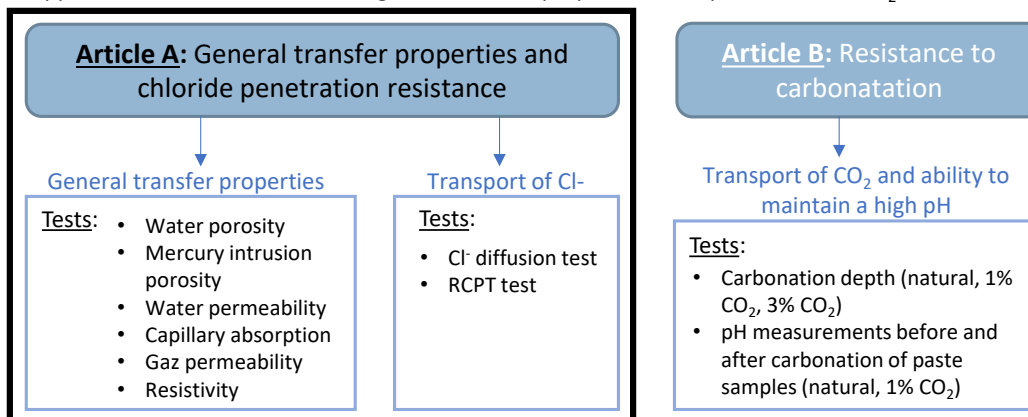
**Theoretical background:** presentation of binders + classical and galvanic corrosion mechanisms



### CORROSION INITIATION

**Objectives:** Estimate the time taken by the aggressive agents ( $\text{Cl}^-$  or  $\text{CO}_2$ ) to reach the reinforcement. Use reliable and representative test methods.

**Approach:** Characterisation of the general transfer properties, transport of  $\text{Cl}^-$  and  $\text{CO}_2$  on concrete.

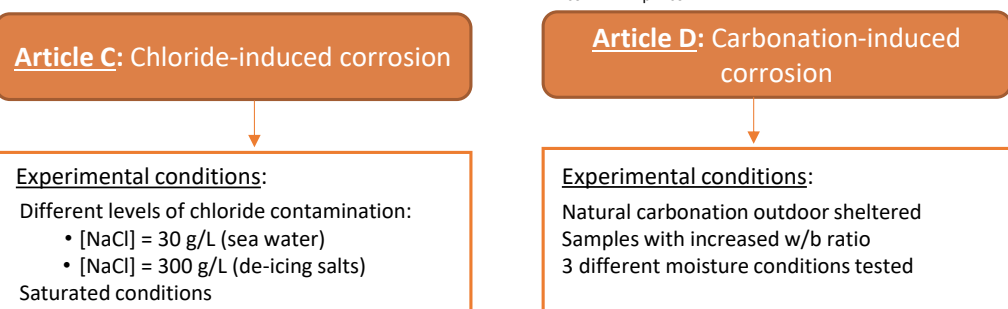


### CORROSION PROPAGATION

**Objectives:** Evaluate the corrosion rates once the rebars have been depassivated. Use reliable and representative test methods.

**Approach:**

- Development of a methodology adapted to low-carbon binders and representative of real structures: galvanic current measurement + mass loss.
- Comparison with traditional electrochemical tests ( $E_{\text{corr}}$ ,  $\rho$ ,  $R_p$ ,  $i_{\text{corr}}$ , Tafel).



**Synthesis chapter:** discussion of articles A, B, C and D

## Transition to Article A

**Article A** focuses on the **initiation period**.

The main objective is to determine the time taken by chloride ions to penetrate through the concrete and to reach the rebar.

**Article A** deals with the **general transfer properties** and **chloride penetration resistance** of LCK, AAS and SSC concretes. The transition from the initiation to the propagation period, characterised by the critical chloride threshold required at the steel concrete interface to initiate corrosion, is not studied. The properties of each concrete are compared with each other and to reference concretes from the literature.

The transfer properties of a concrete are of primary importance as they will largely determine the time taken for external aggressive agents, such as chlorides, to reach the reinforcement which can, under certain conditions, lead to pathologies or to the initiation of corrosion. The pore structure of the concrete is also going to influence the transport of water and oxygen at the steel concrete interface, necessary for the propagation of corrosion (studied in **Articles C and D**).

Chlorides are among the species likely to initiate corrosion if they reach the reinforcement in sufficient quantity. That is why particular attention is paid to the transport of chloride ions in this article, in addition to the general transfer properties, as these both parameters will condition the concrete durability (CO<sub>2</sub> transport and resistance to carbonation will be discussed in **Article B**).



## Chapter 3 – Article A

# General transfer properties and chloride penetration resistance of three low-carbon concretes

## Table of contents

<b>1</b>	<b>Introduction .....</b>	<b>42</b>
<b>2</b>	<b>Materials.....</b>	<b>45</b>
2.1	Raw Materials.....	45
2.2	Mixing and curing .....	48
<b>3</b>	<b>Test methods .....</b>	<b>48</b>
3.1	General transfer properties .....	50
3.1.1	Water porosity .....	50
3.1.2	Mercury intrusion porosity.....	50
3.1.3	Water permeability and capillary absorption .....	50
3.1.4	Gas permeability .....	51
3.1.5	Resistivity.....	51
3.2	Pore solution extraction.....	51
3.3	Chloride transport.....	52
3.3.1	Chloride diffusion test .....	52
3.3.2	RCPT test.....	53
<b>4</b>	<b>Results.....</b>	<b>54</b>
4.1	General transfer properties .....	54
4.1.1	Water porosity .....	54
4.1.2	Mercury intrusion porosity.....	55
4.1.3	Water permeability and capillary absorption .....	57
4.1.4	Gas permeability .....	57
4.1.5	Resistivity.....	59
4.2	Ionic conductivity of the pore solution.....	60
4.3	Chloride transportation in concrete .....	62
4.3.1	Chloride diffusion test .....	62
4.3.2	RCPT test.....	64
<b>5</b>	<b>Discussion .....</b>	<b>66</b>
5.1	Metrology: effect of drying temperature for preconditioning of slag-based binders.....	66
5.2	Metrology: determination of free and bound chlorides for slag-based binders.....	68
5.3	Microstructure and chemistry analysis .....	70
5.4	Comparison with references based on the performance approach.....	74



5.5	<i>Use of a simplified model to characterize resistance to chloride ion penetration .....</i>	<i>76</i>
<b>6</b>	<b>Conclusion .....</b>	<b>79</b>
<b>7</b>	<b>Supplementary data.....</b>	<b>80</b>
<b>8</b>	<b>References.....</b>	<b>83</b>

## **Durability (general transfer properties and chloride penetration resistance) of three low-carbon concretes (low clinker, alkali-activated slag and supersulfated cement)**

Lola Doussang<sup>1</sup>, Gabriel Samson<sup>1</sup>, Fabrice Deby<sup>1</sup>, Bruno Huet<sup>2</sup>, Emmanuel Guillon<sup>2</sup>, Martin Cyr<sup>1</sup>

<sup>1</sup> *Laboratoire de Matériaux et Durabilité des Constructions (LMDC), INSAT/UPS Génie Civil, 135 Avenue de Rangueil, 31077 Toulouse Cedex 04 France.*

<sup>2</sup> *Holcim Innovation Center, 95 rue du Montmurier, F-38070 Saint Quentin Fallavier, France*

### **Abstract**

The general transfer properties (water porosity, mercury intrusion porosimetry, water permeability, capillary absorption, gas permeability and resistivity) and chloride penetration resistance (natural chloride diffusion test and rapid chloride permeability test) of three low-carbon concretes C25/30 (low clinker (LCK) concrete, alkali-activated slag with sodium carbonate (Na<sub>2</sub>CO<sub>3</sub>-AAS) concrete and supersulfated cement (SSC) concrete) were evaluated and compared, in order to identify the strengths and weaknesses of each technology. The results show that the LCK concrete is characterized by “excellent” transfer properties (low water porosity, gas permeability, water permeability and capillary absorption) but high viscosity in the fresh state and very high chloride permeability. AAS and SSC concretes have similar transfer properties, comparable to classical concretes C25/30, and are extremely resistant to chloride penetration. Finally, the use of traditional protocols for durability tests applied to alternative low-carbon binders is questioned and metrology adaptations are proposed.

### **Keywords**

Low-carbon concrete, Durability, Chloride, Transfer properties

## 1 Introduction

### Context of the study

The need to reduce CO<sub>2</sub> emissions in the construction field by the development of more sustainable concretes has been widely demonstrated (Habert et al. 2020; Scrivener, John and Gartner 2018). As the production of Portland cement generates huge amounts of carbon dioxide, a first alternative would be to lower its proportion in the binder by partially replacing it by more environmentally friendly supplementary cementitious materials (SCMs): for example ground granulated blast furnace slag, metakaolin, fly ash, silica fume, natural pozzolans or limestone fillers, depending on the resources available locally (M.C.G. Juenger et al. 2011; Lothenbach, Scrivener and Hooton 2011; Maria C. G. Juenger, Snellings and Bernal 2019; Lakusic 2019). However, the proportion of substitution remains limited to the maximum proportions defined in standards (for instance, EN 206/CN (AFNOR 2022b) in Europe) and also in order to maintain acceptable fresh and hardened properties of the concrete. Another strategy is to use binder without Portland cement. Some promising solutions developed in this sense include alternative cements such as calcium aluminate cements, calcium sulfoaluminate-belite-ferrite cements (largely used in China), magnesium-based cements, supersulfated cements and also alkali-activated binders (Gartner and Sui 2018; M.C.G. Juenger et al. 2011; Habert et al. 2020).

The present study focuses on three low-carbon concrete technologies of the same strength class, C25/30, among those available on the market, chosen because they enable significant reductions in greenhouse emissions to be achieved: low clinker (LCK) concrete, alkali-activated slag with sodium carbonate (Na<sub>2</sub>CO<sub>3</sub>-AAS) concrete and supersulfated cement (SSC) concrete. More specifically, attention is paid to their durability: their general transfer properties and chloride penetration resistance. The transfer properties of a concrete are of primary importance as they will largely determine the time taken for external aggressive agents, such as chlorides, to reach the reinforcement and potentially initiate corrosion. For this reason, this paper pays particular attention to the transport of chloride ions, in addition to the general transfer properties, as both parameters will condition the concrete durability (CO<sub>2</sub> transport and resistance to carbonation will be discussed in Article B).

### Summary of data available in the literature

The **LCK** concrete reduces the proportion of Portland cement in the binder by replacing it by a large quantity of limestone filler. It leads to a concrete with a higher binder volume, made of 27% CEM I and 73% limestone filler in this study. The LCK composition enables therefore to reduce the amount of water while maintaining an acceptable rheology at fresh state, due to an optimized packing and admixture.. The use of limestone filler as an addition in concrete was allowed for the first time in 1965 in Germany, and later, in 2000, by the European Standard EN 197-1 as Portland limestone cements CEM II/A-L (6–20% limestone content) and CEM II/B-L (21–35% limestone content) (Elgalhud, Dhir and Ghataora 2017). Portland limestone cements are now used worldwide, as calcium carbonate is a widely available natural material (Thenepalli et al. 2015), which makes it one of the most commonly used additions, compared to slag or fly ash, for example. Information is available in the literature on Portland concretes with limestone additions and their durability properties. However, in the majority of cases, amount of filler in the binder ranging from 0 to 35% (limestone content up to 50% in some studies) have been

extensively studied because they correspond to standard recommendations. Nevertheless, it remains lower than the 73% filler content of the binder in the LCK concrete of this study. The mechanical strengths of Portland limestone concretes, modulus of elasticity, porosity, water absorption and durability properties (chloride migration and diffusion, carbonation kinetics, sulfate or freeze-thaw resistance, creep and shrinkage) are generally characterized and well-documented for low filler contents (Elgalhud, Dhir and Ghataora 2017; Dhir et al. 2007; Palm et al. 2016; Elgalhud, Dhir and Ghataora 2018; Hooton, Nokken and Thomas 2007). What emerges is that, when the amount of filler in the binder is increased, the concrete properties remain unchanged for 15-20% cement replacement, while the mechanical and durability performances decrease for higher replacement levels (>20% fillers) (Palm et al. 2016; Dhir et al. 2007; Elgalhud, Dhir and Ghataora 2018). The need for granular packing, admixture and low w/b ratio was identified, in order to make these concretes competitive from a durability point of view. Note that the conclusions drawn on Portland limestone concretes can be slightly different depending on the w/b ratio, the strength class of concrete used for the comparison and the quality of limestone (fineness and particle size distribution).

The **AAS** concrete in this study was made with slag as the aluminosilicate precursor, environmentally interesting for being a co-product from the iron making industry, combined with a sodium carbonate alkaline activator to provide a high pH to initiate its reaction. The sodium carbonate was chosen as the activator for its wider availability, and its more eco-friendly manufacturing process, lower cost and lower health risk when used. As opposed to the handling of highly alkaline solutions for sodium silicate or sodium hydroxide in liquid form, which are more commonly used as they are more effective for early strength development (S. Bernal 2016; Awoyera and Adesina 2019). Alkali-activated cements have existed since the 1930s-1940s but research on these materials really intensified in the 1990s, because they showed low environmental impact and good durability properties in aggressive environments, while offering mechanical performance levels similar to those of some Portland cements (J. Provis 2013). Thus, AAS have been extensively studied over the years (Kühl 1908; S.-D. Wang, Scrivener and Pratt 1994; Douglas and Brandstetr 1990; S.-D. Wang 1995; Roy 1999) and their hydration mechanisms, mechanical properties, general transfer properties and durability properties are well documented in the literature (X. Zhang et al. 2020; A. Wang et al. 2020; Awoyera and Adesina 2019; Mohamed 2019; G. Yang, Zhao and Wang 2022; Sun et al. 2022). However, it should be noted that, in the large majority of cases, these studies are performed for activations based on sodium silicate or hydroxide. In comparison, studies on sodium carbonate-based activation (like the one used in this study) are much more limited, although this activator presents the lowest carbon footprint (J. Provis 2013). Moreover, these studies are not often conducted at the concrete scale (rather paste or mortar) (Awoyera and Adesina 2019; Ke 2017; A. Wang et al. 2020). However, the literature agrees that the activator strongly influences the properties of the AAS (J. Zhang et al. 2022; Awoyera and Adesina 2019; Osio-Norgaard, Gevaudan and Srubar 2018; A. Wang et al. 2020) and data on the scale of the concrete are needed to accurately predict the long-term durability of this  $\text{Na}_2\text{CO}_3$ -AAS. Finally, the literature agrees that AAS (regardless of the activator) have mechanical properties comparable to those of Portland cements, together with generally lower porosity than OPC matrices, with smaller pore sizes, which reduce their overall transfer properties and favour greater durability

(Mohamed 2019; Jingxiao Zhang et al. 2022; Sun et al. 2022). Better resistance to chloride penetration and sulphate attack has also been demonstrated (Mohamed 2019; J. Zhang et al. 2022; A. Wang et al. 2020; G. Yang, Zhao and Wang 2022). On the other hand, a higher susceptibility to shrinkage and carbonation than in OPC was identified (A. Wang et al. 2020; G. Yang, Zhao and Wang 2022; Mohamed 2019). The capacity of these matrices to bind chlorides remains poorly quantified and needs further insight (Osio-Norgaard, Gevaudan and Srubar 2018). Of the fifty or so articles reviewed by X. Zhang et al. (2020), only four studies on chloride transport were found and none on carbonation – on Na<sub>2</sub>CO<sub>3</sub>-AAS, for example (the same trend was found in the review by Osio-Norgaard, Gevaudan and Srubar (2018) focusing on chloride). This study will therefore make it possible to position the durability performance of Na<sub>2</sub>CO<sub>3</sub>-AAS concretes, for which information remains limited compared to other activation systems.

Finally, the composition of the **SSC** binder is defined by the European standard EN 15743 (AFNOR 2010a). It consists of a mix of at least 75% slag combined with 5-20% calcium sulphate (anhydrite, gypsum or hemihydrate) and an alkaline activator (0-5% clinker) to obtain a sufficient reactivity. The activation of slag by sulfates was described in 1908 by Kühl (Kühl 1908), but SSC products developed particularly in Europe after the Second World War (1940-1960), due to a lack of Portland cement leading to the standardization of this binder (Papadakis, Venuat and Vandamme 1970). The hydration mechanisms involved, hydration products, micro-structure, mechanical properties and sulfate resistance of SSC have been extensively studied in the literature, in the majority of cases on paste samples (A. Gruskovnjak et al. 2008; Noor-ul-Amin 2014; Angulski da Luz and Hooton 2015; El-Didamony et al. 2016; Matschei, Bellmann and Stark 2005; Singh and Garg 2003). Data concerning their general transfer properties (porosity, density, capillary absorption, gas permeability, resistivity) and their durability performance (shrinkage, freeze-thaw resistance, accelerated carbonation, chloride migration, diffusion and binding, sulfate attack, acid attack, alkali-aggregate reaction) are also available. In summary, from a durability point of view, authors agree that SSC concrete performs extremely well in water saturated and chemically aggressive environments (high resistance to sulfate attack, acid attack, alkali-aggregate reaction and chloride penetration) but is more susceptible to carbonation. However, a limited number of studies have been carried out at the concrete scale (Cyr et al. 2019; Divet and Le Roy 2013; Ioannou et al. 2016; Nguyen et al. 2018; Novak and Sommer 2002; Masoudi 2018; Pinto 2018).

#### Conclusion of the introduction and interest of the article

In summary, some data about the transfer properties and transport of chlorides in the three low-carbon concrete technologies studied are available in the literature. However, it is important to note that the data available for LCK consider a lower amount of filler in the binder (0-50% filler) than that considered in this study (73% filler), which will influence the measured concrete properties. The same situation applies to AAS, where data are available but for a different activator than in this study (sodium carbonate). Furthermore, the tests are not always carried out at the concrete scale, which is the most representative of reality, or concern a very different strength class, thereby making the comparison difficult between the mixtures and the prediction of their durability. The present study aims to fill this gap, by providing data on the general

transfer properties (water porosity, mercury intrusion porosimetry, water permeability, capillary absorption, gas permeability and resistivity) and transport of chlorides (natural chloride diffusion test and rapid chloride permeability test) in the three low-carbon concretes considered (LCK, Na<sub>2</sub>CO<sub>3</sub>-AAS and SSC). These three concretes were selected because they are promising alternatives for reducing greenhouse gas emissions and were designed to have equivalent rheology and strength (self-compacting concrete, C25/30). Thus, in addition to their durability characterization, a comparison of their properties is proposed, in order to identify the strengths and weaknesses of each technology.

## 2 Materials

### 2.1 Raw Materials

The chemical composition of cements and slag used in LCK, AAS and SSC concretes determined by X-ray fluorescence (XRF) is given in Table 2. The quicklime that is part of the composition of AAS is only CaO (100%). Other raw materials were also used, such as limestone filler CaCO<sub>3</sub>, sodium carbonate Na<sub>2</sub>CO<sub>3</sub> and anhydrite CaSO<sub>4</sub>. The carbon footprints from different databases of these raw materials are summarized in Table 3.

Table 2: Chemical composition of the cements and slag used in LCK, AAS and SSC concretes (% in mass) determined by XRF.

	Chemical composition (% in mass)								
	CaO	SiO <sub>2</sub>	Al <sub>2</sub> O <sub>3</sub>	MgO	Fe <sub>2</sub> O <sub>3</sub>	K <sub>2</sub> O	Na <sub>2</sub> O	SO <sub>3</sub>	TiO <sub>2</sub>
CEM I	64.7	20.4	3.9	0.8	5.0	0.6	0.1	2.8	0.2
CEM III/B	50.5	37.7	8.1	4.5	1.9	0.5	0.2	2.0	0.5
GGBS	42.9	37.7	10.3	6.5	0.3	0.4	0.2	1.6	0.7

Table 3: Carbon footprint (in kg eq. CO<sub>2</sub>/t) of the raw materials used in LCK, AAS and SSC concretes from different databases.

	CO <sub>2</sub> footprint <sup>(1)</sup> (kg eq. CO <sub>2</sub> /t)
CEM I	765 <sup>(2)</sup>
Limestone filler	6 <sup>(3)</sup>
GGBS	100 <sup>(2)</sup>
Sodium carbonate	1350 <sup>(3)</sup>
Quicklime	893 <sup>(3)</sup>
Anhydrite	14 <sup>(3)</sup>
CEM III/B	273 <sup>(2)</sup>
Water reducing agent	1850 <sup>(4)</sup>
Sand and aggregates	2.3 <sup>(5)</sup>

<sup>(1)</sup> Value of CO<sub>2</sub> footprint known as A1 (CO<sub>2</sub> associated with the material) in the FDES (Environmental and Health Data Sheet) method. Neither the transport of raw materials (A2) nor the concrete manufacturing stage (A3) is evaluated.

<sup>(2)</sup> French values from SFIC (Syndicat Français de l'Industrie Cimentière) available on (ATILH 2022)

<sup>(3)</sup> From the Swiss database ECOInvent (ecoinvent 2022)

<sup>(4)</sup> Average value used by contractors regardless of the products and their concentration

<sup>(5)</sup> from the French database INIES (INIES 2017)

The binder of the **LCK** was made with 27% CEM I 52.5N CE CP2 and 73% limestone filler Betocarb HP 300 Sassenage from Omya. The particle size distribution for this filler shows two clearly visible populations: the first between 0.5 and 10  $\mu\text{m}$  and the second between 10 and 300  $\mu\text{m}$ . A Blaine specific surface of 3900  $\text{cm}^2/\text{g}$  for the CEM I and 5490  $\text{cm}^2/\text{g}$  for the filler were also measured. The semi-crushed alluvial mix of aggregates ranged from 0 to 20 mm. The combined grading curve is given in Figure 10. Aggregate proportions were optimized to achieve high packing to provide higher mechanical properties, combined with the low water/binder ratio of 0.25. Water reducing agents were also used to improve the workability in the fresh state.

The **AAS** binder was composed of 95% GGBS from Ecocem Fos/Mer as a precursor, with 4% sodium carbonate and 1% quicklime as activators. The latter provided a high pH to initiate dissolution and hydration of the slag. A Blaine specific surface of 5500  $\text{cm}^2/\text{g}$  was measured for the GGBS. The semi-crushed alluvial mix of aggregates ranged from 0 to 16 mm. This concrete had a water/binder ratio of 0.43. A commercial admixture was also used as a water reducing agent.

Finally, the **SSC** binder was composed of 89% GGBS from Ecocem Fos/Mer as the precursor, combined with 8% anhydrite of Lorraine and 3% CEM III/B 42.5N La Malle as alkaline activators to obtain sufficient reactivity. Finally, a limestone filler Orgon BL200 was added to the mixture during concrete formulation. The semi-crushed alluvial mix of aggregates ranged from 0 to 16 mm. This concrete had a water/binder ratio of 0.50 and was combined with water reducing agents.

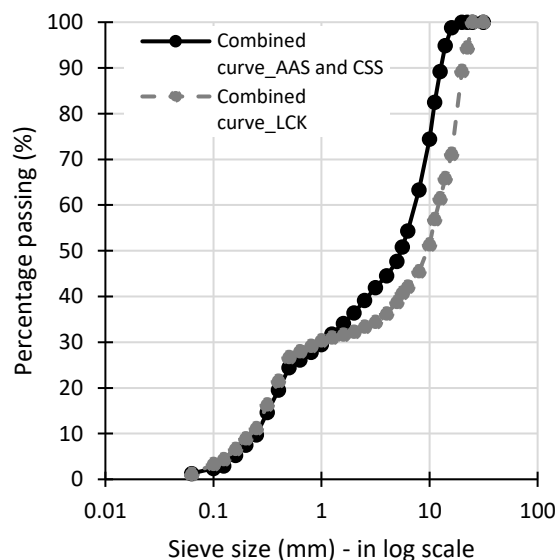


Figure 10: Aggregate grading curves for LCK, AAS and SSC concretes.

The three low-carbon concretes studied were designed to be C25/30 and also self-compacting (spread class SF1). Their respective compositions and characteristics are detailed in Table 4. The compressive strengths given in Table 4 were obtained on cylindrical samples.

*Table 4: Concrete composition, mixture parameters and characteristics in fresh and hardened state of LCK, AAS and SSC together with CO<sub>2</sub> footprint of each concrete, calculated by adding the CO<sub>2</sub> footprints of all raw materials forming part of the mixture (Table 3), considering their proportions.*

		unit	LCK	AAS	SSC
Concrete composition	CEM I	kg/m <sup>3</sup>	136.8		
	Limestone filler	kg/m <sup>3</sup>	375.0		49.1
	GGBS	kg/m <sup>3</sup>		481.7	329.3
	Na <sub>2</sub> CO <sub>3</sub>	kg/m <sup>3</sup>		20.3	
	Quicklime	kg/m <sup>3</sup>		5.1	
	Anhydrite	kg/m <sup>3</sup>			29.6
	CEM III/B	kg/m <sup>3</sup>			11.1
	Water reducing agent	kg/m <sup>3</sup>	6.02	11.15	5.1
	Sand (0-5 mm)	kg/m <sup>3</sup>	678.5	686.5	739.7
	Fine aggregates (5-10 mm)	kg/m <sup>3</sup>	272.1	609.6	656.9
	Coarse aggregates (> 10 mm)	kg/m <sup>3</sup>	827.1	229.6	247.4
	Total water	kg/m <sup>3</sup>	130.0	220.0	210.0
Mixture parameters	w/c ratio <sup>(1)</sup>		0.95	0.43	0.57
	w/b ratio <sup>(2)</sup>		0.25	0.43	0.50
	w <sub>eff</sub> /b ratio <sup>(3)</sup>		0.22	0.40	0.46
	Theoretical specific gravity	kg/m <sup>3</sup>	2425.5	2263.8	2278.3
	Quantity of paste	L/m <sup>3</sup>	318	407	360
	CO <sub>2</sub> footprint	kg eq. CO <sub>2</sub> /m <sup>3</sup>	122	104	50
Concrete characteristics in fresh and hardened state	Inversed cone flow rate (rheology)	seconds	9.7	1.7	2.0
	Abrams cone spread	mm	525	580	490
	Air content	%	1.3	1.2	1.8
	28 days compressive strength	MPa	33.0	33.3	32.0
	90 days compressive strength	MPa	34.4	37.5	40.0

<sup>(1)</sup> The w/c ratio does not consider the inert filler in the cement part: for the LCK the cement means CEM I, for the AAS it means GGBS + Na<sub>2</sub>CO<sub>3</sub> + quicklime, for the SSC it means GGBS + anhydrite + CEM III/B

<sup>(2)</sup> The w/b ratio considers the inert filler in the binder, unlike the w/c ratio <sup>(1)</sup>: for the LCK the binder considers the CEM I + inert fillers, for the AAS there is no difference with <sup>(1)</sup>, for the SSC it considers the inert filler in addition to <sup>(1)</sup>

<sup>(3)</sup> Efficient water to binder ratio, taking into account the water absorption of the aggregates

The carbon footprint of each concrete (without reinforcement) can be calculated directly by adding up the CO<sub>2</sub> footprints of all raw materials (as presented in Table 3) that are part of its composition (as defined in Table 4) only considering their proportion in the formulation. The



results are presented in Table 4 and can be ranked as follows: 122, 104 and 50 kg eq. CO<sub>2</sub>/m<sup>3</sup> for LCK, AAS and SSC respectively. The result associated with a standard concrete made with CEM I of similar strength (C25/30) is around 207 kg eq. CO<sub>2</sub>/m<sup>3</sup>. Therefore, with their significantly reduced carbon footprint (a reduction of at least 40% with respect to CEM I-concrete) for equivalent performances, the three concretes of this study are considered as “low-carbon”.

## **2.2 *Mixing and curing***

For each concrete, the mixing procedure lasted around 5 minutes and followed the same steps. First, the dry aggregates were dry mixed alone in a pan mixer for 1 min to achieve a uniform dispersion. Then, 1/3 of the water was added and the mixing continued for 1 min more. After that, the pan mixer was stopped, the binder was added and mixing continued for 1 min. Finally, the remaining 2/3 of the water with water reducing agent was added with a further 2 minutes of mixing. For each batch, around 50 L of concrete was cast. After the end of the mixing procedure, the cone spread was measured to check the concrete workability. All concrete spreads were between 450 and 600 (Table 4). Then, the concrete was cast in cylindrical (Φ110 mm x 220 mm) moulds in 3 layers, each one being vibrated, covered by a plastic cover to avoid evaporation, and stored in a wet curing room at 20 °C with 95% relative humidity. The specimens were demoulded after 72 h and cured in the same room for 28 days or other duration, depending on the testing date.

## **3 Test methods**

All the tests were performed on concrete samples after curing in a wet curing room with 95% relative humidity. The values presented are an average of several measurements on different samples for repeatability. All the tests performed are summarized in Table 5.

Table 5: Summary of tests performed on LCK, AAS and SSC concretes to characterize their general transfer properties, pore solution and resistance to chloride penetration with the associated standards, together with curing, sample size and preconditioning.

	Test	Standard	Sample curing	Sample shape and size	Sample preconditioning and details	Number of samples for average
<b>GENERAL TRANSFER PROPERTIES</b>	<b>Water porosity (<math>\epsilon</math>)</b>	NF P18-459 (AFNOR 2010b)	28 days, 6 months, 1 year	Cylindrical $\phi$ 110 mm x 220 mm, sawn to a thickness of 50 mm, after discarding the 1 cm-top and bottom	Drying step at 105 °C	3
	<b>Water porosity modified</b>	Based on NF P18-459 (lower drying temperature)	28 days, 6 months, 1 year	$\phi$ 110 mm x 220 mm, sawn to a thickness of 17 mm instead of 50 mm, after discarding the 1 cm-top and bottom	Drying step at 50 °C instead of 105 °C, to avoid destabilization of hydrates such as ettringite or deterioration of the microstructure	9
	<b>Mercury intrusion porosimetry</b>		28 days	$\phi$ 110 mm x 220 mm crushed to select only pieces of paste around 5 mm diameter	Vacuum desiccator for 10 days before testing	3
	<b>Water permeability</b>	EN 12390-8 (AFNOR 2009)	28 days	100 mm cubes		3
	<b>Capillary absorption (<math>A_w</math>)</b>	iso – 15148 (AFNOR 2003)	28 days	$\phi$ 110 mm x 220 mm, sawn to a thickness of 50 mm, after discarding the 1 cm-top and bottom	Side surfaces sealed with a waterproof Sicomin resin	2
	<b>Gas permeability (k)</b>	XP P18-463 (AFNOR 2011)	90 days	$\phi$ 110 mm x 220 mm sawn to a thickness of 50 mm, after discarding the 1 cm-top and bottom	Side surfaces sealed with Devcon bi-component epoxy resin	3
	<b>Gas permeability modified</b>	Based on XP P18-463 (lower drying temperature)	90 days	$\phi$ 110 mm x 220 mm sawn to a thickness of 50 mm, after discarding the 1 cm-top and bottom	Drying until mass stabilization at 45 °C, 65 °C, 80 °C and 105 °C to highlight the influence of drying temperature on the results	3
	<b>Resistivity (<math>\rho</math>)</b>	RILEM TC-154 EMC recommendations (Polder et al. 2000)	28 days, 90 days	Direct measurement on concrete $\phi$ 110 mm x 220 mm ground flat on both ends prior to testing	Measurements made directly after removal from the wet curing room (no saturation under vacuum)	3
<b>PORE SOLUTION</b>	<b>Pore solution extraction</b>	Based on the protocol described in (Cyr et al. 2008)	38 days	Cylindrical $\phi$ 33 mm x 70 mm pastes samples		1
<b>CHLORIDE TRANSPORT</b>	<b>Natural chloride diffusion test (<math>D_{nss}</math>)</b>	EN 12390-11 (AFNOR 2015)	28 days, 90 days	On half $\phi$ 110 mm x 220 mm	All surfaces covered with chloride ion diffusion proof Sicomin resin, except the exposure surface	2
	<b>RCPT test (Q)</b>	ASTM C1202 (ASTM 2012)	28 days, 90 days	$\phi$ 110 mm x 220 mm sawn to a thickness of 50 mm, after discarding the 1cm-top and bottom		3

### **3.1 General transfer properties**

#### **3.1.1 Water porosity**

Water porosity was measured according to NF P18-459 (AFNOR 2010b), on concrete samples after 28 days, 90 days, 6 months and 1 year of curing (humid room with 95% relative humidity). For each curing period and each binder, concrete cylindrical specimens  $\Phi 110$  mm x 220 mm were used and sawn into 3 sub-specimens, each with a thickness of 50 mm, after discarding the 1 cm-top and bottom. This test was repeated as the “water porosity modified test” (except for the age of 90 days), so as to adapt it to the AAS and SSC concretes of this study. These adaptations were motivated by the fact that different authors had drawn attention to the drying temperature used for preconditioning samples made with alternative binders to Portland cement (Cyr et al. 2019; Z. Zhang et al. 2019; Kovtun 2018). The traditional water porosity test from NF P18-459 requires a drying period at  $105 \pm 5$  °C, instead of the lower temperature of 50 °C chosen for the modified test to prevent damage to slag-based samples (e.g. ettringite in SSC). Also, for the modified procedure, the sample thickness was adapted from 50 mm to 17 mm (divided by three) to facilitate the drying at 50 °C, as recommended by Cyr (Cyr et al. 2019). In this case, concrete cylindrical specimens  $\Phi 110$  mm x 220 mm were sawn into 9 sub-specimens having a thickness of 17 mm, after discarding the 1 cm-top and bottom. More details on the choice of these new parameters are given in the Results (4.1.1) and Discussion (5.1) sections.

#### **3.1.2 Mercury intrusion porosity**

MIP was carried out with an AutoPore IV 9500 device from Micrometrics, at 28 days of curing, on concrete samples from cylindrical specimens  $\Phi 110$  mm x 220 mm crushed to select only pieces of mortar around 5 mm diameter. These pieces of “mortar” from concrete samples were conditioned for 10 days in a vacuum desiccator before testing. Tests were done with 2 g of sample and repeated 3 times for each mix composition to obtain representative results.

#### **3.1.3 Water permeability and capillary absorption**

Water permeability and capillary absorption were assessed after 28 days of curing, following EN 12390-8 (AFNOR 2009) and ISO-15148 (AFNOR 2003) standards, respectively. Before capillary absorption, the specimens were stored under the test conditions until the mass of each specimen, measured over 24 hours, had stabilized to within  $\pm 0.1\%$  of its total mass. The main parameters of these tests are summarized in Table 5.

For water permeability, after 28 days of curing, the sample (10 cm cube) was placed in the test device and a pressure of  $500 \pm 50$  kPa was applied to one side of the cube for  $72 \pm 2$  h. The cube was then split in two perpendicularly to the side exposed to the pressurized water. When the split area was dry enough for the water penetration front to be discerned, the maximum depth of penetration was recorded (in mm). Water absorption by partial immersion was determined by measuring the change in mass of the test specimen, the underside of which was in contact with water for a period of at least 24 h.

### 3.1.4 Gas permeability

Gas permeability was measured following XP P18-463 (AFNOR 2011), on samples having undergone 90 days of curing.  $\Phi$ 110 mm x 220 mm samples were sawn to a thickness of 50 mm, after discarding the 1 cm-top and bottom. The side surfaces of the tested specimen were sealed with Devcon bi-component epoxy resin. The samples were then placed in a ventilated chamber at  $80 \pm 5$  °C and permeability measurements were made after 7 and 28 days. Then, samples were placed in a ventilated chamber at  $105 \pm 5$  °C until mass stabilization and a final permeability measurement was performed. A CEMBUREAU device was used for the experiment. The test consisted of applying a constant pressure to the sample. The permeability was then determined from the flow measurement in the steady state. A modified procedure of this test was also proposed for AAS and SSC concretes, with lower drying temperatures but keeping the sample thickness of 50 mm this time, for the same reasons as for the water porosity test. For AAS and SSC samples, the gas permeability measurements were performed with an adapted drying protocol, after mass stabilization at 45 °C, 65 °C, 80 °C and 105 °C. This modified procedure was not applied for the LCK concrete, as it is a Portland cement-based binder, considered adapted to the standard preconditioning.

### 3.1.5 Resistivity

The electrical resistivity is a material property independent of the sample's geometry, quantifying the material resistance to the passage of an electrical current. Direct electrical resistivity measurements on non-reinforced concrete samples  $\Phi$ 110 mm x 220 mm that had been ground flat at both ends prior to testing, were taken at 28 and 90 days of curing. The test set-up was based on RILEM TC-154 EMC (Polder et al. 2000) using a resistance meter from Ohmega. Measurements were taken immediately after the sample was removed from the wet curing room, to avoid drying, which could influence the values of resistivity obtained. The material was considered sufficiently saturated after the curing period and, for this reason, the step of saturation under vacuum was not performed. The concrete sample was placed between two electrodes (conductive metallic plates) separated from the material by thin wet sponges to obtain a good connection. The two electrodes were connected to an Ohmega resistance meter (direct transmission mode). The device gave the total resistance of concrete plus the wet sponges, from which the resistance of the sponges (measured in the same way as described previously) was removed, so as to obtain only the concrete resistance. The associated resistivity ( $\rho$ ) can be calculated with the sample dimensions (Equation (11)).

$$\rho = R * \frac{S}{L} \quad (11)$$

where  $\rho$  is the concrete resistivity ( $\Omega$ .m); R is the concrete resistance given by the resistance meter ( $\Omega$ ); S is the area of the flat faces of the cylindrical specimen ( $m^2$ ); L is the height of the specimen tested (m). Measurements were repeated on three different samples and the average value was taken.

## 3.2 Pore solution extraction

A pore solution extraction was performed on pastes aged for 38 days in order to measure the pH. The ionic concentration of the pore solution was also determined by ICP analysis. Paste

samples were selected (rather than mortar or concrete) to extract a maximum of pore solution by this method, in the absence of aggregates. A Sintco 600 T press was used to perform the extraction as described in greater detail in (Cyr et al. 2008). The pressure was applied with a speed of 3 kN/s up to 1000 kN, where it was maintained for 300 s to extract some millilitres of pore solution. The pore solution was then filtered and immediately analysed with ICP-MS to quantify Na, K, Fe, Al, Mg, Ca, Si species.

### **3.3 Chloride transport**

Chloride transport through the concrete was evaluated in both natural and accelerated conditions, by a natural chloride diffusion test and by the Rapid Chloride Permeability Test (RCPT), respectively. The objective was to assess the performance of concrete with respect to chloride penetration.

#### **3.3.1 Chloride diffusion test**

Chloride transport in natural conditions was characterized by a diffusion test performed according to EN 12390-11 (AFNOR 2015), on concrete after 28 and 90 days of curing. Concrete cylindrical specimens  $\Phi 110$  mm x 220 mm were sawn into two 110 mm high sub-samples and all the surfaces of each half-sample, except the exposure surface, were then covered with chloride ion diffusion proof Sicomin resin. After 24 h of air drying, Five half-samples per mixture (two for the test and three to follow the evolution of chloride penetration in concrete by  $\text{AgNO}_3$  pulverization) were immersed in 50 L of NaCl solution at 30.93 g/L representing natural seawater. The NaCl solution was renewed every 90 days. One half-sample was conditioned in a sealed plastic bag after sawing so that the initial chloride content in the concrete could be analysed.

The reference period for chloride exposure was 90 days, but it was necessary to extend this immersion duration in some cases as chlorides had to penetrate sufficiently far into the material to enable grinding of at least 8 parallel layers of concrete, which were required to achieve the chloride profile. Thus, for samples cured for 28 days, 91 days of immersion in 3% NaCl solution were sufficient to obtain the chloride profile. For samples cured for 90 days, 96 days of immersion were sufficient for LCK concrete, but longer chloride exposure was required for AAS (454 days) and SSC (184 days) concretes.

Once chlorides had penetrated the material sufficiently, profile grinding was carried out, followed by chloride analysis. Total chlorides were determined following standard NF EN 14629 (AFNOR 2007), while free chlorides were determined according to the French procedure recommended by GranDuBé (Hornain 2007). The latter consists of placing 5 g of powder in a beaker with 200 mL of demineralized water and stirring for 3 minutes. The solution is then filtered, rinsed with only 10 mL of demineralized water and acidified with 2 mL of nitric acid. Bound chlorides are calculated as the difference between total chlorides and free chlorides. Finally, the chloride profile obtained enabled the non-steady state diffusion coefficient ( $D_{\text{nss}}$ ) to be determined, and the chloride content at the exposed concrete surface ( $C_s$ ) to be calculated by regression analysis. More precisely,  $D_{\text{nss}}$  and  $C_s$  were determined by fitting Equation (12) to

the experimental data points of the chloride profile, using non-linear least squares regression analysis.

$$C_x = C_i + (C_s - C_i) \left[ 1 - \operatorname{erf} \left( \frac{x}{\sqrt{2D_{nss}t}} \right) \right] \quad (12)$$

where  $C_x$  is the chloride content measured at average depth  $x$  and exposure time  $t$  (% by mass of concrete);  $C_s$  is the calculated chloride content at the exposed surface (% by mass of concrete);  $C_i$  is the initial chloride content (% by mass of concrete);  $x$  is the depth below the exposed surface to the mid-point of the ground layer (m);  $D_{nss}$  is the non-steady state chloride diffusion coefficient ( $\text{m}^2 \text{s}^{-1}$ );  $t$  is the exposure time (seconds).

### 3.3.2 RCPT test

Chloride transport in accelerated conditions was assessed by the RCPT test (Rapid Chloride Permeability Test), following ASTM C1202 (ASTM 2012). The standard voltage of 60 V was applied and the test was run for 6 hours. This test gave the charge that passed through each concrete, which can be related to different levels of resistance to chloride ion penetrability. The main parameters of this test are summarized in Table 5.

## 4 Results

The results are deliberately presented here in a rather succinct manner. A more detailed analysis will be made in the Discussion section.

### 4.1 General transfer properties

#### 4.1.1 Water porosity

Results of water porosity with a drying step at 105 °C or 50 °C are presented in Figure 11 for different periods of curing.

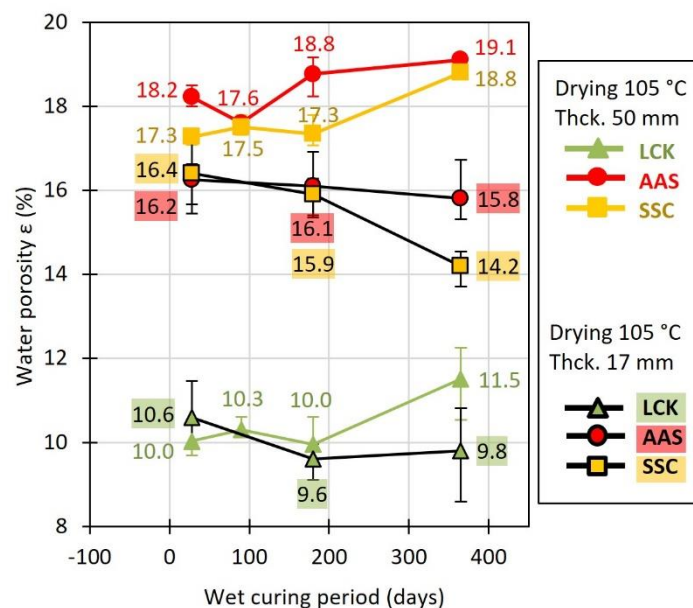


Figure 11: Water porosity,  $\epsilon$ , for LCK (in green), AAS (in red) and SSC (in yellow) concretes after 28 days, 90 days, 180 days and 365 days of wet curing, with a drying step of either 105 °C and a sample thickness of 50 mm (coloured lines) or 50 °C and 17 mm (black lines).

The porosity of concretes obtained with a drying step of 105 °C remained stable over the time for the three formulations studied (considering the error bars). This was also the case for slag-based concretes (AAS and SSC), known to have a slower hydration than CEM I-concretes (Darquennes, Espion and Staquet 2013) and for which a decrease in porosity could have been expected between 28 days and 90 days due to a higher hydration level. This result can possibly be explained by a drying step of 105 °C in the experimental protocol, which is not suitable for slag-based concretes and therefore gives unreliable results, as developed in the discussion in part 5.1. These water porosity values are consistent with those found in the literature: 9% for Portland limestone concrete (50-65% limestone) (Palm et al. 2016), 16-17% for SSC (Divet and Le Roy 2013) and 14% for Na<sub>2</sub>CO<sub>3</sub>-AAS concrete of higher strength class (65 MPa at 28 days instead of 30 MPa here) (Azar et al. 2021).

The porosity of LCK concrete was significantly lower than that of AAS and SSC. This seems logical considering the very low w/b ratio of LCK concrete (0.25 against 0.43 and 0.50, respectively) and the fact that an aggregate optimization was performed to achieve high

packing. Moreover, porosity of AAS and SSC may have been over-estimated because the drying step at 105 °C could have destabilized hydrates or damaged the concrete microstructure (Z. Zhang et al. 2019), as detailed in part 5.1 of the Discussion.

For this reason, water porosity measurements were repeated with a lower drying temperature of 50 °C, a choice based on literature data (Trincal et al. 2020; K. Yang et al. 2016; Z. Zhang et al. 2019; Ismail et al. 2013; Ndiaye, Cyr and Ginestet 2017; Cyr et al. 2019). The results are presented and compared to those with a drying step of 105 °C in Figure 11. A decrease of porosity for AAS (16.2% to 16.1% to 15.8%) and SSC (16.4% to 15.9 to 14.2%) concretes can be observed between 28 days, 180 days and 365 days. This result was expected because the hydration of slag is slower than that of cement and is not complete at 28 days. This trend was not found for results obtained with the drying step of 105 °C, which reinforced the hypothesis that this temperature was too high for slag-based concretes and probably damaged the samples, leading to a misleading porosity assessment. The porosity of LCK concrete remained relatively stable between 28 days, 180 days and 365 days (10.6% to 9.6% to 9.8%), because the hydration of cement was already almost completed at 28 days. No effect of the drying temperature was observed on LCK water porosity, which was expected and suggests that the temperature of 50 °C is sufficient to dry a sample with a reduced thickness of 17 mm.

#### 4.1.2 Mercury intrusion porosity

Mercury intrusion porosity (MIP) was performed to complete the information provided by the water porosity test, such as the pore size distribution, as illustrated on Figure 12 and Figure 13.

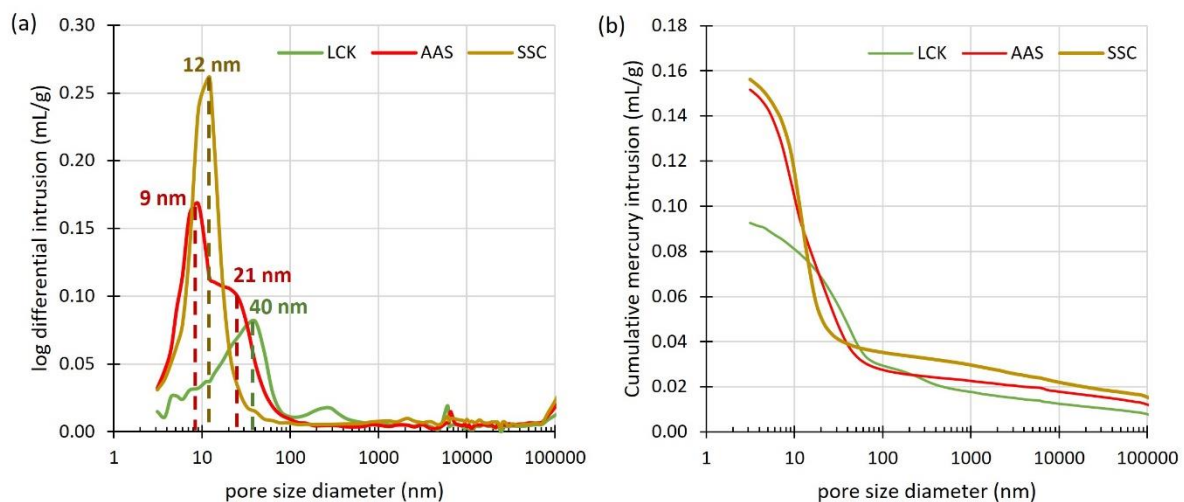


Figure 12: (a) Pore-size distribution and (b) cumulative mercury volume from mercury intrusion for LCK (in green), AAS (in red) and SSC (in yellow) mortar samples removed from concrete after 28 days of cure.



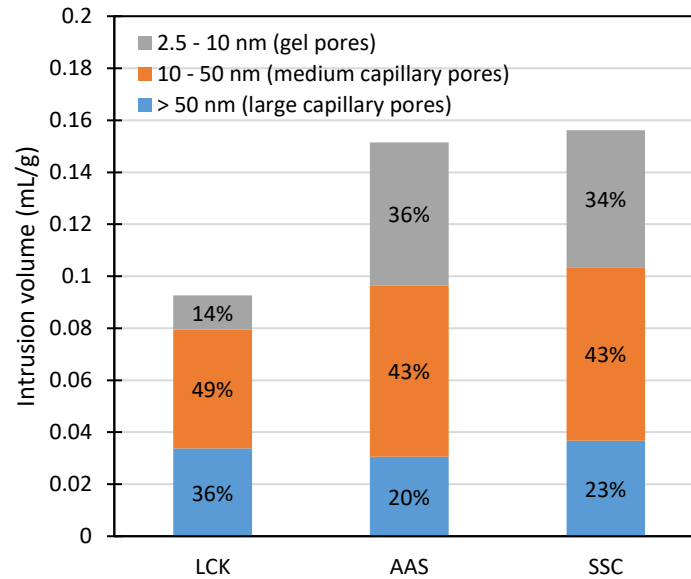


Figure 13: Contribution of the different pore sizes to the total measured mercury porosity (inspired from (Trincal et al. 2020)) for LCK, AAS and SSC mortar samples removed from concrete after 28 days of cure, complementary to the one shown in Figure 12.

Different pore size distributions could be identified between the mortars extracted from the three concretes studied (Figure 12 and Figure 13). LCK concrete was the least porous concrete (10% at 28 days from water porosity measurement), but had larger pore size measured on extracted mortar (average pore diameter: 23 nm) whose distribution was centred around 40 nm. AAS and SSC had a higher concrete water porosity (around 16% at 28 days) with smaller pore size measured on extracted mortars (average pore diameter: 13 nm for both). AAS presented a bimodal pore size distribution centred around 9 and 21 nm, while SSC distribution was centred around 12 nm for the pore entry diameter. The pore size distribution, presented on Figure 13, also clearly highlights that AAS and SSC have a similar porous network. Moreover, Figure 13 shows that, for the three mixtures, about 45% of the porosity is accessible through pores having diameters between 10 and 50 nm (49%, 43% and 43% of its total porosity for LCK, AAS and SSC, respectively), corresponding to medium capillary pores (Mindess, Young and Darwin 1981).

Then, there are some differences between LCK and slag-based binders for the smaller and the larger pore size families. Slag-based binders have twice the porosity accessible through pores of diameter between 2.5 and 10 nm, corresponding to small capillaries of gel pores, (14%, 36% and 34% of the total porosity for LCK, AAS and SSC, respectively), while LCK has more porosity accessible by pores of diameter greater than 50 nm, corresponding to large capillary pores (36%, 20% and 23% of its total porosity for LCK, AAS and SSC, respectively) that favour the transport of water or other aggressive species. These orders of magnitude correspond to the literature data for  $\text{Na}_2\text{CO}_3$ -AAS concrete (Trincal et al. 2020; 2022) and SSC concrete (Divet and Le Roy 2013) and also confirm that slag-based binders have smaller pores than those made with only Portland cement, as reported in the literature (Jingxiao Zhang et al. 2022; Mohamed 2019).

These characteristics regarding the total porosity and the pore size distribution specific to each concrete will influence the transport and durability properties studied later. Finally, the mercury porosity test also gave information about the "mortar porosity" which refers to the porosity of the concrete without the aggregates (paste + sand). The mortar porosity obtained by MIP for each binder was 19%, 28% and 28% for LCK, AAS and SSC, respectively (same distribution as for water porosity).

#### 4.1.3 Water permeability and capillary absorption

The water permeability and capillary absorption of the three concretes are presented in Figure 14.

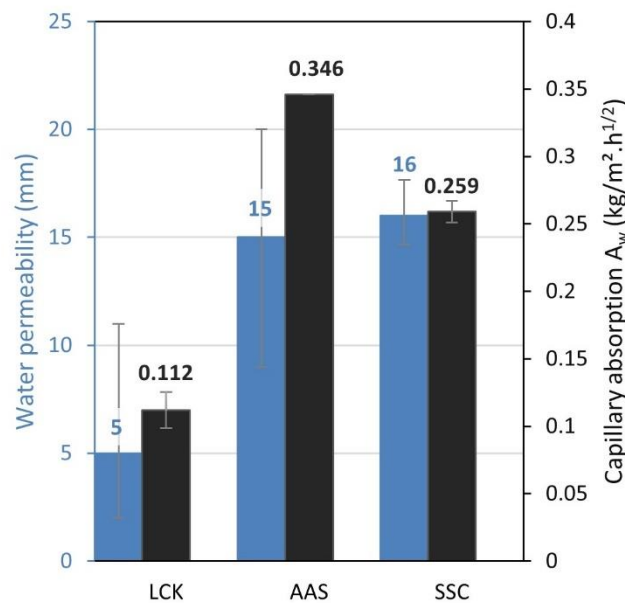


Figure 14: Water permeability (in blue) and capillary absorption (in black) measured on LCK, AAS and SSC concretes after 28 days of curing.

The water permeability of slag-based concretes (AAS and SSC) had the same order of magnitude (Figure 14). This seems reasonable as they already had similar porosity, and porosity can influence permeability. Capillary absorption was slightly higher for AAS than for SSC. For LCK concrete these values were about one third of those of slag-based concretes. This can mainly be explained by LCK's lower porosity, which offsets the large pore entry diameter (section 4.1.2) and thus reduces the water transport. Therefore, LCK concrete is less permeable to water than AAS and SSC.

#### 4.1.4 Gas permeability

The gas permeability of the three concretes previously dried at different temperatures is presented in Figure 15. Contrary to what was done in the water porosity test, the sample thickness was not reduced to adapt to the drying step at lower temperatures (50 mm for all the drying temperatures tested).

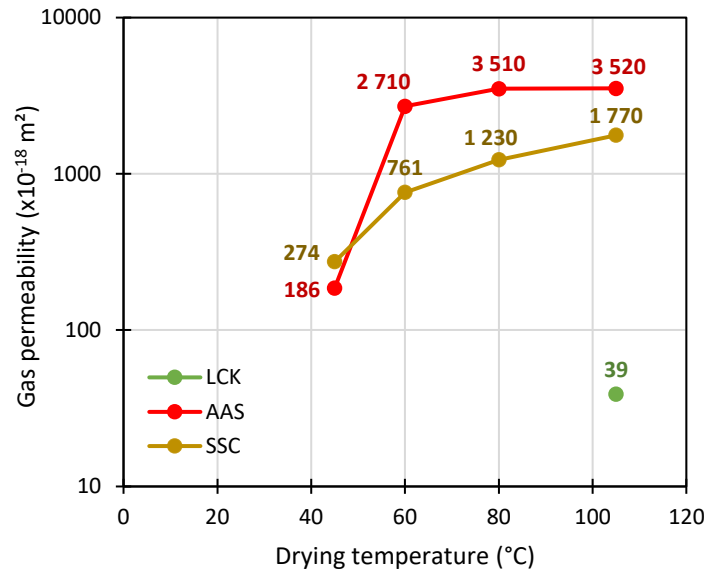


Figure 15: Gas permeability ( $\times 10^{-18} \text{ m}^2$ ) measured on LCK, AAS and SSC concretes after 90 days of curing, for different drying temperatures (105 °C, 80 °C, 60 °C, 45 °C).

Large differences in gas permeability were identified according to the type of binder, whatever the drying temperature used (Figure 15). The gas permeability of slag-based concretes (AAS and SSC) was several orders of magnitude higher than for the LCK concrete, except at the drying temperature of 45 °C. This is consistent with the literature findings (K. Yang et al. 2016) and the previous results presented in section 4.1.1 for porosity, which is a parameter strongly influencing the gas permeability. Nevertheless, for all drying temperatures, AAS gas permeability was around twice that of SSC. The gas permeability, after drying at 105 °C, of the three concretes studied can be ranked from the highest to the lowest as follows: AAS ( $3520 \times 10^{-18} \text{ m}^2$ ) > SSC ( $1770 \times 10^{-18} \text{ m}^2$ ) >> LCK ( $39 \times 10^{-18} \text{ m}^2$ ). However, these values remain higher than those available in the literature for slag-based concretes. For example, for SSC of higher strength class (between 40 and 50 MPa at 28 days) the gas permeability measured in the literature is between 323 (Divet and Le Roy 2013) and 921 (Cyr et al. 2019)  $\times 10^{-18} \text{ m}^2$  (against  $1770 \times 10^{-18} \text{ m}^2$  in this study), which suggests a possible alteration of the material during the test (idem for AAS).

Finally, the comparing gas permeability obtained for lower drying temperatures with that using a drying step at 105 °C, showed a strong effect of the drying temperature on the results. The same trend as for water porosity was observed: the gas permeability measured was high for high drying temperatures and decreased with lower drying temperatures. However, this time, the changes of drying temperature influenced the results strongly (almost a factor 20 for AAS concrete between 105 °C and 45 °C), as discussed in greater detail in section 5.1.

#### 4.1.5 Resistivity

Results of resistivity for different curing periods (28 or 90 days) are presented in Figure 16.

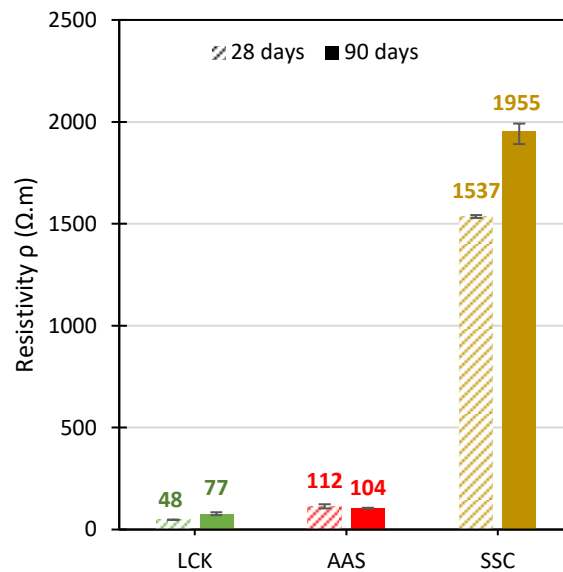


Figure 16: Electrical resistivity of LCK (in green), AAS (in red) and SSC (in yellow) concretes measured with a resistance meter at 28 days (hatched bars) and 90 days (full bars) of curing.

#### Comparison among the three binders

LCK has a lower resistivity than the slag-based concretes, the resistivity of AAS being of the same order of magnitude but slightly higher (Figure 16). The resistivity of SSC was much higher than that of the other two with a factor of more than 100 between AAS and SSC. To summarize, the ranking obtained was the following:  $\rho$  (SSC)  $\gg$   $\rho$  (AAS)  $>$   $\rho$  (LCK). The very high resistivity of the SSC concrete is known in the scientific literature and has been measured by other authors (Masoudi 2018). For AAS, scattered values ranging from 100 to 1000  $\Omega$ .m can be found, the values increasing with the compressive strength (Ma et al. 2016; Noushini 2018; Yu et al. 2022; Azar et al. 2021). Finally, the resistivity of a traditional OPC concrete is generally between 100 and 300  $\Omega$ .m (Ma et al. 2016; Chalhoub 2020; Yu et al. 2022), which means that the replacement by fillers leads to a decrease in the resistivity. To explain the differences between the three matrices, several factors are involved, such as the quantity of paste and the pore structure of the concrete or the conductivity of the pore fluid solution, as discussed in more detail in section 5.3 (AAS is known for its high level of alkalis, for example, which will impact this parameter).

#### Evolution of the resistivity between 28 days and 90 days

An increase of resistivity for LCK and SSC concretes was observed between 28 days and 90 days. In contrast, the resistivity of AAS remained globally constant, whereas an increase with the duration of curing would have been expected, as previously observed (Azar et al. 2021; Azarsa and Gupta 2017; Andrade and Castellote 2011) due to the densification of the microstructure with the slag or cement hydration.

## 4.2 Ionic conductivity of the pore solution

To investigate the composition and the ionic concentration of the pore solutions, an ICP analysis was performed after 38 days of endogenous cure. The cations  $\text{Na}^+$ ,  $\text{K}^+$ ,  $\text{Ca}^{2+}$ ,  $\text{Al}^{3+}$ ,  $\text{Mg}^{2+}$  and  $\text{Fe}^{2+}$  were quantified.  $\text{H}_3\text{O}^+$  ions were neglected because of the high pH of the pore fluid solution. For the AAS binder,  $\text{CO}_3^{2-}$  ions were supplied by sodium carbonate activation, but S. A. Bernal et al. (2015) show that they are completely consumed after about 10 days. As the extraction of pore solution was performed at 38 days of cure here, they are neglected. The amount of  $\text{OH}^-$  ion was deduced as the value needed to maintain electroneutrality for LCK, and from the pH measurements for AAS and SSC due to the presence of other anions, as explained below. It is important to note that the concentration of sulfide species  $\text{S}^{2-}$  was not measured by the ICP analysis because it is difficult to analyse, as it evolves over time and it oxidizes easily. However, the results available in the literature show that its concentration in slag-based binders is not negligible (Mundra et al. 2023). For example, on concretes after 3 months of curing, Ma et al. (2016) measured a concentration between 2000 and 6000 ppm of sulfide in the pore solution of AAS. These results confirmed measurements by A. Gruskovnjak et al. (2006) and Nedeljković et al. (2019) of 260 and 573 mmol/L, respectively, of sulfide in AAS cured for 28 days against negligible amounts for a traditional CEM I-sample. Sulfide ions  $\text{S}^{2-}$  were therefore neglected for LCK. To estimate the amount of sulfides in AAS and SSC, it was deduced as the amount needed to maintain the electroneutrality of the solution. The values obtained were estimations (not direct measurements) of the concentrations present in the pore solution of the three binders at 38 days of curing. These values are not representative of the concentrations at a young age and may still evolve over time. The results are detailed in Table 6 in mg/L with the associated conversion in mmol/L, based on the atomic weight of each species, detailed in Table 11 in the supplementary data.

Table 6: Concentration of the main species present in the pore fluid solution of LCK, AAS and SSC pastes after 38 days of curing (in mg/L and conversion into mmol/L), quantified by ICP analysis for  $\text{Na}^+$ ,  $\text{K}^+$ ,  $\text{Ca}^{2+}$ ,  $\text{Al}^{3+}$ ,  $\text{Mg}^{2+}$ ,  $\text{Fe}^{2+}$ , calculated either from pH measurement or assessed to maintain the electroneutrality for  $\text{OH}^-$  and  $\text{S}^{2-}$  ions.

		Concentration of species in pore fluid solution (38 days' curing)								
		ICP analysis						Calculation	Calculation	
		$\text{Na}^+$	$\text{K}^+$	$\text{Ca}^{2+}$	$\text{Al}^{3+}$	$\text{Mg}^{2+}$	$\text{Fe}^{2+}$	$\text{OH}^-$	$\text{S}^{2-}$	Total ionic concentration
<b>LCK</b>	mg/L	1260	8745	157	0.961	0	0.183			
	mmol/L	55	224	4	0.036	0	0.003	286 <sup>(2)</sup>	0	569
<b>AAS</b>	mg/L	23370	1353	3	204	0	0.341			
	mmol/L	1017	35	0.087	8	0	0.006	112 <sup>(1)</sup>	481 <sup>(2)</sup>	1652
<b>SSC</b>	mg/L	988	1209	637	0.227	0	0			
	mmol/L	43	31	16	0.008	0	0	13 <sup>(1)</sup>	46 <sup>(2)</sup>	149

<sup>(1)</sup> From pH measurements:  $[\text{OH}^-] = 10^{\text{pH}-14}$  (with pH = 13.2, 13.1 and 12.1 for LCK, AAS and SSC, respectively).

<sup>(2)</sup> From electroneutrality.

These data were then used to estimate the conductivity of the pore solution by calculation according to Equation (13) (Pethig 1987)

$$\sigma = \sum_{i=1}^n \lambda_i [X_i] \quad (13)$$

with  $\sigma$  the conductivity of the pore solution in S/m,  $\lambda_i$  the molar conductivity of species  $i$  in  $S.m^2.mol^{-1}$  (taken from the literature and presented in Table 11 of the supplementary data) and  $[X_i]$  the concentration of species  $i$  in the pore solution in  $mol/m^3$  (measured by ICP and available in Table 6)

The contribution of each ionic species to the conductivity of the pore solution is shown in Figure 17 and detailed in Table 12 of the supplementary data. Note that the molar conductivity of  $S^{2-}$  was attributed to the  $HS^-$  ions, another possible ion formed from sulfur (Mundra and Provis 2021), as this characteristic was not found for  $S^{2-}$ .

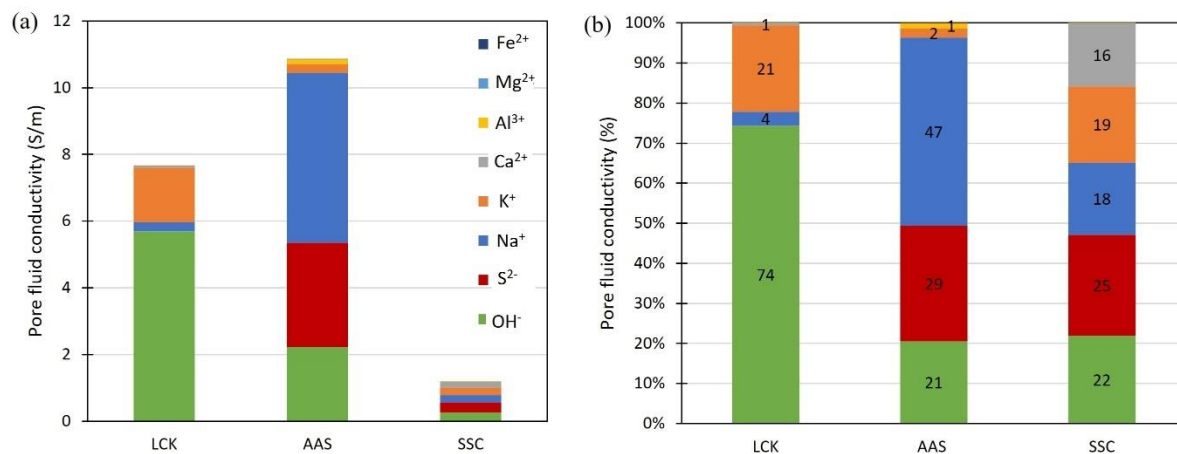


Figure 17: (a) Pore fluid conductivity of LCK, AAS and SSC and (b) contribution of each ionic species to this conductivity ( $OH^-$ ,  $S^{2-}$ ,  $Na^+$ ,  $K^+$ ,  $Ca^{2+}$ ,  $Al^{3+}$ ,  $Mg^{2+}$ ,  $Fe^{2+}$ ).

First of all, it can be noted that the conductivity related to the quantity of ions in the pore solution is very variable for the three mixtures considered (by a factor of around 9 between SSC and AAS) as, the more ions a pore solution contains (Table 6), the more its conductivity increases. It can also be noted that  $OH^-$  ions are the most conductive, followed by alkalis ( $Na^+$ ,  $K^+$ ), as illustrated by their respective molar conductivities, presented in Table 11 in the supplementary data. The conductivity of the SSC is the lowest (1 S/m) and is equitably distributed among  $Ca^{2+}$ ,  $K^+$ ,  $Na^+$ ,  $S^{2-}$  and  $OH^-$  ions. This low conductivity agrees with the high resistivity measured on concrete in section 4.1.5. Then, the LCK has an intermediate conductivity (8 S/m) due mainly to hydroxide (74%) and potassium (21%) ions. Considering that the sample used for the pore solution extraction was saturated (endogenous curing), the pore solution conductivity of LCK is comparable to that obtained by Olsson et al. (2018) on a CEM I. Finally, the AAS binder had the highest conductivity (11 S/m), mainly due to sodium (47%) from the activator, which is sodium carbonate, and also to sulfide (29%) and hydroxide ions (21%). This high conductivity agrees with the low resistivity measured on concrete in the previous section.

### 4.3 Chloride transportation in concrete

#### 4.3.1 Chloride diffusion test

The chloride diffusion resistance of each concrete was assessed from the chloride diffusion test in natural conditions using EN 12390-11. From the chloride profile obtained for each concrete (Figure 18), the respective diffusion coefficient  $D_{nss}$  can be calculated, as summarized in Table 7. The test was performed on concrete after 28 days and 90 days of curing to evaluate the influence of the curing period on the chloride diffusion resistance of each concrete. Only the results after 90 days of curing are presented for the LCK concrete. One sample was analysed per condition. The proposed 95% confidence interval was calculated considering possible variations on the input data. For this purpose, the mathematical fitting required by the EN 12390-11 standard was performed with the two measured  $C_i$  values (on the sample with 28 days of curing and the one with 90 days of curing), and also considering an error of  $\pm 10\%$  on the measured chloride concentrations for each ground layer.

*Table 7: Chloride diffusion coefficient  $D_{nss}$  of LCK, AAS and SSC concretes, after 28 and 90 days of curing, after exposure in saline solution  $[NaCl] = 30.93$  g/L. The meanings of abbreviations are as follows:  $t$  is the exposure time in saline solution,  $C_i$  is the initial chloride content,  $C_s$  is the chloride content at the concrete surface,  $D_{nss}$  is the chloride diffusion coefficient, and  $R^2$  is the square of the linear correlation coefficient. Both  $C_i$  and  $C_s$  are % by mass of concrete.*

Concrete		Chloride exposure		Second Fick's law parameters (Equation (12))		
Curing	Binder	t (days)	$C_i$ (%)	$C_s$ (%)	$D_{nss}$ ( $\times 10^{-12} m^2/s$ )	$R^2$ (exclusion 1 <sup>st</sup> point)
28 days	AAS	91	0.012	$0.15 \pm 0.03$	$0.84 \pm 0.10$	0.954
	SSC	91	0.010	$0.14 \pm 0.01$	$1.06 \pm 0.09$	0.999
90 days	LCK	96	0.015	$0.32 \pm 0.02$	$50.78 \pm 12.06$	0.978
	AAS	454	0.009	$0.42 \pm 0.04$	$0.19 \pm 0.01$	0.997
	SSC	184	0.008	$0.39 \pm 0.04$	$0.58 \pm 0.21$	0.991

Figure 18 shows marked differences in chloride diffusion resistance for the three concretes studied. The type of binder plays an important role in this property, as slag-based concretes (AAS and SSC), which have similar chloride profiles at 28 and 90 days, are much more resistant to chloride diffusion than those made with Portland cement (LCK). This trend has also been observed by other authors (Divet and Le Roy 2013; Yeau and Kim 2005; Roy, Jiang and Silsbee 2000; Türkmen, Gavgalı and Gül 2003; J. Zhang et al. 2022).

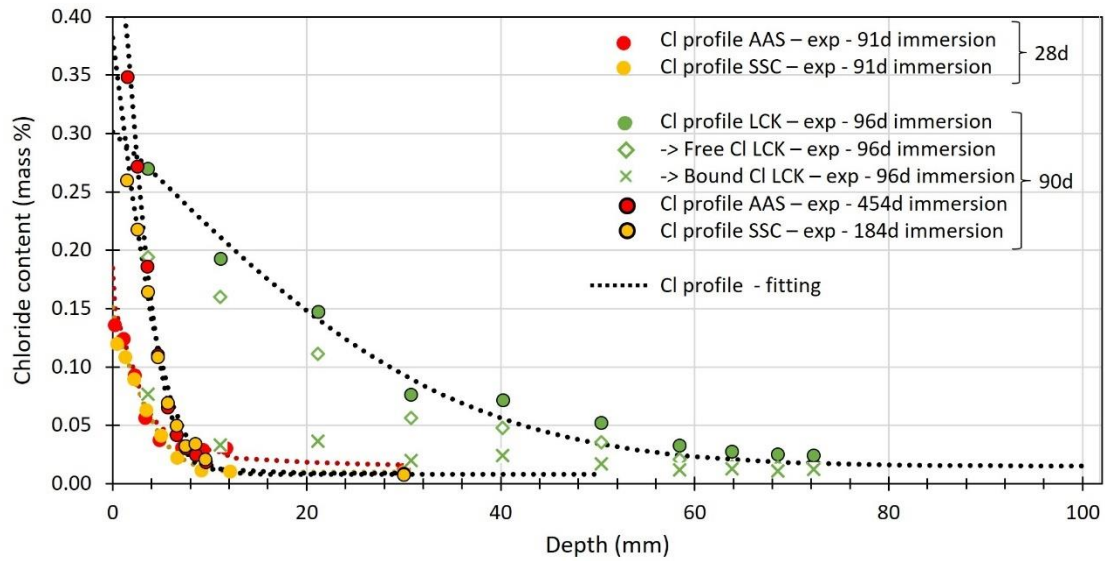


Figure 18: Chloride profile (total chlorides) associated with LCK, AAS and SSC concretes after 28 or 90 days of curing and immersion in NaCl solution at 30.93 g/L. Profiles of free and bound chlorides are also available for LCK concrete after 90 days of curing.

The LCK matrix was characterized by fast transport of chlorides in the concrete, even though it presented a low water porosity of 10% (4.1.1). This chloride diffusion coefficient ( $50.78 \times 10^{-12} \text{ m}^2/\text{s}$ ) is higher than the one found in the literature for OPC based-concretes, which is around  $23 \times 10^{-12} \text{ m}^2/\text{s}$  (IREX 2022) as discussed in greater detail in section 5.4. Figure 18 also shows that the LCK concrete bound a small fraction of the chlorides (on average 25% of bound chlorides among total chlorides), suggesting high chloride diffusion kinetics.

Unlike the LCK matrix, AAS and SSC concretes showed a strong resistance to chloride diffusion, even though the AAS and SSC concretes had a higher porosity, around 16% (but with smaller pore sizes as shown on Figure 12). Similar orders of magnitude for diffusion coefficient ( $D_{\text{NSS}}$ ) are found in the literature for SSC concretes of higher strength class, C45/55 or C50/60 ( $0.07\text{-}0.10 \times 10^{-12} \text{ m}^2/\text{s}$  by Divet and Le Roy (2013)) and AAS concretes of higher strength class ( $0.5 \times 10^{-12} \text{ m}^2/\text{s}$  by J. Zhang et al. (2020)),  $3.73 \pm 1.98 \times 10^{-12} \text{ m}^2/\text{s}$  by Osio-Norgaard, Gevaudan and Srubar (2018). It was not possible to accurately quantify free chlorides using the GranDuBé protocol to estimate the influence of chloride binding on the  $D_{\text{NSS}}$  coefficients, as the procedure was developed for Portland cement binders and gives values out of the expected order of magnitude and not relevant for AAS and SSC concretes. More details are given in the Discussion part 5.2.

Finally, the chloride diffusion coefficient  $D_{\text{NSS}}$  (Table 7) obtained on concretes after 28 days of curing was higher than the one measured on samples after 90 days of curing (lower chloride content and lower penetration depth measured). There is a factor of 4 or 2 for AAS or SSC, respectively, between the two curing periods (results unusable for LCK concrete after 28 days of curing), indicating a significant pore refinement between 28 and 90 days, consistently with the water porosity results at 50 °C presented in Figure 11. This seems logical as slag-based concretes are not entirely hydrated at 28 days and therefore have a less dense porous network and a physical barrier that is less effective in resisting chloride penetration (Jingxiao Zhang et al. 2020).



### 4.3.2 RCPT test

Charge passed,  $Q$ , in the RCPT test and the associated penetration levels of chloride ions for LCK, AAS and SSC concretes after 28 and 90 days of curing, are presented in Figure 19.

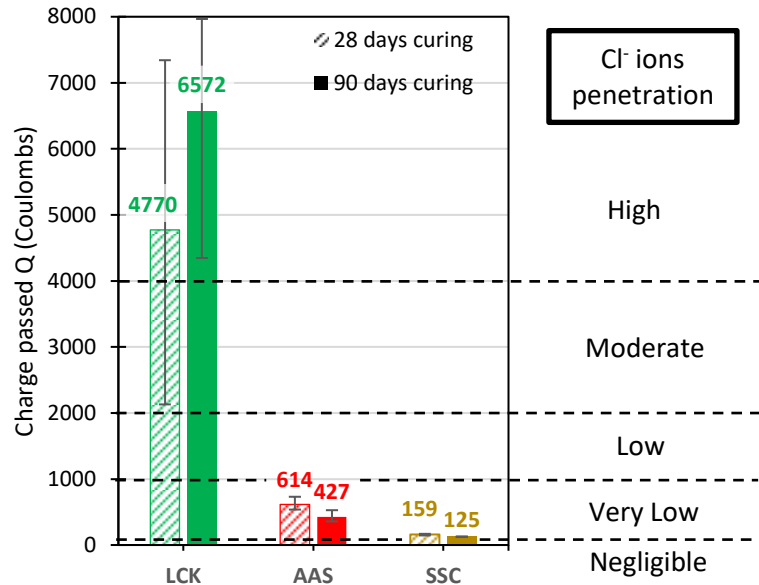


Figure 19: Charge passed,  $Q$ , and the associated penetration levels of chloride ions for LCK, AAS and SSC concretes after 28 days (hatched bars) and 90 days (full bars) of curing, from RCPT test.

The charge passed measured by the RCPT test is directly dependent on the material porosity and the connectivity of the porous network, as well as the presence of ions in the concrete pore solution (free chlorides). The presence of ions makes the electric current transport easier, and thus corresponds to measurement of a high charge passed and so a high permeability to chlorides (Kayali, Khan and Ahmed 2012). Figure 19 shows that charges passed for slag-based concretes are much lower than for LCK concrete. AAS and SSC have a very low charges passed (427 and 125 Coulombs, respectively, at 90 days of curing), i.e. a low chloride permeability, while LCK has high charge passed (6572 Coulombs at the same curing period) corresponding to a high chloride permeability. These results are in accordance with those of the natural chloride diffusion test presented in section 4.3.1 and with literature data (Noushini and Castel 2018; Masoudi 2018), and are discussed in more detail in section 5.3. The charge passed presented in Figure 19 is also proportional to the concrete resistivity presented in Figure 16, as it is obtained by integrating the current over time, which is itself a function of the resistance of the material according to Ohm's law. The proportionality between the charge passed and the resistivity of the concrete is shown in Figure 20, which illustrates that, when the resistivity of the material decreases, i.e. when its conductivity increases, the associated charge passed also increases because the current transport is favoured.

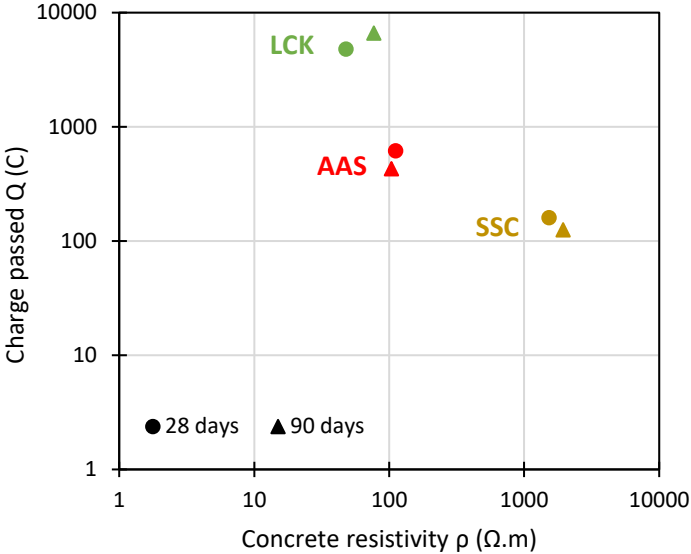


Figure 20: Relationship between the charge passed measured according to the RCPT test and the resistivity of concrete after 28 or 90 days of curing, for LCK, AAS and SSC.

## 5 Discussion

The tests carried out in this work to characterize the durability of the concretes were defined for Portland cement-based binders and it is important not to apply them for alternative binders without questioning their suitability. Sections 5.1 and 5.2 focus on this metrology aspect in order to discuss the relevance of the tests carried out with or without adaptation, to characterize the three low-carbon concretes of the study. The results obtained are then analysed in greater detail in section 5.3, and compared to commonly used references (CEM I, CEM II/A, CEM III/A) using a performance-based approach in section 5.4, before finally being extrapolated in section 5.5 to conclude on the resistance of each concrete to chloride ingress.

### *5.1 Metrology: effect of drying temperature for preconditioning of slag-based binders*

Drying is required as a preconditioning step for several durability tests. As summarized by (Trincal et al. 2022; 2020), the challenge is to use a drying temperature that efficiently removes the water from capillary pores without altering the material's microstructure and chemistry. Therefore, it is important to adapt this temperature to each binder to avoid erroneous conclusions and misinterpretations concerning their durability (possible over- or under-estimation of parameters). The literature shows that the high drying temperatures generally used for Portland cements are not suitable for slag-based binders.

For SSC, a high drying temperature leads to the destabilization of ettringite, which is an important hydrate of this binder (Moranville-Regourd and Kamali-Bernard 2019; Hegazy et al. 2019; M.C.G. Juenger et al. 2011), the proportion of which is estimated at about 30-40% of hydrates by thermodynamic modelling (A. Gruskovnjak et al. 2008; Astrid Gruskovnjak et al. 2011). It has been shown that ettringite is unstable around 60 °C and for higher temperatures (Ndiaye, Cyr, and Ginestet 2017). This result was confirmed by Cyr et al. (2019) by X-ray diffraction measurements on SSC paste samples. They showed that the SSC pastes conditioned at 20 °C (without drying) and 40 °C contain ettringite and gypsum as the main crystalline hydrates while, after drying at 105 °C, these substances are replaced by hemihydrate and anhydrite.

AAS binders do not contain ettringite as a hydration product but some authors have, nevertheless, investigated their suitable drying temperatures (Trincal et al. 2020; K. Yang et al. 2016; Z. Zhang et al. 2019; Ismail, Bernal, Provis, Hamdan, et al. 2013). For Na<sub>2</sub>CO<sub>3</sub>-AAS binders, the optimal drying temperature, according to Trincal et al. (2022), is a temperature between 80 °C and 105 °C, which provides optimal drying kinetics (not too long) and preserves the mechanical strength and mineralogy (only an increase of the pore size was highlighted). In contrast, it is better to avoid the range of 40-60 °C at low relative humidity, as a loss of mechanical strength was detected (more significant at 60 °C). According to the authors, it is possibly attributable to carbonates and C-(A)-S-H reactions, such as desaturation of intercrystallite pores, dissolution/precipitation, carbonation or the fact that higher drying temperatures and kinetics can limit capillary pressure.

The durability parameters that require a preconditioning step at high temperatures in this study are the water porosity test from standard NF P18-459 (105 °C required) and the gas permeability test from XP P18-463 (80 and 105 °C required). To evaluate the influence of the drying temperature on these parameters, the tests were performed at 45 °C, 60 °C, 80 °C and 105 °C on AAS and SSC with a constant sample thickness of 50 mm, as presented in Figure 21.

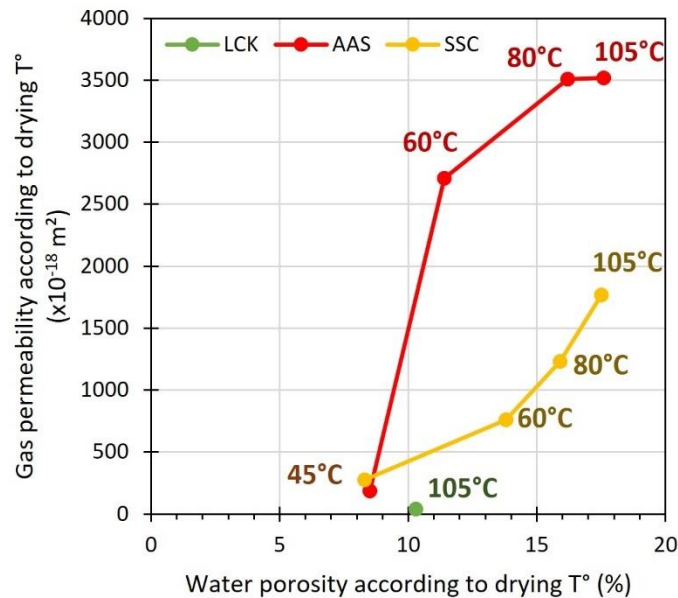


Figure 21: Gas permeability measured for different drying temperatures as a function of water porosity measured for the same drying temperatures, on LCK (in green), AAS (in red) and SSC (in yellow) samples with a constant thickness of 50 mm.

Firstly, it can be observed that the measured porosity increases with the drying temperature used (+9% between 45 °C and 105 °C for AAS and SSC), as more water can be removed from the capillary porosity in addition to all physically sorbed water, and there may also be damage to the material as discussed above. For the drying temperature of 60 °C, the measured increase in porosity is higher for SSC than for AAS, which tends to confirm the literature findings about ettringite destabilization for SSC. Considering conditions of 20 °C and 50% relative humidity (RH) in the laboratory where the tests were performed, the associated dew point (temperature at which the water vapour contained in humid air begins to condense on contact with a cold surface) is 9.3 °C. Assuming a constant dew point of 9.3 °C in the laboratory, a relative humidity of 12.5% can be deduced at 45 °C, 6% RH at 60 °C, 2.5% RH at 80 °C and 1% RH at 105 °C. It has been shown (Baquerizo, Matschei and Scrivener 2016), that ettringite becomes unstable around 5% RH and below, meaning that it is stable with an acceptable reliability for the drying temperature of 45 °C of Figure 21. Finally, the porosity of 8% measured for the drying temperature of 45 °C for slag-based binders seems very low (even lower than that of LCK) and is certainly underestimated due to the low drying temperature, preventing the evaporation of water in the smaller capillary pores, even if a constant mass is reached (Trincal et al. 2022).

Concerning the gas permeability, it increases strongly with the drying temperature used, for the same reasons as explained above. This increase is rather linear for SSC although the values

measured at 45 and 105 °C ( $274$  to  $1770 \times 10^{-18}$  m<sup>2</sup>) differ by a factor of 6. For the AAS concrete, this increase is even higher ( $186$  to  $3520 \times 10^{-18}$  m<sup>2</sup>) with a factor of 19. At 60 °C, the permeability value is already multiplied by 15 compared to the one measured at 45 °C, which is in agreement with damage of the material at this temperature.

Finally, it is important to keep in mind that, at 105 °C, the values were probably over-estimated due to damage of the concrete or an alteration of its microstructure while, at 45 °C the values are surely under-estimated, preventing the evaporation of water in the smaller capillary pores (Cyr et al. 2019). It can be expected that the real water porosity and gas permeability of concrete are between these two extremes.

That is why the temperature of 50 °C was finally adopted, combined with a reduction of the sample thickness to 17 mm (not done for gas permeability but recommended), that is to say 1/3 of its initial thickness, to keep only one acceptable drying temperature for LCK, AAS and SSC in the modified procedures proposed previously. 50 °C was chosen as a compromise considering the destabilization of ettringite around 60 °C and above for SSC and the damage of the material observed from 60 °C for the gas permeability measurement of AAS. Moreover, at the chosen temperature of 50 °C, the associated relative humidity of 10%, considering a constant dew point of 9.3 °C, ensures the stability of ettringite (Baquerizo, Matschei, and Scrivener 2016). No particular recommendations were necessary for the LCK as behaviour similar to that of a Portland cement is expected during drying. Mechanical strength measurements on 4x4x16 cm<sup>3</sup> mortar samples were made in parallel on AAS (Figure 24 in supplementary data) and no decrease was observed after drying at 50 °C, as previously reported (Trincal et al. 2022; Azar et al. 2021).

Finally, Figure 21 shows that the drying temperature still has considerable influence on the results obtained. The temperature of 50 °C is proposed in this study for the thermal preconditioning of low-carbon binders but it remains preferable, when possible, to favour direct tests on a pathology without prior thermal preconditioning (RCPT, migration or diffusion tests to assess the performance of concrete against chloride penetration for example) for greater reliability and representativity of the real conditions. It should thus be recommended to avoid using only general durability indicators such as porosity and permeability to qualify the long-term behaviour of these binders and to adapt the conditioning to the concrete constituents.

## **5.2 Metrology: determination of free and bound chlorides for slag-based binders**

It is well known that slag-based binders (such as AAS and SSC) are resistant to chloride penetration due to their high binding capacities (observation of chloride binding by hydration products using XRD, TGA, etc.), but few studies in the literature deal with the quantification of free and bound chlorides in such matrices. For example, Osio-Norgaard, Gevaudan, and Srubar (2018) proposed a review of 66 articles dealing with chloride transport in AAS binders but, among them, only one investigates chloride binding (by NaSi-AAS), following ASTM C1152 for acid-soluble chloride (total chloride) and ASTM C1218 for water-soluble chloride (free chloride) (Ismail, Bernal, Provis, Hamdan, et al. 2013).

As presented in part 4.3.1, it was not possible to quantify free chlorides accurately in this study by using the French protocol (Hornain 2007) for AAS and SSC concretes, as the procedure was developed for Portland-based materials and is quite sensitive to experimental conditions (stirring time, amount of water added, temperature, chlorides bound differently than for OPC...) (Chalhoub 2020). Extremely high free chloride contents were found (equal to or greater than total chlorides), as presented in Table 13 in the supplementary data, whereas slag-based binders are known for their higher ability to bind chlorides compared to Portland cement (Nguyen et al. 2018; G. Yang, Zhao and Wang 2022; J. Zhang et al. 2022; 2020; Ye, Huang and Chen 2019).

Some later investigations showed that it is mentioned by the standard ASTM C1218 for the determination of water soluble chloride in mortar and concrete, that “sulfides are known to interfere with the determination of chloride content”, as the slag contains “concentrations of sulfide capable of such interference and of producing erroneously high test results”, which confirms the previous findings (ASTM International 2017). A treatment with hydrogen peroxide is proposed in the standard to eliminate such interference by oxidizing the sulfides. Actually, this interference of sulfides in the determination of chloride content is mostly documented in the literature in other fields, such as analytical chemistry, environment or water treatment (Altunbulduk, zu K ocker and Frenzel 1995; Pargar, Koleva, and Klaas Van Breugel 2017; Wu et al. 2021; ASTM International 2017; Technical committee ISO/TC 147/SC 2 1989, 92). The standard ISO 9297:1989 in the field of water quality, explains that sulfides ( $S^{2-}$ ) hinder the determination of chloride in water, forming insoluble silver compounds, while thiosulfate ( $S_2O_3^{2-}$ ) ions form complexes with silver ions (Technical committee ISO/TC 147/SC 2 1989).

A test that allows better quantification of free and bound chlorides is the fixation isotherm test, where the concrete is crushed to a certain particle size and the depletion of the NaCl solution in contact with it is measured (Ke, Bernal and Provis 2017). This test was performed by (Ye, Huang and Chen 2019), and illustrates a higher chloride binding capacity of AAS (including  $Na_2CO_3$ -AAS) compared to OPC, particularly at high NaCl concentrations. The bound chloride content in AAS pastes equilibrated at 1.0 M NaCl condition ranges from 13.7 to 19.7 mg/g, i.e. 70%–150% higher than that of pure OPC pastes with a similar L/S ratio (Ye, Huang and Chen 2019). However this is a time-consuming test, which is no longer widely used. Quantitative analysis by ionic chromatography is also possible and some rare determinations of free and bound chlorides for AAS and SSC binders can be found in the literature.

Nguyen et al. (2018) succeeded in quantifying free and bound chlorides in SSC pastes and (Ismail, Bernal, Provis, San Nicolas, et al. 2013) quantified free and bound chlorides in NaSi-AAS pastes, following ASTM C1152 for acid-soluble chloride (total chloride) and ASTM C1218 for water-soluble chloride (free chloride). Neither of these groups state whether they used hydrogen peroxide. J. Zhang et al. (2020) quantified free chlorides in one NaSi+NaOH-AAS concrete, in accordance with the Chinese standard JTJ270-98 (Tianjin Harbour Engineering Institute 1998), where 2 g of concrete powder is put into 50 mL distilled water and shaken for 20 min. Twenty-four hours later, the suspension is filtered, 20 mL is put into a flask with 2 drops of phenolphthalein and diluted  $H_2SO_4$  is added until the solution becomes

colourless. Afterwards, 10 drops of  $K_2CrO_4$  solution are added and 0.02 mol/L  $AgNO_3$  solution is used to titrate until the solution becomes red. The volume of  $AgNO_3$  solution consumed is recorded and used to calculate the free chloride content. However, the free chloride values obtained were not compared to the total chloride values to quantify the chloride binding capacity.

Finally, some authors have proposed quantifying the chloride binding ability of AAS by alternative methods such as by experimental work on model hydrates and simulated pore solution (Ke et al. 2017) or by modelling (Mundra et al. 2020b). The main conclusions are that AAS and SSC binders have strong ability to bind chlorides. For example, Nguyen et al. (2018) found that, at 28 days, 87% of total chlorides measured were bound by SSC hydrates in pastes cast with 3%wt NaCl in the mix. This is much higher than the proportion of bound chlorides measured for the LCK concrete in section 4.3.1 (between 15% and 40% with an average of 25%, depending on the grinding depths).

### ***5.3 Microstructure and chemistry analysis***

This part highlights the characteristics of each of the low-carbon concretes of similar mechanical performances, by coupling the analysis of their microstructure and their chemistry (results obtained in section 4 and summarized in Table 8). These new elements give a better understanding of the performance of LCK, AAS and SSC against the penetration of aggressive agents.

Table 8: Summary of test results obtained for LCK, AAS and SSC concretes to characterize their general transfer properties, pore solution and performance against chloride penetration.

	Test or property measured	Unit	Sample curing	LCK	AAS	SSC
GENERAL TRANSFER PROPERTIES	Water porosity ( $\epsilon$ ) (105 °C)	%	28 days	10.0	18.2	17.3
			90 days	10.3	17.6	17.5
			6 months	10.0	18.8	17.3
			1 year	11.5	19.1	18.8
	Water porosity modified (50 °C)	%	28 days	10.6	16.2	16.4
			6 months	9.6	16.1	15.9
			1 year	9.8	15.8	14.2
	Mortar porosity from MIP	%	28 days	19	28	28
	Average pore diameter from MIP	nm	28 days	23	13	13
	Pore entry diameter of the largest pore size from MIP	nm	28 days	40	9 and 21	12
	Water permeability	mm	28 days	5	16	15
	Capillary absorption ( $A_w$ )	kg/m <sup>2</sup> .h <sup>1/2</sup>	28 days	0.112	0.259	0.346
	Gas permeability (k) (105 °C)	x10 <sup>-18</sup> m <sup>2</sup>	90 days	39	3520	1770
	Gas permeability modified (80 °C, 60 °C, 45 °C)	x10 <sup>-18</sup> m <sup>2</sup>	90 days	-	3510	1230
-				2710	761	
-				186	274	
Resistivity ( $\rho$ )	$\Omega$ .m	28 days	48	112	1537	
		90 days	77	104	1955	
PORE SOLUTION	Ionic conductivity of the pore solution ( $\sigma$ )	S/m	38 days	8	11	1
	Concentration of species in pore fluid solution	mmol/L	38 days	569	1652	149
CHLORIDE TRANSPORT	Natural chloride diffusion test ( $D_{nss}$ )	x10 <sup>-12</sup> m <sup>2</sup> /s	28 days	-	0.84 ± 0.10	1.06 ± 0.09
			90 days	50.78 ± 12.06	0.19 ± 0.01	0.58 ± 0.21
	RCPT test (Q)	Coulombs	28 days	4770	614	159
			90 days	6572	427	125

### Low clinker (LCK)

The results of section 4, summarized in Table 8, show that, in general, LCK concrete has good transfer properties: low porosity (water or MIP), low water and gas permeability, and low capillary absorption. This is mainly due to the low w/b ratio (0.25) of this mixture, combined with an optimized granular packing, which, on the one hand, balances the reduced cement content of this mixture (27% of the binder) and thus maintains the desired mechanical resistances (C25/30) and, on the other hand, minimizes the transfer properties (physical barrier). This is positive from a durability point of view. However, the drawback of this low w/b ratio is a more viscous concrete that is more difficult to handle (impact on rheology despite an optimized admixture), with a reversed cone flow rate of 9.7 s (Table 4).



The other weak point of this matrix is its low resistance to chloride penetration and diffusion, which depends mainly on the chemistry of its hydration products (influencing the chloride binding) and its pore structure (influencing the diffusive transport), as demonstrated mathematically by Ollivier et al. (2002). Despite its reduced porosity, a high chloride diffusion coefficient,  $D_{\text{nss}}$ , high charge passed in the RCPT test and low resistivity were measured for LCK. This can be explained by its low clinker content ( $137 \text{ kg/m}^3$  or 27% of the binder), which is responsible for a lower chloride-binding capacity on the one hand, and for high conductivity (thus low resistivity) because there are fewer hydrates to trap ions, on the other hand. Lower Portland cement content means a reduced capacity to bind chlorides, as shown in Figure 18: the LCK concrete bound few chlorides, which, combined with its very low resistivity presented in section 4.1.5 can partly explain the fast chloride ingress. This observation is in agreement with other studies for which the chloride diffusion coefficient measured on Portland limestone (30% limestone) concretes ( $13.6\text{--}23.5 \times 10^{-12} \text{ m}^2/\text{s}$ ) was considerably higher than on Portland cement ( $7.0\text{--}8.0 \times 10^{-12} \text{ m}^2/\text{s}$ ) (Bertolini, Lollini and Redaelli 2007; Lollini, Redaelli and Bertolini 2014, 2016). The review by Elgalhud, Dhir and Ghataora (2018) estimates that the chloride ingress of a Portland limestone concrete with 35% limestone can increase by about 65% compared to a concrete without limestone. This increase will be even higher for 73% limestone (as in the LCK of the study). Finally, and to a lesser extent, LCK has a majority of capillary pores ( $>10 \text{ nm}$ ), 85% according to Figure 13, and this promotes the mobility of chloride ions (Jingxiao Zhang et al. 2020). The physical barrier resisting penetration of aggressive agents is high (reduced transfer properties due to a low w/b ratio), but is counterbalanced by a low chemical barrier due to the low clinker content.

#### Slag-based binders (AAS and SSC)

The results of section 4, summarized in Table 8, show that AAS and SSC concretes have several similar transfer properties: same porosity (water and MIP), similar pore sizes, same water permeability, and high capillary absorption and gas permeability in both cases. In general, these transfer properties are high compared to those of LCK (except for pore size), due to a higher w/b ratio (about twice as high) and a higher paste volume (318 L for LCK, compared to 407 L for AAS and 360 L for SSC). In detail, the lower paste volume of SSC concrete (360 L) compared to AAS (407 L) is balanced by a higher w/b ratio (0.50 vs. 0.43 for AAS), resulting in similar transfer properties. Moreover, the high w/b ratio of these mixtures provides higher flowability than that of LCK concrete (flow rate 5 times as high) and thus easier workability.

Then, both matrices offer very good performance against chlorides: low chloride diffusion coefficient,  $D_{\text{nss}}$ , and low charge passed during the RCPT test in both cases, but of different orders of magnitude. The chloride diffusion coefficient (at 90 days of curing) of AAS concrete ( $0.19 \pm 0.01 \times 10^{-12} \text{ m}^2/\text{s}$ ) is lower than that of SSC ( $0.58 \pm 0.21 \times 10^{-12} \text{ m}^2/\text{s}$ ), which suggests a difference in the diffusive transport and/or chloride binding capacity between the two binders. A difference in diffusive transport is possible because of the higher capillary absorption, gas permeability and charge passed measured on AAS than on SSC (even though the values are of the same order of magnitude compared to those of the LCK), as well as a much lower resistivity, which would be in line with stronger diffusion mechanisms for AAS. However, the fact that the  $D_{\text{nss}}$  coefficient, which takes the chloride binding into account, is lower for AAS than for

SSC suggests a stronger chloride binding capacity of AAS, compensating for the higher diffusion. The mechanisms of chloride binding for AAS and SSC depend on their hydration products. For  $\text{Na}_2\text{CO}_3$ -AAS, 40% to 70% of the total bound chlorides are bound by hydrotalcite and monocarbonates (Ye, Huang and Chen 2019). These are hydration products called Layered Double Hydroxides (LDH) and represent between 22 and 40% of the solid phases, according to thermodynamic modelling (Mundra et al. 2020b; Ke et al. 2020). The chloride binding mechanism is either anion exchange in their intermediate layer or surface absorption in the electrical double layer (Ke et al. 2017). C-A-S-H also contributes to chloride binding (surface adsorption as the principal mechanism), but to a lesser extent than LDH (Ke et al. 2017). The chloride binding by SSC is governed principally by the formation of Friedel's salts from ettringite and by hydrotalcite (K. S. Nguyen et al. 2018), which make up between 25% and 47% of the solid phases, according to thermodynamic modelling (A. Gruskovnjak et al. 2008), following the same mechanisms as the one described for AAS.

Finally, a difference in ionic charge between the two mixtures can also be identified, as the SSC binder has lower charge passed (125 C at 90 days) than AAS (427 C) and a much higher resistivity (1955  $\Omega\cdot\text{m}$  versus 104  $\Omega\cdot\text{m}$  for AAS at 90 days). The low ionic charges (charge passed and resistivity) of the SSC can be explained by the very small amount of ions in its pore solution (149 mmol/L), leading to a very low conductivity (1 S/m) (Dean et al. 2006; Bu and Weiss 2014). Then, although SSC has a high porosity (water and MIP), its low pore diameter leads to more tortuosity and involves the double layer effects that reduce the mobility of remaining ions. Finally, SSC has a lower paste volume (360 L) than AAS (407 L), which also favours lower resistivity (Azarsa and Gupta 2017). Concerning AAS, although its porosity and pore size are similar to those of SSC, its higher ionic charge can mainly be explained by a very high concentration of species in its pore solution (1652 mmol/L), due to the high sodium content (Figure 17) brought by activation with sodium carbonate, leading to a high conductivity (11 S/m). Finally, unlike LCK concrete, AAS and SSC have a weaker physical barrier against aggressive agents, which is balanced by a strong chemical barrier against chlorides (summarized in Table 9).

*Table 9: Performance of each concrete considering the general transfer properties, chloride transport and rheology. The “+” symbol is associated with good performance (“++” indicating very good performance), and the “-” symbol with poorer performance.*

	<b>Associated results</b>	<b>LCK</b>	<b>AAS</b>	<b>SSC</b>
Porosity (water, MIP)	Figure 11 Figure 12 Figure 13	++	-	-
Capillary absorption	Figure 14	++	-	-
Water permeability	Figure 14	+	-	-
Gas Permeability	Figure 15	+	--	--
Resistivity	Figure 16	-	-	++
Conductivity	Figure 17	-	-	++
Cl- diffusion	Figure 18	--	++	++
RCPT	Figure 19	-	+	+
Rheology	Table 4	-	+	+

#### **5.4 Comparison with references based on the performance approach**

In order to better position the performance of the three low-carbon concretes studied (LCK, AAS and SSC), a comparison was made with commonly used reference concretes (CEM I, CEM II/A, CEM III/A), using the performance-based approach as illustrated in Figure 22. General transfer properties, such as water porosity, resistivity, gas permeability, and capillary absorption were compared between the three low-carbon concretes of the study and three reference concretes, as were their natural chloride diffusion coefficient and their carbon footprint.

The reference concretes were chosen to have a strength class equal or close to that of the concretes in this study, which is C25/30. Thus, only the references C20/25, C25/30 and C30/37 were considered, in order to remain comparable to the concretes studied and because they had sufficiently complete databases (5 references for CEM I, 4 references for CEM II/A and 1 reference for CEM III/A) to be representative of the characteristics of the various reference concretes.

The database of the national project PERFDUB (IREX 2022) was used to make the comparisons because this project allowed the evaluation of many characteristics related to the durability of concretes considering various binders. It was also interesting because its data were published and involved cross testing between several laboratories (Turcry et al. 2021). In total, the PERFDUB database is composed of 42 concretes. For the calculation of carbon footprints, 765, 676 and 437 kg eq. CO<sub>2</sub>/m<sup>3</sup>, respectively, were taken for the CEM I, CEM II/A and CEM III/A according to the French values from SFIC (Syndicat Français de l’Industrie Cimentière) available on (ATILH 2022).

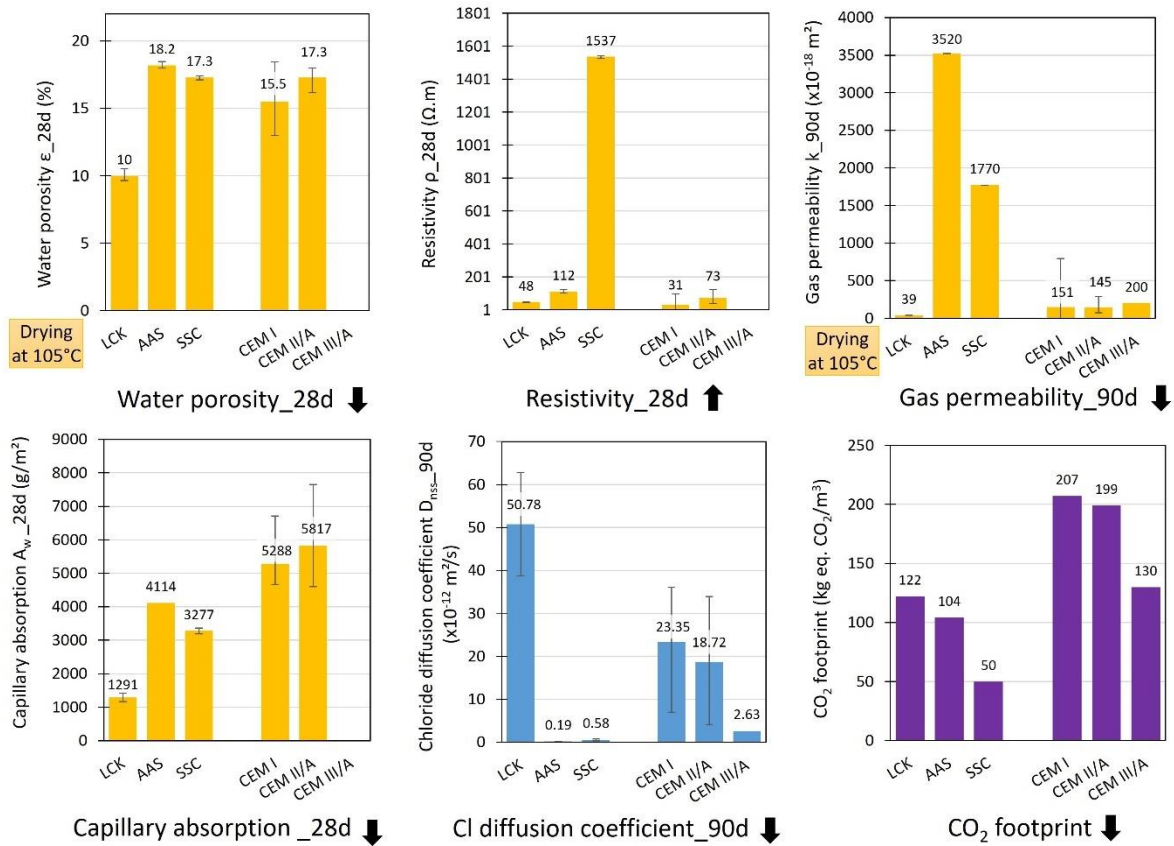


Figure 22: Comparison of LCK, AAS and SSC general transfer properties, chloride transport and CO<sub>2</sub> footprint with those of reference concretes (CEM I, CEM II/A and CEM III/A) of similar strength class from the PERFDUB database. An upward arrow indicates that a high value is aimed for the considered property, in order to have a maximum performance from a durability point of view (inversely with a downward arrow).

Concerning general transfer properties (bar charts in yellow in Figure 22)

Due to its low w/b ratio, LCK has low porosity and capillary absorption compared to the references, while AAS and SSC have porosity located in the high average of the references and slightly lower capillary absorption (keeping in mind that, for a drying temperature of 105 °C, the porosities are surely over-estimated for slag-based binders, as discussed in section 5.1). LCK and AAS have resistivity of the same order of magnitude as that of the references (similar to CEM I for LCK and to CEM II/A for AAS), while SSC has very high resistivity, mostly due to its low concentration of ions in the pore fluid solution. The same observations can be made at 90 days of curing, as detailed in Figure 25 in the supplementary data. Gas permeability is low for LCK concrete due to its low w/b ratio, while it is extremely high (several orders of magnitude higher) for AAS and SSC compared to the references, because of damage of the sample microstructure during the preconditioning in temperature. Except for this biased result, the three low-carbon concretes studied have similar or better transfer properties than the reference concretes of similar strength, which makes them competitive and attractive in addition to their reduced carbon footprints, which are slightly lower than that of CEM III/A for LCK and AAS and even 2.5 times lower for SSC.

### Concerning chloride transport (bar chart in blue on Figure 22)

The resistance to chloride penetration of the three concretes studied and the three references proposed varied according to the binder considered. In general, the more slag the binder contained, the more resistant the concrete was to chloride penetration. Thus, CEM III/A concrete was more resistant to chloride penetration than CEM I and CEM II/A binders. AAS and SSC concretes were even less permeable to chlorides than the references because they contained a larger amount of slag. In addition to different diffusive transport, these mixtures are known to strongly bind chlorides to their hydration products (even though this could not be quantified experimentally as explained in section 5.2). This slows down the penetration of chlorides through the material (Ke et al. 2017; K. S. Nguyen et al. 2018). In contrast, LCK concrete is very permeable to chlorides despite its low porosity because it has a reduced clinker content (27% of its binder). Less CEM I means a lower capacity to bind chlorides by the formation of Friedel salts. This result has also been reported in the literature by other authors (Carrinho 2018). Therefore, the natural chloride diffusion coefficient of LCK is twice the one of the CEM I-concrete reference. Despite its good transfer properties, it is advisable to avoid the use of this formulation of LCK concrete in a marine environment, contrary to AAS and SSC concretes, which are extremely efficient in chloride-rich areas.

#### ***5.5 Use of a simplified model to characterize resistance to chloride ion penetration***

The objective of this section is to use a "simplified model" as an interpretation tool, to characterize the resistance to chloride penetration of the three concretes studied, while remaining aware that more elaborate and realistic models exist. The aim is to use the experimental data obtained previously in order to obtain orders of magnitude and trends of time required for chloride to reach a rebar at a certain concrete cover. The idea is to use the solution of Fick's second law for a semi-infinite case with a constant boundary condition  $C_s$  and initial condition  $C_i$  (Equation (14)), using the natural chloride diffusion coefficient,  $D_{nss}$ , obtained experimentally on concrete cured for 90 days and immersed in reconstituted seawater (presented in section 4.3.1).

$$C(x, t) = C_i + (C_s - C_i) \left[ 1 - \operatorname{erf} \left( \frac{x}{\sqrt{D_{nss} t}} \right) \right] \quad (14)$$

where  $C(x, t)$  (% by mass of concrete) is the chloride content measured at average depth  $x$  (m) and exposure time  $t$  (seconds);  $C_s$  is the calculated chloride content at the exposed surface (% by mass of concrete);  $C_i$  is the initial chloride content (% by mass of concrete);  $D_{nss}$  is the non-steady state chloride diffusion coefficient ( $\text{m}^2 \cdot \text{s}^{-1}$ ).

It has been shown that “chloride-transport tests (...) can be used as inputs to models to provide reasonably reliable predictions of performance under certain limitations” (Alexander and Thomas 2015), as confirmed by (Koenders, Imamoto, and Soive 2022), and that the estimation of the time needed for chlorides to reach a rebar at a defined depth from Fick's second law provides good matches to reality (Lliso-Ferrando et al. 2022). The use of the non-steady state diffusion coefficient  $D_{nss}$  allows the diffusion of chlorides through the concrete, as well as the concrete's chloride binding capacity, to be considered in an indirect way (without the use of chloride fixation isotherms for each matrix).

A first hypothesis taken here is that the model considers only the diffusion mechanism, while other chloride transport processes may take place (Jingxiao Zhang et al. 2022). It is also assumed that  $D_{nss}$  is constant over time, even though it is shown in the literature that it is temperature dependent (Alexander and Thomas 2015) and time dependent (Tran et al. 2020; Andrade and Castellote 2011), until it reaches a constant value after 5 to 10 years of service (Andrade, Castellote and d'Andrea 2011). Therefore, this hypothesis may lead to a slight overestimation of the kinetics obtained. To approach a stabilized  $D_{nss}$  value more closely, the model is used for the 90 days of cure. The parameters  $C_i$ ,  $C_s$  and  $D_{nss}$  are those presented in Table 7.

From this point, for a given cover  $x$ , it is possible to calculate, using a solver, the diffusion time required for chlorides to reach a critical concentration,  $C_{crit}$ , (meaning that  $C(x,t)$  is taken equal to  $C_{crit}$ ) at the reinforcement for each concrete, as illustrated in Figure 23.  $C_{crit}$  is the critical chloride concentration threshold that alters the rebar passive film stability and leads to corrosion initiation. A wide range of values have been suggested for this parameter in the literature (Ueli Angst et al. 2009; Ueli Angst 2011; U. M. Angst 2019; U. M. Angst et al. 2022; Gao et al. 2019). The value of 0.4% is often chosen for  $C_{crit}$  in the case of aerated conditions, while 1% is recommended in immersed conditions as the oxygen is little renewed and more chlorides are needed to initiate corrosion (Deby 2008; U. M. Angst et al. 2022). Therefore,  $C_{crit}$  is fixed at 1%/binder mass in this study, as the diffusion coefficient  $D_{nss}$  is measured in seawater (immersed conditions). For the LCK, the cement and limestone filler are considered in the binder. It corresponds to a threshold  $C_{crit}$  of 0.211, 0.224 and 0.184 % by mass of concrete for the LCK, AAS and SSC mixtures respectively.

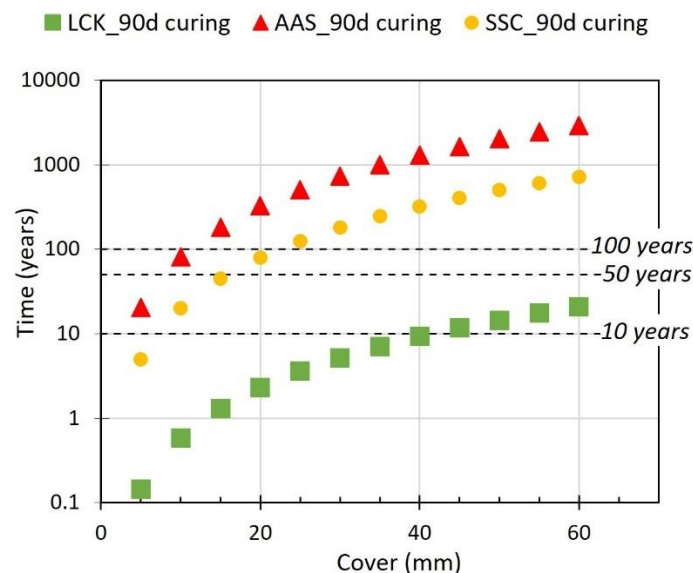


Figure 23: Time required to reach the critical chloride threshold (1%/binder mass) at the reinforcement for each concrete, considering different covers from 10 to 60 mm.

Figure 23 illustrates the very different chloride penetration resistances of the three concretes considered in this study, which were formulated to have the same strength class C25/30. These are approximate values and cannot be taken as certain. However, they allow the three low-

carbon concretes to be compared. For LCK concrete, the critical chloride threshold (1%/binder mass) at the reinforcement is reached much faster than for the slag-based formulations, despite a low porosity. This is due to its low clinker content, which results in a low chloride binding capacity (section 4.3.1) and a low resistivity (section 4.1.5). In 5.2 years, the threshold of 1% chlorides/binder mass is reached at the reinforcement for a 30 mm cover. Finally, it seems that the LCK concrete does not guarantee a 50-year service life, even for a thick cover (60 mm). In contrast, slag-based formulations are more resistant to chloride penetration, as they are known to have a high chloride binding capacity. AAS concrete appears to perform best despite the similar porosities and much higher resistivity of SSC concrete. This difference can be partly explained by a different diffusion kinetics and a different chloride binding capacity due to the presence of different hydrates between the two. For example, for a 30 mm cover, the critical chloride threshold will be reached after 5.2 years, 181 years and 736 years for LCK, SSC and AAS, respectively. Increasing the cover by 5 mm significantly increases the time taken for chlorides to reach the reinforcement: 2 years more for LCK, 65 years for SSC and 266 years for AAS by moving from 30 to 35 mm.

The French classification PERFDUB led to the creation of the standard FD P18-480 (AFNOR 2022a) that details thresholds to be respected based on different durability parameters, depending on the exposure class. There are two exposure classes related to chloride exposure: XS (risk of corrosion induced by the chlorides present in the sea water) and XD (risk of corrosion induced by chlorides having a non-marine origin, de-icing salts for example). To be classified XS or XD, a concrete has to reach a performance threshold defined from a chloride migration test performed after 90 days of curing ( $D_{rcm\_90d}$ ) and modulated by an aging factor  $\alpha$ , which is a parameter describing the decrease of the apparent diffusion coefficient of chloride ions in concrete with time. It is calculated by considering the composition of the binder (proportions of slag, fly ash or silica fume). For LCK, the associated aging factor  $\alpha$  (calculated according to FD P18-480 (AFNOR 2022a)) is 0.30, as against 0.45 for AAS and SSC. No chloride migration test was performed in this study, but the Perfdub report (Turcry et al. 2021) shows a proportionality between migration coefficient ( $D_{rcm}$ ) and chloride diffusion coefficient ( $D_{nss}$  measured in this study). The comparison is therefore made directly with  $D_{nss}$  measured after 90 days of curing, presented in section 4.3.1. Although the  $D_{rcm\_90d}$  thresholds presented in Table 10 have not been defined for slag-based binders, AAS and SSC concretes could be classified as XS3m (tidal or splash zone) and XD3tf (very frequent salting), while LCK concrete does not achieve XS1 (exposed to air carrying sea salt but not in direct contact with sea water) and XD1 (moderate humidity) classes, as reported in Table 10.

Table 10: XS and XD PERFDUB classification of LCK, AAS and SSC concretes, with the associated thresholds (chloride migration coefficient  $D_{rcm}$ ) from to FD P18-480 that must not be exceeded.

	<b>LCK</b>	<b>AAS</b>	<b>SSC</b>
XS classification	-	XS3m ( $3 \times 10^{-12}$ m <sup>2</sup> /s)	XS3m ( $3 \times 10^{-12}$ m <sup>2</sup> /s)
XD classification	-	XD3tf ( $9 \times 10^{-12}$ m <sup>2</sup> /s)	XD3tf ( $9 \times 10^{-12}$ m <sup>2</sup> /s)

## 6 Conclusion

The general transfer properties and chloride penetration resistance of LCK, Na<sub>2</sub>CO<sub>3</sub>-AAS and SSC concretes were investigated. These three low-carbon concretes were designed to have equivalent rheology and mechanical resistances (self-compacting concrete, C25/30). A comparison of their durability performances between each other and with commonly used reference concretes is presented. The following conclusions can be drawn:

- The tests performed to characterize the durability of concretes made with alternative binders require some adaptations. For the water porosity and gas permeability, a drying temperature of 50 °C instead of 105 °C, combined with a reduction of the sample thickness, should be recommended for the preconditioning of slag-based samples. For the determination of free and bound chlorides in slag-based binders, ionic chromatography or water soluble chloride analysis combined with hydrogen peroxide should be favoured over redox electrode.
- General durability indicators such as water porosity, water permeability or capillary absorption, should be considered with caution, as they are not suitable alone to evaluate the durability of low-carbon concretes exposed to chlorides. They have shown contradictory conclusions compared to the natural chloride diffusion or RCPT test, which should therefore be favoured.
- The LCK concrete has better transfer properties than reference concretes of similar strength (CEM I, CEM II/A, CEM III/A) due to its low w/b ratio, but this low ratio also results in a higher viscosity. The AAS and SSC concretes studied have transfer properties similar to those of reference concretes, which makes them and the LCK competitive and attractive, in addition to their reduced carbon footprint.
- Due to its reduced clinker content, the LCK concrete is very permeable to chlorides, even when compared to traditional concretes. Its use in the presence of chloride should be avoided as it does not fulfil the criteria of exposure classes XS1 and XD1.
- The slag-based concretes AAS and SSC are extremely resistant to chloride penetration and are even better than the references, mainly because of their high ability to bind chlorides. They are perfectly suited to use in a marine environment, even for the most unfavourable exposure classes, XS3m (tidal or splash zone) and XD3tf (very frequent salting).

This article has focused on chloride penetration resistance, but these same low-carbon concretes will be evaluated with respect to carbonation resistance in a forthcoming paper.



## 7 Supplementary data

Related to 4.2

Table 11: Molar conductivity (Pethig 1987; Abba et al. 2014; Rupiasih et al. 2018; Kubota, Mochizuki and Yokoi 1988) and atomic weight of the main cations and anions present in the pore fluid solution of LCK, AAS and SSC specimens.

	Cations						Anions	
	Na <sup>+</sup>	K <sup>+</sup>	Ca <sup>2+</sup>	Al <sup>3+</sup>	Mg <sup>2+</sup>	Fe <sup>2+</sup>	OH <sup>-</sup>	S <sup>2-</sup>
Molar conductivity $\lambda$ (S.m <sup>2</sup> .mol <sup>-1</sup> ).10 <sup>-4</sup>	50.1	73.5	119	189	106.1	108	198.6	65*
Atomic weight (g/mol)	22.99	39.1	40.08	26.98	24.31	55.85	17	32.1

\* Molar conductivity,  $\lambda$ , of HS<sup>-</sup> instead of S<sup>2-</sup>, which is another possible ion formed from sulfur

Table 12: Conductivity of the pore fluid solution of LCK, AAS and SSC pastes after 38 days of curing, as the sum of the conductivity of all cations and anions, calculated according to Equation (13).

		LCK	AAS	SSC
Contribution of each species to the conductivity of the pore fluid solution (S/m)	Na <sup>+</sup>	0.27	5.09	0.22
	K <sup>+</sup>	1.64	0.25	0.23
	Ca <sup>2+</sup>	0.05	0.00	0.19
	Al <sup>3+</sup>	0.00	0.14	0.00
	Mg <sup>2+</sup>	0.00	0.00	0.00
	Fe <sup>2+</sup>	0.00	0.00	0.00
	OH <sup>-</sup>	5.69	2.23	0.26
S <sup>2-</sup>	0.00	3.13	0.30	
Conductivity of the pore fluid solution (S/m)		7.65	10.85	1.19

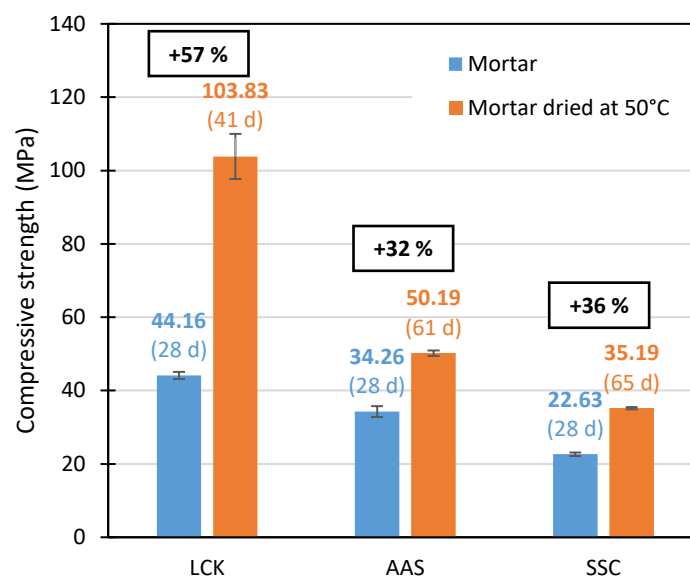
Related to 5.1

Figure 24: Compressive strengths measured on LCK, AAS and SSC  $4 \times 4 \times 16 \text{ cm}^3$  mortar samples, after 28 days of wet curing (in blue) or after drying at  $50^\circ \text{C}$  until a constant mass was reached (in orange).

Related to 5.2

Table 13: Concentration of total and free chlorides (per mass of concrete) determined using the GranDuBé protocol on an AAS (left hand side) and an SSC (right hand side) sample after the chloride diffusion test presented in section 3.3.1. The bound chlorides are calculated as the difference between total and free chloride contents.

Depth of the ground layer (mm)	Mass % of Cl <sup>-</sup> (AAS)		
	Total Cl <sup>-</sup> (analyses)	Free Cl <sup>-</sup> (analyses)	Bound Cl <sup>-</sup> (calculation)
1.07 to 2.06	0.3484	0.3328	0.0156
2.06 to 3.07	0.2717	0.2567	0.015
3.07 to 4.03	0.1864	0.1888	-0.0025
4.03 to 5.08	0.1103	0.1209	-0.0107
5.08 to 6.03	0.0656	0.0787	-0.0131
6.03 to 7.04	0.0420	0.0661	-0.0241
7.04 to 8.00	0.0305	0.0513	-0.0206
8.00 to 9.02	0.0249	0.0437	-0.0188
9.02 to 9.98	0.0187	0.0384	-0.0197

Depth of the ground layer (mm)	Mass % of Cl <sup>-</sup> (SSC)		
	Total Cl <sup>-</sup> (analyses)	Free Cl <sup>-</sup> (analyses)	Bound Cl <sup>-</sup> (calculation)
0.93 to 1.91	0.2600	0.2736	-0.0136
1.91 to 2.97	0.2178	0.2343	-0.0166
2.97 to 3.86	0.1645	0.1744	-0.0099
3.86 to 4.96	0.1086	0.1117	-0.0031
4.96 to 5.88	0.0693	0.0687	0.0006
5.88 to 6.88	0.0499	0.0542	-0.0044
6.88 to 7.89	0.0323	0.0373	-0.0050
7.89 to 8.97	0.0341	0.0322	0.0019

Related to 5.4

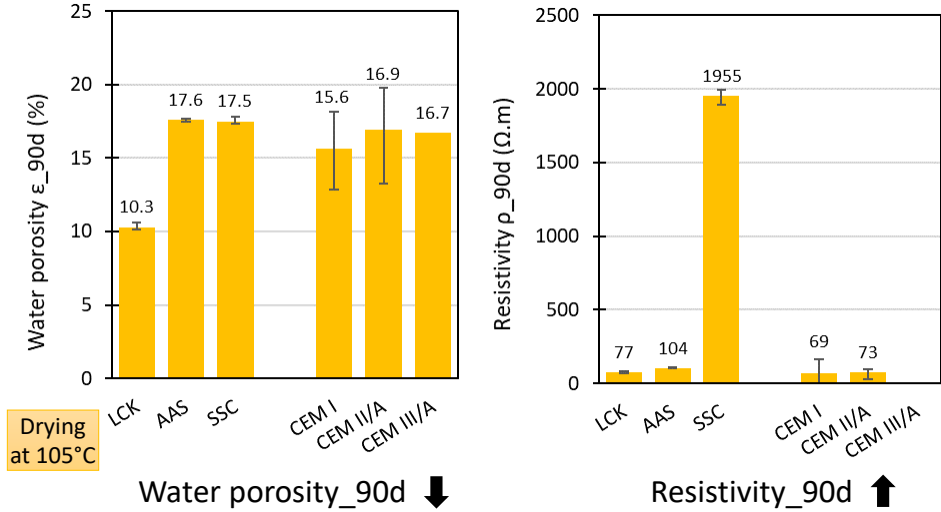


Figure 25: Comparison of LCK, AAS and SSC water porosity and resistivity after 90 days of curing, with those of reference concretes (CEM I, CEM II/A and CEM III/A) of similar strength class from the PERFDUB database. The arrow illustrates the direction in which the considered property is the best from a durability point of view.

## 8 References

- Abba, P., J. Gongwala, S. Laminsi, and J.-L. Brisset. 2014. 'The Effect of the Humid Air Plasma on the Conductivity of Distilled Water', *International Journal of Research in Chemistry and Environment*, 4 (1): 25–30.
- AFNOR. 2003. 'ISO-15148 : Détermination Du Coefficient d'absorption d'eau Par Immersion Partielle'.
- AFNOR. 2007. 'NF EN 14629 : Mesurage Du Taux de Chlorure d'un Béton Durci'.
- AFNOR. 2009. 'EN 12390-8: Profondeur de Pénétration d'eau Sous Pression'.
- AFNOR. 2010a. 'NF EN 15743 : Ciment Sursulfaté - Composition, Spécifications et Critères de Conformité'.
- AFNOR. 2010b. 'NF P18-459 : Essai de Porosité et de Masse Volumique'.
- AFNOR. 2011. 'XP P18-463 : Essai de Perméabilité Aux Gaz Sur Béton Durci'.
- AFNOR. 2015. 'EN 12390-11 : Détermination de La Résistance Du Béton à La Pénétration Des Chlorures, Diffusion Unidirectionnelle'.
- AFNOR. 2022a. 'FD P 18-480'.
- AFNOR. 2022b. 'NF EN 206/CN'.
- Alexander, Mark, and Michael Thomas. 2015. 'Service Life Prediction and Performance Testing — Current Developments and Practical Applications'. *Cement and Concrete Research* 78 (December): 155–64. <https://doi.org/10.1016/j.cemconres.2015.05.013>.
- Altunbulduk, Tahir, Heinz Meier zu Köcker, and Wolfgang Frenzel. 1995. 'Studies on the Elimination of Sulfide Interference in the Potentiometric Determination of Chloride Using Ion Selective Electrodes in a Flow Injection System'. *Fresenius' Journal of Analytical Chemistry* 351 (7): 593–98. <https://doi.org/10.1007/BF00323331>.
- Andrade, C., M. Castellote, and R. d'Andrea. 2011. 'Measurement of Ageing Effect on Chloride Diffusion Coefficients in Cementitious Matrices'. *Journal of Nuclear Materials* 412 (1): 209–16. <https://doi.org/10.1016/j.jnucmat.2010.12.236>.
- Andrade, C, and Marta Castellote. 2011. 'Chloride Aging Factor of Concrete Measured by Means of Resistivity', 8.
- Angst, Ueli. 2011. 'Chloride Induced Reinforcement Corrosion in Concrete: Concept of Critical Chloride Content – Methods and Mechanisms'. Doctoral thesis, Norges teknisk-naturvitenskapelige universitet, Fakultet for ingeniørvitenskap og teknologi, Institutt for konstruksjonsteknikk. <https://ntnuopen.ntnu.no/ntnu-xmlui/handle/11250/236720>.
- Angst, Ueli, Bernhard Elsener, Claus K. Larsen, and Øystein Vennesland. 2009. 'Critical Chloride Content in Reinforced Concrete — A Review'. *Cement and Concrete Research* 39 (12): 1122–38. <https://doi.org/10.1016/j.cemconres.2009.08.006>.
- Angst, Ueli M. 2019. 'Predicting the Time to Corrosion Initiation in Reinforced Concrete Structures Exposed to Chlorides'. *Cement and Concrete Research* 115 (January): 559–67. <https://doi.org/10.1016/j.cemconres.2018.08.007>.
- Angst, Ueli M., O. Burkan Isgor, Carolyn M. Hansson, Alberto Sagüés, and Mette Rika Geiker. 2022. 'Beyond the Chloride Threshold Concept for Predicting Corrosion of Steel in Concrete'. *Applied Physics Reviews* 9 (1): 011321. <https://doi.org/10.1063/5.0076320>.
- Angulski da Luz, C., and R.D. Hooton. 2015. 'Influence of Curing Temperature on the Process of Hydration of Supersulfated Cements at Early Age'. *Cement and Concrete Research* 77 (November): 69–75. <https://doi.org/10.1016/j.cemconres.2015.07.002>.
- ASTM. 2012. 'C1202-12: Test Method for Electrical Indication of Concretes Ability to Resist Chloride Ion Penetration'. ASTM International. <https://doi.org/10.1520/C1202-12>.
- ASTM International. 2017. 'ASTM C1218 / C1218M-17, Standard Test Method for Water-Soluble Chloride in Mortar and Concrete'. West Conshohocken, PA.
- ATILH. 2022. 'Ciments et LHR : Analyse et Inventaire Du Cycle de Vie (ACV/ICV), Déclaration Environnementale Produit (DEP)'. Infociments. June 2022. <https://www.infociments.fr/ciments/ciments-declaration-environnementale-inventaire-analyse-du-cycle-de-vie>.

- Awoyera, Paul, and Adeyemi Adesina. 2019. 'A Critical Review on Application of Alkali Activated Slag as a Sustainable Composite Binder'. *Case Studies in Construction Materials* 11 (December): e00268. <https://doi.org/10.1016/j.cscm.2019.e00268>.
- Azar, Patrick, Gabriel Samson, Fabrice Deby, Hugo Lahalle, Virginie Benavent, Vincent Trincal, and Martin Cyr. 2021. 'Chloride-Induced Corrosion in Ordinary and Alkali-Activated Concrete'. *11th ACI/RILEM International Conference on Cementitious Materials and Alternative Binders for Sustainable Concrete*, June 2021.
- Azarsa, Pejman, and Rishi Gupta. 2017. 'Electrical Resistivity of Concrete for Durability Evaluation: A Review'. *Advances in Materials Science and Engineering* 2017: 1–30. <https://doi.org/10.1155/2017/8453095>.
- Baquerizo, Luis G., Thomas Matschei, and Karen L. Scrivener. 2016. 'Impact of Water Activity on the Stability of Ettringite'. *Cement and Concrete Research* 79 (January): 31–44. <https://doi.org/10.1016/j.cemconres.2015.07.008>.
- Bernal, Susan. 2016. 'Advances in Near-Neutral Salts Activation of Blast Furnace Slags'. *RILEM Technical Letters* 1 (June): 39. <https://doi.org/10.21809/rilemtechlett.2016.8>.
- Bernal, Susan A., John L. Provis, Rupert J. Myers, Rackel San Nicolas, and Jannie S. J. van Deventer. 2015. 'Role of Carbonates in the Chemical Evolution of Sodium Carbonate-Activated Slag Binders'. *Materials and Structures* 48 (3): 517–29. <https://doi.org/10.1617/s11527-014-0412-6>.
- Bertolini, L, F Lollini, and E Redaelli. 2007. 'Influence of Concrete Composition on Parameters Related to the Durability of Reinforced Concrete Structures.' In . Guimarães, Portugal.
- Bu, Yiwen, and Jason Weiss. 2014. 'The Influence of Alkali Content on the Electrical Resistivity and Transport Properties of Cementitious Materials'. *Cement and Concrete Composites* 51 (August): 49–58. <https://doi.org/10.1016/j.cemconcomp.2014.02.008>.
- Carrinho, Diogo José Scheepers. 2018. 'Resistance to Chloride-Ion Penetration of Different Concrete Mixtures Subjected to Long-Term Immersion Tests'. *Materials Science*, 11.
- Chalhoub, Chantal. 2020. 'Study of the Initiation and Propagation Phases of Chloride Induced Corrosion in Reinforced Concrete Structures'. Thesis, Toulouse: Université Toulouse 3 Paul Sabatier.
- Cyr, Martin, Ludovic André, Mailys Ruau, Nicolas Musikas, and Laurent Frouin. 2019. 'Durability of Supersulfated Cement with Improved Early Strength'. *15th International Congress on the Chemistry of Cement, Prague, Czech Republic*.
- Cyr, Martin, Patrice Rivard, Francis Labrecque, and Alain Daidié. 2008. 'High-Pressure Device for Fluid Extraction from Porous Materials: Application to Cement-Based Materials'. *Journal of the American Ceramic Society* 91 (8): 2653–58. <https://doi.org/10.1111/j.1551-2916.2008.02525.x>.
- Darquennes, Aveline, Bernard Espion, and Stéphanie Staquet. 2013. 'How to Assess the Hydration of Slag Cement Concretes?' *Construction and Building Materials, Special Section on Recycling Wastes for Use as Construction Materials*, 40 (March): 1012–20. <https://doi.org/10.1016/j.conbuildmat.2012.09.087>.
- Dean, Sw, Mt Bassuoni, Ml Nehdi, and Tr Greenough. 2006. 'Enhancing the Reliability of Evaluating Chloride Ingress in Concrete Using the ASTM C 1202 Rapid Chloride Penetrability Test'. *Journal of ASTM International* 3 (3): 13403. <https://doi.org/10.1520/JAI13403>.
- Deby, Fabrice. 2008. 'Approche Probabiliste de La Durabilité Des Bétons En Environnement Marin'. University of Toulouse.
- Dhir, R. K., M. C. Limbachiya, M. J. McCarthy, and A. Chaipanich. 2007. 'Evaluation of Portland Limestone Cements for Use in Concrete Construction'. *Materials and Structures* 40 (5): 459–73. <https://doi.org/10.1617/s11527-006-9143-7>.
- Divet, Loïc, and Robert Le Roy. 2013. 'Étude de La Durabilité Vis-à-Vis de La Corrosion Des Armatures Des Bétons Formulés Avec Des Ciments à Forte Teneur En Laitier de Haut Fourneau'. *BLPC*, no. 280–281 (November).
- Douglas, E., and J. Brandstetr. 1990. 'A Preliminary Study on the Alkali Activation of Ground Granulated Blast-Furnace Slag'. *Cement and Concrete Research* 20 (5): 746–56. [https://doi.org/10.1016/0008-8846\(90\)90008-L](https://doi.org/10.1016/0008-8846(90)90008-L).
- ecoinvent. 2022. 'ecoinvent Database'. Ecoinvent. 2022. <https://ecoinvent.org/the-ecoinvent-database/>.

- El-Didamony, Ha, A.A Amer, E.M Ewais, and K Shokry. 2016. 'Physico-Chemical and Mechanical Properties of Supersulphated Cement Pastes'. *Bulletin of Faculty of Science, Zagazig University* 2016 (2016): 54–67. <https://doi.org/10.21608/bfszu.2016.31065>.
- Elgalhud, Abdurrahman A., Ravindra K. Dhir, and Gurmel Ghataora. 2018. 'Chloride Ingress in Concrete: Limestone Addition Effects'. *Magazine of Concrete Research* 70 (6): 292–313. <https://doi.org/10.1680/jmacr.17.00177>.
- Elgalhud, Abdurrahman A., Ravindra K. Dhir, and Gurmel S. Ghataora. 2017. 'Carbonation Resistance of Concrete: Limestone Addition Effect'. *Magazine of Concrete Research* 69 (2): 84–106. <https://doi.org/10.1680/jmacr.16.00371>.
- Gao, Yanhong, Yingying Zheng, Junzhi Zhang, Jiandong Wang, Xiaoyun Zhou, and Yurong Zhang. 2019. 'Randomness of Critical Chloride Concentration of Reinforcement Corrosion in Reinforced Concrete Flexural Members in a Tidal Environment'. *Ocean Engineering* 172 (January): 330–41. <https://doi.org/10.1016/j.oceaneng.2018.11.038>.
- Gartner, Ellis, and Tongbo Sui. 2018. 'Alternative Cement Clinkers'. *Cement and Concrete Research, Report of UNEP SBCI Working group on low-CO2 eco-efficient cement-based materials*, 114 (December): 27–39. <https://doi.org/10.1016/j.cemconres.2017.02.002>.
- Gruskovnjak, A., B. Lothenbach, L. Holzer, R. Figi, and F. Winnefeld. 2006. 'Hydration of Alkali-Activated Slag: Comparison with Ordinary Portland Cement'. *Advances in Cement Research* 18 (3): 119–28. <https://doi.org/10.1680/adcr.2006.18.3.119>.
- Gruskovnjak, A., B. Lothenbach, F. Winnefeld, R. Figi, S.-C. Ko, M. Adler, and U. Mäder. 2008. 'Hydration Mechanisms of Super Sulphated Slag Cement'. *Cement and Concrete Research* 38 (7): 983–92. <https://doi.org/10.1016/j.cemconres.2008.03.004>.
- Gruskovnjak, Astrid, Barbara Lothenbach, Frank Winnefeld, Beat Münch, Renato Figi, Suz-Chung Ko, Michael Adler, and Urs Mäder. 2011. 'Quantification of Hydration Phases in Supersulfated Cements: Review and New Approaches'. *Advances in Cement Research* 23 (6): 265–75. <https://doi.org/10.1680/adcr.2011.23.6.265>.
- Habert, G., S. A. Miller, V. M. John, J. L. Provis, A. Favier, A. Horvath, and K. L. Scrivener. 2020. 'Environmental Impacts and Decarbonization Strategies in the Cement and Concrete Industries'. *Nature Reviews Earth & Environment* 1 (11): 559–73. <https://doi.org/10.1038/s43017-020-0093-3>.
- Hegazy, A., A. Khalil, E. El-Alfi, and M. El-Shahat. 2019. 'Durability of Supersulphated Cement Pastes Activated with Portland Cement in Magnesium Chloride Solution'. *Egyptian Journal of Chemistry* 62 (6): 1145–55. <https://doi.org/10.21608/ejchem.2019.6563.1579>.
- Hooton, Doug, Michelle Nokken, and M. Thomas. 2007. 'Portland-Limestone Cement: State-of-the-Art Report and Gap Analysis For CSA A 3000'. *SN3053*, January.
- Hornain, H. 2007. 'GranDuBé : Grandeurs Associées à La Durabilité Des Bétons'. *Presses Des Ponts*.
- INIES. 2017. 'INIES: Les Données Environnementales et Sanitaires de Référence Pour Le Bâtiment'. 2017. <https://www.base-inies.fr/iniesV4/dist/consultation.html>.
- Ioannou, Socrates, Atef Badr, Kaloyana Kostova, Kevin Paine, and Tim Ibell. 2016. 'Utilization of Fabric Formwork for Improving the Durability of Concrete from Supersulfated Cement'. *Key Engineering Materials* 711 (September): 615–21. <https://doi.org/10.4028/www.scientific.net/KEM.711.615>.
- IREX. 2022. 'Projet National PERFDUB'. 2022. <https://www.perfdub.fr/>.
- Ismail, Idawati, Susan A. Bernal, John L. Provis, Sinin Hamdan, and Jannie S. J. van Deventer. 2013. 'Drying-Induced Changes in the Structure of Alkali-Activated Pastes'. *Journal of Materials Science* 48 (9): 3566–77. <https://doi.org/10.1007/s10853-013-7152-9>.
- Ismail, Idawati, Susan A. Bernal, John L. Provis, Rackel San Nicolas, David G. Brice, Adam R. Kilcullen, Sinin Hamdan, and Jannie S. J. van Deventer. 2013. 'Influence of Fly Ash on the Water and Chloride Permeability of Alkali-Activated Slag Mortars and Concretes'. *Construction and Building Materials* 48 (November): 1187–1201. <https://doi.org/10.1016/j.conbuildmat.2013.07.106>.
- Juenger, Maria C. G., Ruben Snellings, and Susan A. Bernal. 2019. 'Supplementary Cementitious Materials: New Sources, Characterization, and Performance Insights'. *Cement and Concrete Research* 122 (August): 257–73. <https://doi.org/10.1016/j.cemconres.2019.05.008>.

- Juenger, M.C.G., F. Winnefeld, J.L. Provis, and J.H. Ideker. 2011. 'Advances in Alternative Cementitious Binders'. *Cement and Concrete Research* 41 (12): 1232–43. <https://doi.org/10.1016/j.cemconres.2010.11.012>.
- Kayali, Obada, Mohammad Khan, and M. Sharfuddin Ahmed. 2012. 'The Role of Hydrotalcite in Chloride Binding and Corrosion Protection in Concretes with Ground Granulated Blast Furnace Slag'. *Cement and Concrete Composites* 34 (8): 936–45. <https://doi.org/10.1016/j.cemconcomp.2012.04.009>.
- Ke, Xinyuan. 2017. 'Improved Durability and Sustainability of Alkali-Activated Slag Cements'. Phd, University of Sheffield. <http://etheses.whiterose.ac.uk/17557/>.
- Ke, Xinyuan, Susan A. Bernal, Oday H. Hussein, and John L. Provis. 2017. 'Chloride Binding and Mobility in Sodium Carbonate-Activated Slag Pastes and Mortars'. *Materials and Structures* 50 (6): 252. <https://doi.org/10.1617/s11527-017-1121-8>.
- Ke, Xinyuan, Susan A. Bernal, and John L. Provis. 2017. 'Uptake of Chloride and Carbonate by Mg-Al and Ca-Al Layered Double Hydroxides in Simulated Pore Solutions of Alkali-Activated Slag Cement'. *Cement and Concrete Research* 100 (October): 1–13. <https://doi.org/10.1016/j.cemconres.2017.05.015>.
- Ke, Xinyuan, Susan A. Bernal, John L. Provis, and Barbara Lothenbach. 2020. 'Thermodynamic Modelling of Phase Evolution in Alkali-Activated Slag Cements Exposed to Carbon Dioxide'. *Cement and Concrete Research* 136 (October): 106158. <https://doi.org/10.1016/j.cemconres.2020.106158>.
- Koenders, Eddie, Kei-ichi Imamoto, and Anthony Soive, eds. 2022. *Benchmarking Chloride Ingress Models on Real-Life Case Studies—Marine Submerged and Road Sprayed Concrete Structures: State-of-the-Art Report of the RILEM TC 270-CIM*. Vol. 37. RILEM State-of-the-Art Reports. Cham: Springer International Publishing. <https://doi.org/10.1007/978-3-030-96422-1>.
- Kovtun, M. 2018. 'Effect of Preconditioning on Durability Indices of Alkali-Activated Concretes'. *SP* 326, 19.1-19.6.
- Kubota, Eiji, Yoshiaki Mochizuki, and Masatoki Yokoi. 1988. 'Conductivity of Iron(II) Sulfate in Aqueous Solution at Various Temperatures'. *The Chemical Society of Japan* 61 (10): 3723–24.
- Kühl, H. 1908. Verfahren zur Herstellung von Zement aus Hochofenschlacke. German Patent No. 237777, issued 1908.
- Lakusic, Stjepan. 2019. 'Research Challenges for Broader Application of Alternative Binders in Concrete'. *Journal of the Croatian Association of Civil Engineers* 71 (10): 877–88. <https://doi.org/10.14256/JCE.2729.2019>.
- Lliso-Ferrando, J.R., I. Gasch, A. Martínez-Iberón, and M. Valcuende. 2022. 'Effect of Macrocell Currents on Rebar Corrosion in Reinforced Concrete Structures Exposed to a Marine Environment'. *Ocean Engineering* 257 (August): 111680. <https://doi.org/10.1016/j.oceaneng.2022.111680>.
- Lollini, Federica, Elena Redaelli, and Luca Bertolini. 2014. 'Effects of Portland Cement Replacement with Limestone on the Properties of Hardened Concrete'. *Cement and Concrete Composites* 46 (February): 32–40. <https://doi.org/10.1016/j.cemconcomp.2013.10.016>.
- Lollini, Federica, Elena Redaelli, and Luca Bertolini. 2016. 'A Study on the Applicability of the Efficiency Factor of Supplementary Cementitious Materials to Durability Properties'. *Construction and Building Materials* 120 (September): 284–92. <https://doi.org/10.1016/j.conbuildmat.2016.05.031>.
- Lothenbach, Barbara, Karen Scrivener, and R. D. Hooton. 2011. 'Supplementary Cementitious Materials'. *Cement and Concrete Research*, Conferences Special: Cement Hydration Kinetics and Modeling, Quebec City, 2009 & CONMOD10, Lausanne, 2010, 41 (12): 1244–56. <https://doi.org/10.1016/j.cemconres.2010.12.001>.
- Ma, Qianmin, Sreejith V. Nanukuttan, P. A. Muhammed Basheer, Yun Bai, and Changhui Yang. 2016. 'Chloride Transport and the Resulting Corrosion of Steel Bars in Alkali Activated Slag Concretes'. *Materials and Structures* 49 (9): 3663–77. <https://doi.org/10.1617/s11527-015-0747-7>.
- Masoudi, Rana. 2018. 'Examining Compositions, Hydration Mechanisms and Properties of Supersulfated Cement for Use in Concrete'. University of Toronto.

- Matschei, T., F. Bellmann, and J. Stark. 2005. 'Hydration Behaviour of Sulphate-Activated Slag Cements'. *Advances in Cement Research* 17 (4): 167–78. <https://doi.org/10.1680/adcr.2005.17.4.167>.
- Mindess, S., J.F. Young, and D. Darwin. 1981. *Concrete*. USA: Prentice Hall.
- Mohamed, Osama Ahmed. 2019. 'A Review of Durability and Strength Characteristics of Alkali-Activated Slag Concrete'. *Materials* 12 (8): 1198. <https://doi.org/10.3390/ma12081198>.
- Moranville-Regourd, Micheline, and Siham Kamali-Bernard. 2019. 'Cements Made From Blastfurnace Slag'. In *Lea's Chemistry of Cement and Concrete*, 469–507. Elsevier. <https://doi.org/10.1016/B978-0-08-100773-0.00010-1>.
- Mundra, Shishir, Dale P. Prentice, Susan A. Bernal, and John L. Provis. 2020. 'Modelling Chloride Transport in Alkali-Activated Slags'. *Cement and Concrete Research* 130 (April): 106011. <https://doi.org/10.1016/j.cemconres.2020.106011>.
- Mundra, Shishir, and John L. Provis. 2021. 'Mechanisms of Passivation and Chloride-Induced Corrosion of Mild Steel in Sulfide-Containing Alkaline Solutions'. *Journal of Materials Science* 56 (26): 14783–802. <https://doi.org/10.1007/s10853-021-06237-x>.
- Mundra, Shishir, Gabriel Samson, Giulia Masi, Rebecca Achenbach, David M. Bastidas, Susan A. Bernal, Maria C. Bigozzi, et al. 2023. 'Application of Electrochemical Methods for Studying Steel Corrosion in Alkali-activated Materials'. *Materials and Corrosion*, February, maco.202313743. <https://doi.org/10.1002/maco.202313743>.
- Ndiaye, Khadim, Martin Cyr, and Stéphane Ginestet. 2017. 'Durability and Stability of an Ettringite-Based Material for Thermal Energy Storage at Low Temperature'. *Cement and Concrete Research* 99 (September): 106–15. <https://doi.org/10.1016/j.cemconres.2017.05.001>.
- Nedeljković, Marija, Bahman Ghiassi, Sieger van der Laan, Zhenming Li, and Guang Ye. 2019. 'Effect of Curing Conditions on the Pore Solution and Carbonation Resistance of Alkali-Activated Fly Ash and Slag Pastes'. *Cement and Concrete Research* 116 (February): 146–58. <https://doi.org/10.1016/j.cemconres.2018.11.011>.
- Nguyen, Khanh Son, Anh Toan Nguyen-Phung, Hong Thai Le, Thanh Tri Ho, Tri Huynh Nguyen-Ngoc, Soon Poh Yap, Nobuhiro Chijiwa, and Nobuaki Otsuki. 2018. 'Chloride Binding Ability and Anti-Corrosion Properties of Supersulfated Cement in Seawater/Sand Mixing Concrete'. In *Proceedings of the 4th Congrès International de Géotechnique - Ouvrages - Structures*, edited by Hoang-Hung Tran-Nguyen, Henry Wong, Frederic Ragueneau, and Cuong Ha-Minh, 8:367–76. Singapore: Springer Singapore. [https://doi.org/10.1007/978-981-10-6713-6\\_36](https://doi.org/10.1007/978-981-10-6713-6_36).
- Noor-ul-Amin. 2014. 'An Overview on Comparative Study of Alternatives for Ordinary Portland Cement'. *Journal of Basic and Applied Chemistry* 4 (6): 15–22.
- Noushini, Amin. 2018. 'Durability of Geopolymer Concrete in Marine Environment'. Sydney, Australia: The University of New South Wales.
- Noushini, Amin, and Arnaud Castel. 2018. 'Performance-Based Criteria to Assess the Suitability of Geopolymer Concrete in Marine Environments Using Modified ASTM C1202 and ASTM C1556 Methods'. *Materials and Structures* 51 (6): 146. <https://doi.org/10.1617/s11527-018-1267-z>.
- Novak, D, and H Sommer. 2002. 'A New Low-Heat Sulfate Resistant Binder for Mass Concrete, HPC and SCC'. *Proceedings of the International Conference Held at the University of Dundee, Scotland, Challenges of Concrete Construction*, 5 (September): 213–22. <https://doi.org/10.1680/scc.31777>.
- Ollivier, Jean-Pierre, Myriam Carcassès, Jean-Philippe Bigas, and Olivier Truc. 2002. 'Diffusion Des Chlorures Dans Le Béton Saturé'. *Revue Française de Génie Civil* 6 (2): 227–50. <https://doi.org/10.1080/12795119.2002.9692363>.
- Olsson, Nilla, Barbara Lothenbach, Véronique Baroghel-Bouny, and Lars-Olof Nilsson. 2018. 'Unsaturated Ion Diffusion in Cementitious Materials – The Effect of Slag and Silica Fume'. *Cement and Concrete Research* 108 (June): 31–37. <https://doi.org/10.1016/j.cemconres.2018.03.007>.
- Osio-Norgaard, Jorge, Juan Pablo Gevaudan, and Wil V. Srubar. 2018. 'A Review of Chloride Transport in Alkali-Activated Cement Paste, Mortar, and Concrete'. *Construction and Building Materials* 186 (October): 191–206. <https://doi.org/10.1016/j.conbuildmat.2018.07.119>.

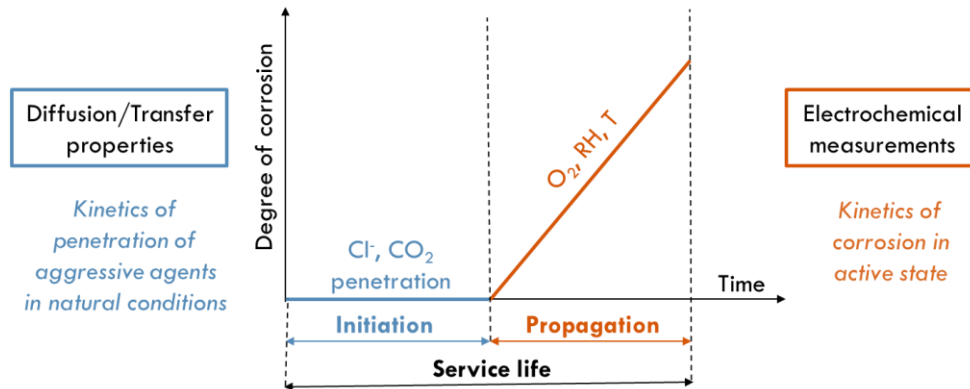


- Palm, Sebastian, Tilo Proske, Moien Rezvani, Stefan Hainer, Christoph Müller, and Carl-Alexander Graubner. 2016. 'Cements with a High Limestone Content – Mechanical Properties, Durability and Ecological Characteristics of the Concrete'. *Construction and Building Materials* 119 (August): 308–18. <https://doi.org/10.1016/j.conbuildmat.2016.05.009>.
- Papadakis, M., M. Venuat, and J. Vandamme. 1970. *Industrie de La Chaux, Du Ciment et Du Plâtre*. Dunod. Paris.
- Pargar, Farhad, Dessi Koleva, and Klaas Van Breugel. 2017. 'Determination of Chloride Content in Cementitious Materials: From Fundamental Aspects to Application of Ag/AgCl Chloride Sensors'. *Sensors* 17 (11): 2482. <https://doi.org/10.3390/s17112482>.
- Pethig, R. 1987. 'Dielectric Properties of Body Tissues'. *Clinical Physics and Physiological Measurement* 8 (4A): 5–12. <https://doi.org/10.1088/0143-0815/8/4A/002>.
- Pinto, Sabrina Requião. 2018. 'Durabilidade de compositos com cimento supersulfatado: estudo da literatura'. *Revista Técnico-Científica do Crea-PR - ISSN 2358-5420 – Ed. Especial* –, 12.
- Polder, R., C. Andrade, B. Elsener, Ø. Vennesland, J. Gulikers, R. Weidert, and M. Raupach. 2000. 'RILEM TC 154-EMC Recommendations: Test Methods for on Site Measurement of Resistivity of Concrete'. *Materials and Structures* 33 (December): 603–11.
- Provis, John. 2013. *Alkali Activated Materials: State-of-the-Art Report, RILEM TC 224-AAM*. New York: Springer.
- Roy, Della M. 1999. 'Alkali-Activated Cements Opportunities and Challenges'. *Cement and Concrete Research* 29 (2): 249–54. [https://doi.org/10.1016/S0008-8846\(98\)00093-3](https://doi.org/10.1016/S0008-8846(98)00093-3).
- Roy, Della M, Weimin Jiang, and M. R Silsbee. 2000. 'Chloride Diffusion in Ordinary, Blended, and Alkali-Activated Cement Pastes and Its Relation to Other Properties'. *Cement and Concrete Research*, Papers presented at the Symposium on 'Transport Properties and Microstructure of Cement-Based Systems', 30 (12): 1879–84. [https://doi.org/10.1016/S0008-8846\(00\)00406-3](https://doi.org/10.1016/S0008-8846(00)00406-3).
- Rupiasih, Ni Nyoman, Made Sumadiyasa, Department of Physics, Faculty of Mathematics and Natural Sciences, Udayana University, Kampus Bukit Jimbaran, Bali 80362, Indonesia, I Ketut Putra, Department of Physics, Faculty of Mathematics and Natural Sciences, Udayana University, Kampus Bukit Jimbaran, Bali 80362, Indonesia, Ni Made Rasmini, and Department of Physics, Faculty of Mathematics and Natural Sciences, Udayana University, Kampus Bukit Jimbaran, Bali 80362, Indonesia. 2018. 'Study on Transport Properties of Chitosan Membrane in Different Types of Electrolytes'. *Journal of Mathematical and Fundamental Sciences* 50 (2): 182–91. <https://doi.org/10.5614/j.math.fund.sci.2018.50.2.6>.
- Scrivener, Karen L., Vanderley M. John, and Ellis M. Gartner. 2018. 'Eco-Efficient Cements: Potential Economically Viable Solutions for a Low-CO<sub>2</sub> Cement-Based Materials Industry'. *Cement and Concrete Research* 114 (December): 2–26. <https://doi.org/10.1016/j.cemconres.2018.03.015>.
- Singh, Manjit, and Mridul Garg. 2003. 'Behaviour of Low Heat Sulphate Resistant Cement in Aggressive Media'. *INDIAN J. ENG. MATER. SCI.*, 4.
- Sun, Xiaogang, Yingliang Zhao, Jingping Qiu, and Jun Xing. 2022. 'Review: Alkali-Activated Blast Furnace Slag for Eco-Friendly Binders'. *Journal of Materials Science* 57 (3): 1599–1622. <https://doi.org/10.1007/s10853-021-06682-8>.
- Technical committee ISO/TC 147/SC 2. 1989. 'ISO 9297:1989, Qualité de l'eau — Dosage Des Chlorures — Titration Au Nitrate d'argent Avec Du Chromate Comme Indicateur (Méthode de Mohr)'.  
Thenepalli, Thriveni, Ahn Young Jun, Choon Han, Chilakala Ramakrishna, and Ji-whan Ahn. 2015. 'A strategy of precipitated calcium carbonate (CaCO<sub>3</sub>) fillers for enhancing the mechanical properties of polypropylene polymers'. *Korean Journal of Chemical Engineering* 32 (6): 1009–22. <https://doi.org/10.1007/s11814-015-0057-3>.
- Tianjin Harbour Engineering Institute. 1998. 'JTJ 270-1998: Testing Code of Concrete for Port and Waterway Engineering'.
- Tran, Quang, Pratanu Ghosh, Petr Lehner, and Petr Konečný. 2020. 'Determination of Time Dependent Diffusion Coefficient Aging Factor of HPC Mixtures'. *Key Engineering Materials* 832 (February): 11–20. <https://doi.org/10.4028/www.scientific.net/KEM.832.11>.
- Trincal, V., V. Benavent, H. Lahalle, B. Balsamo, G. Samson, C. Patapy, Y. Jainin, and M. Cyr. 2022. 'Effect of Drying Temperature on the Properties of Alkali-Activated Binders - Recommendations for Sample Preconditioning'. *Cement and Concrete Research* 151 (January): 106617. <https://doi.org/10.1016/j.cemconres.2021.106617>.

- Trincal, V., V. Benavent, H. Lahalle, G. Samson, C. Patapy, Y. Jainin, and M. Cyr. 2020. 'Preconditioning of Specimens - Drying Influence on Alkali-Activated and Geopolymer Mortar'. In *XV International Conference on Durability of Building Materials and Components. EBook of Proceedings*. CIMNE. <https://doi.org/10.23967/dbmc.2020.155>.
- Turcry, Ph., F. Cassagnabère, F. Jacquemot, and M. Guéguen Minerbe. 2021. 'National Project PERFDUB: General report of working group GT1'.
- Türkmen, İbrahim, Mehmet Gavgalı, and Rüstem Gül. 2003. 'Influence of Mineral Admixtures on the Mechanical Properties and Corrosion of Steel Embedded in High Strength Concrete'. *Materials Letters* 57 (13): 2037–43. [https://doi.org/10.1016/S0167-577X\(02\)01136-9](https://doi.org/10.1016/S0167-577X(02)01136-9).
- Wang, Aiguo, Yi Zheng, Zuhua Zhang, Kaiwei Liu, Yan Li, Liang Shi, and Daosheng Sun. 2020. 'The Durability of Alkali-Activated Materials in Comparison with Ordinary Portland Cements and Concretes: A Review'. *Engineering* 6 (6): 695–706. <https://doi.org/10.1016/j.eng.2019.08.019>.
- Wang, Shao-Dong. 1995. 'Alkaline Activation of Slag'. Phd, University of London.
- Wang, Shao-Dong, Karen L. Scrivener, and P. L. Pratt. 1994. 'Factors Affecting the Strength of Alkali-Activated Slag'. *Cement and Concrete Research* 24 (6): 1033–43. [https://doi.org/10.1016/0008-8846\(94\)90026-4](https://doi.org/10.1016/0008-8846(94)90026-4).
- Wu, Dan, Yinglu Hu, Ying Liu, and Runyu Zhang. 2021. 'Review of Chloride Ion Detection Technology in Water'. *Applied Sciences* 11 (23): 11137. <https://doi.org/10.3390/app112311137>.
- Yang, G., J. Zhao, and Y. Wang. 2022. 'Durability Properties of Sustainable Alkali-Activated Cementitious Materials as Marine Engineering Material: A Review'. *Materials Today Sustainability* 17 (March): 100099. <https://doi.org/10.1016/j.mtsust.2021.100099>.
- Yang, Kai, Changhui Yang, Bryan Magee, Sreejith Nanukuttan, and Jianxiong Ye. 2016. 'Establishment of a Preconditioning Regime for Air Permeability and Sorptivity of Alkali-Activated Slag Concrete'. *Cement and Concrete Composites* 73 (October): 19–28. <https://doi.org/10.1016/j.cemconcomp.2016.06.019>.
- Ye, Hailong, Le Huang, and Zhijian Chen. 2019. 'Influence of Activator Composition on the Chloride Binding Capacity of Alkali-Activated Slag'. *Cement and Concrete Composites* 104 (November): 103368. <https://doi.org/10.1016/j.cemconcomp.2019.103368>.
- Yeau, Kyong Yun, and Eun Kyum Kim. 2005. 'An Experimental Study on Corrosion Resistance of Concrete with Ground Granulate Blast-Furnace Slag'. *Cement and Concrete Research* 35 (7): 1391–99. <https://doi.org/10.1016/j.cemconres.2004.11.010>.
- Yu, Qi, Xiaomei Wan, Tiejun Zhao, Teng Wang, Xiao Han, and Zhongtao Sun. 2022. 'Investigation on Resistance of Chloride Penetration of Alkali Activated Slag Concrete and Related Electrical Test Methods'. *Materials Reports* 36 (5).
- Zhang, Jingxiao, Yuwei Ma, Jie Hu, Hao Wang, and Zuhua Zhang. 2022. 'Review on Chloride Transport in Alkali-Activated Materials: Role of Precursors, Activators and Admixtures'. *Construction and Building Materials* 328 (April): 127081. <https://doi.org/10.1016/j.conbuildmat.2022.127081>.
- Zhang, Jingxiao, Yuwei Ma, Jiazheng Zheng, Jie Hu, Jiyang Fu, Zuhua Zhang, and Hao Wang. 2020. 'Chloride Diffusion in Alkali-Activated Fly Ash/Slag Concretes: Role of Slag Content, Water/Binder Ratio, Alkali Content and Sand-Aggregate Ratio'. *Construction and Building Materials* 261 (November): 119940. <https://doi.org/10.1016/j.conbuildmat.2020.119940>.
- Zhang, Xuanhan, Kaidi Long, Wei Liu, Lixiao Li, and Wu-Jian Long. 2020. 'Carbonation and Chloride Ions' Penetration of Alkali-Activated Materials: A Review'. *Molecules* 25 (21): 5074. <https://doi.org/10.3390/molecules25215074>.
- Zhang, Zuhua, Yingcan Zhu, Huajun Zhu, Yu Zhang, John L. Provis, and Hao Wang. 2019. 'Effect of Drying Procedures on Pore Structure and Phase Evolution of Alkali-Activated Cements'. *Cement and Concrete Composites* 96 (February): 194–203. <https://doi.org/10.1016/j.cemconcomp.2018.12.003>.

## Durability of reinforcement in three low-carbon concretes

**Theoretical background:** presentation of binders + classical and galvanic corrosion mechanisms



### CORROSION INITIATION

**Objectives:** Estimate the time taken by the aggressive agents ( $\text{Cl}^-$  or  $\text{CO}_2$ ) to reach the reinforcement. Use reliable and representative test methods.

**Approach:** Characterisation of the general transfer properties, transport of  $\text{Cl}^-$  and  $\text{CO}_2$  on concrete.

#### Article A: General transfer properties and chloride penetration resistance

##### General transfer properties

- Tests:**
- Water porosity
  - Mercury intrusion porosity
  - Water permeability
  - Capillary absorption
  - Gas permeability
  - Resistivity

##### Transport of $\text{Cl}^-$

- Tests:**
- $\text{Cl}^-$  diffusion test
  - RCPT test

#### Article B: Resistance to carbonation

##### Transport of $\text{CO}_2$ and ability to maintain a high pH

- Tests:**
- Carbonation depth (natural, 1%  $\text{CO}_2$ , 3%  $\text{CO}_2$ )
  - pH measurements before and after carbonation of paste samples (natural, 1%  $\text{CO}_2$ )

### CORROSION PROPAGATION

**Objectives:** Evaluate the corrosion rates once the rebars have been depassivated. Use reliable and representative test methods.

**Approach:**

- Development of a methodology adapted to low-carbon binders and representative of real structures: galvanic current measurement + mass loss.
- Comparison with traditional electrochemical tests ( $E_{\text{corr}}$ ,  $\rho$ ,  $R_p$ ,  $i_{\text{corr}}$ , Tafel).

#### Article C: Chloride-induced corrosion

##### Experimental conditions:

- Different levels of chloride contamination:
- $[\text{NaCl}] = 30 \text{ g/L}$  (sea water)
  - $[\text{NaCl}] = 300 \text{ g/L}$  (de-icing salts)
- Saturated conditions

#### Article D: Carbonation-induced corrosion

##### Experimental conditions:

- Natural carbonation outdoor sheltered  
Samples with increased w/b ratio  
3 different moisture conditions tested

**Synthesis chapter:** discussion of articles A, B, C and D

## Transition to Article B

[Article A](#) characterized the general transfer properties of LCK, AAS and SSC concretes, and the corrosion initiation period in presence of chlorides. The results showed the LCK concrete is characterized by “excellent” transfer properties (low water porosity, gas permeability, water permeability and capillary absorption) but a very high chloride permeability. AAS and SSC concretes have similar transfer properties, comparable to classical concretes C25/30, and are extremely resistant to chloride penetration.

[Article B](#) also focuses on the **initiation period**, but this time when LCK, AAS and SSC concretes are exposed to carbonation, as the associated drop in pH could lead to corrosion initiation.

The objective is to determine the time taken by the **carbonation** front to penetrate through the concrete and to reach the rebar. The ability of each binder to maintain a high **pH** during the carbonation process has also to be studied, as these two aspects must be considered together, to determine a risk of corrosion initiation.



## Chapter 4 – Article B

# Resistance to carbonation of low-carbon concretes through natural and accelerated tests

## Table of contents

<b>1</b>	<b>Introduction .....</b>	<b>96</b>
<b>2</b>	<b>Materials.....</b>	<b>99</b>
2.1	Raw Materials.....	99
2.2	Carbon footprint of concrete .....	101
2.3	Mixing and curing .....	104
<b>3</b>	<b>Test methods .....</b>	<b>104</b>
3.1	Natural and accelerated carbonation rate.....	106
3.2	pH measurement and sample analysis before and after carbonation.....	107
3.2.1	<i>Before carbonation: pH and ICP analysis on pore solution extraction.....</i>	<i>107</i>
3.2.2	<i>After carbonation: pH by suspension method and X-ray diffraction (XRD) analysis .</i>	<i>108</i>
<b>4</b>	<b>Results.....</b>	<b>109</b>
4.1	CO <sub>2</sub> transport in concrete .....	109
4.1.1	<i>Carbonation rate in natural conditions.....</i>	<i>109</i>
4.1.2	<i>Carbonation rate in accelerated conditions.....</i>	<i>112</i>
4.2	pH measurement before and after carbonation.....	115
4.3	Pore solution composition before carbonation .....	115
4.4	XRD on carbonated pastes .....	117
<b>5</b>	<b>Discussion .....</b>	<b>118</b>
5.1	Carbonation resistance of LCK, AAS and SSC concretes .....	119
5.1.1	<i>Physical and chemical analysis.....</i>	<i>119</i>
5.1.2	<i>pH analysis.....</i>	<i>122</i>
5.1.3	<i>Use of a simplified model to characterize resistance to carbonation .....</i>	<i>124</i>
5.2	Representativity of accelerated carbonation tests for low-carbon concretes.....	126
5.2.1	<i>Comparison between natural (<math>k_{nat}</math>) and accelerated (<math>k_{acc}</math>) carbonation rates.....</i>	<i>127</i>
5.2.2	<i>Comparison of pH between natural and accelerated conditions .....</i>	<i>128</i>
5.2.3	<i>Recommendations to characterize the resistance to carbonation of low-carbon concretes</i>	<i>129</i>
5.3	Multi-criteria analysis.....	130
<b>6</b>	<b>Conclusion .....</b>	<b>133</b>
<b>7</b>	<b>Supplementary data.....</b>	<b>134</b>
<b>8</b>	<b>References.....</b>	<b>138</b>



## **Resistance to carbonation of low-carbon concretes (low clinker, alkali-activated slag and supersulfated cement) through natural and accelerated tests**

Lola Doussang<sup>1</sup>, Gabriel Samson<sup>1</sup>, Fabrice Deby<sup>1</sup>, Bruno Huet<sup>2</sup>, Emmanuel Guillon<sup>2</sup>, Martin Cyr<sup>1</sup>

<sup>1</sup> *Laboratoire de Matériaux et Durabilité des Constructions (LMDC), INSAT/UPS Génie Civil, 135 Avenue de Ranguéil, 31077 Toulouse Cedex 04 France.*

<sup>2</sup> *Holcim Innovation Center, 95 rue du Montmurier, F-38070 Saint Quentin Fallavier, France*

### **Abstract**

The carbonation resistance, considering the carbonation rates and the ability to maintain a high pH during the carbonation process, of three low-carbon concretes C25/30 (low clinker (LCK) concrete, alkali-activated slag with sodium carbonate (Na<sub>2</sub>CO<sub>3</sub>-AAS) concrete and supersulfated cement (SSC) concrete) was evaluated and compared to identify the behavior of each binder. The results in natural and accelerated conditions showed that the three binders are quite sensitive to carbonation, especially for short curing times, with different carbonation processes involved depending on their hydration products and pore solution chemistry. Recommendations are proposed to improve their performances. The relevance of accelerated tests at 1 and 3% CO<sub>2</sub> to characterize the carbonation of low-carbon concretes is also discussed. Finally, for both conditions it appears that the LCK has a low porosity which acts as an efficient physical barrier to slow down the CO<sub>2</sub> diffusion, but a limited amount of portlandite to act as a buffer pH. The SSC is characterized by a rapid carbonation and a low ability to maintain a high pH, contrary to the AAS, which carbonates quickly but has a strong ability to maintain a high pH (pH > 9 after 11 months at 1% CO<sub>2</sub> or 18 months in natural carbonation) governed by the amount of alkali ions in its pore solution.

### **Keywords**

Low-carbon concrete, Low clinker, Alkali-activated slag, Supersulfated, Durability, Carbonation, pH



## 1 Introduction

### Context of the study

The necessity to develop more sustainable concretes to reduce CO<sub>2</sub> emissions in the construction field is well known nowadays (Habert et al. 2020; Scrivener, John, and Gartner 2018). To face this environmental challenge, substitution of Portland cement by local supplementary cementitious materials (SCMs) in the binder or technologies without Portland cement have been developed (E. Gartner and Sui 2018; M.C.G. Juenger et al. 2011; Habert et al. 2020).

The present study focuses on the durability of three low-carbon concrete technologies of same strength class C25/30 among those available on the market: low clinker (LCK) concrete, alkali-activated slag with sodium carbonate (Na<sub>2</sub>CO<sub>3</sub>-AAS) concrete and supersulfated cement (SSC) concrete. In Europe, a large part of the concretes produced have to comply with exposure class XC (corrosion induced by carbonation). The characterization of LCK, AAS and SSC concretes with respect to this exposure class is therefore a major concern addressed in this study (keeping in mind that only the SSC complies with the EN 206 standard)). Their general transfer properties and resistance to chloride penetration have already been discussed in a previous article (Article A). More specifically, attention is paid in this paper on their resistance to carbonation, considering their carbonation rates and their ability to maintain a high pH during the carbonation process. These two aspects are of primary importance, as the time taken for the carbonation front to reach the reinforcement must be considered together with the pH drop in the material caused by the carbonation reactions, to determine a risk of corrosion initiation. If the carbonation front reaches the rebars, it becomes harmful, because a pH value of 9 leads to depassivation of the steels and thus to corrosion.

### Summary of data available in the literature

The **LCK** concrete reduces the proportion of Portland cement in the binder and therefore its water demand. In return, it contains a high amount of limestone filler to maintain an acceptable rheology (binder made of 27% CEM I and 73% limestone filler in this study) thanks to an optimized granular packing and admixture. LCK being a CEM I-based concrete, the mechanisms involved during the carbonation process have been extensively studied and are well understood (Vagelis G. Papadakis, Vayenas, and Fardis 1991; von Greve-Dierfeld et al. 2020; Angst et al. 2020; Rodrigues et al. 2020). The following successive reactions take place. The CO<sub>2</sub> naturally present in the atmosphere penetrates the porosity of the concrete and dissolves in the pore water to form carbonic acid, releasing H<sub>3</sub>O<sup>+</sup> ions during the reaction. To balance this drop in pH, some hydrates will dissolve, such as portlandite Ca(OH)<sub>2</sub>, which is very soluble and acts as a pH buffer by releasing OH<sup>-</sup> ions. Carbonation progressively leads to the decalcification of concrete with the reaction between carbonate ions and Ca-bearing phases, to form calcite CaCO<sub>3</sub>. Calcite also helps to fill the porosity of the concrete and thus slows down the diffusion of CO<sub>2</sub>. As Portland limestone cements CEM II/A-L (6–20% limestone content) and CEM II/B-L (21–35% limestone content) are standardized binders, information about their carbonation resistance is available in the literature (Palm et al. 2016; Dhir et al. 2007; Elgalhud, Dhir, and Ghataora 2018), but in the majority of cases for replacement levels by fillers ranging from 0 to 50%, which is still lower than the 73% filler content in the LCK.

The review of (Elgalhud, Dhir, and Ghataora 2017) shows that the carbonation of concrete increases with increasing limestone content: the carbonation rates are not altered for 15-20% cement replacement, but increase strongly for higher amounts of filler (increase of the carbonation depths in the order of 50% with 30% limestone content). Accelerated carbonation tests at 3–5% CO<sub>2</sub>, of Portland limestone cements are considered representative to natural indoor exposure. A good correlation between natural and accelerated carbonation rates is found and the same hydrates are observed for both conditions. These conclusions are confirmed by other studies (Palm et al. 2016; Dhir et al. 2007; Hooton, Nokken, and Thomas 2007).

The **AAS** concrete in this study is made with slag as aluminosilicate precursor, combined with a sodium carbonate alkaline activator. The sodium carbonate is chosen as activator for its wider availability, manufacturing process more eco-friendly, lower cost and health risk with handling highly alkaline solutions compared to sodium silicate or sodium hydroxide in liquid form (S. Bernal 2016; Awoyera and Adesina 2019). AAS have been extensively studied over the years, but studies focusing on sodium carbonate-based activation remains limited, while this parameter strongly influences the resistance to carbonation (K. Zhao et al. 2020; X. Zhang et al. 2020; Puertas, Palacios, and Vázquez 2006). Of the five articles focusing on AAS reviewed by (X. Zhang et al. 2020), no study on carbonation were found on Na<sub>2</sub>CO<sub>3</sub>-AAS. However, most of the studies agree that AAS have a higher susceptibility to carbonation than Portland cements, regardless of the activator type, with higher carbonation rates observed, both in natural and accelerated conditions (Mohamed 2019; A. Wang et al. 2020; X. Zhang et al. 2020). The literature also draws attention to the carbonation rates and pH obtained under accelerated conditions ( $\geq 3\text{-}4\%$  CO<sub>2</sub>), which are more severe and not representative anymore of the natural conditions, due to changes in the phase equilibrium at those concentration levels (S. A. Bernal et al. 2012; K. Zhao et al. 2020). Both studies were conducted on AAS activated by sodium silicate or a mix of sodium silicate and sodium hydroxide. Moreover, different mechanisms are involved during the carbonation process, due to a different pore solution and hydration products than in Portland cements, as AAS do not contain portlandite to act as a pH buffer. Carbonation mechanisms in Na<sub>2</sub>CO<sub>3</sub>-AAS and their influence on the pH of the pore solution have been recently studied and the new insights provided enable to better understand the chemical processes taking place during the carbonation, particularly through thermodynamic modelling (Ke et al. 2020; 2018). They highlighted the role of alkali ions, widely available in the pore solution, in maintaining a high pH. A complementary experimental approach is now necessary, with tests at the material scale, to confirm these explanations.

Finally, **SSC** is a standardized binder defined by the European standard EN 15743 (AFNOR 2010). It consists of a mix of at least 75% of slag combined with 5-20% calcium sulphate and an alkaline activator (0-5% clinker) to obtain a sufficient reactivity. The literature agrees that this binder has a lower initial pH than the other two matrices (around 12) and carbonates rapidly, as it does not contain portlandite to buffer its pH (Noor-ul-Amin 2014; Cyr et al. 2019; Divet and Le Roy 2013; Ioannou et al. 2016; Novak and Sommer 2002). However, relatively little information is available on the carbonation rates at the concrete scale in natural conditions and about the associated mechanisms, which are different from those of a CEM I-based concrete.

Accelerated tests are sometimes used on this binder (50% CO<sub>2</sub>) without questioning their representativity (Divet and Le Roy 2013).

#### Conclusion of the introduction and interest of the article

In summary, some data are available in the literature about the carbonation rates in the three low-carbon concrete technologies studied, either in natural or accelerated conditions. However, the data available for LCK considers a lower amount of filler in the binder (0-50% filler) than that considered in this study (73% filler), and the experimental data for AAS focused mainly on other activators types, which will influence the measured carbonation resistance. Significantly less information is available regarding the pH in these matrices after carbonation, which is not often considered in the analysis of resistance to carbonation. Therefore, the present study aims to provide experimental data on the carbonation rates measured at the concrete scale (in natural and in accelerated conditions at 1 or 3% CO<sub>2</sub>) and on pH in the pore solution before and after carbonation (in natural and in accelerated conditions at 1% CO<sub>2</sub>). The relevance of accelerated carbonation tests to characterize the carbonation of low-carbon concretes is also questioned, comparing the carbonation rates, pH and hydrates, obtained in both conditions. The question raised is to know how different technologies of low-carbon concretes C25/30 perform compared to traditional Portland cements with respect to carbonation, considering that their different compositions will involve different mechanisms during the carbonation process. To answer this question, it is proposed to compare their carbonation resistance, based on carbonation rates and the ability to maintain a high pH during the carbonation process, to conclude on their use in environments exposed to carbonation.

## 2 Materials

### 2.1 Raw Materials

The chemical composition of cements and slag used in LCK, AAS and SSC concretes determined by X-ray fluorescence (XRF) is given in Table 14. The quicklime that is part of the composition of AAS is only CaO (100%). Other raw materials were also used, such as limestone filler CaCO<sub>3</sub>, sodium carbonate Na<sub>2</sub>CO<sub>3</sub> and anhydrite CaSO<sub>4</sub>. The carbon footprints from different databases of these raw materials are summarized in Table 15.

Table 14: Chemical composition of the cements and slag used in LCK, AAS and SSC concretes (% in mass) determined by XRF.

	Chemical composition (% in mass)								
	CaO	SiO <sub>2</sub>	Al <sub>2</sub> O <sub>3</sub>	MgO	Fe <sub>2</sub> O <sub>3</sub>	K <sub>2</sub> O	Na <sub>2</sub> O	SO <sub>3</sub>	TiO <sub>2</sub>
CEM I	64.7	20.4	3.9	0.8	5.0	0.6	0.1	2.8	0.2
CEM III/B	50.5	37.7	8.1	4.5	1.9	0.5	0.2	2.0	0.5
GGBS	42.9	37.7	10.3	6.5	0.3	0.4	0.2	1.6	0.7

Table 15: Carbon footprint (in kg eq.CO<sub>2</sub>/t) of the raw materials used in LCK, AAS and SSC concretes from different databases.

	CO <sub>2</sub> footprint <sup>(1)</sup> (kg eq.CO <sub>2</sub> /t)
CEM I	765 <sup>(2)</sup>
Limestone filler	6 <sup>(3)</sup>
GGBS	17 to 100 <sup>(2)</sup>
Sodium carbonate	1350 <sup>(3)</sup>
Quicklime	893 <sup>(3)</sup>
Anhydrite	14 <sup>(3)</sup>
CEM III/B	273 <sup>(2)</sup>
Water reducing agent	1850 <sup>(4)</sup>
Sand and aggregates	2.3 <sup>(5)</sup>

<sup>(1)</sup> Value of CO<sub>2</sub> footprint known as A1 (CO<sub>2</sub> associated with the material) in the FDES (Environmental and Health Data Sheet) method. Neither the transport of raw materials (A2) nor the concrete manufacturing stage (A3) is evaluated.

<sup>(2)</sup> French values from SFIC (Syndicat Français de l'Industrie Cimentière) available on (ATILH 2022): 17 kg eq.CO<sub>2</sub>/t is the former value and 100 kg eq.CO<sub>2</sub>/t the new one.

<sup>(3)</sup> From the Swiss database ECOInvent (ecoinvent 2022)

<sup>(4)</sup> Average value used by contractors regardless of the products and their concentration

<sup>(5)</sup> from the French database INIES (INIES 2017)

The binder of the **LCK** was made with 27% CEM I 52,5N CE CP2 and 73% limestone filler Betocarb HP 300 Sassenage from Omya. A Blaine specific surface of 3900 cm<sup>2</sup>/g for the CEM I and 5490 cm<sup>2</sup>/g for the filler were measured. The semi-crushed alluvial mix of aggregates ranged from 0 to 20 mm. Aggregate proportions were optimized to achieve high packing to provide higher mechanical properties, combined with the low water/binder ratio of 0.25. Water reducing agents were also used to improve the workability in the fresh state.

The **AAS** binder was composed of 95% GGBS from Ecocem Fos/Mer as a precursor, with 4% sodium carbonate and 1% quicklime as activators. The latter provided a high pH to initiate dissolution and hydration of the slag. A Blaine specific surface of 5500 cm<sup>2</sup>/g was measured for the GGBS. The semi-crushed alluvial mix of aggregates ranged from 0 to 16 mm. This concrete had a water/binder ratio of 0.43. A commercial admixture was also used as a water reducing agent.

Finally, the **SSC** binder was composed of 89% GGBS from Ecocem Fos/Mer as the precursor, combined with 8% anhydrite of Lorraine and 3% CEM III/B 42.5N La Malle as alkaline activators to obtain sufficient reactivity. Finally, a limestone filler Orgon BL200 was added to the mixture during concrete formulation. The semi-crushed alluvial mix of aggregates ranged from 0 to 16 mm. This concrete had a water/binder ratio of 0.50 and was combined with water reducing agents.

The three low-carbon concretes studied were designed to be C25/30 and also self-compacting (spread class SF1), according to NF EN 206/CN. Their respective compositions and characteristics are detailed in Table 16. The compressive strengths given in Table 16 were obtained on cylindrical samples  $\phi$ 110 mm x 220 mm.

*Table 16: Concrete composition, mixture parameters and characteristics in fresh and hardened state of LCK, AAS and SSC together with CO<sub>2</sub> footprint of each concrete, calculated by adding the CO<sub>2</sub> footprints of all raw materials forming part of the mixture (Table 15), considering their proportions.*

		unit	LCK	AAS	SSC
Concrete composition	CEM I	kg/m <sup>3</sup>	136.8		
	Limestone filler	kg/m <sup>3</sup>	375.0		49.1
	GGBS	kg/m <sup>3</sup>		481.7	329.3
	Na <sub>2</sub> CO <sub>3</sub>	kg/m <sup>3</sup>		20.3	
	Quicklime	kg/m <sup>3</sup>		5.1	
	Anhydrite	kg/m <sup>3</sup>			29.6
	CEM III/B	kg/m <sup>3</sup>			11.1
	Water reducing agent	kg/m <sup>3</sup>	6.02	11.15	5.1
	Sand (0-5 mm)	kg/m <sup>3</sup>	678.5	686.5	739.7
	Fine aggregates (5-10 mm)	kg/m <sup>3</sup>	272.1	609.6	656.9
	Coarse aggregates (> 10 mm)	kg/m <sup>3</sup>	827.1	229.6	247.4
	Total water	kg/m <sup>3</sup>	130.0	220.0	210.0
Mixture parameters	w/c ratio <sup>(1)</sup>		0.95	0.43	0.57
	w/b ratio <sup>(2)</sup>		0.25	0.43	0.50
	w <sub>eff</sub> /b ratio <sup>(3)</sup>		0.22	0.40	0.46
	Theoretical specific gravity	kg/m <sup>3</sup>	2425.5	2263.8	2278.3
	Quantity of paste	L/m <sup>3</sup>	318	407	360
	CO <sub>2</sub> footprint	kg eq. CO <sub>2</sub> /m <sup>3</sup>	122	65 to 104	23 to 50
Concrete characteristics in fresh and hardened state	Inversed cone flow rate (rheology)	seconds	9.7	1.7	2.0
	Abrams cone spread	mm	525	580	490
	Air content	%	1.3	1.2	1.8
	28 days compressive strength	MPa	33.0	33.3	32.0
	90 days compressive strength	MPa	34.4	37.5	40.0

<sup>(1)</sup> The w/c ratio does not consider the inert filler in the cement part: for the LCK the cement means CEM I, for the AAS it means GGBS + Na<sub>2</sub>CO<sub>3</sub> + quicklime, for the SSC it means GGBS + anhydrite + CEM III/B

<sup>(2)</sup> The w/b ratio considers the inert filler in the binder, unlike the w/c ratio <sup>(1)</sup>: for the LCK the binder considers the CEM I + inert fillers, for the AAS there is no difference with <sup>(1)</sup>, for the SSC it considers the inert filler in addition to <sup>(1)</sup>

<sup>(3)</sup> Efficient water to binder ratio, taking into account the water absorption of the aggregates

## 2.2 Carbon footprint of concrete

The three concretes studied are considered as « low-carbon concretes » because for performances equivalent to that of a reference concrete, they have a reduced carbon footprint. In this study, the concrete taken as reference is made with traditional Portland cement and was chosen to have a formulation representative to that of a standard concrete of similar strength (C25/30). This reference is made with 260 kg/m<sup>3</sup> of CEM I, 220 kg/m<sup>3</sup> of water, 2 kg/m<sup>3</sup> of superplasticizer and 1700 kg/m<sup>3</sup> of aggregates.

The carbon footprint of each concrete (without reinforcement) is directly calculated adding up the CO<sub>2</sub> footprints of each raw materials (as presented in Table 15) that are part of its composition (as defined in Table 16), only considering their proportion in the formulation.

The carbon footprint of each raw materials comes from different databases such as the French values from SFIC (Syndicat Français de l'Industrie Cimentière) for CEM I and CEM III/B, available on (ATILH 2022), or the Swiss database ECOInvent (ecoinvent 2022) for the limestone filler, sodium carbonate, quicklime and anhydrite.

The carbon footprint attributed to the GGBS has often changed over time and also varies according to the countries due to variations in the carbon allocations attributed to its production. In France for example, 17 kg eq. CO<sub>2</sub>/ton was taken into account a few years ago considering the slag as a co-product of steelmaking, while the last one decided by the AFGC DIOGEN working group in 2022 is 100 kg eq. CO<sub>2</sub>/ton (taking into account an economic allocation of 83 kg eq. CO<sub>2</sub>/ton and an allocation of 17 kg eq. CO<sub>2</sub>/ton for the grinding and transport) (Cerib 2022). Both carbon footprints are considered in this section in order to have a range associated with these two extremes. For the United States and Canada, a carbon footprint slightly higher of 147 kg eq. CO<sub>2</sub>/ton was adopted in 2020 for example (Slag cement association and ASTM International 2020).

For the superplastizers the value of 1850 kg eq. CO<sub>2</sub>/ton is taken as it is the average value used by contractors regardless of the products and their concentration, while the estimation of 2.3 kg eq. CO<sub>2</sub>/ton is chosen for sand and aggregates from the French database INIES (INIES 2017). Finally, the carbon footprint calculated for each concrete is presented in Figure 26 and compared to the one of the reference made with CEM I.

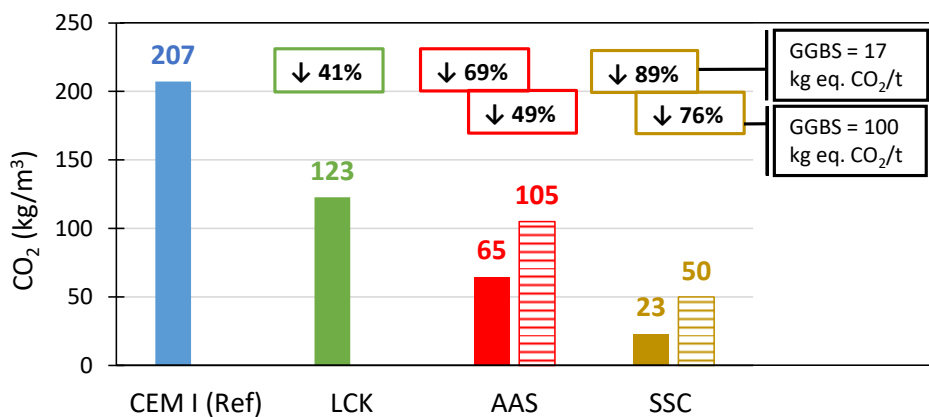


Figure 26: Carbon footprint of the three low-carbon concretes studied (LCK, AAS and SSC) in comparison with the one of a reference concrete of equivalent resistance class (C25/30) made with CEM I.

As the production of clinker is responsible for huge emissions of carbon dioxide, the three concretes studied propose either to lower its proportion in the binder (LCK), by partially replacing it by limestone fillers to maintain an acceptable rheology. In this way, the LCK concrete reduces the proportion of CEM I in the binder from 260 kg/m<sup>3</sup> to 137 kg/m<sup>3</sup>, which enables to achieve 41% CO<sub>2</sub> reduction.

Another option is to change the binder technology itself as for AAS and SSC concretes, which are slag-based binders combined with sulfate and/or alkaline activators to enhance their reactivity. These two concretes are mainly made with GGBS, which is considered more environmentally friendly than clinker because it is a by-product from iron industry (765 kg eq. CO<sub>2</sub>/t for CEM I versus 17 to 100 kg eq. CO<sub>2</sub>/t for GGBS) reused in the manufacture of concrete. These technologies (AAS and SSC) enable to save 49 to 69% and 76 to 89% CO<sub>2</sub> respectively, compared to CEM I-concrete.

The CO<sub>2</sub> footprint associated to each binder presented in Figure 26, corresponds to ranges available in the literature (Cyr et al. 2019; Habert, d’Espinoze de Lacaillerie, and Roussel 2011; Palm et al. 2016; Ioannou 2019), with a margin of error on the carbon footprint associated to slag and some variations in formulations.

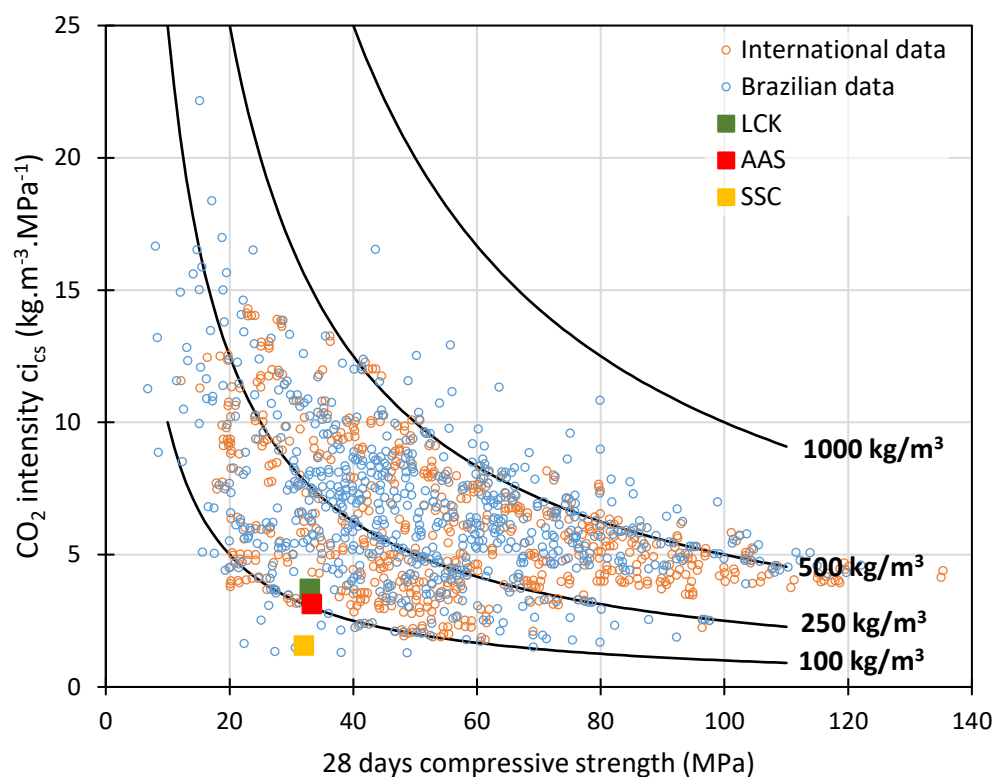


Figure 27: Estimated CO<sub>2</sub> intensity ( $ci_{cs}$ ) versus 28 days compressive strength from (Damineli et al. 2010), versus those of LCK, AAS and SSC concretes. The lines represent concretes with the same amount of total CO<sub>2</sub>.

Finally, Figure 27 presents the calculated CO<sub>2</sub> intensity ( $ci_{cs}$ ) versus 28 days compressive strength for Brazilian and international data dispersion, from (Damineli et al. 2010). It can be observed that high strength concretes have generally lower CO<sub>2</sub> intensity. Figure 27 also shows the CO<sub>2</sub> intensity of LCK, AAS and SSC concretes with respect to the literature data. The three low-carbon concretes studied enable to achieve low CO<sub>2</sub> intensity, around 100 kg/m<sup>3</sup> for LCK and AAS and even lower for SSC, for these strength ranges.



### **2.3 *Mixing and curing***

For each concrete, the mixing procedure lasted around 5 minutes and followed the same steps. First, the dry aggregates were dry mixed alone in a pan mixer for 1 min to achieve a uniform dispersion. Then, 1/3 of the water was added and the mixing continued for 1 min more. After that, the pan mixer was stopped, the binder was added and mixing continued for 1 min. Finally, the remaining 2/3 of the water with water reducing agent was added with a further 2 minutes of mixing. For each batch, around 50 L of concrete was cast. After the end of the mixing procedure, the cone spread was measured to check the concrete workability. All concrete spreads were between 450 and 600 mm (Table 16). Then, the concrete was cast in cylindrical ( $\Phi$ 110 mm x 220 mm) moulds in 3 layers, each one being vibrated, covered by a plastic cover to avoid evaporation, and stored in a wet curing room at 20 °C with 95% relative humidity. The specimens were demoulded after 72 h and cured in the same room for 28 days or other duration, depending on the testing date.

### **3 Test methods**

All the tests are done after curing in a wet curing room with 95% relative humidity. The values presented come from an average of several measurements on different samples for the repeatability. All the tests performed are summarized in Table 17.

Table 17: Summary of tests performed on LCK, AAS and SSC concretes to characterize their performance against carbonation, with the associated standards, as well as samples size, curing and preconditioning.

	Test	Standard	Conditions	Sample shape and size	Sample curing	Sample preconditioning	Number of samples for average
CARBONATION	Carbonation rate in <u>natural</u> conditions ( $k_{nat}$ )	EN12390-10 (AFNOR 2018)	65% HR – 20 °C	Prismatic 100 x 100 x 400 mm <sup>3</sup>	Demolded at 24h or 72h and not cured	Insulation of the extremities to have a radial carbonation	1
			Outside sheltered	Cylindrical $\phi$ 110 mm x 220 mm	Demolded after 7 days and wet cured for other 7 days	None	3
	Carbonation rate in <u>accelerated</u> conditions ( $k_{acc}$ )	EN 12390-12 (AFNOR 2020)	1% CO <sub>2</sub> -65% RH-20 °C	Prismatic 100 x 100 x 400 mm <sup>3</sup>	Demolded at 24h and cured under water for 27 days	After the curing period, placed for 14 days at 20 °C and 57% RH	2
			3% CO <sub>2</sub> -57% RH-20 °C	Cylindrical $\phi$ 110 mm x 220 mm	Demolded at 3 days and wet cured for 2 days	None	3
pH MEASUREMENT	pH measurement on paste <u>before</u> carbonation	Based on the protocol described in (Cyr et al. 2008)	Pore solution extraction	Cylindrical $\phi$ 33 mm x 70 mm	Endogenous curing period of 38 days	Measurement immediately after pore solution extraction	1
		Protocol described in (W.-C. Wang et al. 2021)	Suspension method	Cylindrical $\phi$ 33 mm x 70 mm crushed until to obtain a powder	Endogenous curing period of 38 days		1
	pH measurement on paste <u>after</u> carbonation	Protocol described in (W.-C. Wang et al. 2021)	Suspension method	Cylindrical $\phi$ 33 mm x 70 mm crushed until to obtain a powder	Endogenous curing period of 5 days	Carbonation: <ul style="list-style-type: none"> <li>• Outside sheltered for 18 months</li> <li>• 1% CO<sub>2</sub>-65% RH-20°C for 11 months</li> </ul>	2
COMPLEMENTARY ANALYSES	ICP analysis of the pore solution before carbonation			Pore solution from extraction	Endogenous curing period of 38 days	Analysis immediately after pore solution extraction and pH measurement	1
	XRD on carbonated pastes		<ul style="list-style-type: none"> <li>• Outside sheltered for 9 months</li> <li>• 1% CO<sub>2</sub>-65% RH-20 °C for 2 months</li> </ul>	Cylindrical $\phi$ 33 mm x 70 mm crushed until to obtain a powder	Endogenous curing period of 5 days	Sieving < 80 $\mu$ m	1

### 3.1 Natural and accelerated carbonation rate

CO<sub>2</sub> transport through the concretes was evaluated both in natural and accelerated conditions. Natural conditions are more reliable and representative of the reality, but as carbonation is a slow phenomenon, accelerated conditions are often used to predict carbonation resistance of the material without having to wait for too long. Natural and accelerated carbonation rates were assessed in parallel in two laboratories according to EN 12390-10 (AFNOR 2018) or EN 12390-12 (AFNOR 2020), respectively. For this reason, different sample's geometries and carbonation conditions were tested, as detailed in Table 18.

Table 18: Details of natural and accelerated carbonation conditions of cylindrical and prismatic samples as well as pH measurements done in parallel on paste, as presented in section 3.2.

Standard	Natural conditions					Accelerated conditions	
	EN 12390-10					EN 12390-12	EN 12390-12 adapted with 1% CO <sub>2</sub> and without preconditioning
Exposure conditions	Laboratory conditions: 20 °C and 65% RH		Outside sheltered			Climatic chamber: 3% CO <sub>2</sub> , 20 °C, 57% RH	Climatic chamber: 1% CO <sub>2</sub> , 20 °C, 65% RH
Age of samples before carbonation exposure	24 h	72 h	24 h	72 h	14 days	42 days (28d curing + 14d preconditioning)	5 days
Carbonation depth deadlines	90, 180, 365 days	90, 180, 365 days	90, 180, 365 days	90, 180, 365 days	90, 180, 365 days	7, 28, 70, 112 days	60, 133, 153 days
Cylindrical sample*					X		X
Prismatic sample*	X	X	X	X		X	
pH measurement on paste			X (5 days curing)				X (5 days curing)

\* Dimensions available in Table 17.

For **natural carbonation**, two exposure conditions were tested: (1) laboratory conditions at 20 °C and 65% RH in order to have a controlled environment and a repeatable test (also easier for comparisons with literature data) and (2) outside sheltered to investigate real conditions that might be encountered on site. For both conditions, different ages for carbonation exposure were tested to quantify the influence of this parameter on the carbonation kinetics. A group of prismatic samples 100 x 100 x 400 mm<sup>3</sup> is demolded at 24h, while a second group is demolded at 72h (24h to 72h are the age for which 50% of the compressive strength at 28 days is achieved depending on the mixtures) and are immediately placed on carbonation site. Finally, for the

exposure outside sheltered, an additional condition is tested on cylindrical samples  $\phi 110$  mm x 220 mm demolded after 7 days and cured in wet curing room with 95% relative humidity for other 7 days before to be placed on carbonation site. Prismatic samples are covered with adhesive aluminum foil at their extremity to ensure a radial carbonation. After the exposure period is done, a slice of 50 mm of the prismatic sample is broken to test its carbonation depth. The remains of the sample returns to the carbonation site. For cylindrical samples, they are just split in two for the evaluation of the carbonation depth. The measurement of the carbonation front is done at 90, 180 and 365 days by pulverization of phenolphthalein for all the specimens and also with rainbow indicator for the cylindrical samples.

**Accelerated carbonation** was also performed at 1% and 3% CO<sub>2</sub>. In the case of 3% CO<sub>2</sub>, prismatic samples (100 x 100 x 400 mm<sup>3</sup>) are demolded at 24h and then preconditioned with a drying step to reduce their RH according to EN 12 390-12, as their carbonation takes place in a climatic chamber. For the preconditioning, the sample is demolded at 24h and immersed in water. Then at 28 days, it is removed from water and placed for 14 days at  $20 \pm 2$  °C and  $57 \pm 7$  % RH. Finally, it is placed in a climatic chamber at 3% CO<sub>2</sub>, 20 °C and 57% RH. The measurement of the carbonation front is done at 7, 28, 70 and 112 days following the same procedure as for natural carbonation. In the case of 1% CO<sub>2</sub>, cylindrical samples  $\phi 110$  mm x 220 mm are demolded at 5 days and immediately placed in a climatic chamber at 1% CO<sub>2</sub>, 20 °C and 65% HR, without preconditioning. The measurement of the carbonation front is done at 60, 133 and 153 days following the same procedure as for natural carbonation.

### ***3.2 pH measurement and sample analysis before and after carbonation***

As the arrival of the carbonation front in the material is associated with a pH drop of the pore solution, pH measurements before and after carbonation (natural carbonation in a sheltered outside environment (around 0.04% CO<sub>2</sub>) and accelerated carbonation in a climatic chamber at 1% CO<sub>2</sub> and 65% RH) were also carried out on paste (Table 18). In parallel to these pH measurements, additional analyses are performed before (ICP analyses) and after (XRD) carbonation on these same samples. For this purpose, pastes associated with the three matrices studied were cast (same w/b ratio as for the concrete) in plastic molds  $\phi 33$  mm x 70 mm, then kept in endogenous cure for 38 days for the pastes which will be used for the measurement of pH before carbonation and for 5 days for the samples which will be placed in carbonation for the measurement of the pH after carbonation.

#### ***3.2.1 Before carbonation: pH and ICP analysis on pore solution extraction***

After the endogenous curing period of 38 days, the samples are unmolded and used to perform a pore solution extraction, allowing a direct pH measurement on the collected pore solution. Paste samples are used (compared to mortar or concrete) to extract a maximum of pore solution by this method, removing the presence of aggregates. This is the most commonly used and reliable method to get a direct pH measurement of the pore solution (Behnood, Van Tittelboom, and De Belie 2016). A Sintco 600 T press was used to perform the extraction as described more in detail by (Cyr et al. 2008). The pressure was applied with a speed of 3 kN/s up to 1000 kN where it is maintained for 300 s to extract some milliliters of pore solution. The pH

measurement is performed immediately after the extraction with a SensION +Ph31 pH-meter previously calibrated between pH 11 and 13.

The ionic concentration of the pore solution was also determined by ICP analysis. After the pH measurement, the pore solution was filtered and immediately analyzed with ICP-MS to quantify Na, K, Fe, Al, Mg, Ca, Si species.

### *3.2.2 After carbonation: pH by suspension method and X-ray diffraction (XRD) analysis*

After a curing period of 5 days, the paste samples are unmolded and manually crushed to obtain a powder in order to accelerate their complete carbonation. They are then placed in carbonation either outside under shelter or in a climatic chamber at 1% CO<sub>2</sub> and 65% RH, taking care to spread the powder in a thin layer and to stir it once a week to ensure its complete carbonation.

This time the use of pore solution extraction for pH measurement is not possible for carbonated samples, which have dried during the carbonation time and therefore are no longer wet enough to extract a sufficient amount of solution by this method (De Weerd et al. 2019). To enable pH measurement on carbonated samples, other pH measurement methods have been proposed in the literature (Räsänen and Penttala 2004; Vogler et al. 2020; W.-C. Wang et al. 2021). The "suspension" pH measurement method of (W.-C. Wang et al. 2021) was finally chosen for its robustness, ease of execution and good repeatability (standard deviation < 0.1). It consists of grinding the sample on which the pH measurement is to be performed into a powder, in less than 15 min if it is not carbonated (machine RETSCH – RS 100 used for grinding in this study), sieving it with a 80 µm sieve, and then preparing a suspension to be used for the pH measurement by mixing 10 g of powder with 10 mL of demineralized water. This suspension is then mixed for 5 min with a magnetic bar on a magnetic stirring plate (speed of 400 rpm), and the pH measurement is performed immediately after, with a previously calibrated pH-meter. The pH measurement with the suspension method is performed on the fully carbonated samples, after 18 months of natural carbonation and after 11 months of accelerated carbonation. Each pH measurement is repeated twice per binder type. Before the pH measurement, the samples are pulverized with rainbow (colored indicator) in order to ensure their complete carbonation and to obtain an estimate of the pH of the sample to calibrate the pH-meter as accurately as possible.

In parallel to the pH measurement with the suspension method, a part of the carbonated powder is collected and sieved at 80 µm to make a qualitative XRD analysis of the hydrates present after natural and accelerated carbonation. Analyses were done either outside under shelter after 9 months of carbonation, or in a climatic chamber at 1% CO<sub>2</sub> and 65% RH after 2 months of carbonation. For XRD analyses, a Bruker D8 diffractometer with a copper radiation source (Cu K $\alpha$ ,  $\lambda = 1.54 \text{ \AA}$ ) was used. The anticathode voltage was 40 kV, and the electric current intensity was 40 mA. Angles from 2 $\theta$  5° to 70° were scanned with a total scan duration of 15 min per sample. Mineral identification was carried out using the Bruker-AXS DIFFRACplus Eva v4 software and the 2015 ICDD PDF database.

## 4 Results

The results are deliberately presented here in a rather succinct manner. A more detailed analysis will be made in the discussion section.

### 4.1 $CO_2$ transport in concrete

#### 4.1.1 Carbonation rate in natural conditions

Kinetics of natural carbonation measured for LCK, AAS and SSC concretes are presented on Figure 38 (supplementary data) and the associated carbonation rates are summarized in Table 19. Different exposure conditions have been tested in two different laboratories to study their influence on the carbonation rates and to estimate an interval of carbonation kinetics in natural conditions, as they are not always controlled (the sheltered exposition depends on the exterior temperature and relative humidity for example) which can give variable results (Thomas and Matthews 1992). Different periods of curing before carbonation exposure have also been tested to evaluate their influence on the carbonation rates, as illustrated on Figure 28.

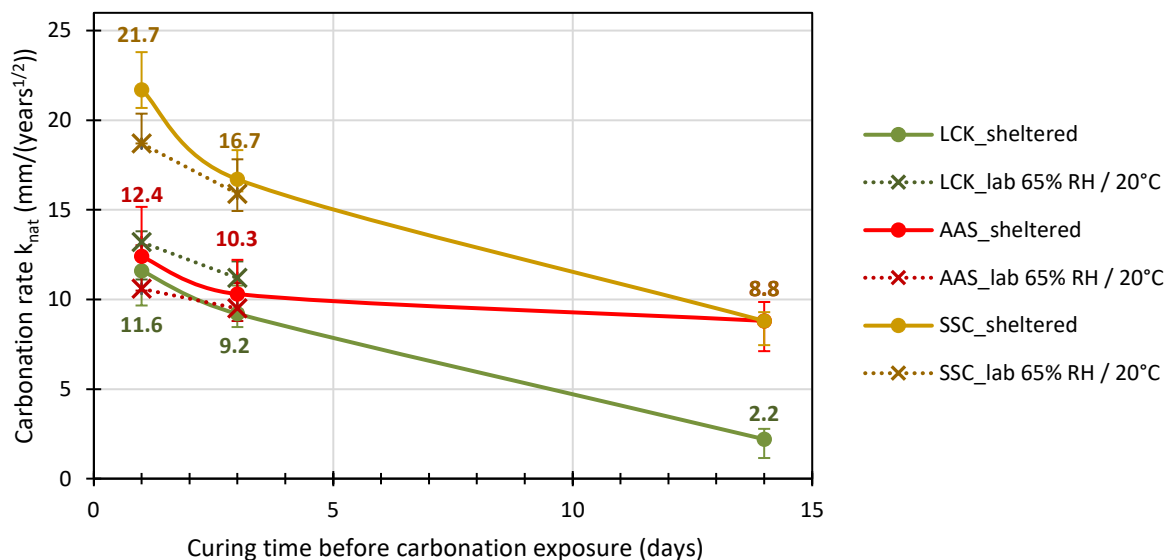


Figure 28: Carbonation rates measured for LCK, AAS and SSC concretes either in laboratory conditions (dashed lines) or in outside sheltered conditions (full lines), for samples exposed to carbonation after 1, 3 or 14 days of curing. Values of carbonation rates for laboratory conditions are available in Table 19 for reasons of readability.

#### Influence of exposure conditions on the carbonation rates

About the two exposure conditions tested (laboratory conditions 20 °C-65% RH and outside sheltered), it seems they have not a major influence on the carbonation rates, as the results obtained in both conditions are close (Figure 28), as also observed by (Hainer, Proske, and Graubner 2015) for CEM I, CEM II/A-LL, CEM II/B-M, CEM III/A and CEM I with 50% limestone fillers, types of concrete. For LCK samples cured 24h or 72h before carbonation exposure, the carbonation rate is slightly higher in laboratory conditions, while it is the contrary

for AAS and SSC, even if the difference between the two is not very significant (between 5 and 15% difference). The same behavior than for LCK was observed by (Thomas and Matthews 1992; Elgalhud, Dhir, and Ghataora 2017) on concrete made with Portland cement.

Influence of the curing time before carbonation exposure on the carbonation rates

A clear influence of the curing time on the carbonation rates can be identified on Figure 28. For the three mixtures, the carbonation rates decrease when the curing period before exposure increases, which was already observed by different authors in the literature, for various types of binder (Thomas and Matthews 1992; Sisomphon and Franke 2007; Hainer, Proske, and Graubner 2015; von Greve-Dierfeld et al. 2020; Huy Vu et al. 2019; Elgalhud, Dhir, and Ghataora 2017). It is mainly due to a higher hydration of the concrete and therefore a denser microstructure increasing the curing time, which slows down the CO<sub>2</sub> ingress in the porous network.

Figure 29 presents the evolution of the compressive strengths measured on LCK, AAS and SSC concretes from 1 day to 90 days of wet curing. Figure 30 is a complementary representation, presenting the evolution of the compressive strengths measured on AAS and SSC concretes, relatively to those of the LCK concrete. Both figures illustrate mechanical resistances that develop at different rates, corresponding to different hydration rates, according to the type of binder. At young age, AAS and SSC have lower mechanical resistances than the LCK, and even much lower for the SSC. At 28 days, similar compressive strengths than the LCK are reached, and the three concretes have a similar strength class C25/30. Finally, after 90 days of curing the mechanical resistances of AAS and SSC even exceed those of the LCK. Therefore, on Figure 28, the SSC concrete is less resistant to carbonation because it has a lower hydration rate than the AAS and the LCK, as illustrated on Figure 30.

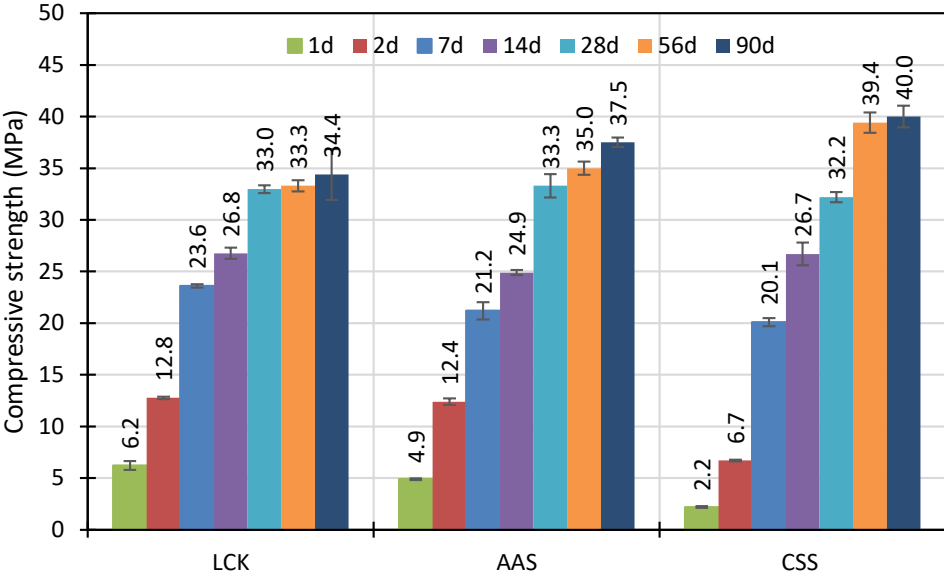


Figure 29: Evolution of the compressive strengths measured on LCK, AAS and SSC concretes (cylindrical samples  $\phi 110\text{ mm} \times 220\text{ mm}$ ), from 1 day to 90 days.

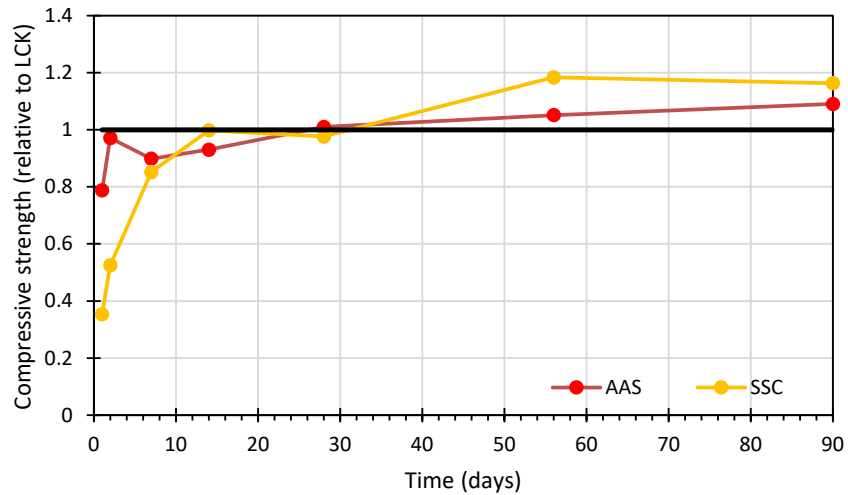


Figure 30: Evolution of the compressive strengths measured on AAS and SSC concretes, from 1 day to 90 days, relatively to those of the LCK concrete (corresponding to the black line).

On Figure 28, curing period before carbonation exposure seems to have a lower impact on the AAS concrete compared to the other, to slow down the carbonation rates, as discussed more in detail in section 5.1. It mainly slows down the carbonation kinetics significantly only at a young age (between 24 and 72 hours) for AAS. Afterwards, this benefit is less important (almost the same rate measured at 72 h and 14 days of cure) contrary to LCK and SSC. For the LCK and SSC concretes, on the other hand, waiting 14 days instead of 24 h before carbonation allows the natural carbonation rates measured afterwards to be reduced 5 and 2.5 times, respectively (compared to 1.4 for AAS). Waiting 72 h instead of 24 h (which is more realistic on site) allows to gain a factor of 4, 1.2 or 2 on the carbonation rates of LCK, AAS and SSC, respectively. It is mainly due to a more advanced hydration, as illustrated on Figure 29. The curing time before exposure to carbonation can therefore be an interesting parameter to improve the resistance to carbonation of the three concretes, as discussed more in details in section 5.1.3.

#### Comparison of the carbonation rates between the three mixtures

To compare the carbonation kinetics between the three mixtures, it is necessary to consider the curing time of the samples before exposure because it has a strong influence on the results, as explained previously. The hierarchy of the carbonation rates between the three binders are different, according to the curing time considered. The LCK and AAS samples placed in natural carbonation at 24 h or 72 h of curing show similar carbonation rates, while it is twice as important for the SSC (Figure 28). This trend is different for the samples placed in carbonation after 14 days of curing, where this time the carbonation rates of the slag-based binders are similar, contrary to those of the LCK which is 4 times less important. This observation corresponds to the literature data (Hainer, Proske, and Graubner 2015; Lye, Dhir, and Ghataora 2016; von Greve-Dierfeld et al. 2020; Sisomphon and Franke 2007; Huy Vu et al. 2019), as slag-based concretes have a slow hydration rate and do not contain portlandite as main hydrate to maintain their basicity (buffer pH) and to slow down the carbonation process (Leemann et al. 2015; Leemann and Moro 2016).



Table 19: Summary of natural and accelerated carbonation rates measured for LCK, AAS and SSC concretes, for samples exposed to carbonation after different periods of curing.

Exposure conditions	Natural carbonation rate mm/(years <sup>1/2</sup> )					Accelerated carbonation rate mm/(years <sup>1/2</sup> )	
	Laboratory conditions: 20 °C and 65% RH		Outside sheltered			Climatic chamber: 1% CO <sub>2</sub> , 20 °C, 65% RH	Climatic chamber: 3% CO <sub>2</sub> , 20 °C, 57% RH
Age of carbonation exposure	24 h	72 h	24 h	72 h	14 days	5 days	42 days (28d curing + 14d preconditioning)
Sample type	Prismatic	Prismatic	Prismatic	Prismatic	Cylindrical	Cylindrical	Prismatic
<b>LCK</b>	13.2	11.2	11.6	9.2	2.2	32.8	50.1
<b>AAS</b>	10.6	9.5	12.4	10.3	8.8	48.6	75.2
<b>SSC</b>	18.7	15.9	21.7	16.7	8.8	50.4	71.1

#### 4.1.2 Carbonation rate in accelerated conditions

Kinetics of carbonation measured for LCK, AAS and SSC concretes exposed to accelerated conditions (climatic chamber either at 1% or 3% CO<sub>2</sub>) are presented on Figure 39 (supplementary data) and the associated carbonation rates are summarized in Table 19. The comparison of the accelerated carbonation kinetics with the natural ones is proposed on Figure 31.

In addition, a comparison with kinetics measured on classical CEM I-concretes from the literature is also proposed: average based on data available in (F Hunkeler 2016; Thomas and Matthews 1992; von Greve-Dierfeld et al. 2020; Palm et al. 2016; Müller et al. 2014; F Hunkeler 2012; Balayssac, Détriché, and Grandet 1995; Huy Vu et al. 2019) for natural carbonation and average based on data available in (Holt et al. 2009; F Hunkeler 2016; K. Zhao et al. 2020) for accelerated carbonation. In total 24 CEM I-concretes from the literature are considered and more specifically the results presented in natural carbonation are the average of 8 samples for the condition of 1 day of curing, 9 samples for 7 days of curing and 4 samples for 28 days of curing. In accelerated carbonation, the results proposed are the average of 2 samples at 1% CO<sub>2</sub> and only 1 sample at 3% CO<sub>2</sub>.

Some differences in the experimental parameters, between those used to characterize the carbonation rate of LCK, AAS and SSC and those used in the literature for CEM I-concretes must be noted, but the goal here is to have an order of magnitude and a trend of carbonation kinetics obtained on traditional CEM I-concretes. First, the references from the literature are C30/37 (instead of C25/30 in this study), exposed to natural carbonation after either 1 day, 7 days of curing (instead of 72h) or 28 days of curing (instead of 14 days) and exposed to 1% CO<sub>2</sub> after 7 days of curing (instead of 5 days), and to 3% CO<sub>2</sub> after 28 days of curing (instead of 28 days of curing and 14 days of preconditioning in this study).

These reference concretes will be referred as « CEM I-concretes from the literature » afterwards.

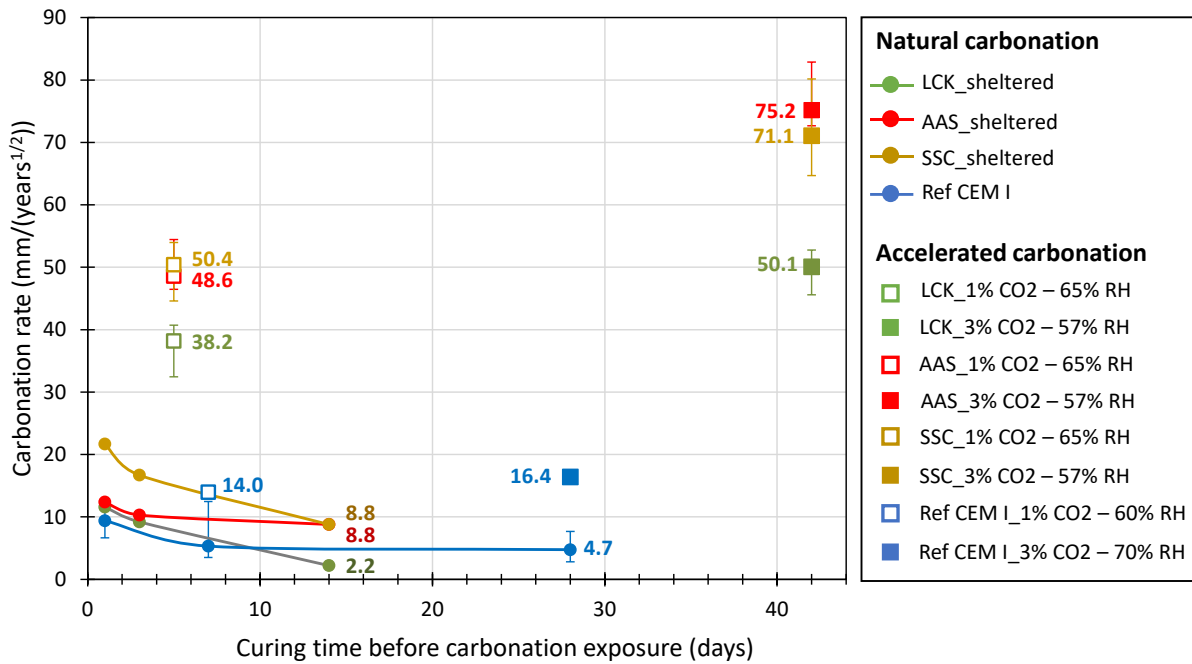


Figure 31: Carbonation rates measured experimentally for LCK, AAS and SSC concretes either in natural conditions (sheltered) or in accelerated conditions (1% CO<sub>2</sub> - 65% RH or 3% CO<sub>2</sub> - 57% RH), for different curing times before carbonation exposure. All the values of natural carbonation rates are available on Table 19 for reasons of readability. A comparison with kinetics measured on several concretes made with CEM I (C30/37) from the literature is also proposed. Average based on data available in (F Hunkeler 2016; Thomas and Matthews 1992; von Greve-Dierfeld et al. 2020; Palm et al. 2016; Müller et al. 2014; F Hunkeler 2012; Balayssac, Détriché, and Grandet 1995; Huy Vu et al. 2019) for natural carbonation and average based on data available in (Holt et al. 2009; F Hunkeler 2016; K. Zhao et al. 2020) for accelerated carbonation.

#### Comparison between natural and accelerated carbonation rates

Moving from natural carbonation to accelerated carbonation at 1% CO<sub>2</sub> for LCK, AAS and SSC concretes, increases carbonation kinetics by a factor of 4 to 7. For the carbonation rates measured for samples exposed at 3% CO<sub>2</sub>, they are around 40 to 50% higher than the one measured at 1% CO<sub>2</sub>, as illustrated in Figure 31.

The experimental accelerated carbonation rates obtained for LCK, AAS and SSC correspond to ranges available in the literature: between 32 and 40 mm/ $\sqrt{\text{years}}$  measured for concretes with 35 to 50% limestone filler (instead of 73% for LCK) at 2 to 4% CO<sub>2</sub> (Dhir et al. 2007; Palm et al. 2016); 40 mm/ $\sqrt{\text{years}}$  at 3% CO<sub>2</sub> measured for AAS concretes (NaOH and NaOH+NaSi as activation) (K. Zhao et al. 2020) and between 41 and 63 mm/ $\sqrt{\text{years}}$  at 4% CO<sub>2</sub> for SSC concretes of slightly higher strength class (Ioannou et al. 2016; Ioannou 2012; Cyr et al. 2019).

For both accelerated conditions of carbonation, slag-based binders have similar carbonation rates while the one of LCK is 1.5 times lower. Finally, concerning the carbonation rates, the same hierarchy is found between the mixtures as for the samples placed in natural carbonation

after long curing periods (14 days), except an inversion between AAS and SSC at 3% CO<sub>2</sub>, but with different ratios. These observations and the representativity of accelerated carbonation tests for the low-carbon concretes considered, are discussed more in details in section 5.2. The conversion factors from accelerated to natural carbonation rates are shown in Table 20.

*Table 20: Ratio of accelerated carbonation rate (1% or 3% CO<sub>2</sub>) to natural carbonation rate (outside sheltered for 24h, 72h and 14 days of curing before carbonation exposure). The associated experimental parameters are presented in Table 18.*

	Ratio accelerated carbonation rate (1% or 3% CO <sub>2</sub> ) / natural carbonation rate (outside sheltered)		
Age of exposure to natural carbonation	24h	72h	14 days
Sample type	Prismatic	Prismatic	cylindrical
	<b>1% CO<sub>2</sub></b>		
Refs CEM I	1.5	2.6	3.0
LCK	2.8	3.6	15.0
AAS	4.0	4.8	5.6
SSC	2.3	3.0	5.7
	<b>3% CO<sub>2</sub></b>		
Refs CEM I	1.9	3.3	3.8
LCK	4.3	5.4	22.7
AAS	6.0	7.3	8.5
SSC	3.3	4.3	8.1

#### Comparison between low-carbon concretes and CEM I-concretes carbonation rates

Finally, Figure 31 shows that, similarly to low-carbon concretes, the carbonation rates under accelerated conditions are higher than those measured under natural conditions for CEM I-concretes from the literature, but in different ratios (Table 20), as CEM I hydrates more rapidly and is less influenced by the curing time. It can be observed on Figure 31, that the CEM I-concretes from the literature tend to carbonate more slowly than the three low-carbon concretes studied (keeping in mind that the CEM I-concretes from the literature are of higher strength class C30/37). The carbonation rates of slag-based binders remain higher than the references made with CEM I, especially for short curing times, due to a slower hydration and an absence of portlandite, as explained previously in 4.1.1. The LCK concrete has an intermediate behavior, but carbonates faster than the CEM I-concretes from the literature, as it contains less portlandite to maintain a high basicity and to slow down the carbonation process. This observation is in agreement with those of other authors, who show that for concretes of equal strength, the carbonation of Portland limestone cement-concrete with 35% limestone filler is already 32% higher than the corresponding Portland cement (Elgalhud, Dhir, and Ghataora 2017).

#### 4.2 pH measurement before and after carbonation

pH measurements done on pastes before and after carbonation (either natural or accelerated at 1% CO<sub>2</sub>) for LCK, AAS and SSC are summarized in Table 21.

Table 21: pH values of LCK, AAS and SSC pastes measured before and after natural (outside sheltered) or accelerated (1% CO<sub>2</sub> - 65% RH – 20 °C) carbonation, by extraction or suspension method.

	Samples curing and conservation before pH measurement	Method	pH		
			LCK	AAS	SSC
Non-carbonated samples	38 days curing	Extraction	13.2	13.1	12.1
		Suspension	13.0	13.0	12.0
Carbonated samples	5 days curing and 18 months in natural carbonation (outside sheltered)	Suspension	8.9	11.0	8.6
	5 days curing and 11 months in accelerated carbonation (1% CO <sub>2</sub> , 65% RH)	Suspension	8.1	9.8	8.5

For non-carbonated samples, a good repeatability is observed between the extraction and suspension pH measurement methods, which allows to validate the suspension method, considering that the error of the pH electrode is 0.1. A pH drop is observed after carbonation, which was expected. pH values drop below 9 for LCK and SSC, which is known to be the limit at which the steel depassivates when the carbonation front reaches the reinforcement (Angst et al. 2020). This is the case for both natural and accelerated carbonation conditions. On the contrary, the pH remains high for the AAS (over 9), as discussed more in detail in the discussion parts 5.1.2 and 5.2.2.

#### 4.3 Pore solution composition before carbonation

To investigate the composition and the ionic concentration of the pore solutions, and understand its influence on the carbonation resistance, an ICP analysis was performed after 38 days of endogenous cure. The cations Na<sup>+</sup>, K<sup>+</sup>, Ca<sup>2+</sup>, Al<sup>3+</sup>, Mg<sup>2+</sup> and Fe<sup>2+</sup> were quantified. H<sub>3</sub>O<sup>+</sup> ions are neglected due to the high pH of the pore fluid solution. For the AAS binder, CO<sub>3</sub><sup>2-</sup> ions are supplied by activation with sodium carbonate, but (S. A. Bernal et al. 2015) shows that they are completely consumed after about 10 days. As the extraction of pore solution is performed here at 38 days of cure, they are neglected. The amount of OH<sup>-</sup> ions was deduced to maintain electroneutrality for LCK, and from the pH measurements for AAS and SSC due to the presence of other anions, as explained below. It is important to note that the concentration of sulfide species S<sup>2-</sup> was not measured by the ICP analysis, because it is difficult to analyze as it evolves over time and it oxidizes easily. However, the results available in the literature highlights that its concentration in slag-based binders is not negligible (Mundra et al. 2023). For example, (Ma et al. 2016) measured on concretes after 3 months of curing a concentration of sulfide in the

pore solution of AAS between 2000 and 6000 ppm. These results are confirmed by (A. Gruskovnjak et al. 2006; Nedeljković et al. 2019), which measured 260 and 573 mmol/L of sulfide in AAS cured 28 days, respectively, against negligible amounts for a traditional CEM-I sample. Sulfide ions  $S^{2-}$  are therefore neglected for LCK. To estimate the amount of sulfides in AAS and SSC, the latter was deduced in order to maintain the electroneutrality of the solution. The values obtained are estimations (not direct measurements) of the concentrations present in the pore solution of the three binders at 38 days of curing. These values are not representative of the concentrations at a young age and may evolve over time. The results are detailed in Table 22 in mg/L with the associated conversion in mol/L, based on the atomic weight of each species.

*Table 22: Concentration of the main species present in the pore fluid solution of LCK, AAS and SSC pastes after 38 days of curing (in mg/L and conversion in mmol/L), quantified by ICP analysis for  $Na^+$ ,  $K^+$ ,  $Ca^{2+}$ ,  $Al^{3+}$ ,  $Mg^{2+}$ ,  $Fe^{2+}$ , calculated either from pH measurement or to maintain the electroneutrality for  $OH^-$  and  $S^{2-}$  ions.*

		Concentration of species in pore fluid solution (38 days curing)								
		ICP analysis						Calculation	Calculation	
		$Na^+$	$K^+$	$Ca^{2+}$	$Al^{3+}$	$Mg^{2+}$	$Fe^{2+}$	$OH^-$	$S^{2-}$	Tot.
<b>LCK</b>	mg/L	1260	8745	157	0.961	0	0.183			
	mmol/L	55	224	4	0.036	0	0.003	286 <sup>(2)</sup>	0	569
<b>AAS</b>	mg/L	23370	1353	3	204	0	0.341			
	mmol/L	1017	35	0.087	8	0	0.006	112 <sup>(1)</sup>	481 <sup>(2)</sup>	1652
<b>SSC</b>	mg/L	988	1209	637	0.227	0	0			
	mmol/L	43	31	16	0.008	0	0	13 <sup>(1)</sup>	46 <sup>(2)</sup>	149

<sup>(1)</sup> From pH measurements:  $[OH^-] = 10^{pH-14}$  (with pH = 13.2, 13.1 and 12.1 for LCK, AAS and SSC, respectively).

<sup>(2)</sup> From electroneutrality.

As illustrated by Table 22, the total quantity of ions in the pore solution is very variable for the three mixtures considered (by factor around 11 between SSC and AAS). The ionic composition is also unique for each matrix, due to the initial raw materials used. Before carbonation, the pore solution of LCK consists mainly of  $OH^-$  ions (50%) and  $K^+$  ions (39%), which guarantee a high pH (13.2) and a strong alkalinity. The pore solution of AAS consists rather in  $Na^+$  ions (62%) in very large quantities, brought by the sodium carbonate activator, which are responsible for a high pH (13.1) and a very high alkalinity, and  $S^{2-}$  ions (29%) from slag. For SSC, its pore solution contains much less ions than AAS or LCK (149 mmol/L against 569 mmol/L for LCK and 1652 mmol/L for AAS), in particular  $OH^-$ , which comes from the lower initial pH (12.1). The ionic species of its pore solution are mainly  $S^{2-}$  ions (31%) from slag, 50% alkalis (29%  $Na^+$  and 21%  $K^+$ ) and  $Ca^{2+}$  (11%).

#### 4.4 XRD on carbonated pastes

To evaluate the representativity of the accelerated tests compared to the natural ones, a XRD of the carbonation products obtained in both conditions is performed for comparison purposes. Figure 32 compares the X-ray diffractograms obtained on each matrix after 9 months of natural carbonation and after 2 months of accelerated carbonation. It highlights that the same hydrates are present after natural and accelerated carbonation (1% CO<sub>2</sub>), for LCK, AAS and SSC, as discussed more in detail in section 5.2. For LCK, calcite is identified as the main carbonation product, while for AAS CaCO<sub>3</sub> polymorphs (calcite, vaterite) are mainly observed and for SSC, CaCO<sub>3</sub> polymorphs (calcite, aragonite) as well as gypsum and also anhydrite, which was present in excess. The associated carbonation mechanisms are discussed in section 5.1.1. It corresponds to the hydrates commonly observed after carbonation for the three mixtures: for cement-based materials (Savija and Luković 2016), for AAS (Ke et al. 2020; T. N. Nguyen et al. 2022; Ye, Cai, and Tian 2020), and for SSC (Bentur and Mindess 2007; Majumdar, Singh, and Evans 1981).

## 5 Discussion

Section 5.1 focuses on the performances of each concrete against carbonation, by a detailed analysis of the carbonation rates and the pH evolution, while section 5.2 discusses the relevance of accelerated carbonation tests to characterize low-carbon concretes and in particular slag-based binders, before summarizing the durability results obtained in the form of a multi-criteria analysis in section 5.3. The results obtained in Section 4, on which the discussion is based, are summarized in Table 23. The associated test methods were recapitulated in Table 17.

Table 23: Summary of test results obtained for LCK, AAS and SSC concretes to characterize their performance against carbonation.

	Test and conditions	Unit	Conditions	Sample curing	LCK	AAS	SSC
CARBONATION	Carbonation rate in <u>natural</u> conditions ( $k_{nat}$ )	mm/(years <sup>1/2</sup> )	65% HR – 20 °C	24 h	13.2	10.6	18.7
				72 h	11.2	9.5	15.9
			Outside sheltered	24 h	11.6	12.4	21.7
				72 h	9.2	10.3	16.7
				14 days	2.2	8.8	8.8
			Carbonation rate in <u>accelerated</u> conditions ( $k_{acc}$ )	mm/(years <sup>1/2</sup> )	1% CO <sub>2</sub> -65% RH-20 °C	5 days	38.2
3% CO <sub>2</sub> -57% RH-20 °C	28 days (+ 14 days preconditioning)	50.1			75.2	71.1	
pH MEASUREMENT	pH on paste <u>before</u> carbonation		Pore solution extraction	38 days	13.2	13.1	12.1
			Suspension method	38 days	13.0	13.0	12.0
	pH on paste <u>after</u> carbonation (suspension method)		Natural: outside sheltered	5 days	8.9	11.0	8.6
			1% CO <sub>2</sub> -65% RH-20 °C	5 days	8.1	9.8	8.5
COMPLEMENTARY ANALYSES	ICP analysis of the pore solution before carbonation	mmol/L		38 days	Table 22		
	XRD on carbonated pastes	qualitative analysis	<ul style="list-style-type: none"> <li>Outside sheltered</li> <li>1% CO<sub>2</sub>-65% RH-20 °C</li> </ul>	5 days	Figure 32		

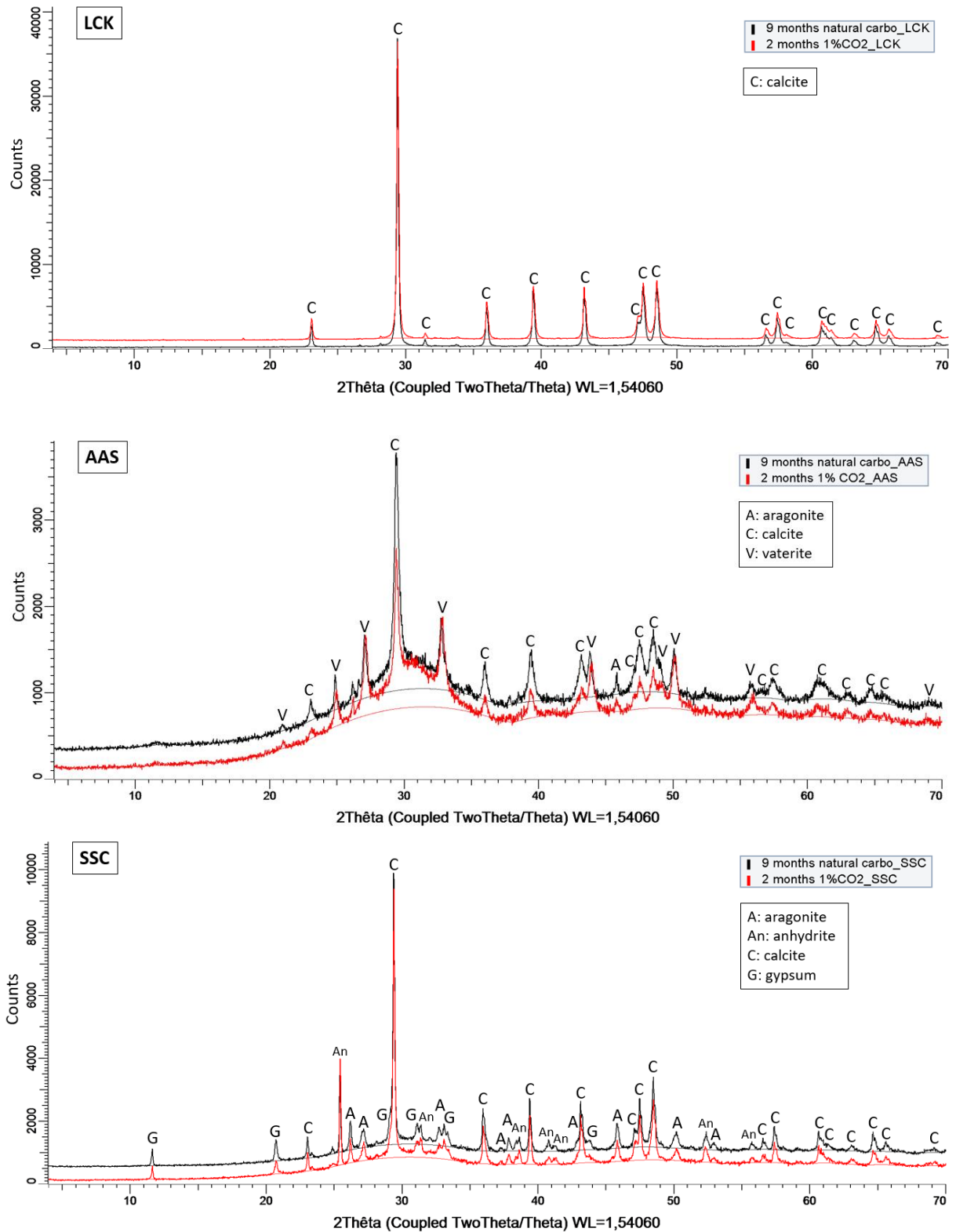


Figure 32: X-ray diffractograms obtained on LCK, AAS and SSC pastes after 5 days of curing and 9 months in natural carbonation or 2 months in accelerated carbonation at 1% CO<sub>2</sub>. Legend: A: aragonite, An: anhydrite, C: calcite, G: gypsum, V: vaterite.

## **5.1 Carbonation resistance of LCK, AAS and SSC concretes**

This part proposes to bring further explanations to the carbonation resistance of LCK, AAS and SSC concretes. Section 5.1.1 analyses their physical and chemical characteristics to explain the results obtained, while section 5.1.2 focuses on the pH of each binder before and after carbonation. Finally, in section 5.1.3 the carbonation rates obtained are extrapolated to conclude about the performance of each concrete against carbonation.

### *5.1.1 Physical and chemical analysis*

#### Low clinker (LCK)

**LCK** has a low w/b ratio (0.25) resulting in low porosity (10.3 %) and low gas permeability ( $39 \times 10^{-18} \text{ m}^2$ ), which provides an effective physical barrier to  $\text{CO}_2$  penetration (Article A). In addition, its mechanical strengths and microstructure develop rapidly due to the rapid hydration of CEM I, which reinforces this physical barrier. An important chemical barrier against carbonation is its reservoir of portlandite  $\text{Ca}(\text{OH})_2$ , which acts as a pH buffer by forming calcite  $\text{CaCO}_3$  with the  $\text{CO}_2$  that penetrates the material, whose larger molar volume allows to densify the microstructure. These reactions are well known because they are the same as in a classical Portland cement, with the difference that this reservoir is much more limited since the binder of LCK consists in only 27% clinker. The other 73% are limestone filler, which act only as a physical barrier, therefore limiting the efficiency of the chemical barrier. Before carbonation, its pore solution contains a significant amount of  $\text{OH}^-$  ions compared to the other two matrices (286 mmol/L, compared to 112 mmol/L for AAS and 13 mmol/L for SSC), which will be available to buffer the pH during the carbonation process (data from Table 22).

More precisely, a study conducted by TC RILEM 281-CCC shows that the natural carbonation rates of conventional concretes (Portland and blended Portland cements such as LCK) depend mainly on the w/CaO ratio (where w is the mass of water in the concrete, and CaO is the mass of CaO reactive in the binder paste of the concrete) and water/binder ratio (Gluth et al. 2022; Leemann et al. 2015; Leemann and Moro 2016; von Greve-Dierfeld et al. 2020). The source of CaO considered for LCK is the one from CEM I (Table 14), and not the filler because it is not reactive as it does not fix the  $\text{CO}_2$  (Table 26 in the supplementary data). It is observed that the higher is this w/CaO ratio, the higher are the associated carbonation rates in general (Gluth et al. 2022). Yet this ratio is rather high for LCK compared to other blended Portland cements (called BCC) in the literature, as illustrated in Figure 33 which will be presented and analysed in detail later.

#### Slag-based binders (AAS and SSC)

AAS and SSC concretes have similar transfer properties, higher than LCK, resulting from higher w/b ratios (0.43 for AAS and 0.50 for SSC): water porosity of about 17.5% and very high gas permeability (Article A). It should be noted, however, that these parameters are probably overestimated due to a too high drying temperature (105 °C), which can lead to damage of the material (Article A). The physical barrier for these two matrices is therefore much less effective than for LCK, which is intensified by a slower hydration of the slag



(especially for SSC (Collier et al. 2014; Noor-ul-Amin 2014)) and therefore a slower development of the microstructure and the mechanical resistances and a lesser quantity of hydrates able to trap CO<sub>2</sub>. The chemical barrier against carbonation is also different since AAS and SSC do not contain portlandite to act as a pH buffer. Different mechanisms are involved, due to a different pore solution and hydration products.

The mechanism of CO<sub>2</sub> binding for **Na<sub>2</sub>CO<sub>3</sub>-AAS** consists in a first step in the formation of Na-carbonate products as intermediate products, due to the reaction between the CO<sub>2</sub> and the sodium brought by the activator, and in a second step in the formation of Ca-carbonate products due to the decalcification of C-(N)-A-S-H and the reaction of calcium with Na-carbonate products (Ke et al. 2020; 2018; T. N. Nguyen et al. 2022). The pore solution analysis of AAS before carbonation (Table 22) highlights that a large amount of Na<sup>+</sup> ions (1017 mmol/L of sodium ions among the 1652 mmol/L of total ions) are available to trap the CO<sub>2</sub> by the formation of Na-carbonate products. Then, on one hand, the formation of Ca-carbonate products (calcite, vaterite) leads to the decrease of porosity (same as for Portland cements) (Ke et al. 2018) and, on the other hand, a high pH is maintained as sodium and hydroxide ions are released during this process (reactions are detailed in (Ke et al. 2020; T. N. Nguyen et al. 2022)). This maintains a cyclic hydration process, as sodium and hydroxide ions can then react with the anhydrous slag to form new C-(N)-A-S-H, which will carbonate and so on. In addition, the presence of monocarbonates, which are carbonated into calcite during the carbonation process, also enables to buffer the pH of pore solution (Ke et al. 2020). The chemical barrier of AAS against carbonation is therefore mainly governed by the amount of alkali ions contained in its pore solution and brought by the activator Na<sub>2</sub>CO<sub>3</sub>.

The hydrates of **SSC** are principally C-S-H and ettringite. Carbonation in this type of binder leads to the decomposition of ettringite C<sub>3</sub>A.3CaSO<sub>4</sub>.32H<sub>2</sub>O, which reacts with CO<sub>2</sub>, to form mainly calcite polymorphs CaCO<sub>3</sub> (calcite, aragonite) and gypsum CaSO<sub>4</sub>.2H<sub>2</sub>O (Bentur and Mindess 2007; Majumdar, Singh, and Evans 1981). This reaction also leads to an increase in porosity (Divet and Le Roy 2013), which reduces the efficiency of the physical barrier. The remaining anhydrite observed in Figure 32, was initially present in excess. Calcium ions present in the pore solution (16 mmol/L), which are available in higher amount than in the other two matrices, can also contribute to the formation of calcite or aragonite. The alkalinity of the system (low Na<sup>+</sup> and K<sup>+</sup> concentrations in Table 22 compared to the others binders), and generally the low quantity of hydroxides ions in the pore solution (only 13 mmol/L of OH<sup>-</sup> ions in Table 22, available before carbonation to buffer the pH) are thus the main parameters governing the carbonation resistance of SSC (Ioannou 2012). Since the chemical barrier is limited for this binder, the physical barrier must be improved to slow the penetration of CO<sub>2</sub>. (Cyr et al. 2019) explains that “the ettringite must be protected by closing the porous network as much as possible, which is commonly achieved by reducing the water content”. A low w/b ratio is therefore necessary to achieve acceptable carbonation resistances, which was not the case here (i.e w/b = 0.5) to achieve self-compacting concrete. Another alternative that has been studied to reduce this deficiency was the use of fabric formwork that promote a better surface quality of the concrete (Ioannou et al. 2016): an approximately 35% reduction in carbonation depth was possible.

The study conducted by TC RILEM 281-CCC shows, by analysis of literature data, that for concretes and mortars based on AAS and other alternative cements, the correlation between  $w/\text{CaO}$  ratio and the carbonation rates is not so evident (as illustrated by Figure 3 in (Gluth et al. 2022)) and that other parameters must be considered in these matrices (Gluth et al. 2022; Sisomphon and Franke 2007). This is explained by the fact that slag generally contains a non-negligible amount of MgO (in the range 5-14 wt.%) and AAS resistance to carbonation is mainly governed by the amount of alkali ions contained in its pore solution (S. A. Bernal et al. 2012). The carbonation rate of AAS concretes would instead be governed by the  $w/(\text{CaO} + \text{MgO}_{\text{eq}} + \text{Na}_2\text{O}_{\text{eq}} + \text{K}_2\text{O}_{\text{eq}})$  ratio, where “the equivalent masses reflect the theoretical maximum  $\text{CO}_2$  binding capacity of the respective oxides, analogous to the binding capacity of CaO on a molar basis” (Gluth et al. 2022). For SSC, anhydrite  $\text{CaSO}_4$  and fillers  $\text{CaCO}_3$  are not considered in the CaO reactive as they do not fix the  $\text{CO}_2$ .

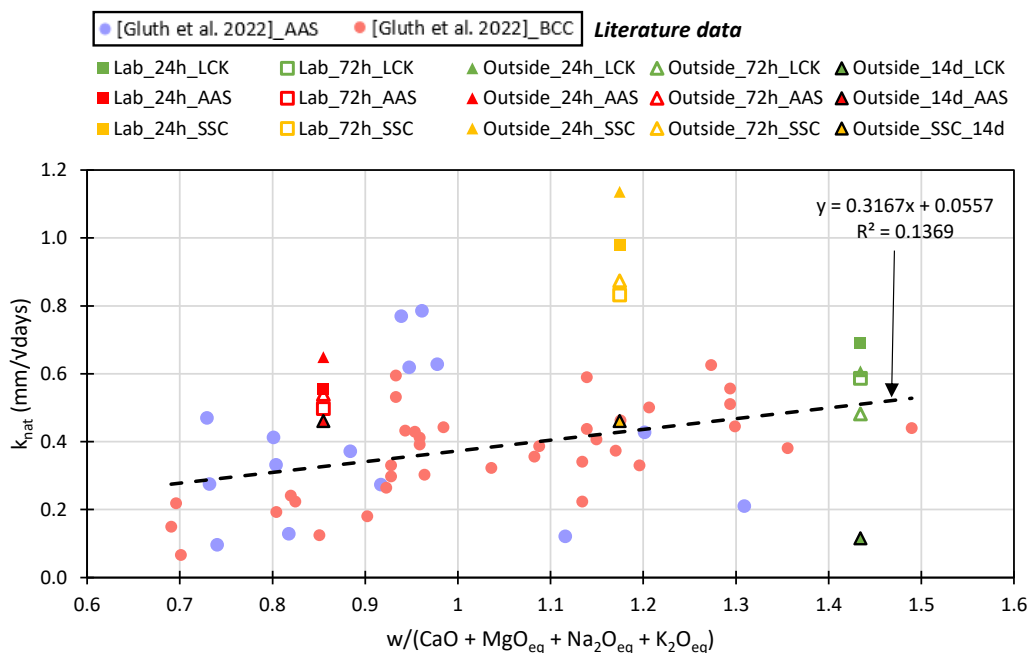


Figure 33: Natural carbonation rates  $k_{\text{nat}}$  versus  $w/(\text{CaO} + \text{MgO}_{\text{eq}} + \text{Na}_2\text{O}_{\text{eq}} + \text{K}_2\text{O}_{\text{eq}})$  ratio from (Gluth et al. 2022) for AAS and BCC (blended Portland cement) concretes and mortars, supplemented by LCK, AAS and SSC data of this study. The dashed line is a linear fit through AAS and BCC data points.

Figure 33 shows the correlation from (Gluth et al. 2022) between natural carbonation rate and  $w/(\text{CaO} + \text{MgO}_{\text{eq}} + \text{Na}_2\text{O}_{\text{eq}} + \text{K}_2\text{O}_{\text{eq}})$  ratio for both AAS (in purple) and BCC (in red) concretes and mortars. BCC refers to blended Portland cement with a high percentage of SCMs ( $\geq 66\%$  of the binder), mostly slag or fly ash. These data were extracted from the literature for a wide range of concretes and mortars of different compressive strengths (details available in (Gluth et al. 2022)). The database contains data for 125 AAS and 74 BCC. The points associated with the LCK, AAS and SSC concretes of this study were then added to Figure 33 (details in Table 26 in supplementary data), after calculation from the composition of the raw materials (Table 16). It can thus be observed that logically LCK concrete has a behaviour that is close to that of BCC, while AAS concrete has a behaviour similar to that of the AAS from the database. However, SSC concrete deviates from the identified correlation for short curing periods, as it

was shown in the literature that this binder has a low hydration kinetics and an insufficient curing leads to a decomposition of the ettringite and an increase of the porosity, resulting a dusting or pulverization of the concrete skin (Moranville-Regourd and Kamali-Bernard 2019; Novak and Sommer 2002). The strong dispersion of the data that allowed to establish this correlation suggests that other factors influence the resistance to carbonation of AAS and SSC, such as the curing time (as highlighted on Figure 28), that will strongly influence the development of the microstructure and the carbonate-binding reaction products formed.

### 5.1.2 *pH analysis*

The main problem with carbonation is that it causes a drop in pH in the material, which can subsequently lead to corrosion initiation if it falls below the  $\text{pH} = 9$  threshold. It is therefore important to correlate the carbonation kinetics obtained with pH values for each concrete, as the carbonation rate alone is not sufficient to draw conclusions about corrosion risk. For example, a rapid carbonation that does not lead to a pH drop below 9 would not be problematic for the durability of the material.

Figure 34 presents the pH measured on pastes samples with the suspension method, before carbonation and after 18 months of natural carbonation or 11 months of accelerated carbonation at 1%  $\text{CO}_2$ . As shown in Figure 34, the pH of the three matrices before carbonation (after 38 days of wet curing) is highly alkaline and ranges from 13.0 for LCK and AAS to 12.0 for SSC. This is in line with the pH values available in the literature: 13.2 to 13.5 for CEM I, 12.0 for SSC (Novak and Sommer 2002; Kraft et al. 2022). For AAS the pH measured after 28 days of curing vary according to the activator: 13.2-13.7 for NaSi-AAS (Kraft et al. 2022; A. Gruskovnjak et al. 2006) to 14.0 for AAS activated by a mix of sodium hydroxide and sodium silicate (Nedeljković et al. 2018). After complete carbonation of the materials, a drop in pH is observed for the three binders. In this section, the comparison focuses on the pH measured after natural carbonation, as the pH obtained after accelerated carbonation are studied in section 5.2.2.

It can be seen that after complete carbonation, the LCK and SSC matrices have their pH dropped below 9 (8.9 for LCK and 8.6 for SSC), which means that depassivation of the reinforcement and initiation of corrosion would be possible once the carbonation front has reached the rebar. This decrease of alkalinity is due to the dissolution of  $\text{CO}_2$  in the pore solution, which generates  $\text{H}_3\text{O}^+$  ions and subsequently a drop in pH (when the portlandite has been consumed for LCK).

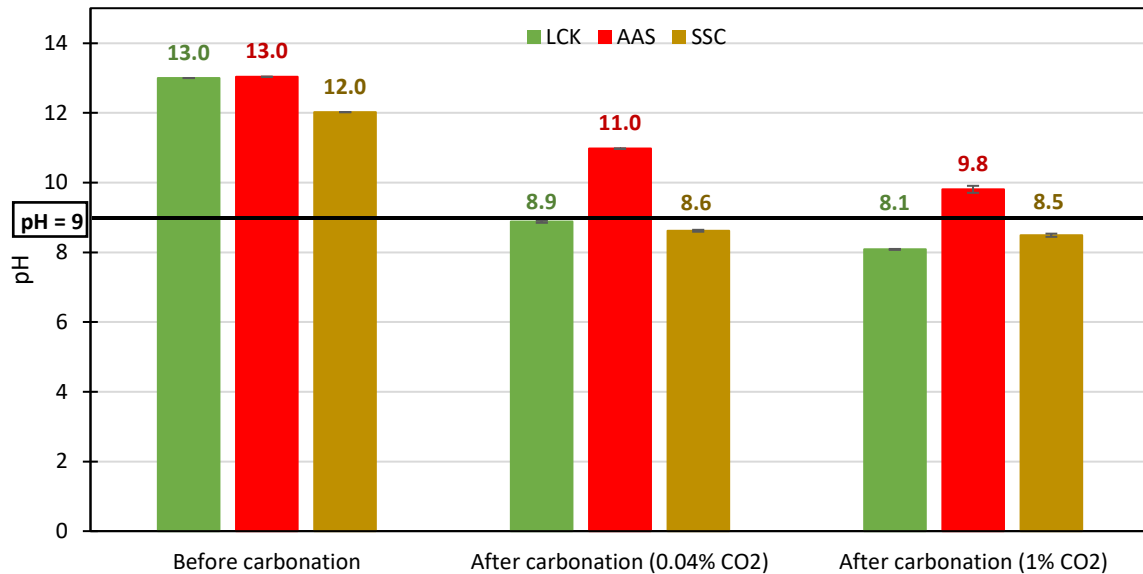


Figure 34: Evolution of pH before carbonation (38 days curing) and after 18 months of natural carbonation (outside sheltered) or 11 months of accelerated carbonation (1% CO<sub>2</sub>), for LCK, AAS and SSC samples. pH values obtained following the suspension method presented in section 3.2.2.

On the contrary, for the AAS binder the pH after carbonation remains above the critical threshold of pH = 9 (11.0 measured in natural carbonation), which questions if the sample was entirely carbonated. To verify the complete carbonation of the sample (paste in powder form), it was manually grinded to 80 µm and pulverized by rainbow, prior to pH measurement. The rainbow analysis revealed a uniform green colour (pH between 9 and 10) which suggests that carbonation was complete but did not cause a pH drop below 9. This is partly due to its high concentration of alkalis and the formation of Ca-carbonate products during the carbonation process, which enables to buffer the pH of pore solution, as explained previously. It means that for AAS, the arrival of the carbonation front at the reinforcement might not lead to depassivation of the reinforcement, nor to corrosion initiation, as quickly as for the other binders.

(Nedeljković et al. 2018) also measured the evolution of pH in AAS pastes both with suspension method and directly after pore fluid solution extraction, and also find a high pH (superior to 12) after 1 year in natural carbonation (the higher value measured can probably be explained by a different activation system: NaOH + NaSi). Other studies in the literature also confirm that the AAS binder maintains a high pH after natural carbonation (S. A. Bernal et al. 2012; Ke et al. 2020). In addition, several tests performed on reconstituted pore solutions, as well as the analysis of existing alkali-activated slag-based structures in Europe, show that the concrete is still sound after several decades of service (Deja 2002; Xu and Provis 2008). For example, (Deja 2002) analysed a C25/30 Na<sub>2</sub>CO<sub>3</sub>-AAS concrete used for wall panels in Kraków, and observed after 27 years of carbonation (field tests), an increase of compressive strength, a denser microstructure, an average of 11 mm carbonation depth, and an absence of corrosion, probably because the carbonation front did not reached the reinforcement.

### 5.1.3 Use of a simplified model to characterize resistance to carbonation

The objective of this section is to use a "simplified model" as an interpretation tool to characterize the resistance to carbonation of the three concretes studied, while being aware that more elaborate and realistic models exist. The aim is to obtain orders of magnitude and trends of time required for the carbonation front to reach the rebar in each concrete, considering different cover depths, different curing time and based on the experimental data obtained previously, while being aware that more elaborate and realistic models exist. The idea is to use Fick's first law (Equation (15)), which empirically considers the depths of carbonation  $x_c$  proportional to the square root of time exposure  $t$  (V. G. Papadakis, Vayenas, and Fardis 1989).

$$x_c = k\sqrt{t} \quad (15)$$

Where  $x_c$  is the carbonation depth (in mm),  $k$  is the carbonation coefficient in mm/year<sup>1/2</sup> and  $t$  is the exposure time (years).

The carbonation coefficient  $k$  is generally calculated using a law of diffusion (Sisomphon and Franke 2007), but for this practical application it is taken equal to the natural carbonation rates obtained experimentally ( $k_{nat}$ ), presented in section 4.1.1. The use of the experimental carbonation rates in natural conditions ( $k_{nat}$ ) allows to consider the diffusion of CO<sub>2</sub> through the concrete as well as its reaction with the matrix in an indirect way. Here it is assumed to take  $k_{nat}$  constant over time, even though it was shown in the literature that it tends to decrease with the hydration evolution during the carbonation process (Huy Vu et al. 2019) or with the blocking of the pores by the carbonation products for LCK and AAS (Belda Revert et al. 2017). Therefore, this hypothesis may lead to a slight overestimation of the kinetics obtained. From this point, for a given cover  $x$ , knowing the carbonation rate for specific experimental conditions, it is possible to calculate the time required for the carbonation front to reach the reinforcement for each binder, as illustrated in Figure 35. These predictions are valid for the experimental conditions considered (curing time before carbonation, indoor or outdoor exposure under shelter, RH) and cannot be generalized to other conditions. For this purpose, Figure 35 shows the times required for the carbonation front to reach the reinforcement in the case of natural carbonation in outdoor sheltered conditions. The indoor exposure condition "laboratory conditions: 20 °C and 65% RH" is not considered for reasons of readability of the figure and because it was shown in section 4.1.1 that the carbonation rates were similar to those outdoor under shelter. On the other hand, predictions for three different curing times (1 day, 3 days, 14 days) are proposed since it was observed in the same part, that this parameter had a strong influence on the measured carbonation rates. In this way, it gives an order of magnitude of possible predictions for different experimental conditions.

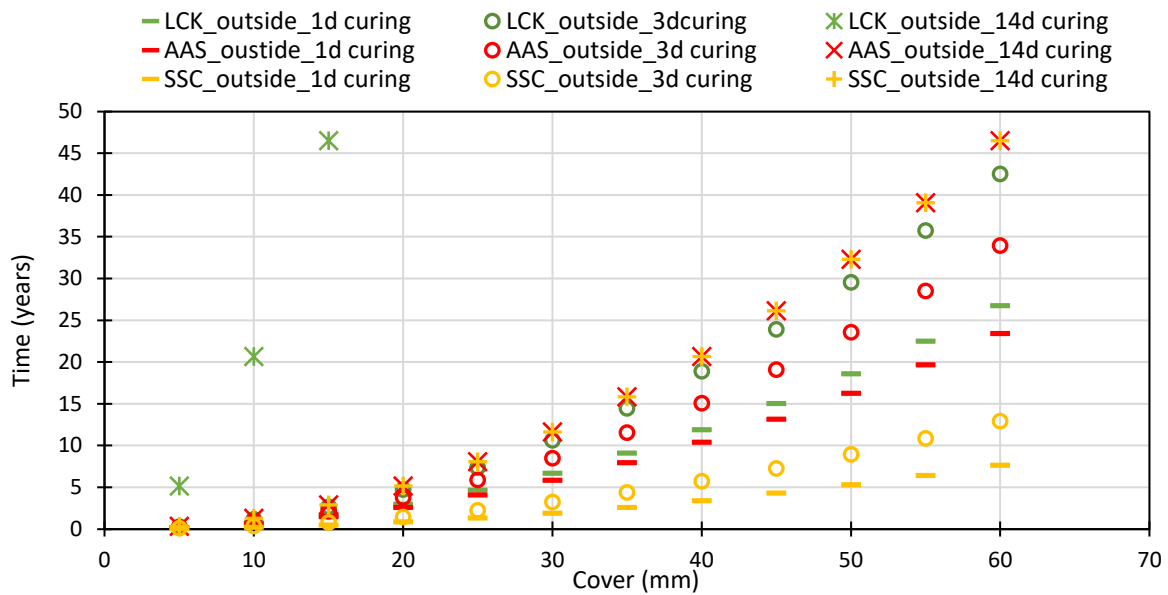


Figure 35: Time required for the carbonation front to reach the reinforcement for each binder, considering different covers from 10 to 60 mm. The associated numerical values are presented in Table 27, in the supplementary data.

Figure 35 illustrates the carbonation resistance of the three concretes studied, which were formulated to have the same strength class C25/30. The associated numerical values are presented in Table 27, in the supplementary data. The first consequence in term of durability, is that the three concretes seem quite sensitive to carbonation. For short curing time (1 or 3 days), between only 2-3 years for SSC, 6-8 years for AAS and 6-11 years for LCK, are needed for the carbonation front to reach the reinforcement for a 30 mm cover (Table 27). Furthermore, in order to achieve a 50-year service life for the concrete, a 60 mm cover would not be sufficient to ensure that the carbonation front has not reached the reinforcement for the three concretes (except for LCK cured 14 days, which shows better performances). Increasing the cover by 5 mm enables to slow down the arrival of the carbonation front to the rebar by a factor of 1.2 to 1.6, while for a same cover, waiting for 3 days of cure instead of 1 day allows to slow down the arrival of the carbonation front by a factor of 1.5 to 1.7. Finally, increasing the cover by 5 mm slows down the arrival of the carbonation front in the same order of magnitude as waiting for 3 days of curing instead of 1 day (the increase in curing time being slightly more effective).

Finally, moving from 1 day to 14 days of curing strongly improves the carbonation resistance, as the time necessary for the carbonation front to reach the rebar is multiplied by 27, 6 or 2 for LCK, AAS and SSC, respectively. The importance of curing on low CO<sub>2</sub> concretes is clear (Figure 35), which shows the emergency to change the practices and habits on site to develop their use while maintaining an acceptable durability. However, these results must be nuanced and considered carefully as it is important to keep in mind that, as explained above, they are surely overestimated due to the fact that a constant carbonation rate is assumed in this section, whereas in reality it decreases with time (Gluth et al. 2022). For example, analysis of existing Na<sub>2</sub>CO<sub>3</sub>-AAS-based structures in Europe, shows that the concrete experiments lower carbonation depths after several decades of service: 11 mm measured on field after 27 years of carbonation (Deja 2002) or 3 to 8 mm after 18 years of natural carbonation (Xu and Provis

2008). Similarly, there is no report in the literature of existing CSS-based structures experiencing significant degradation from corrosion initiation by carbonation, suggesting a possible slowdown in carbonation rates over the years (not taken into account in this section).

The French classification PERFDUB leads to the creation of the standard FD P18-480 (AFNOR 2022) that details threshold to reach based on different durability parameters, depending on the exposure class. To be classified XC (corrosion induced by carbonation), a concrete has to reach a performance threshold defined from an accelerated carbonation test done at 3% CO<sub>2</sub> ( $k_{acc\_3\% CO_2}$ ) according to XP P18-458 (AFNOR 2008), and modulated by the resistivity ( $\rho_{90d}$ ) measured after 90 days of curing according to XP P18-481 (AFNOR 2021), which are summarized in Table 24. The standards used in this study are RILEM TC-154 EMC recommendations (Polder et al. 2000) and EN 12390-12 (AFNOR 2020) for resistivity and accelerated carbonation at 3% CO<sub>2</sub> respectively, but are similar to the one required by PERFDUB (except 57% RH against 65% RH required by PERFDUB for accelerated carbonation, 90 days of curing required as opposed to 28 days here and preconditioning at 45 °C as opposed to 20 °C in this study). Although the thresholds presented in Table 24 have not been defined for slag-based binders, AAS and SSC concretes could be classified as XC1 (permanently dry or wet), while LCK concrete can be classified as XC2 (humid, rarely dry), as illustrated in Table 24.

*Table 24: Resistivity  $\rho$  after 90 days of curing (Article A) and accelerated carbonation rate  $k_{acc\_3\% CO_2}$ , corresponding to LCK, AAS and SSC concretes, as well as the associated thresholds (accelerated carbonation rate  $k_{acc\_3\% CO_2}$ ) from FD P18-480 defined for XC exposure class. The red colour means that the concrete is below the threshold required, while the green colour means that the concrete is above this threshold.*

		<b>LCK</b>	<b>AAS</b>	<b>SSC</b>
<b>Resistivity <math>\rho_{90d}</math> (<math>\Omega.m</math>)</b>	<i>experimental</i>	77	104	1955
<b>Accelerated carbonation rate <math>k_{acc\_3\% CO_2}</math> (<math>mm/(days)^{0.5}</math>)</b>	<i>experimental</i>	2.6	3.9	3.7
<b><math>k_{acc\_3\% CO_2}</math> (<math>mm/(days)^{0.5}</math>)</b>	XC1	4	4	4
<b>Threshold FD P 18-480</b>	XC2	3	3.5	3.5
(duration of use of the project: 50 years)	XC3	1.8	2.2	2.2
	XC4	1.8	2.2	3

## 5.2 Representativity of accelerated carbonation tests for low-carbon concretes

This section discusses the representativity of accelerated tests to characterize the carbonation resistance of low-carbon concretes, comparing the carbonation kinetics in section 5.2.1 and pH values in section 5.2.2, in natural and accelerated conditions, before making recommendations in section 5.2.3. Particular attention is paid to slag-based binders, for which the literature reports that accelerated carbonation with a high level of carbon dioxide is too aggressive compared to natural conditions and not representative for this type of binder (Bernal et al. 2012; Nedeljković et al. 2018; Nguyen et al. 2022; Zhao et al. 2020).

### 5.2.1 Comparison between natural ( $k_{nat}$ ) and accelerated ( $k_{acc}$ ) carbonation rates

To evaluate the representativity of accelerated carbonation tests compared to natural conditions, a first approach is to compare the carbonation rates obtained in both conditions. If the relation presented on Equation (16) is verified, then it can be considered that the accelerated carbonation is representative of the natural conditions (V. G. Papadakis, Vayenas, and Fardis 1989):

$$\frac{k_{acc}}{k_{nat}} = \sqrt{\frac{C_{CO_2,acc}}{C_{CO_2,nat}}} \quad (16)$$

Where  $k_{acc}$  is the carbonation rate obtained in accelerated conditions,  $k_{nat}$  is the carbonation rate obtained in natural conditions,  $C_{CO_2,acc}$  is the concentration of  $CO_2$  used for the accelerated test (1 or 3% in this study) and  $C_{CO_2,nat}$  is the concentration of  $CO_2$  in natural conditions (commonly taken equal to 0.04%).

This comparison is made on Figure 36, which represents the accelerated versus natural carbonation rates of LCK, AAS and SSC. Note that the comparison at 1%  $CO_2$  (Figure 36 (a)) is done only for LCK, AAS and SSC having 72h of curing in natural conditions to be as close as possible as accelerated conditions (5 days curing). The comparison at 3%  $CO_2$  (Figure 36 (b)) is done only for LCK, AAS and SSC having 14 days of curing in natural conditions to be as close as possible as accelerated conditions (28 days curing). In addition to the results from this study, data from the literature for AAS (in purple) and BCC (in red) concretes and mortars are displayed (study conducted by TC RILEM 281-CCC (Gluth et al. 2022)). BCC refers to blended Portland cement with a high percentage of SCMs ( $\geq 66\%$  of the binder).

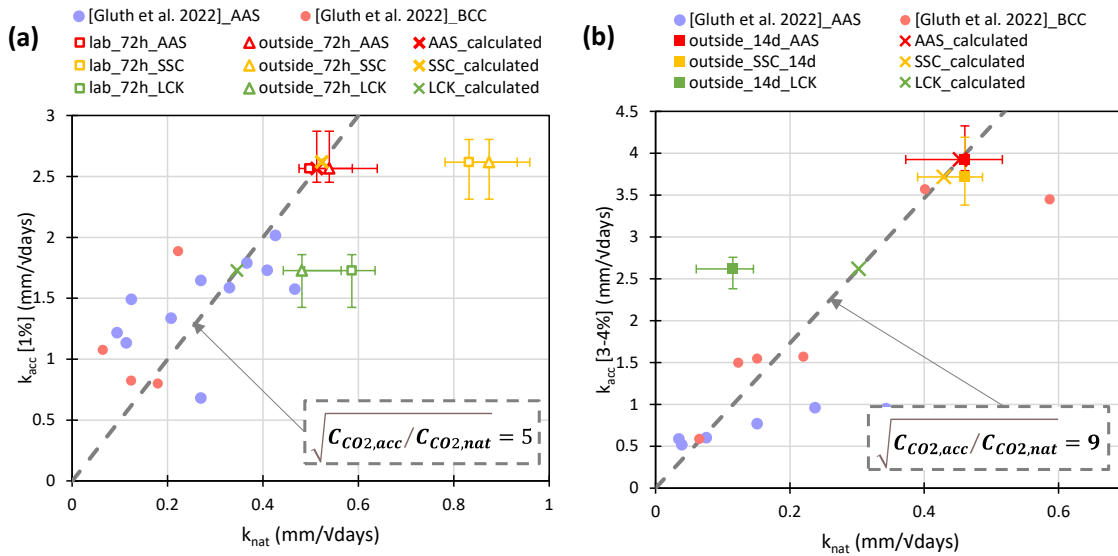


Figure 36: Carbonation rates measured in accelerated conditions  $k_{acc}$  at (a) 1%  $CO_2$  and (b) 3%  $CO_2$ , versus those measured in natural conditions for LCK, AAS and SSC of this study, supplemented by AAS and BCC (blended Portland cement) concretes and mortars from (Gluth et al. 2022). The “calculated” points are obtained from Equation (16).

Figure 36 shows a good correlation for the AAS of this study, both in accelerated carbonation at 1% and 3%  $CO_2$ , which confirms the behavior of the others AAS from the database. However, the correlation works only approximatively for LCK and SSC because a difference is observed with respect to the ratio of the roots of the concentrations (dashed lines).



The predictions at 1% CO<sub>2</sub> underestimate the natural carbonation kinetics for LCK and SSC (Figure 36 (a)). This difference could be partly explained by slightly different RH and curing period between natural (65% RH in laboratory conditions and 72h curing) and accelerated (57% RH and 5 days curing) conditions. Two more days of cure at young age can lead to significant differences in carbonation rate on these binders (Figure 28), contrary to AAS. By making a linear extrapolation between 3 and 5 days of cure, predictions of the right order of magnitude are obtained.

The difference between the predictions at 3% CO<sub>2</sub> and the natural carbonation kinetics for LCK (Figure 36 (b)), can partly be explained by the preconditioning step and a much faster drying (compared to AAS and SSC) due to a coarser porosity (Figure 12 and Figure 13 in article A). For the test at 3% CO<sub>2</sub>, after the 28 days of curing the samples are placed for 14 days at 20 ± 2 °C and 57 ± 7% RH to reduce their RH before the climatic chamber. As a result, carbonation will be further accelerated at 1% or 3% CO<sub>2</sub>. For the test in natural conditions, no preconditioning was performed and the samples have dried more slowly. These slower drying kinetics, in natural carbonation, explain the lower carbonation rates obtained compared to those expected.

### 5.2.2 *Comparison of pH between natural and accelerated conditions*

Another way to evaluate the representativity of an accelerated test is to compare the pH obtained after natural and accelerated carbonation. A different pH would be an indication of different mechanisms and vice versa.

As shown in Figure 34, the pH measured after accelerated carbonation is lower than after natural carbonation for all three formulations (difference of 0.8 for LCK, 1.2 for AAS, 0.1 for SSC), probably because of a more advanced carbonation level. However, in both cases (natural or accelerated carbonation), the pH remains below the pH = 9 threshold for LCK and SSC, and above the pH = 9 threshold for AAS. The conclusions regarding the risk of corrosion remain the same if natural or accelerated carbonation is performed. Therefore, the accelerated carbonation at 1% CO<sub>2</sub> can be considered as representative of natural conditions from the pH point of view for LCK et SSC, but for AAS the pH difference of 1.2 between the two conditions may also be an indicator that the reactions involved differ, and the results have to be considered carefully.

However, the conservation of such a high pH after accelerated carbonation for AAS was not expected as different behaviors are observed in the literature. (S. A. Bernal et al. 2012) observed by thermodynamic simulations on AAS activated by NaOH+NaSi, a pH drop to pH = 9 in the case of accelerated carbonation at 4% CO<sub>2</sub> whereas under natural conditions the pH does not lower below 10. This change in the pH of the carbonated pore solution is explained by the carbonation products formed which are not the same under natural and accelerated carbonation (transition zone calculated between 0.1% and 0.15% CO<sub>2</sub> but differences identified with XRD from 3-5% CO<sub>2</sub>). Sodium bicarbonates (NaHCO<sub>3</sub> or nahcolite) are formed preferentially for high CO<sub>2</sub> levels compared to hydrous sodium carbonates (Na<sub>2</sub>CO<sub>3</sub> or natron) present during natural carbonation.

The pH measurements performed in this study on AAS, after accelerated carbonation at 1% CO<sub>2</sub>, did not allow to reproduce these results (pH > 9 measured by the suspension method). This can partly be explained by the fact that the AAS in this study is different from the one considered for the tests and simulations in the paper by (S. A. Bernal et al. 2012): activator Na<sub>2</sub>CO<sub>3</sub> used instead of NaOH+NaSi, for which different carbonation mechanisms are observed (Ke et al. 2020; 2018). In addition, the simulations were performed with accelerated carbonation at 4% CO<sub>2</sub>, compared to 1% CO<sub>2</sub> used for the tests in this study, which enables to preserve better the hydrates observed in natural conditions. Some studies observed experimentally that the carbonation products obtained at 1% CO<sub>2</sub> are comparable to those obtained in natural carbonation (for calcium carbonates, but not necessarily for sodium carbonates) for AAS (Ke et al. 2018; S. A. Bernal et al. 2013), which explains the similar pH measured. This observation was confirmed in this study, where XRD after natural and accelerated carbonation (Figure 32), revealed similar hydration products (calcium carbonates) for the three binders studied.

### 5.2.3 *Recommendations to characterize the resistance to carbonation of low-carbon concretes*

To avoid misinterpretation of the results, it would be advisable to accelerate carbonation for low-carbon concretes at 1% CO<sub>2</sub>, if needed, rather than at 3% CO<sub>2</sub>.

The results of Section 5.2.1 and 5.2.2, highlighted that the accelerated carbonation tests at 1% CO<sub>2</sub>:

- Allow to correctly predict natural carbonation rates for AAS, as well as LCK and SSC for curing times identical to natural conditions (Figure 36).
- Allow to find the same hierarchy between the mixtures for carbonation rates as for natural conditions (Figure 31). « It is also noted that the testing program of RILEM TC 247-DTA gave similar relative performance rankings of a diverse set of AAC from natural and accelerated carbonation testing, indicating the usefulness of accelerated testing at least for the purpose of comparison between samples, if not in an absolute sense” (Gluth et al. 2020).
- Allow to preserve hydrates similar to those observed after carbonation in natural conditions, and consequently to preserve a similar pore solution (Figure 32).
- Allow to find the same conclusion regarding the risk of corrosion (pH higher or lower than 9) as for natural carbonation (Figure 34), despite differences between the two conditions (difference of 0.8 for LCK, 1.2 for AAS, 0.1 for LCK).

The results in Section 5.2.1 show that the accelerated carbonation tests at 3% CO<sub>2</sub>:

- Correctly predict natural carbonation rates for AAS and SSC but not for LCK, due to inadequate preconditioning (inefficient drying at 20 °C due to its low porosity) (Figure 36).
- Do not maintain the same hierarchy between the mixtures for carbonation rates as under natural conditions: AAS concrete carbonates faster than SSC at 3% CO<sub>2</sub> whereas it was the opposite in natural conditions and at 1% CO<sub>2</sub> (Figure 31).

- Are further away from natural conditions than the 1% CO<sub>2</sub> tests, and therefore lead to changes in phase equilibrium and hydrates more pronounced, according to the literature (Ke et al. 2018; Bernal et al. 2013; Zhang et al. 2017).
- Do not allow to find the same conclusions regarding the risk of corrosion as in natural carbonation, because the changes of hydrates lead to pH lower than 9 for AAS (contrary to natural carbonation) according to the literature (Ke et al. 2018; Bernal et al. 2013; Zhang et al. 2017).
- In addition, the RILEM TC 281-CCC study shows that for CO<sub>2</sub> concentrations of 3% and more, there is no more correlation between carbonation rate and  $w/(CaO + MgO_{eq} + Na_2O_{eq} + K_2O_{eq})$  ratio for AAS and BCC, as it was the case in natural conditions (Gluth et al. 2022). This absence of correlation indicates that the relevance of these tests is limited or that other parameters are potentially involved (microstructural damage...). A weak correlation was observed at 1% CO<sub>2</sub> for AAS and BCC, due to the high scatter of data.

Finally, it is important to keep in mind that even if carbonation test at 1% CO<sub>2</sub> can be used for the ranking of the low-carbon concretes, the ratio for moving from accelerated to natural carbonation kinetics is specific to each binder, as presented in Table 20. These data are interesting because they are rarely found in the literature for these new concretes. Therefore, it would be wrong to use the ratio associated to a classical CEM I-based concrete to low-carbon concretes.

### 5.3 Multi-criteria analysis

The aim of this last section is to investigate the consequences in terms of durability, of three low-carbon concretes having similar strength class (C25/30) and equivalent rheology (self-compacted). The proposed approach is to summarize the durability results obtained, in this paper and a previous one (Article A), in the form of a multi-criteria analysis formula by formula, with durability recommendations for each concrete. For this purpose, their performances are compared to that of a CEM III/A concrete, chosen as reference because due to its composition defined by the European Standard EN 197-1 (AFNOR 2012) (contains between 35 and 64% clinker and at least 36% slag), it is also a concrete with a reduced carbon footprint (117 kg eq. CO<sub>2</sub>/m<sup>3</sup> considering 400 kg eq.CO<sub>2</sub>/t associated to cement CEM III/A according to the French values from SFIC (Syndicat Français de l'Industrie Cimentière) available on (ATILH 2022)). For the comparison, it should be noted that the CEM III/A concrete in question has a strength class C35/45 (contrary to C25/30 for the concretes in the study) and a consistency class of S4 (as opposed to SF1 in this study), and therefore performs better than the LCK, AAS and SSC (Huy Vu et al. 2019). The properties of the three concretes and the reference considered for the multicriteria analysis are summarized in Table 28, available in the supplementary data.

Figure 37 summarizes the multicriteria analysis of LCK, AAS and SSC concretes compared to the reference concrete CEM III/A (data from Huy Vu et al. 2019), in the form of radar diagrams considering the CO<sub>2</sub> footprint, water porosity, gas permeability, natural chloride diffusion and natural carbonation rate (either inside or outside sheltered). All the properties presented are

measured after 90 days of curing, except the natural carbonation rate (after 1-day curing). Each diagram of the Figure 37 corresponds to one type of concrete (LCK, AAS or SSC) and illustrates their performance with respect of the properties listed above, in comparison with CEM III/A concrete (data from Huy Vu et al. 2019). In practical terms, for each property, a ratio is calculated between the performance of the concrete under consideration and that of the reference concrete. The dashed line represents the ratio calculated for the reference (CEM III/A) which is equal to 1, the values of the other concretes being calculated relatively to the reference. A ratio less than 1 illustrates a higher performance than the reference and vice versa for a ratio higher than 1, which illustrates a lower performance than the reference. Another representation of radar diagrams by properties instead than by formula is proposed on Figure 40 in the supplementary data.

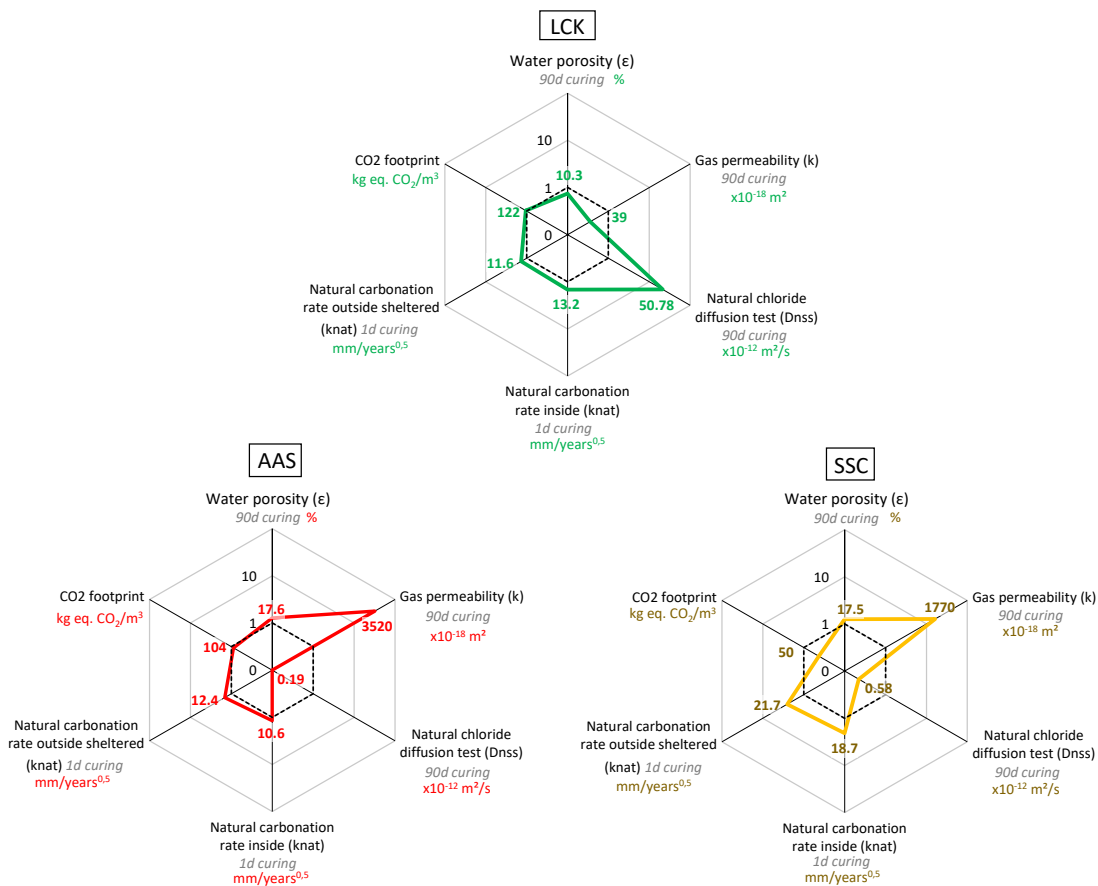


Figure 37: Multicriteria analysis of LCK, AAS and SSC concretes compared to a CEM III/A concrete taken as reference, based on the water porosity, gas permeability, natural chloride diffusion, natural carbonation rate, CO<sub>2</sub> footprint and compressive strength. The dashed line represents the performance of the reference (summarized in Table 28 in the supplementary data) taken equal to 1, the values of the other concretes being calculated relatively to the reference. Note that a log scale is used for reasons of readability.

For **LCK** concrete, the carbon footprint and carbonation rates are of same order of magnitude as for CEM III/A. Its porosity and consequently its gas permeability are lower, due to a low w/b ratio of 0.25, which provides an effective physical barrier against the penetration of aggressive agents. However, the compensation of this low w/b ratio is a more viscous concrete and therefore more difficult to handle, with a flow rate of reversed rate cone of 9.69 s (Table 16).

Moreover, this concrete offers acceptable resistance to carbonation for a curing time of more than 3 days (Figure 35), and would be adapted for this type of exposure (exposure class XC2). On the other hand, the weak point of this matrix is its low resistance to chlorides diffusion, with a diffusion coefficient  $D_{\text{ns}}$  20 times higher than that of the reference concrete, due to a low resistivity and a low amount of clinker which is responsible for a low chloride-binding capacity (Figure 9 of Article A). It is therefore advisable to avoid its use in marine environment, because its efficient transfer properties are not sufficient to guarantee a service life of 50 years, even with a large cover, as it was shown in Article A.

For **AAS** concrete, the carbon footprint and carbonation rates are also of similar order of magnitude as for CEM III/A, but it is characterized by a strong ability to maintain a high pH after carbonation, due to the large amount of alkali ions contained in its pore solution. On the other hand, its water porosity as well as its gas permeability are higher, partly due to a measurement protocol with high drying temperature (105 °C) which probably damage the material, as discussed in Article A. This binder is extremely efficient in chloride-rich areas, with a natural diffusion coefficient  $D_{\text{ns}}$  12 times lower than that of CEM III/A, due the strong ability of slag to bind chlorides. Its use in marine environments should therefore be encouraged (adapted for the most severe exposure classes). Finally, it is possible to improve its transfer properties and its resistance to carbonation by optimizing its composition, because the current formulation does not ensure a service life of 50 years for exposure to carbonation (section 5.1.3), even if it was shown previously that this concrete as a strong ability to maintain a  $\text{pH} > 9$  after carbonation (section 5.1.2). For example, the literature suggests the reduction of the w/b ratio, the addition of CLDHs which have interlayer ion exchangeability (Ke 2017; Ke, Bernal, and Provis 2016; Ke et al. 2018) or other components able to consume carbonate ions such as  $\text{Ca}(\text{OH})_2$ ,  $\text{Zn}(\text{OH})_2$ ,  $\text{ZnCl}_2$  and thus to decrease the carbonation depth by 30 to 45% (He et al. 2018).

Finally, for **SSC** concrete, its carbon footprint is greatly reduced compared to CEM III/A (2.5 times smaller), but its transfer properties and carbonation rates are higher: lower physical barrier due to a high w/b ratio (0.50), absence of portlandite to maintain a high pH and thus slow down carbonation, combined with a low hydration kinetic which makes its characteristics very dependent on the curing duration. However, this binder offers very good performance against chlorides, with a very low amount of ions in its pore solution leading to a high resistivity and on the other hand a diffusion coefficient  $D_{\text{ns}}$  4 times lower than that of CEM III/A due to a strong ability to bind chlorides, which allows to guarantee the required service life of 50 years. It is therefore recommended for a use in marine environments (adapted for the most severe exposure classes). Otherwise, it is possible to optimize its transfer properties to improve its physical barrier and its resistance to carbonation, reducing its w/b ratio even if this also results in an increase in mechanical resistance, or increasing the curing time before carbonation (favor prefabrication if the constraints on site do not allow it). These changes are necessary to achieve acceptable carbonation resistances and to develop their use, and also require to change the concrete design habits in favour of a performance-based approach focusing on durability performance instead of mechanical resistances, and the practices on site.

## 6 Conclusion

The carbonation resistance of LCK, Na<sub>2</sub>CO<sub>3</sub>-AAS and SSC concretes was investigated, considering the carbonation rates and the ability to maintain a high pH during the carbonation process, as summarized in Table 25. The relevance of accelerated carbonation tests to characterize the carbonation of low-carbon concretes was also questioned. Finally, the comparison of their durability properties (on a larger scale than just considering carbonation) against a CEM III/A reference concrete was also proposed. The following conclusions can be drawn:

- These three low-carbon concretes, designed to be C25/30 and self-compacting, have been compared with each other and are quite sensitive to carbonation. Nevertheless, their performances can be improved reducing their w/b ratio or extending their curing time (to more than 3 days) to improve their physical barrier against CO<sub>2</sub> diffusion.
- The importance of curing on low CO<sub>2</sub> concretes is clear, which shows the emergency to change the practices and habits on site to develop their use while maintaining an acceptable durability.
- If needed, it is recommended to performed accelerated tests at 1% CO<sub>2</sub> rather than at 3% CO<sub>2</sub>, to preserve as much as possible the hydrates and reactions observed in natural conditions. The tests carried out within the scope of this study, showed that the accelerated tests at 1% CO<sub>2</sub> seemed to be representative of the natural conditions and could be used at least for the purpose of comparison between samples, if not in an absolute sense. Similar relative performance rankings and same hierarchy between the mixtures are found for the carbonation rates and pH.
- The three concrete technologies studied have confirmed they can be competitive and promising low-carbon solutions, compared to a CEM III/A, if used in the suitable environments and by adapting the current mix design and on-site practices to achieve desired durability performance.

*Table 25: Conclusion about the carbonation resistance, based on carbonation rates, PERFDUB classification and ability to maintain a high pH during the carbonation process.*

	LCK	AAS	SSC
Natural carbonation rates (mm/(years <sup>1/2</sup> )):			
• Short curing time (3 d)	• 9.2	• 10.3	• 16.7
• Long curing time (≥ 14 d)	• 2.2	• 8.8	• 8.8
Exposure class according to PERFDUB classification	XC2 (humid, rarely dry)	XC1(permanently dry or wet)	XC1(permanently dry or wet)
pH after carbonation:			
• Natural carbonation	• 8.9	• 11.0	• 8.6
• Accelerated carbonation (1% CO <sub>2</sub> )	• 8.1	• 9.8	• 8.5
Carbonation resistance	<b>Medium</b> (slower carbonation and limited ability to maintain a high pH)	<b>Medium</b> (rapid carbonation but strong ability to maintain a high pH)	<b>Low</b> (rapid carbonation and low ability to maintain a high pH)

## 7 Supplementary data

### Related to 4.1.1

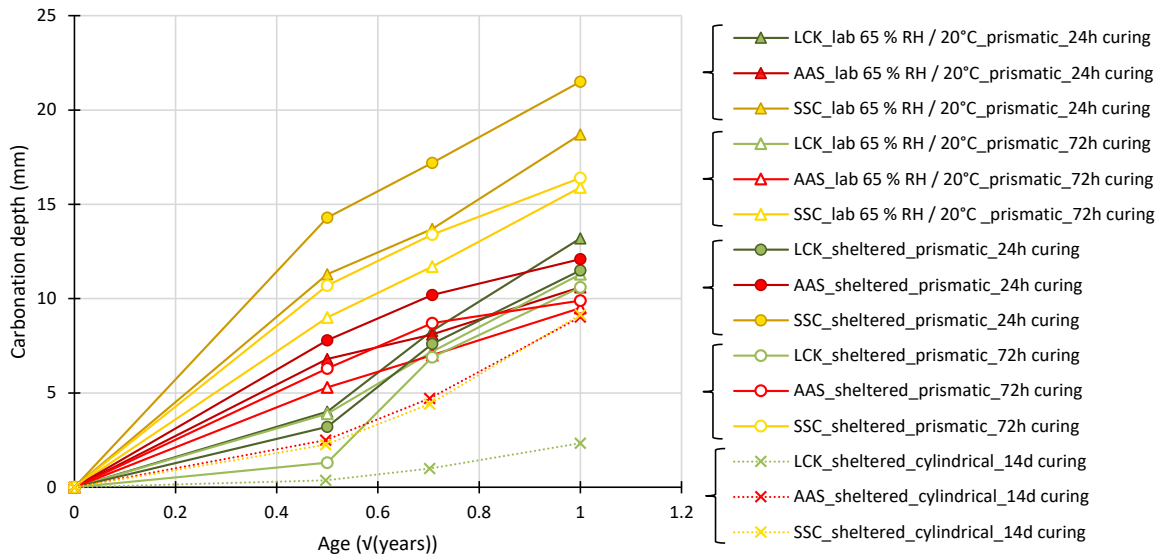


Figure 38: Kinetics of natural carbonation measured for LCK, AAS and SSC concretes in laboratory conditions (65% HR / 20 °C) or in outside sheltered conditions, for samples exposed to carbonation after different periods of curing (24h or 72h for prismatic samples and 14 days for cylindrical samples).

### Related to 4.1.2

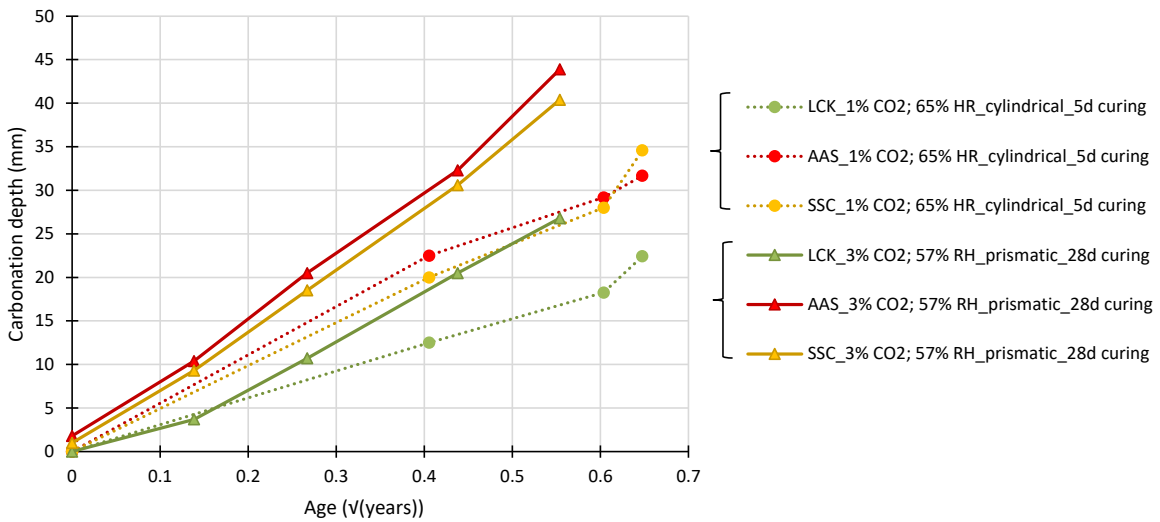


Figure 39: Kinetics of carbonation measured for LCK, AAS and SSC concretes in accelerated conditions: climatic chamber at (1) 1% CO<sub>2</sub> - 65% RH – 20 °C for cylindrical samples aged of 5 days of curing (dashed lines) or (2) 3% CO<sub>2</sub> - 57% RH – 20 °C for prismatic samples aged of 28 days of curing and 14 days of preconditioning (solid lines).

Related to 5.1.1

Table 26: Mass of CaO, MgO, Na<sub>2</sub>O, K<sub>2</sub>O in the binder paste of LCK, AAS and SSC concretes, (including the contributions from the solid binder and the activator). Na<sub>2</sub>O, K<sub>2</sub>O, and MgO were converted to “equivalent” masses (designated Na<sub>2</sub>O<sub>eq</sub>, K<sub>2</sub>O<sub>eq</sub>, and MgO<sub>eq</sub> respectively) by multiplying them by the ratio of the molar mass of CaO to the molar mass of the respective oxide, as explained in (Gluth et al. 2022).

	Unit	LCK	AAS	SSC
<b>CaO</b>	kg/m <sup>3</sup>	88.5	211.7	146.9
<b>MgO</b>	kg/m <sup>3</sup>	1.1	31.3	21.9
<b>MgO<sub>eq</sub></b>	kg/m <sup>3</sup>	1.5	43.6	30.5
<b>Na<sub>2</sub>O</b>	kg/m <sup>3</sup>	0.1	1.0	0.7
<b>Na<sub>2</sub>O<sub>eq</sub></b>	kg/m <sup>3</sup>	0.1	0.9	0.6
<b>K<sub>2</sub>O</b>	kg/m <sup>3</sup>	0.8	1.9	1.4
<b>K<sub>2</sub>O<sub>eq</sub></b>	kg/m <sup>3</sup>	0.5	1.2	0.8
<b>CaO + MgO<sub>eq</sub> + Na<sub>2</sub>O<sub>eq</sub> + K<sub>2</sub>O<sub>eq</sub></b>	kg/m <sup>3</sup>	90.6	257.3	178.8
<b>water</b>	kg/m <sup>3</sup>	130	220	210
<b>water/(CaO + MgO<sub>eq</sub> + Na<sub>2</sub>O<sub>eq</sub> + K<sub>2</sub>O<sub>eq</sub>)</b>		1.4	0.9	1.2

Related to 5.1.3

Table 27: Time required for the carbonation front to reach the reinforcement for each concrete, considering different covers from 10 to 60 mm (M: time in months), associated to Figure 35.

cover (cm)	t (years)								
	LCK			AAS			SSC		
	1d curing	3d curing	14d curing	1d curing	3d curing	14d curing	1d curing	3d curing	14d curing
<b>5</b>	0.2 (2 M)	0.3 (4 M)	5.2	0.2 (2 M)	0.2 (3 M)	0.3 (4 M)	0.1 (1 M)	0.1 (1 M)	0.3 (4 M)
<b>10</b>	0.7 (9 M)	1.2	21	0.7 (8 M)	0.9 (11 M)	1.3	0.2 (3 M)	0.4 (4 M)	1.3
<b>15</b>	1.7	2.7	46	1.5	2.1	2.9	0.5 (6 M)	0.8 (10 M)	2.9
<b>20</b>	3.0	4.7	83	2.6	3.8	5.2	0.8 (10 M)	1.4	5.2
<b>25</b>	4.6	7.4	129	4.1	5.9	8.1	1.3	2.2	8.1
<b>30</b>	6.7	11	186	5.9	8.5	12	1.9	3.2	12
<b>35</b>	9.1	14	253	8.0	12	16	2.6	4.4	16
<b>40</b>	12	19	331	10	15	21	3.4	5.7	21
<b>45</b>	15	24	418	13	19	26	4.3	7.3	26
<b>50</b>	19	30	517	16	24	32	5.3	9.0	32
<b>55</b>	22	36	625	20	29	39	6.4	11	39
<b>60</b>	27	43	744	23	34	46	7.6	13	46



Related to 5.3

*Table 28: Summary of the properties measured experimentally on LCK, AAS, SSC and CEM III/A concretes, used to represent Figure 37 and Figure 40.*

	Test or property measured	Unit	Sample curing	LCK *	AAS *	SSC *	CEM III/A **
<b>MECHANICAL PROPERTIES</b>	<b>Compressive strength</b>	MPa	28 days	33.0	33.3	32.0	36.7
			90 days	34.4	37.5	40.0	41.7
<b>GENERAL TRANSFER PROPERTIES</b>	<b>Water porosity (<math>\epsilon</math>)</b> (105 °C)	%	90 days	10.3	17.6	17.5	13.8
	<b>Gas permeability (k)</b> (105 °C)	E-18 m <sup>2</sup>	90 days	39	3520	1770	109
<b>CHLORIDE TRANSPORT</b>	<b>Natural chloride diffusion test (<math>D_{nss}</math>)</b>	$\times 10^{-12}$ m <sup>2</sup> /s	90 days	50.78 ± 12.06	0.19 ± 0.01	0.58 ± 0.01	2.4

\* Article A

\*\* (Huy Vu et al. 2019)

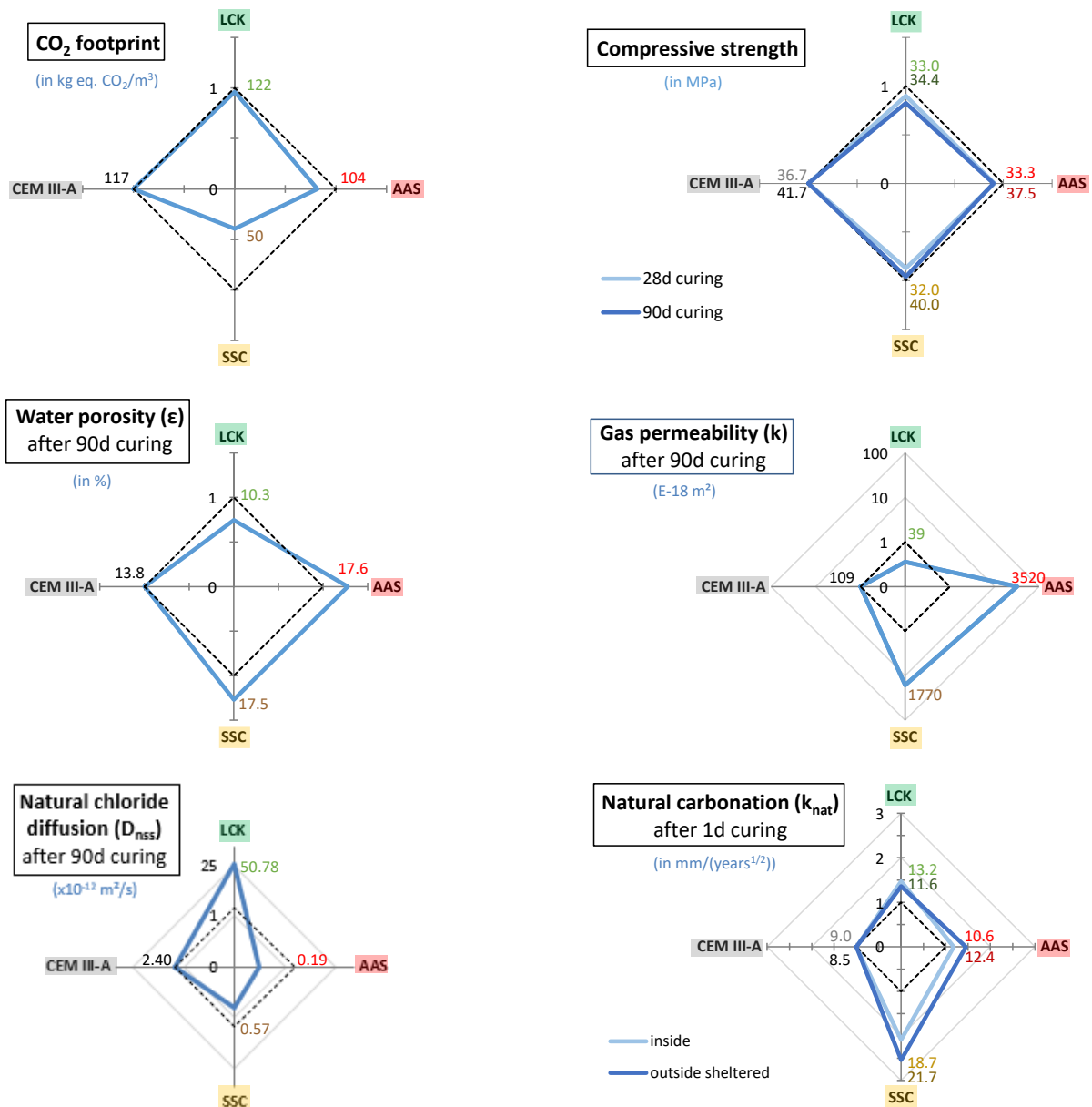


Figure 40: Multicriteria analysis of LCK, AAS and SSC concretes compared to a CEM III/A concrete taken as reference, based on the CO<sub>2</sub> footprint, compressive strength, water porosity, gas permeability, natural chloride diffusion and natural carbonation rate. The dashed line represents the performance of the reference (CEM III/A concrete) taken equal to 1, the values of the other concretes being calculated relatively to the reference. Note that a log scale is used for the natural chloride diffusion and gas permeability for reasons of readability.

## 8 References

- AFNOR. 2008. ‘XP P18-458’.
- AFNOR. 2010. ‘NF EN 15743 : Ciment Sursulfaté - Composition, Spécifications et Critères de Conformité’.
- AFNOR. 2012. ‘NF EN 197-1 Ciment - Partie 1 : Composition, Spécifications et Critères de Conformité Des Ciments Courants’.
- AFNOR. 2018. ‘EN 12390-10 : Détermination de La Résistance à La Carbonatation Du Béton à Des Niveaux Atmosphériques de Dioxyde de Carbone’.
- AFNOR. 2020. ‘EN 12390-12 : Détermination de La Résistance à La Carbonatation Du Béton - Méthode de La Carbonatation Accélérée’.
- AFNOR. 2021. ‘XP P18-481’.
- AFNOR. 2022. ‘FD P 18-480’.
- Angst, Fabrizio Moro, Mette Geiker, Sylvia Kessler, Hans Beushausen, Carmen Andrade, Jukka Lahdensivu, et al. 2020. ‘Corrosion of Steel in Carbonated Concrete: Mechanisms, Practical Experience, and Research Priorities – a Critical Review by RILEM TC 281-CCC’. *RILEM Technical Letters* 5 (December): 85–100. <https://doi.org/10.21809/rilemtechlett.2020.127>.
- ATILH. 2022. ‘Ciments et LHR : Analyse et Inventaire Du Cycle de Vie (ACV/ICV), Déclaration Environnementale Produit (DEP)’. Infociments. June 2022. <https://www.infociments.fr/ciments/ciments-declaration-environnementale-inventaire-analyse-du-cycle-de-vie>.
- Awoyera, Paul, and Adeyemi Adesina. 2019. ‘A Critical Review on Application of Alkali Activated Slag as a Sustainable Composite Binder’. *Case Studies in Construction Materials* 11 (December): e00268. <https://doi.org/10.1016/j.cscm.2019.e00268>.
- Balayssac, J P, H. Détriché, and J. Grandet. 1995. ‘Effects of Curing upon Carbonation of Concrete’. *Construction and Building Materials* 9 (2): 91–95.
- Behnood, Ali, Kim Van Tittelboom, and Nele De Belie. 2016. ‘Methods for Measuring PH in Concrete: A Review’. *Construction and Building Materials* 105 (February): 176–88. <https://doi.org/10.1016/j.conbuildmat.2015.12.032>.
- Belda Revert, Andres, Klaaetje De Weerd, Karla Hornbostel, and Mette Rica Geiker. 2017. ‘State-of-the-Art Report: Service Life Modelling, Carbonation of Concrete and Corrosion in Carbonated Concrete’. ISBN No. 82-7482-106-8. Norwegian University of Science and Technology.
- Bentur, Arnon, and Sidney Mindess. 2007. *Fibre Reinforced Cementitious Composites*. 2nd ed. Modern Concrete Technology Series. London ; New York: Taylor & Francis.
- Bernal, Susan. 2016. ‘Advances in Near-Neutral Salts Activation of Blast Furnace Slags’. *RILEM Technical Letters* 1 (June): 39. <https://doi.org/10.21809/rilemtechlett.2016.8>.
- Bernal, Susan A., John L. Provis, David G. Brice, Adam Kilcullen, Peter Duxson, and Jannie S.J. van Deventer. 2012. ‘Accelerated Carbonation Testing of Alkali-Activated Binders Significantly Underestimates Service Life: The Role of Pore Solution Chemistry’. *Cement and Concrete Research* 42 (10): 1317–26. <https://doi.org/10.1016/j.cemconres.2012.07.002>.
- Bernal, Susan A., John L. Provis, Rupert J. Myers, Rackel San Nicolas, and Jannie S. J. van Deventer. 2015. ‘Role of Carbonates in the Chemical Evolution of Sodium Carbonate-Activated Slag Binders’. *Materials and Structures* 48 (3): 517–29. <https://doi.org/10.1617/s11527-014-0412-6>.
- Bernal, Susan A., John L. Provis, Brant Walkley, Rackel San Nicolas, John D. Gehman, David G. Brice, Adam R. Kilcullen, Peter Duxson, and Jannie S.J. van Deventer. 2013. ‘Gel Nanostructure in Alkali-Activated Binders Based on Slag and Fly Ash, and Effects of

- Accelerated Carbonation’. *Cement and Concrete Research* 53 (November): 127–44. <https://doi.org/10.1016/j.cemconres.2013.06.007>.
- Cerib. 2022. ‘Impact Carbone Des Laitiers de Haut Fourneau Utilisés Dans Les Ciments’. July 2022. <https://www.cerib.com/impact-carbone-des-laitiers-de-haut-fourneau-utilises-dans-les-ciments/>.
- Collier, N.C., N.B. Milestone, L.E. Gordon, and S.-C. Ko. 2014. ‘The Suitability of a Supersulfated Cement for Nuclear Waste Immobilisation’. *Journal of Nuclear Materials* 452 (1–3): 457–64. <https://doi.org/10.1016/j.jnucmat.2014.05.078>.
- Cyr, Martin, Ludovic André, Mailys Ruau, Nicolas Musikas, and Laurent Frouin. 2019. ‘Durability of Supersulfated Cement with Improved Early Strength’. *15th International Congress on the Chemistry of Cement, Prague, Czech Republic*.
- Cyr, Martin, Patrice Rivard, Francis Labrecque, and Alain Daidié. 2008. ‘High-Pressure Device for Fluid Extraction from Porous Materials: Application to Cement-Based Materials’. *Journal of the American Ceramic Society* 91 (8): 2653–58. <https://doi.org/10.1111/j.1551-2916.2008.02525.x>.
- Damineli, Bruno L., Fernanda M. Kemeid, Patricia S. Aguiar, and Vanderley M. John. 2010. ‘Measuring the Eco-Efficiency of Cement Use.’ *Cement and Concrete Composites* 32 (8): 555–62. <https://doi.org/10.1016/j.cemconcomp.2010.07.009>.
- De Weerd, K., G. Plusquellec, A. Belda Revert, M.R. Geiker, and B. Lothenbach. 2019. ‘Effect of Carbonation on the Pore Solution of Mortar’. *Cement and Concrete Research* 118 (April): 38–56. <https://doi.org/10.1016/j.cemconres.2019.02.004>.
- Deja, J. 2002. ‘Carbonation Aspects of Alkali Activated Slag Mortars and Concretes’. *Silicates Industriels* 67: 37–42.
- Dhir, R. K., M. C. Limbachiya, M. J. McCarthy, and A. Chaipanich. 2007. ‘Evaluation of Portland Limestone Cements for Use in Concrete Construction’. *Materials and Structures* 40 (5): 459–73. <https://doi.org/10.1617/s11527-006-9143-7>.
- Divet, Loïc, and Robert Le Roy. 2013. ‘Étude de La Durabilité Vis-à-Vis de La Corrosion Des Armatures Des Bétons Formulés Avec Des Ciments à Forte Teneur En Laitier de Haut Fourneau’. *BLPC*, no. 280–281 (November).
- ecoinvent. 2022. ‘ecoinvent Database’. Ecoinvent. 2022. <https://ecoinvent.org/the-ecoinvent-database/>.
- Elgalhud, Abdurrahman A., Ravindra K. Dhir, and Gurmeh Ghataora. 2018. ‘Chloride Ingress in Concrete: Limestone Addition Effects’. *Magazine of Concrete Research* 70 (6): 292–313. <https://doi.org/10.1680/jmacr.17.00177>.
- Elgalhud, Abdurrahman A., Ravindra K. Dhir, and Gurmeh S. Ghataora. 2017. ‘Carbonation Resistance of Concrete: Limestone Addition Effect’. *Magazine of Concrete Research* 69 (2): 84–106. <https://doi.org/10.1680/jmacr.16.00371>.
- Gartner, Ellis, and Tongbo Sui. 2018. ‘Alternative Cement Clinkers’. *Cement and Concrete Research*, Report of UNEP SBCI Working group on low-CO<sub>2</sub> eco-efficient cement-based materials, 114 (December): 27–39. <https://doi.org/10.1016/j.cemconres.2017.02.002>.
- Gluth, Gregor J. G., Kamel Arbi, Susan A. Bernal, Dali Bondar, Arnaud Castel, Sundararaman Chithiraputhiran, Alireza Dehghan, et al. 2020. ‘RILEM TC 247-DTA Round Robin Test: Carbonation and Chloride Penetration Testing of Alkali-Activated Concretes’. *Materials and Structures* 53 (1): 21. <https://doi.org/10.1617/s11527-020-1449-3>.
- Gluth, Gregor J. G., Xinyuan Ke, Anya Vollpracht, Lia Weiler, Susan A. Bernal, Martin Cyr, Katja Dombrowski-Daube, et al. 2022. ‘Carbonation Rate of Alkali-Activated Concretes and High-Volume SCM Concretes: A Literature Data Analysis by RILEM TC 281-CCC’. *Materials and Structures* 55 (8): 225. <https://doi.org/10.1617/s11527-022-02041-4>.

- Greve-Dierfeld, Stefanie von, Barbara Lothenbach, Anya Vollpracht, Bei Wu, Bruno Huet, Carmen Andrade, César Medina, et al. 2020. ‘Understanding the Carbonation of Concrete with Supplementary Cementitious Materials: A Critical Review by RILEM TC 281-CCC’. *Materials and Structures* 53 (6): 136. <https://doi.org/10.1617/s11527-020-01558-w>.
- Gruskovnjak, A., B. Lothenbach, L. Holzer, R. Figi, and F. Winnefeld. 2006. ‘Hydration of Alkali-Activated Slag: Comparison with Ordinary Portland Cement’. *Advances in Cement Research* 18 (3): 119–28. <https://doi.org/10.1680/adcr.2006.18.3.119>.
- Habert, G., J.B. d’Espinoze de Lacaillerie, and N. Roussel. 2011. ‘An Environmental Evaluation of Geopolymer Based Concrete Production: Reviewing Current Research Trends’. *Journal of Cleaner Production* 19 (11): 1229–38. <https://doi.org/10.1016/j.jclepro.2011.03.012>.
- Habert, G., S. A. Miller, V. M. John, J. L. Provis, A. Favier, A. Horvath, and K. L. Scrivener. 2020. ‘Environmental Impacts and Decarbonization Strategies in the Cement and Concrete Industries’. *Nature Reviews Earth & Environment* 1 (11): 559–73. <https://doi.org/10.1038/s43017-020-0093-3>.
- Hainer, Stefan, Tilo Proske, and Carl-Alexander Graubner. 2015. ‘Einfluss der Nachbehandlung auf das Karbonatisierungsverhalten von Beton aus klinkerarmen Zementen’. *Beton- und Stahlbetonbau* 110 (1): 41–49. <https://doi.org/10.1002/best.201400042>.
- He, Juan, Qie Gao, Yonghua Wu, and Xiaolin Pu. 2018. ‘Study on Improvement of Carbonation Resistance of Alkali-Activated Slag Concrete’. *Construction and Building Materials* 176 (July): 60–67. <https://doi.org/10.1016/j.conbuildmat.2018.04.117>.
- Holt, Erika E, Hannele P Kuosa, Markku T Leivo, and Erkki J Vesikari. 2009. ‘Deterioration by Frost, Chloride and Carbonation Interactions Based on Combining Field Station and Laboratory Results’. <https://doi.org/10.13140/2.1.3994.5926>.
- Hooton, Doug, Michelle Nokken, and M. Thomas. 2007. ‘Portland-Limestone Cement: State-of-the-Art Report and Gap Analysis For CSA A 3000’. *SN3053*, January.
- Hunkeler, F. 2012. ‘Requirements for the Carbonation Resistance of Concrete Mixes’.
- Hunkeler, F. 2016. ‘Swiss Requirements for the Carbonation Resistance of Concrete for the Exposure Classes XC3, XC4 and XD’. *9th International Concrete Conference 2016, Environment, Efficiency and Economic Challenges for Concrete*, July, 14.
- Huy Vu, Quoc, Gabriel Pham, Alain Chonier, Eric Brouard, Sundar Rathnarajan, Radhakrishna Pillai, Ravindra Gettu, et al. 2019. ‘Impact of Different Climates on the Resistance of Concrete to Natural Carbonation’. *Construction and Building Materials* 216 (August): 450–67. <https://doi.org/10.1016/j.conbuildmat.2019.04.263>.
- INIES. 2017. ‘INIES: Les Données Environnementales et Sanitaires de Référence Pour Le Bâtiment’. 2017. <https://www.base-inies.fr/iniesV4/dist/consultation.html>.
- Ioannou, Socrates. 2012. ‘An Assessment of the Performance of Calcium Sulfoaluminate and Supersulfated Cements for Use in Concrete’. PhD, UK: University of Bath.
- Ioannou, Socrates. 2019. ‘Alternative Cementitious Solutions for Sustainable Concrete in the Gulf Region’. *CPI – Concrete Plant International*, no. 6.
- Ioannou, Socrates, Atef Badr, Kaloyana Kostova, Kevin Paine, and Tim Ibell. 2016. ‘Utilization of Fabric Formwork for Improving the Durability of Concrete from Supersulfated Cement’. *Key Engineering Materials* 711 (September): 615–21. <https://doi.org/10.4028/www.scientific.net/KEM.711.615>.
- Juenger, M.C.G., F. Winnefeld, J.L. Provis, and J.H. Ideker. 2011. ‘Advances in Alternative Cementitious Binders’. *Cement and Concrete Research* 41 (12): 1232–43. <https://doi.org/10.1016/j.cemconres.2010.11.012>.

- Ke, Xinyuan. 2017. 'Improved Durability and Sustainability of Alkali-Activated Slag Cements'. Phd, University of Sheffield. <http://etheses.whiterose.ac.uk/17557/>.
- Ke, Xinyuan, Susan A. Bernal, and John L. Provis. 2016. 'Controlling the Reaction Kinetics of Sodium Carbonate-Activated Slag Cements Using Calcined Layered Double Hydroxides'. *Cement and Concrete Research* 81 (March): 24–37. <https://doi.org/10.1016/j.cemconres.2015.11.012>.
- Ke, Xinyuan, Susan A. Bernal, John L. Provis, and Barbara Lothenbach. 2020. 'Thermodynamic Modelling of Phase Evolution in Alkali-Activated Slag Cements Exposed to Carbon Dioxide'. *Cement and Concrete Research* 136 (October): 106158. <https://doi.org/10.1016/j.cemconres.2020.106158>.
- Ke, Xinyuan, Maria Criado, John L. Provis, and Susan A. Bernal. 2018. 'Slag-Based Cements That Resist Damage Induced by Carbon Dioxide'. *ACS Sustainable Chemistry & Engineering* 6 (4): 5067–75. <https://doi.org/10.1021/acssuschemeng.7b04730>.
- Kraft, Bettina, Rebecca Achenbach, Horst-Michael Ludwig, and Michael Raupach. 2022. 'Hydration and Carbonation of Alternative Binders'. *Corrosion and Materials Degradation* 3 (1): 19–52. <https://doi.org/10.3390/cmd3010003>.
- Leemann, Andreas, and Fabrizio Moro. 2016. 'Carbonation of Concrete: The Role of CO<sub>2</sub> Concentration, Relative Humidity and CO<sub>2</sub> Buffer Capacity'. *Materials and Structures* 50 (August): 30. <https://doi.org/10.1617/s11527-016-0917-2>.
- Leemann, Andreas, Peter Nygaard, Josef Kaufmann, and Roman Loser. 2015. 'Relation between Carbonation Resistance, Mix Design and Exposure of Mortar and Concrete'. *Cement and Concrete Composites* 62 (September): 33–43. <https://doi.org/10.1016/j.cemconcomp.2015.04.020>.
- Lye, Chao-Qun, Ravindra K. Dhir, and Gurmel S. Ghataora. 2016. 'Carbonation Resistance of GGBS Concrete'. *Magazine of Concrete Research* 68 (18): 936–69. <https://doi.org/10.1680/jmacr.15.00449>.
- Ma, Qianmin, Sreejith V. Nanukuttan, P. A. Muhammed Basheer, Yun Bai, and Changhui Yang. 2016. 'Chloride Transport and the Resulting Corrosion of Steel Bars in Alkali Activated Slag Concretes'. *Materials and Structures* 49 (9): 3663–77. <https://doi.org/10.1617/s11527-015-0747-7>.
- Majumdar, A. J., B. Singh, and T. J. Evans. 1981. 'Glass Fibre-Reinforced Supersulphated Cement'. *Composites* 12 (3): 177–83. [https://doi.org/10.1016/0010-4361\(81\)90500-0](https://doi.org/10.1016/0010-4361(81)90500-0).
- Mohamed, Osama Ahmed. 2019. 'A Review of Durability and Strength Characteristics of Alkali-Activated Slag Concrete'. *Materials* 12 (8): 1198. <https://doi.org/10.3390/ma12081198>.
- Moranville-Regourd, Micheline, and Siham Kamali-Bernard. 2019. 'Cements Made From Blastfurnace Slag'. In *Lea's Chemistry of Cement and Concrete*, 469–507. Elsevier. <https://doi.org/10.1016/B978-0-08-100773-0.00010-1>.
- Müller, Harald S., Raphael Breiner, Jack S. Moffatt, and Michael Haist. 2014. 'Design and Properties of Sustainable Concrete'. *Procedia Engineering* 95: 290–304. <https://doi.org/10.1016/j.proeng.2014.12.189>.
- Mundra, Shishir, Gabriel Samson, Giulia Masi, Rebecca Achenbach, David M. Bastidas, Susan A. Bernal, Maria C. Bignozzi, et al. 2023. 'Application of Electrochemical Methods for Studying Steel Corrosion in Alkali-activated Materials'. *Materials and Corrosion*, February, maco.202313743. <https://doi.org/10.1002/maco.202313743>.
- Nedeljković, Marija, Bahman Ghiassi, Sieger van der Laan, Zhenming Li, and Guang Ye. 2019. 'Effect of Curing Conditions on the Pore Solution and Carbonation Resistance of Alkali-Activated Fly Ash and Slag Pastes'. *Cement and Concrete Research* 116 (February): 146–58. <https://doi.org/10.1016/j.cemconres.2018.11.011>.

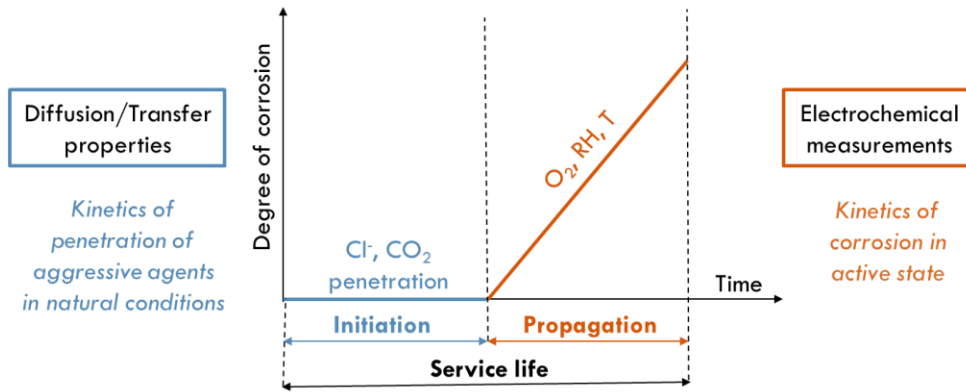
- Nedeljković, Marija, Yibing Zuo, Kamel Arbi, and Guang Ye. 2018. 'Carbonation Resistance of Alkali-Activated Slag Under Natural and Accelerated Conditions'. *Journal of Sustainable Metallurgy* 4 (1): 33–49. <https://doi.org/10.1007/s40831-018-0166-4>.
- Nguyen, Thi Nhan, Quoc Tri Phung, Ziyou Yu, Lander Frederickx, Diederik Jacques, Dimitrios Sakellariou, Alexandre Dauzeres, Jan Elsen, and Yiannis Pontikes. 2022. 'Alteration in Molecular Structure of Alkali Activated Slag with Various Water to Binder Ratios under Accelerated Carbonation'. *Scientific Reports* 12 (1): 5524. <https://doi.org/10.1038/s41598-022-09491-4>.
- Noor-ul-Amin. 2014. 'An Overview on Comparative Study of Alternatives for Ordinary Portland Cement'. *Journal of Basic and Applied Chemistry* 4 (6): 15–22.
- Novak, D, and H Sommer. 2002. 'A New Low-Heat Sulfate Resistant Binder for Mass Concrete, HPC and SCC'. *Proceedings of the International Conference Held at the University of Dundee, Scotland, Challenges of Concrete Construction*, 5 (September): 213–22. <https://doi.org/10.1680/scc.31777>.
- Palm, Sebastian, Tilo Proske, Moien Rezvani, Stefan Hainer, Christoph Müller, and Carl-Alexander Graubner. 2016. 'Cements with a High Limestone Content – Mechanical Properties, Durability and Ecological Characteristics of the Concrete'. *Construction and Building Materials* 119 (August): 308–18. <https://doi.org/10.1016/j.conbuildmat.2016.05.009>.
- Papadakis, V. G., C. G. Vayenas, and M. N. Fardis. 1989. 'A Reaction Engineering Approach to the Problem of Concrete Carbonation'. *AIChE Journal* 35 (10): 1639–50. <https://doi.org/10.1002/aic.690351008>.
- Papadakis, Vagelis G., Costas G. Vayenas, and Michael N. Fardis. 1991. 'Fundamental Modeling and Experimental Investigation of Concrete Carbonation'. *Materials Journal* 88 (4): 363–73. <https://doi.org/10.14359/1863>.
- Polder, R., C. Andrade, B. Elsener, Ø. Vennesland, J. Gulikers, R. Weidert, and M. Raupach. 2000. 'RILEM TC 154-EMC Recommendations: Test Methods for on Site Measurement of Resistivity of Concrete'. *Materials and Structures* 33 (December): 603–11.
- Puertas, F., M. Palacios, and T. Vázquez. 2006. 'Carbonation Process of Alkali-Activated Slag Mortars'. *Journal of Materials Science* 41 (10): 3071–82. <https://doi.org/10.1007/s10853-005-1821-2>.
- Räsänen, V., and V. Penttala. 2004. 'The PH Measurement of Concrete and Smoothing Mortar Using a Concrete Powder Suspension'. *Cement and Concrete Research* 34 (5): 813–20. <https://doi.org/10.1016/j.cemconres.2003.09.017>.
- Rodrigues, Romain, Stéphane Gaboreau, Julien Gance, Ioannis Ignatiadis, and Stéphanie Betelu. 2020. 'Corrosion of Carbon Steel in Concrete: Current Knowledge of Corrosion Mechanisms and Non-Destructive Testing of Corrosion Rates'.
- Savija, B., and M. Luković. 2016. 'Carbonation of Cement Paste: Understanding Challenges, and Opportunities'. *Construction and Building Materials* 117: 285–301.
- Scrivener, Karen L., Vanderley M. John, and Ellis M. Gartner. 2018. 'Eco-Efficient Cements: Potential Economically Viable Solutions for a Low-CO<sub>2</sub> Cement-Based Materials Industry'. *Cement and Concrete Research* 114 (December): 2–26. <https://doi.org/10.1016/j.cemconres.2018.03.015>.
- Sisomphon, Kritsada, and Lutz Franke. 2007. 'Carbonation Rates of Concretes Containing High Volume of Pozzolanic Materials'. *Cement and Concrete Research* 37 (12): 1647–53. <https://doi.org/10.1016/j.cemconres.2007.08.014>.
- Slag cement association, and ASTM International. 2020. 'Environmental Product Declaration for Slag Cement'. United States and Canada.

- Thomas, M D A, and J D Matthews. 1992. 'Carbonation of Fly Ash Concrete'. *Magazine of Concrete Research*, no. 1: 12.
- Vogler, Nico, Mathias Lindemann, Philipp Drabetzki, and Hans-Carsten Kühne. 2020. 'Alternative PH-Indicators for Determination of Carbonation Depth on Cement-Based Concretes'. *Cement and Concrete Composites* 109 (May): 103565. <https://doi.org/10.1016/j.cemconcomp.2020.103565>.
- Wang, Aiguo, Yi Zheng, Zuhua Zhang, Kaiwei Liu, Yan Li, Liang Shi, and Daosheng Sun. 2020. 'The Durability of Alkali-Activated Materials in Comparison with Ordinary Portland Cements and Concretes: A Review'. *Engineering* 6 (6): 695–706. <https://doi.org/10.1016/j.eng.2019.08.019>.
- Wang, Wei-Chien, Wei-Hsing Huang, Ming-Yu Lee, Hoang Trung Hieu Duong, and Ya-Hui Chang. 2021. 'Standardized Procedure of Measuring the PH Value of Cement Matrix Material by Ex-Situ Leaching Method (ESL)'. *Crystals* 11 (4): 436. <https://doi.org/10.3390/cryst11040436>.
- Xu, Hua, and John L Provis. 2008. 'Characterization of Aged Slag Concretes'. *ACI Materials Journal* 105 (2): 131–39.
- Ye, Hailong, Rongjin Cai, and Zushi Tian. 2020. 'Natural Carbonation-Induced Phase and Molecular Evolution of Alkali-Activated Slag: Effect of Activator Composition and Curing Temperature'. *Construction and Building Materials* 248 (July): 118726. <https://doi.org/10.1016/j.conbuildmat.2020.118726>.
- Zhang, Jian, Caijun Shi, Zuhua Zhang, and Zhihua Ou. 2017. 'Durability of Alkali-Activated Materials in Aggressive Environments: A Review on Recent Studies'. *Construction and Building Materials* 152 (October): 598–613. <https://doi.org/10.1016/j.conbuildmat.2017.07.027>.
- Zhang, Xuanhan, Kaidi Long, Wei Liu, Lixiao Li, and Wu-Jian Long. 2020. 'Carbonation and Chloride Ions' Penetration of Alkali-Activated Materials: A Review'. *Molecules* 25 (21): 5074. <https://doi.org/10.3390/molecules25215074>.
- Zhao, Kai, Yongning Liang, Tao Ji, Yue Lu, and Xujian Lin. 2020. 'Effect of Activator Types and Concentration of CO<sub>2</sub> on the Steel Corrosion in the Carbonated Alkali-Activated Slag Concrete'. *Construction and Building Materials* 262 (November): 120044. <https://doi.org/10.1016/j.conbuildmat.2020.120044>.



## Durability of reinforcement in three low-carbon concretes

**Theoretical background:** presentation of binders + classical and galvanic corrosion mechanisms



### CORROSION INITIATION

**Objectives:** Estimate the time taken by the aggressive agents ( $\text{Cl}^-$  or  $\text{CO}_2$ ) to reach the reinforcement. Use reliable and representative test methods.

**Approach:** Characterisation of the general transfer properties, transport of  $\text{Cl}^-$  and  $\text{CO}_2$  on concrete.

#### Article A: General transfer properties and chloride penetration resistance

##### General transfer properties

- Tests:**
- Water porosity
  - Mercury intrusion porosity
  - Water permeability
  - Capillary absorption
  - Gas permeability
  - Resistivity

##### Transport of $\text{Cl}^-$

- Tests:**
- $\text{Cl}^-$  diffusion test
  - RCPT test

#### Article B: Resistance to carbonation

##### Transport of $\text{CO}_2$ and ability to maintain a high pH

- Tests:**
- Carbonation depth (natural, 1%  $\text{CO}_2$ , 3%  $\text{CO}_2$ )
  - pH measurements before and after carbonation of paste samples (natural, 1%  $\text{CO}_2$ )

### CORROSION PROPAGATION

**Objectives:** Evaluate the corrosion rates once the rebars have been depassivated. Use reliable and representative test methods.

**Approach:**

- Development of a methodology adapted to low-carbon binders and representative of real structures: galvanic current measurement + mass loss.
- Comparison with traditional electrochemical tests ( $E_{\text{corr}}$ ,  $\rho$ ,  $R_p$ ,  $i_{\text{corr}}$ , Tafel).

#### Article C: Chloride-induced corrosion

##### Experimental conditions:

- Different levels of chloride contamination:
- $[\text{NaCl}] = 30 \text{ g/L}$  (sea water)
  - $[\text{NaCl}] = 300 \text{ g/L}$  (de-icing salts)
- Saturated conditions

#### Article D: Carbonation-induced corrosion

##### Experimental conditions:

- Natural carbonation outdoor sheltered  
Samples with increased w/b ratio  
3 different moisture conditions tested

**Synthesis chapter:** discussion of articles A, B, C and D

## Transition to Article C

Articles A and B previously focused on the study of corrosion initiation, either by chlorides (Article A) or by carbonation (Article B). About chlorides, the results from Article A showed the LCK concrete is characterized by a very high chloride permeability, despite “excellent” transfer properties (low water porosity, gas permeability, water permeability and capillary absorption) due to a low w/b ratio. This was partly explained by its low clinker content (137 kg/m<sup>3</sup> or 27% of the binder), which is responsible on one hand for a lower chloride-binding capacity, and on the other hand for a high conductivity (thus a low resistivity) because there are less hydrates to trap ions. Its majority of capillary pores (>10 nm), also promotes the mobility of chloride ions. Its use for exposure classes XS or XD is not recommended. On the contrary, the AAS and SSC concretes are both extremely resistant to chloride penetration. For AAS, the more important diffusion mechanisms and its low resistivity, seem to be balanced by a stronger chloride binding capacity. For SSC, the lower diffusive transport and the very low amount of ions in its pore solution leads to a high resistivity, in favour of a reduced chloride mobility. Both are adapted for exposure classes XS3m (tidal or splash zone) and XD3tf (very frequent salting).

In Article C it is now proposed to focus on the **propagation period**, in the case of **chloride-induced corrosion**. The objective is to quantify the **corrosion rates** developed, after the arrival of chlorides at the rebar, in active state. There is still a lack of information regarding the compatibility of low-carbon binders with rebars and the associated corrosion kinetics. Moreover, the literature reports difficulties to assess the corrosion resistance of slag-based binders with classical electrochemical tests (corrosion potential  $E_{\text{corr}}$ , polarization resistance  $R_p$ ). It justifies the proposition of an alternative method in this article to study the corrosion propagation.



## Chapter 5 – Article C

# Chloride-induced corrosion of steel in three low-carbon concretes studied by galvanic current measurements

## Table of contents

<b>1</b>	<b>Introduction .....</b>	<b>150</b>
<b>2</b>	<b>Materials.....</b>	<b>155</b>
2.1	Raw Materials.....	155
2.2	Mix design.....	155
2.3	Specimen characteristics and preparation: anode and cathode.....	157
<b>3</b>	<b>Test methods .....</b>	<b>160</b>
3.1	Overview of the experimental campaign.....	160
3.2	Classic electrochemical measurements .....	160
3.3	Galvanic current measurement.....	163
3.4	Autopsy of the anodes .....	164
<b>4</b>	<b>Results.....</b>	<b>167</b>
4.1	Classic electrochemical measurement.....	167
4.2	Galvanic coupling between anode and cathode.....	172
4.3	Classic electrochemical measurement after galvanic coupling .....	175
4.4	Autopsy of the anodes .....	176
<b>5</b>	<b>Discussion .....</b>	<b>180</b>
5.1	Galvanic current ( $I_g$ ).....	180
5.2	Total corrosion current ( $i_{tot}$ ): contributions of galvanic current between anode and cathode ( $i_g$ ) and local current at the anode ( $i_{mi-anode}$ ) .....	181
5.3	Methodology: interest and perspectives of the galvanic current method .....	184
5.4	Assessment of the corrosion risk in the three low-carbon concretes considered.....	186
<b>6</b>	<b>Conclusion .....</b>	<b>188</b>
<b>7</b>	<b>Supplementary data.....</b>	<b>189</b>
<b>8</b>	<b>References.....</b>	<b>190</b>



## **Chloride-induced corrosion of steel in three low-carbon concretes studied by galvanic current measurements**

Lola Doussang<sup>1</sup>, Gabriel Samson<sup>1</sup>, Fabrice Deby<sup>1</sup>, Bruno Huet<sup>2</sup>, Emmanuel Guillon<sup>2</sup>, Martin Cyr<sup>1</sup>

<sup>1</sup> *Laboratoire des Matériaux et Durabilité des Constructions (LMDC), INSAT/UPS Génie Civil, 135 Avenue de Ranguel, 31077 Toulouse Cedex 04 France.*

<sup>2</sup> *Holcim Innovation Center, 95 rue du Montmurier, F-38070 Saint Quentin Fallavier, France*

### **Abstract**

An evaluation of the corrosion rate due to chloride contamination is carried out on three low-carbon concretes (low clinker (LCK), alkali-activated slag (AAS) and supersulfated cement (SSC)), by a galvanic current measurement combined with mass loss on the rebar. This method, not widely used in the literature, consists in measuring the galvanic current exchanged between a chloride-contaminated anode and a passive cathode, spatially separated. The influence of two chloride concentrations on the corrosion rates is studied: [NaCl] = 30 g/L (seawater) or 300 g/L (de-icing salts). Finally, a comparison with classical electrochemical measurements (corrosion potential  $E_{\text{corr}}$ , polarization resistance  $R_p$ ) is carried out. The results show that the galvanic current depends mainly on the potential difference and the total resistance (polarization resistances and materials resistances) between the anode and the cathode, as well as on the chloride concentration. The measured galvanic current is low at 30 g/L for AAS and LCK and then becomes significant at 300 g/L, while it remains negligible on the SSC binder for both concentrations. The corrosion rates of activated anodes due to chlorides are nevertheless high for the three low-carbon binders, because the total current density is composed of the measured galvanic current, to which is added to a high local current density at the anode.

### **Keywords**

Galvanic current, Chloride-induced corrosion, Low-carbon concretes, Durability, Low clinker, Alkali-activated slag, Supersulfated cement

## 1 Introduction

### Context of the study

The production of Portland cement requires a large amount of resources and energy, resulting in high CO<sub>2</sub> emissions. Thus, the development of more eco-friendly concretes to meet the current environmental challenges is gaining more and more interest worldwide (Habert et al. 2020; Scrivener, John, and Gartner 2018). The characterization of their behaviour against corrosion due to chlorides, which is among the main causes of structural degradation, becomes crucial to achieve sustainable constructions. The present study focuses on three different low-carbon concretes, having a reduced carbon footprint, ranging from -40 to -75% (Article B), compared to that of a traditional concrete of same strength class made only with CEM I: low clinker (LCK) concrete, alkali-activated slag with sodium carbonate (AAS) concrete and supersulfated cement (SSC) concrete.

In absence of corrosion, the reinforcement in Portland cement (PC) concretes is protected by a dense layer of iron oxides called “passive film”, which is created spontaneously at the surface of the rebar due to the high pH of concrete. However, chlorides from seawater or de-icing salts are aggressive agents able to cause the rupture of the passive film, and therefore an initiation of corrosion, threatening the service life of marine concrete structures and structures exposed to cold region requiring de-icing salts, respectively.

As proposed by Tutti (Tuutti 1982), the service life of reinforced concrete structures can be divided into two main time periods: an initiation stage, where the rebar remains passive, corresponding to the time needed for the chlorides to reach the reinforcement and a propagation stage, associated to an active state of corrosion and characterized by high corrosion rates. The transition between these two successive stages was until now attributed to a critical chloride threshold at the reinforcement, which has recently been nuanced by (Angst et al. 2022), who proposes alternative approaches based on a more continuous transition between passive and active corrosion.

This article will focus on the corrosion kinetics associated to the "propagation" phase, as the initiation phase was investigated in Article A, based on the transfer properties of each concrete. Corrosion rates and mechanisms associated to chloride-induced corrosion in CEM I-based concretes have been extensively studied in the literature as it is an important issue for the durability of structures, but little information is available for LCK, AAS and SSC binders.

### Summary of data available in the literature

#### Electrochemical methods

Commonly applied electrochemical techniques for studying steel corrosion (not exhaustive) are open circuit potential (OCP), linear polarization resistance (LPR) measurements or concrete electrical resistivity measurement (Mundra et al. 2023). As there is no standardized procedure to perform these electrochemical measurements, laboratory setups vary, considering different medium of study, steel electrode, aggressive environment or analytical techniques, which makes the comparison of the results obtained complicated and the consensus on the risk of corrosion in concrete not always obvious (Angst et al. 2009).

Most studies of the corrosion of steel in low-carbon binders have been performed using established techniques and recommendations developed for PC. Uncertainties exist regarding the application of these classical electrochemical measurements and the associated data analysis commonly used for PC concretes, to study reinforcement corrosion in slag-based binders.

The OCP, also referred as the corrosion potential ( $E_{\text{corr}}$ ), is generally used to assess the onset of steel corrosion by a potential drop or the corrosion state of the rebars, according to ASTM C876-22b (ASTM International 2022). The OCP value of steel in slag-based binders has been reported to be much electronegative than in PC, in the range of -400 to -700mV (Criado et al. 2018; Mundra, Bernal, et al. 2017; Zhang, Xi, et Yang 2021). It was explained by the consumption of oxygen in the pore solution of concrete, by reduced sulphur species from slag, leading to a very reducing environment and low corrosion potential values (Criado et al. 2018; Mundra, Bernal, et al. 2017; Runci, Serdar, et Provis 2019). The use of previously mentioned recommendations (ASTM International 2022) for the interpretation of potential values in slag-based binders, could lead to misleading interpretations, if applied without modifications (Criado et Provis 2018; Mundra et al. 2023; Runci, Serdar, et Provis 2019; Zhang, Xi, et Yang 2021).

The LPR measurement consists in applying small polarisation with respect to OCP ( $\pm 5\text{-}20$  mV), considering to sweep the linear part of the potential-current curve, to determine the value of linear polarization resistance ( $R_p$ ), and then the associated corrosion current  $i_{\text{corr}}$ , from the Stern-Geary relation (Mundra et al. 2023; Rodrigues et al. 2020; Zhang, Xi, et Yang 2021). For PC-concretes,  $R_p < 40 \text{ k}\Omega\cdot\text{cm}^2$  combined with a potential drop of approximately -200 mV, has been established as an indicator to assess the onset of steel corrosion (Angst et al. 2017). This interpretation is not transposable to slag-based binders, for which the  $R_p$  value not only represents the oxidation reaction of iron, but also depends on the oxidation reaction of sulphur (Mundra et al. 2023; Mundra and Provis 2021). Moreover, the use of the Stern-Geary relation to calculate the corrosion current requires the knowledge of a constant B, specific to the composition of each binder. It can be determined with Tafel curves obtained with much higher polarization with respect to OCP than for LPR. The empirical value of B is commonly accepted for PC-based samples (52 mV for passive steel and 26 mV for active steel) (C. Andrade and Alonso 1996; C. Andrade and González 1978). Such studies are required for low-carbon concretes. Finally, the LPR measurement is not optimal for characterizing corrosion kinetics due to localized chloride corrosion, because the Stern-Geary equation is only applicable in the case of uniform corrosion, which is not satisfied with localized corrosion spots observed with chloride induced corrosion, which brings uncertainties around the corrosion currents obtained with this method (Angst et Büchler 2015; Mundra et al. 2023).

The electrical resistivity of concrete is a material property quantifying its resistance to the passage of an electrical current. It will influence the corrosion rate (both microcell or galvanic), and transport properties of the material (C. Andrade et al. 1992; Hornbostel, Larsen, and Geiker 2013; Raupach 1996). The resistivity will be specific to each low-carbon concrete and is influenced by the pore network, the pore solution or the degree of saturation (Alonso et Andrade 1987; Angst et al. 2020; Bu et Weiss 2014; Noushini 2018).



### Results available for each binder

A summary of the corrosion rates measured on the three low-carbon binders studied is proposed hereafter.

The **LCK** is a binder made of 27% CEM I and 73% limestone filler in this study. (Elgalhud, Dhir, and Ghataora 2018) proposes an evaluation of chloride-induced corrosion resistance of PC with limestone fillers. They reported that only 13 studies deal with the corrosion rates due to chlorides in this type of binder. The studies reviewed focused only on samples made with 0-35% filler, which is much lower than the substitution level considered in this study (73%). The main findings show that the corrosion rates measured in the limestone filler-based concrete are generally higher than those measured in the corresponding Portland cement-based reference (moderate to high increase). Some parameters were also identified as having a strong influence on the measured corrosion rates, such as the level of cement replacement by fillers, the w/b ratio or the fineness of the limestone filler used (Diab, Mohamed, and Aliabdo 2016; Diab, Aliabdo, and Mohamed 2015). Further research is nevertheless required to assess the corrosion kinetics in LCK concrete of the study, which has a different composition (27% CEM I and 73% limestone filler), but a very low water-cement ratio (0.25), to confirm these findings.

The **AAS** concrete in this study is made with slag as aluminosilicate precursor, combined with a sodium carbonate ( $\text{Na}_2\text{CO}_3$ ) alkaline activator. Many authors have investigated the corrosion rates due to chlorides in AAS with NaOH or  $\text{Na}_2\text{SiO}_3$  activation and a lot of data are now available (N. Gartner et al. 2021; Ma et al. 2016; Mangat, Ojedokun, and Lambert 2021; Runci, Provis, and Serdar 2023; Tahri et al. 2021; W. Wang et al. 2017). However, no study focusing on  $\text{Na}_2\text{CO}_3$  activation has been found. The literature reports that the differences in pore solution composition affect the results of electrochemical measurements, which leads to difficulties in their interpretation to assess the corrosion resistance of AAS (Criado et Provis 2018; Mundra et al. 2023; Runci, Serdar, et Provis 2019; Zhang, Xi, et Yang 2021). The high concentration of reduced sulfur species from slag, in the pore solution of AAS, leads to an additional redox couple to take into account in addition to  $\text{Fe}/\text{Fe}^{2+}$ . Moreover, several authors have identified a particular steel-concrete interface in AAS binders, where the traditional passive film based on iron oxides is partially replaced by an iron-sulfur complex (Criado et Provis 2018; Mundra, Criado, et al. 2017; Runci, Serdar, et Provis 2019; Zhang, Xi, et Yang 2021), whose influence on the initiation and propagation of corrosion remains still unclear and requires further investigation. This results in unusually electronegative corrosion potentials at the passive state and low polarisation resistances, as well as different anode polarization curves compared to PC, which could be misinterpreted as an indication of active corrosion at the rebar (Aperador Chaparro, Hernando Bautista Ruiz, et De Jesús Torres Gómez 2011; Criado et al. 2018; Criado et Provis 2018; Mundra, Bernal, et al. 2017), using the recommendations developed for PC without modification. Similarly, polarization measurements often give overestimated corrosion rates for AAS (due to the presence of sulphur in slag) according to recommendations of the RILEM Technical Committee 154-EMC (C. Andrade and Alonso 2004), while they are correlated with autopsies where no visual corrosion is detected (Criado et al. 2018). Establishing and validating corrosion testing methods suitable for AAS remains one of the major obstacle to their commercialization and their adoption in standards (Runci, Serdar, and Provis 2019).

The composition of the **SSC** binder is defined by the European standard EN 15743 (AFNOR 2010). Concerning the SSC, no information regarding the corrosion kinetics has been found in the literature, and more generally no electrochemical characterization, to the author's knowledge. The durability studies on SSC concretes highlight a strong resistance to chloride diffusion, thanks to a strong binding capacity of slag (Ismail, Bernal, Provis, Hamdan, et al. 2013; K. S. Nguyen et al. 2018), and also a high resistivity (Masoudi 2018) which is in line with the previous observations. Nevertheless, further studies are needed to characterize the corrosion kinetics in this binder. Finally, since SSC is a slag-based binder, many of the difficulties and questions raised in relation to the application and interpretation of the electrochemical tests for the AAS binder, also apply to SSC.

#### Conclusion of the introduction and interest of the article

In summary, on one hand complementary studies about the corrosion rates in LCK concrete are required, as the data available are limited and focus only on limestone filler replacement ranging from 0 to 35%. On the other hand, classical electrochemical measurements commonly used for PC have been identified as unsuitable for reporting the corrosion state of reinforcement in binders with high slag content (such as AAS and SSC), due to a more complex interpretation of the results (Criado et al. 2018; Mundra et al. 2023; Mundra, Bernal, et al. 2017), which justifies the proposal of an alternative method.

Therefore, the present study aims to overcome this gap by proposing an original approach, based on the evaluation of the corrosion rate of three low-carbon concretes of same strength class C25/30 in the case of chloride-induced corrosion, with galvanic current measurements associated to mass loss of the rebar. Galvanic coupling is a method that allows to measure the galvanic current ( $I_g$ ) flowing between an anode (active reinforced mortar) and a cathode (passive reinforced concrete) spatially separated. This direct technique is interesting because it gives a value of galvanic current which is not influenced by the binder type, as it does not require an externally applied current or voltage, but only records the current which is spontaneously exchanged due to corrosion reactions. The current measured is then compared to the mass loss of the rebar, which is also a direct and reliable measurement, proportional to the total currents to which the anode has been subjected. Moreover, the proposed set up enables to quantify the localized aspect of corrosion initiated by chlorides (from the previous mass loss and galvanic current) in addition to the galvanic contribution, which is not negligible at the structure level and which is not often considered by laboratory tests (Chalhoub, François, and Carcasses 2019). No data about corrosion kinetics due to chlorides from galvanic current measurements is available in the literature for these three low-carbon concretes, but this method has already been validated on PC-based binders (Chalhoub, François, and Carcasses 2019; Jiang et al. 2021; Lliso-Ferrando et al. 2022). The influence on the galvanic current of two chloride concentrations to contaminate the anodes,  $[\text{NaCl}] = 30 \text{ g/L}$  (sea water) and  $[\text{NaCl}] = 300 \text{ g/L}$  (de-icing salts), is studied. Finally, the results obtained from the galvanic current measurements are discussed in comparison with classical electrochemical techniques (OCP, resistivity and  $R_p$ ).

## Nomenclature

### ABBREVIATIONS

**AAS** alkali-activated slag  
**C/A** cathode to anode surface ratio  
**CE** counter electrode  
**GGBS** ground granulated blast furnace slag  
**LCK** low clinker content  
**LPR** linear polarization resistance  
**OCP** open circuit potential  
**PC** Portland cement  
**RE** reference electrode  
**SCI** steel/concrete interface  
**SSC** supersulfated cement  
**w/b** water to binder ratio  
**WE** working electrode  
**ZRA** zero resistance ammeter

### SYMBOLS

**B** constant from Stern-Geary relation, calculated from Tafel test [V]  
 **$\beta_a$**  anodic Tafel slope [V/dec]  
 **$\beta_c$**  cathodic Tafel slope [V/dec]  
 **$E_{\text{corr}}$**  corrosion potential [mV/ref]  
 **$i_g$**  apparent galvanic current density [ $\mu\text{A}/\text{cm}^2$ ]  
 **$I_g$**  galvanic current [ $\mu\text{A}$ ]  
 **$i_{\text{mi-anode}}$**  apparent local current density at anode scale, calculated [ $\mu\text{A}/\text{cm}^2$ ]  
 **$i_{\text{mi-Rp}}$**  apparent current density obtained by LPR measurement [ $\mu\text{A}/\text{cm}^2$ ]  
 **$i_{\text{mi-Tafel}}$**  apparent current density obtained by fitting the polarization curve from Tafel test with the Butler-Volmer equation [ $\mu\text{A}/\text{cm}^2$ ]  
 **$i_{\text{tot}}$**  total current density [ $\mu\text{A}/\text{cm}^2$ ]  
 **$I_{\text{tot}}$**  total current [ $\mu\text{A}$ ]  
 **$R_e$**  electrolyte resistance [ $\Omega$ ]  
 **$R_p$**  value of linear polarization resistance [ $\Omega.\text{cm}^2$ ]  
 **$\Delta E_{\text{A-C}}$**  potential difference between anode (A) and cathode (C) [mV]  
 **$\rho$**  resistivity [ $\Omega.\text{m}$ ]

## 2 Materials

### 2.1 Raw Materials

The chemical composition of raw materials used in low clinker content (LCK), alkali-activated slag (AAS) and supersulfated cement (SSC) concretes and mortars, determined by X-ray fluorescence (XRF), are given in Table 29. The Blaine specific surfaces of CEM I, GGBS and limestone filler are 3900, 5500 and 5490 cm<sup>2</sup>/g, respectively.

Table 29: Chemical composition of cements and slag (% in mass) used in LCK, AAS and SSC concretes and mortars, determined by XRF.

	Chemical composition (% in mass)								
	CaO	SiO <sub>2</sub>	Al <sub>2</sub> O <sub>3</sub>	MgO	Fe <sub>2</sub> O <sub>3</sub>	K <sub>2</sub> O	Na <sub>2</sub> O	SO <sub>3</sub>	TiO <sub>2</sub>
CEM I	64.7	20.4	3.9	0.8	5.0	0.6	0.1	2.8	0.2
CEM III/B	50.5	37.7	8.1	4.5	1.9	0.5	0.2	2.0	0.5
GGBS	42.9	37.7	10.3	6.5	0.3	0.4	0.2	1.6	0.7

For the concrete design, a semi-crushed alluvial mix of aggregates ranged from 0 to 20 mm for LCK and from 0 to 16 mm for AAS and SSC. As for the mortar design, a normalized sand CEN EN 196-1 (0-2 mm) was used for practical reasons.

### 2.2 Mix design

The three low-carbon concretes studied are designed to be C25/30 and also self-compacting (spread class SF1). Their respective compositions, as well as some properties at fresh and hardened state, are detailed in Table 30. The binder of the LCK is made with 27% CEM I and 73% limestone filler, while AAS and SSC are both slag-based binders activated either by sodium carbonate and quicklime or by anhydrite and CEM III/B, respectively. Water reducing agents are used to improve the workability at fresh state for all mixes. The three concretes studied are considered as « low-carbon » because they have a significant reduced carbon footprint (Table 30) compared to the one of a standard concrete made with CEM I of similar strength (C25/30) which is around 207 kg eq. CO<sub>2</sub>/m<sup>3</sup> (Article B). The compressive strengths given in Table 30 are obtained on cylindrical samples  $\Phi$ 110 mm x 220 mm for concrete and on 40 mm x 40 mm x 160 mm samples for mortar.

For the needs of the experimental campaign, to achieve low material cover, the concrete compositions presented above were adapted to the mortar scale, using the concrete equivalent mortar method (Schwartzentruber and Catherine 2000). As explained in this paper, “its principle is to design a mortar, deduced from the concrete composition and called concrete equivalent mortar”, for which the rheological properties are similar to those of concrete. It consists in keeping the specific surface of aggregates constant between the concrete and the mortar. In return, the quantity of paste is increased during the change of scale (Table 30), which is not an inconvenient in the context of this study because a chloride contamination will be performed on these mortar samples afterwards, which will allow the chlorides to reach the reinforcement faster. A normalized sand CEN EN 196-1 (0-2 mm) is used to make the mortar, instead of the same sand used for the concrete, for practical reasons. To take into account the

difference in water absorption between the aggregates, the water content of the mortar is corrected to keep the same  $w_{\text{eff}}/b$  ratio as the concrete (Table 30). Finally, validation tests were carried out to evaluate and compare the characteristics of the mortar with those of the initial concrete. Its compressive strength and water porosity after 28 days of curing, were measured and compared to those of the concrete (Table 30). The results revealed higher compressive strengths (except for SSC) and a higher water porosity on mortar samples, due to a higher paste volume and the different type of aggregates.

Table 30: Composition and characteristics at fresh and hardened state of LCK, AAS and SSC concretes and mortars.

	<b>Concrete</b>			<b>Mortar</b>		
	<b>LCK</b>	<b>AAS</b>	<b>SSC</b>	<b>LCK</b>	<b>AAS</b>	<b>SSC</b>
<b>Composition (kg)</b>						
<i>CEM I</i>	136.8			162.3		
<i>Limestone filler</i>	375.0		49.1	445.0		58.7
<i>GGBS</i>		481.7	329.3		560.7	393.9
<i>Na<sub>2</sub>CO<sub>3</sub></i>		20.3			23.6	
<i>Quicklime</i>		5.1			5.9	
<i>Anhydrite</i>			29.6			35.4
<i>CEM III/B</i>			11.1			13.3
<i>Water reducing agent</i>	6.02	11.15	5.1	7.1	13.0	6.1
<i>Normalized sand (0-2 mm)</i>				1520.4	1269.6	1407.8
<i>Sand (0-5 mm)</i>	678.5	686.5	739.7			
<i>Fine aggregates (5-10 mm)</i>	272.1	609.6	656.9			
<i>Coarse aggregates (&gt; 10 mm)</i>	827.1	229.6	247.4			
<i>Total water</i>	130.0	220.0	210.0	194.1	288.8	280.9
<b>Mixture parameters</b>						
<i>w/b ratio</i>	0.25	0.43	0.50	0.23	0.41	0.47
<i>w<sub>eff</sub>/b ratio</i>	0.22	0.40	0.46	0.22	0.40	0.46
<i>Theoretical specific gravity (kg/m<sup>3</sup>)</i>	2425.5	2263.8	2278.2	2336.1	2174.7	2202.2
<i>Paste volume (L/m<sup>3</sup>)</i>	318	407	360	417	506	461
<i>CO<sub>2</sub> footprint (eq. CO<sub>2</sub>/m<sup>3</sup>)</i>	122	104	50			
<b>Characteristics at fresh and hardened state</b>						
<i>Inversed cone flow rate (rheology) (seconds)</i>	9.7	1.7	2.0			
<i>Cone spread (mm)</i>	525	580	490			
<i>Air content (%)</i>	1.3	1.2	1.8			
<i>28 days compressive strength (MPa)</i>	33.0	33.3	32.0	44.2	34.3	22.6
<i>28 days water porosity (%)</i>	10.6	16.2	16.4	12.5	20.4	18.9

## 2.3 Specimen characteristics and preparation: anode and cathode

### 2.3.1 Geometry

Two types of samples are used for this experiment: anodes (reinforced mortar) and cathodes (reinforced concrete). The dimensions and geometries of each are presented in Figure 46. The anode is made of mortar to have a small sample size. The small cover (8.5 mm) allows to reduce the arrival time of chlorides to the rebar, while the small size rebar compared to the cathode (ratio of 55) allows to maximize the exchanged current values (Revert et al. 2019; Chalhoub, François, and Carcasses 2019; Andrade et al. 1992).

### 2.3.2 Preparation of steel rebars

Rebars (ribbed carbon steel) are selected without initial corrosion spots and used “as received”, with the mill scale. Deliberately no cleaning treatment is performed to eliminate the defects of the steel or to have a uniform steel surface, to stay representative of real conditions. Then, rebars are cut with a band saw, at the lengths specified in Figure 41, and one extremity is drilled with a drill machine, at 15 mm depth.

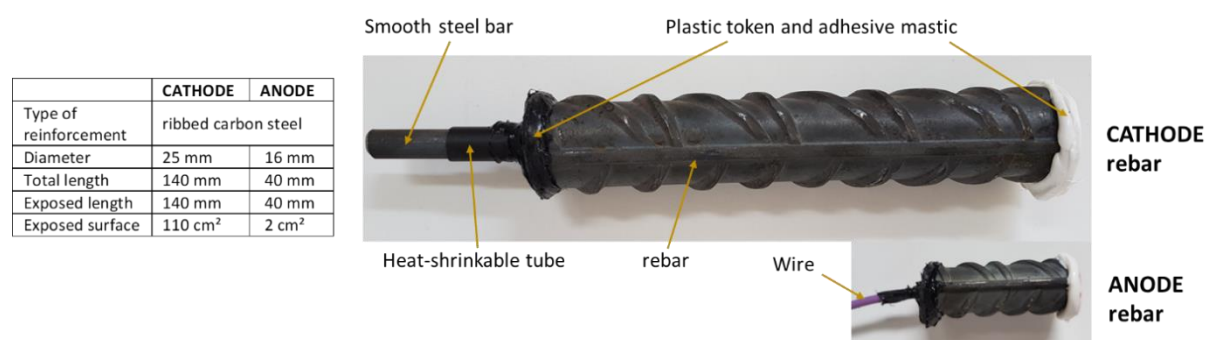


Figure 41: Rebar dimensions and preparation for cathode and anode samples.

The rebar is then cleaned with compressed air and precisely weighed (as initial mass). For cathode samples, a smooth steel bar of 8 mm diameter and 65 mm length (same steel as the rebar to avoid the creation of a galvanic current) is mechanically slotted into the previous drilled extremity of the rebar with a hammer. If needed, the smooth steel bar can be slightly sanded to fit easily with the hole. A good electrical contact between the two pieces of steel is checked with a multimeter. The purpose of this mechanical connection is to avoid the use of welding: on one hand the tin used for the welding could generate a galvanic current with the rebar and on the other hand it is difficult to remove, which make it unsuitable to make a precise measurement of the loss of mass (section 3.4.1). The smooth steel bar is then covered with a heat-shrinkable tube to avoid polarization that will be applied on the rebar during the electrochemical tests.

The same steps are performed for the anodes, but with an electric wire instead of the smooth steel bar (no need of heat-shrinkable tube as the electrical wire is already protected). Therefore, the steel surfaces in contact with concrete are respectively 110 cm<sup>2</sup> for the cathode and 2 cm<sup>2</sup> for the anode. Finally, to insulate the cut surfaces of the rebar, a plastic token is stuck on each extremity with a polymer adhesive mastic (Bostik MSP 107) and let dry 24h (Figure 41). The

goal is to avoid crevice corrosion or galvanic current that could appear between the cut surface and the side surface of the steel ribbed bar because of their different surface condition.

### 2.3.3 Casting and curing

For **cathodes**, concrete samples are cast in a cylindrical cardboard mold ( $\text{Ø}110 \times 220 \text{ mm}$ ) with a cover of 42.5 mm. A polyacetal disc ( $\text{Ø}110 \times 20 \text{ mm}$ ) drilled in its center  $\text{Ø} 8.4 \text{ mm}$ , is placed in the bottom of the mold and used to center the rebar by inserting the smooth steel bar in its hole (Figure 42 and Figure 43). Then, the mold is filled in 3 layers of concrete, each of them being vibrated approximately 30 s holding the rebar by hand. After casting, the surface of concrete specimen is covered with a plastic cover to avoid evaporation. The different steps of preparation for the cathodes are summarized on Figure 42.

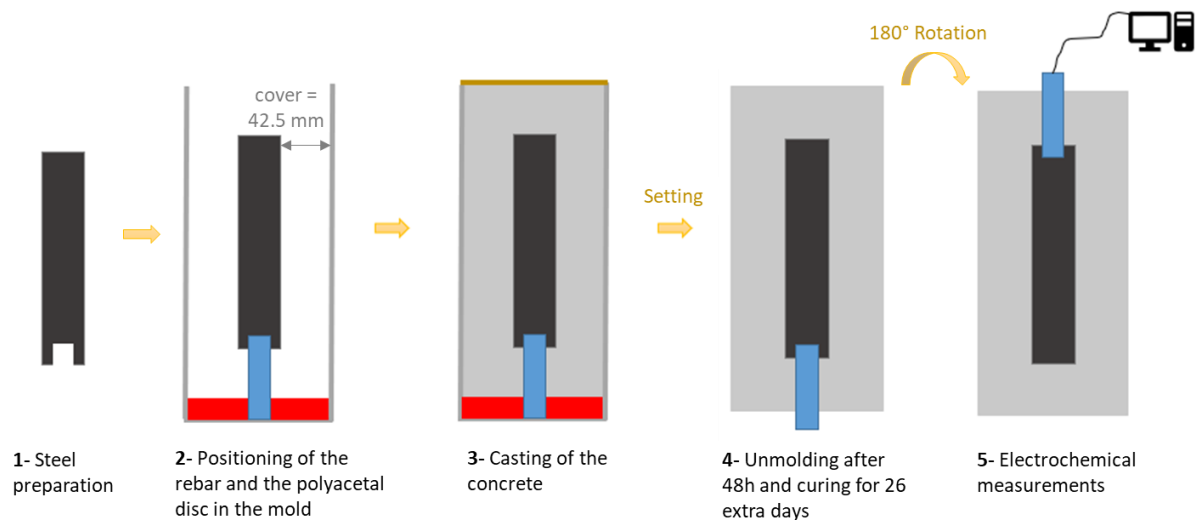


Figure 42: Steps for cathodes preparation.

For **anodes**, mortar samples are cast in a cylindrical plastic mold ( $\text{Ø}33 \times 70 \text{ mm}$ ) with a cover of 8.5 mm. This time, a hole is made in the mold cover, allowing the wire to be adjusted to the desired position to center the rebar. Finally, the specimens (concrete and mortar) are placed in a wet curing room at  $20 \text{ °C}$ , with a relative humidity of approximately 95%, unmolded after 48h and cured for 26 days more in the same room. During the curing period, the top and bottom surface of the anode are covered with adhesive mastic to ensure a unidirectional penetration of the chlorides later on (Figure 43).

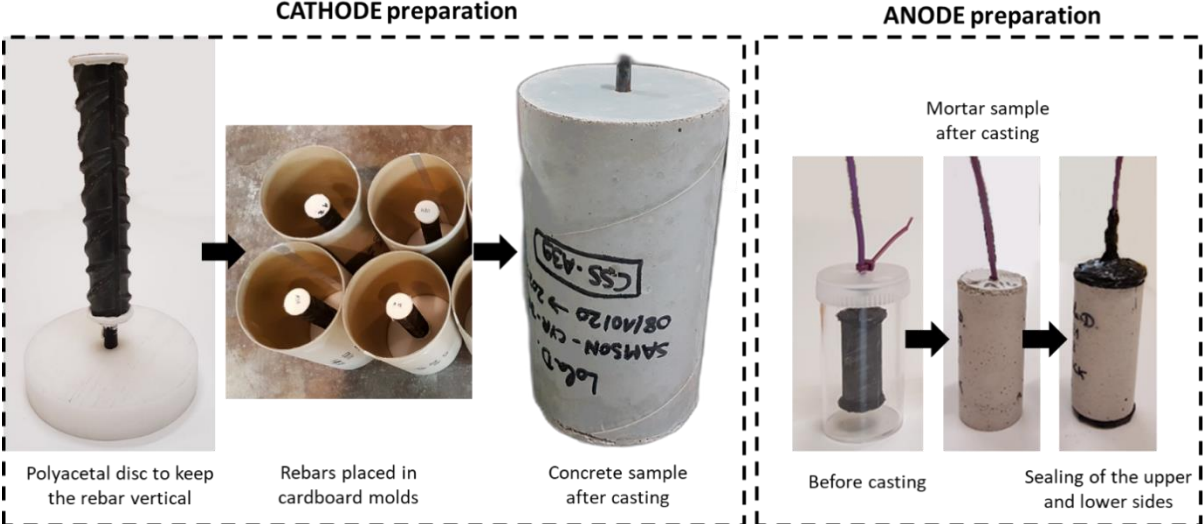


Figure 43: Focus on some main preparation steps for anode and cathode.



### 3 Test methods

#### 3.1 Overview of the experimental campaign

The galvanic current measurement is performed between a cathode (reinforced concrete) and an anode (reinforced mortar) of same formulation. Different preparation steps are performed in parallel on anodes and cathodes, as illustrated in Figure 44. The middle boxes summarize the tests performed and the blank ones correspond to the results presented in this paper. The experimental protocol used in this study is inspired by the literature (Chalhoub, François, and Carcasses 2019; Revert et al. 2019).

The cathodes and anodes are cast and cured for 28 days, before being characterized at passive state by classic electrochemical tests presented in section 3.2. The anodes are then dried at 50 °C until a constant mass is reached (about 15 days) and immersed in a 30g/L or 300g/L NaCl solution until the chlorides have reached the rebar (about 11 days). The aim of the drying step is to accelerate the penetration of the chlorides into the sample. A check is made with silver nitrate on additional samples, frequently split, to verify that the chlorides have reached the rebar. The corrosion potential  $E_{\text{corr}}$  is also monitored to ensure that it is stabilized after the drop due to chloride contamination. One anode not contaminated by chlorides (0 g/L) by formula, is also conserved as reference. After that, the active anodes are again characterized to follow the evolution of the electrochemical parameters (corrosion potential  $E_{\text{corr}}$ , resistivity  $\rho$ , value of linear polarisation resistance  $R_p$ , apparent current density  $i_{\text{mi-Rp}}$ ).

Finally, galvanic coupling is performed by coupling a passive cathode with an active anode, spatially separated, as explained in section 3.3. Since the active steel of the anode has a different corrosion potential  $E_{\text{corr}}$  than the passive steel of the cathode, it generates a galvanic current  $I_g$  between the two, which is recorded for 90 days using a potentiostat.

At the end of the coupling, after a last electrochemical characterization on anode samples ( $E_{\text{corr}}$ ,  $\rho$ ,  $R_p$ ,  $i_{\text{mi-Rp}}$ ), they are split to visually observe the presence of corrosion, and then the corrosion products are quantified by a mass loss measurement (section 3.4.1) following ASTM G01-03 (ASTM International 2012). The mass loss obtained is used to calculate the associated total current  $I_{\text{tot}}$  using Faraday's law (section 3.4.2). Finally, the mortar is recovered to quantify the chloride concentration at the steel-concrete interface (section 3.4.3).

#### 3.2 Classic electrochemical measurements

##### 3.2.1 Linear polarisation resistance

To measure the classical electrochemical properties of passive and active steel, polarization tests were performed on cathode and anode samples. The linear polarisation resistance (LPR) measurement summarized in Figure 45, allows to obtain different parameters: the resistivity  $\rho$  and the polarization resistance  $R_p$ , and to estimate the apparent current density  $i_{\text{mi-Rp}}$ . The measurement is performed using a BioLogic SP-50 potentiostat and a three-electrode set-up with the reinforcement as working electrode (WE), a reference electrode (RE) Ag/AgCl and a titanium mesh as counter electrode (CE). The reinforced sample is partly immersed in a NaOH solution (at pH = 12.5) to avoid leaching of alkalis.

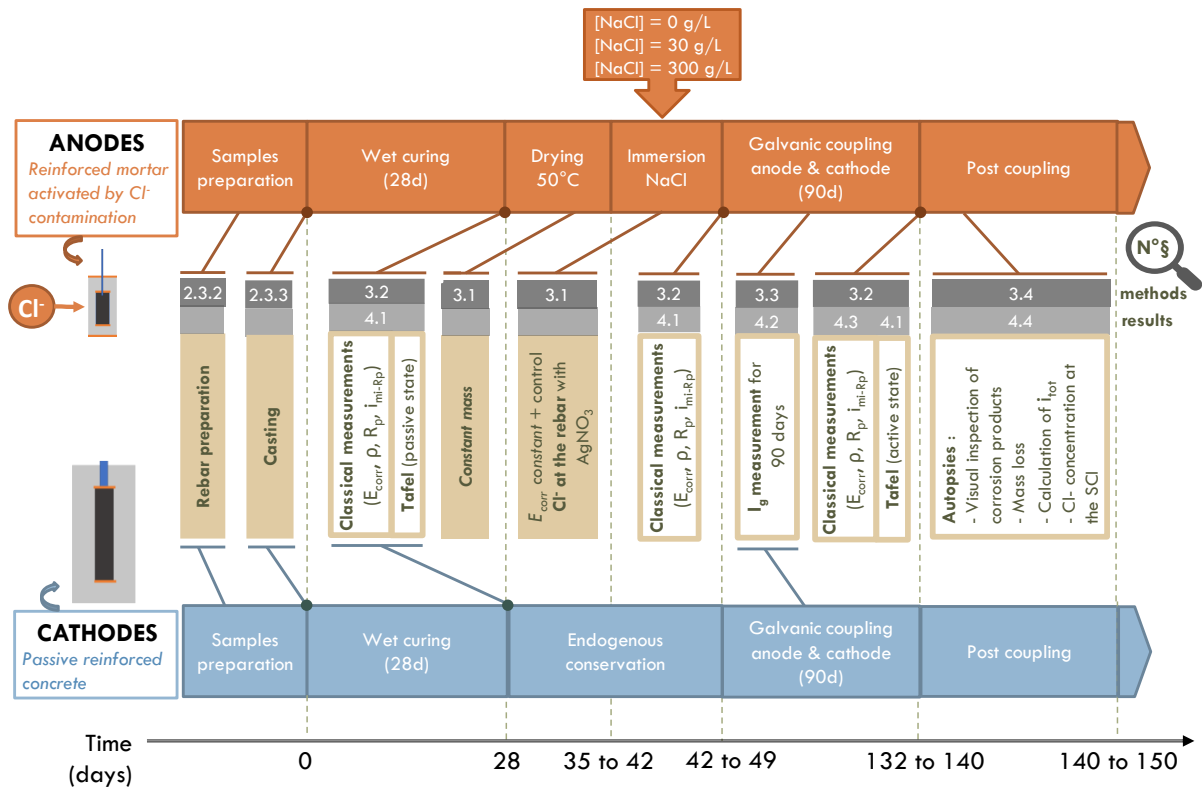


Figure 44: Overview of the experimental campaign associated with the classical measurements and the galvanic current measurement. The blank boxes correspond to the measurements presented in this article. In grey, the paragraph number of the article (methods and results), to which each step refers.

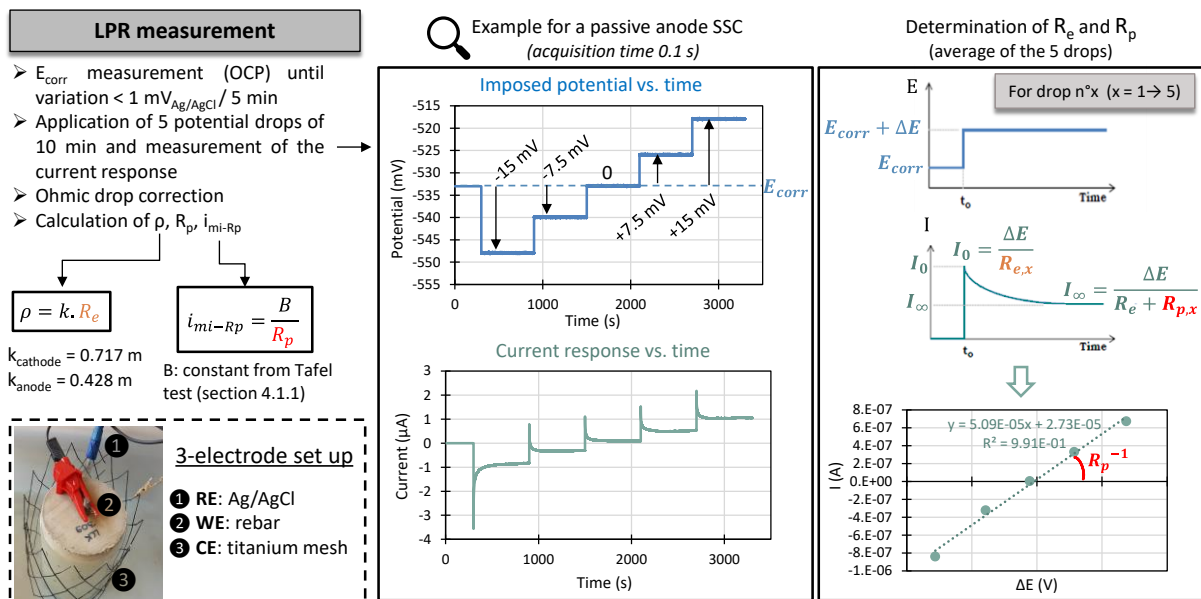


Figure 45: Details of LPR test to obtain the following parameters  $E_{corr}$ ,  $\rho$ ,  $R_p$ ,  $i_{mi-Rp}$ .

The LPR technique is based on the one described in (Laurens et al. 2016) with some adaptations. First, the corrosion potential  $E_{\text{corr}}$ , also frequently called open circuit potential (OCP) in other studies (Mundra et al. 2023), is recorded and the LPR test is run only when a stable value is measured (variation  $< \pm 1$  mV/5 min).

Then, the protocol consists in applying five successive potential drops of -15, -7.5, 0, +7.5 and +15 mV, chosen to generate a reversible polarization within a range of  $\pm 15$  mV, with respect to the OCP (Figure 45). Each potential drop lasts 600 s (duration chosen to reach a steady current response) and the data are acquired with a sample period of 0.1 s.

For each potential drop, a current response composed by an instantaneous part and an asymptotic part, is recorded (Figure 45 - right). Based on Ohm law, the instantaneous response for each step enables to determine the electrolyte resistance  $R_e$  that can be converted into resistivity  $\rho$  by multiplying it by a geometric factor  $k$  obtained from a numerical model on the COMSOL Multiphysics® finite elements software ( $k = 0.717$  m for cathodes and  $k = 0.428$  m for anodes) (Chalhoub 2020).

The asymptotic response quantified the polarization behavior of the steel by the polarization resistance  $R_p$  parameter. As the reference electrode is located at the concrete surface, an ohmic drop correction between WE and RE is applied using Ohm law, to take into account the concrete resistance (Laurens et al. 2016). For that, at each potentiostatic step  $\Delta E$  ( $n^{\circ}x$ ) applied, the concrete/mortar resistance  $R_{e,x}$  needs to be determined from the instantaneous part of the current response  $I_0$  (Equation (17)).  $R_e$  being the average of the five different  $R_{e,x}$  (for drop  $n^{\circ}x$ ,  $x = 1 \rightarrow 5$ ).

$$R_{e,x} = \frac{\Delta E}{I_0} \quad (17)$$

Then, based on Ohm law, the potential response of steel can be deduced subtracting at each step of the protocol the concrete/mortar resistance multiplied by the value of the asymptotic current to the potential value at the concrete surface.

Finally, the apparent current density  $i_{mi-Rp}$  (in  $\mu\text{A}/\text{cm}^2$ ), can be deduced by the Stern-Geary equation (Equation (18)).

$$i_{mi-Rp} = \frac{B}{R_p} \quad (18)$$

Where  $i_{mi-Rp}$  ( $\mu\text{A}/\text{cm}^2$ ) is the apparent current density,  $R_p$  is the value of linear polarisation resistance ( $\Omega.\text{cm}^2$ ) and  $B$  (V) is a constant determined by a Tafel test (section 3.2.2).

In this context (localized corrosion due to chlorides) the equation of Stern-Geary is normally not applicable (applicable only for uniform corrosion), that is why apparent current densities are presented in the rest of the study. The current density is called apparent, because the surface considered in active state is that of the rebar whereas the latter is not uniformly active in reality (localized corrosion spots).

### 3.2.2 Tafel

A Tafel test was performed on 28 days aged anodes after wet curing (passive state) and on anodes after 90 days of galvanic coupling (active state), after waiting for their complete depolarization. This is an intrusive test because the strong polarization of the rebar moves it away from its equilibrium potential ( $E_{corr}$ ) in an irreversible way, and therefore the samples used are removed from the experimental campaign afterwards.

The test is performed here by polarizing the rebar first cathodically and then anodically, by successive potential steps, until reaching  $\pm 333$  mV with respect to OCP (details in Figure 61 in supplementary data). Each step lasts 1800 s, except for both steps at  $\pm 333$  mV that last 2700 s. This is the same method as for the LPR measurement, for which the test principle is described in (Laurens et al. 2016), but for a larger polarization range in order to obtain the full polarization curve of the rebar. Finally, a correction of the ohmic drop is performed.

The advantage of this method compared to a constant scan rate is that for high levels of polarization the stabilization time of the current response can be long. The polarization from OCP to the anodic branch then back to OCP (same thing for the cathodic branch), allows to approximate the value of the stabilized current for each step, by averaging the ascendant asymptotic response with the descendant one, as illustrated in Figure 19 in (Laurens et al. 2016).

Finally, the Tafel test allows to obtain different electrochemical parameters ( $\beta_a$ ,  $\beta_c$ ,  $i_{mi-Tafel}$ ) by fitting the curve obtained with the equation of the Butler-Volmer model (Equation (19)).

$$i = i_{mi-Tafel} \left( \exp \left( \ln(10) \frac{E - E_{corr}}{\beta_a} \right) - \exp \left( \ln(10) \frac{E - E_{corr}}{\beta_c} \right) \right) \quad (19)$$

Where  $E_{corr}$  is the OCP ( $V_{ref}$ ) of the uniform corrosion system at equilibrium,  $i$  is the net current density ( $A/m^2$ ) flowing through the metal-electrolyte interface of the uniform system forced at potential  $E$  (involving a polarization with respect to the equilibrium potential  $E_{corr}$ ),  $i_{mi-Tafel}$  is the corrosion current density ( $A/m^2$ ), corresponding to the exchange current density of the uniform corrosion system,  $\beta_a$  and  $\beta_c$  are anodic and cathodic Tafel slopes (V/dec) of the electrochemical system, respectively.

The constant  $B$ , used in the Stern-Geary equation (Equation (18)) is calculated according to Equation (20), from anodic and cathodic Tafel slopes  $\beta_a$  and  $\beta_c$ .

$$B = \frac{\beta_a \cdot \beta_c}{\ln(10)(\beta_a + \beta_c)} \quad (20)$$

### 3.3 Galvanic current measurement

A galvanic coupling is performed for 90 days by connecting a passive cathode and an active anode (contaminated by NaCl = [30 g/L] or [300 g/L]) spatially separated, as shown in Figure 46. A coupling with a passive anode is also performed (NaCl = [0 g/L]) to verify that the associated galvanic current  $I_g$  is negligible. The fact that the anode and cathode are spatially separated allows to not only focus on the corrosion kinetics at the local scale of the anode, but also to quantify the current exchanged at a larger scale, as is the case in a real structure where a localized part of the reinforcement network is activated and is coupled to the rest of the passive steel. The test is done in a NaOH solution at pH = 12.5, to get closer to the pore solution of the

studied concretes and to limit the leaching of alkalis. To avoid carbonation of the solution, the test is carried out in a sealed tank.

The galvanic current  $I_g$  exchanged between anode and cathode is recorded over time (90 days) using the ZRA mode of a BioLogic SP-50 potentiostat. It consists in applying zero volt between both samples and then measuring the current  $I_g$  and the potential  $E_{\text{corr}}$  versus the RE. An example of a galvanic current  $I_g$  versus time curve that is recorded is presented on Figure 46. There is first a transient behaviour and then quickly a stabilization of the galvanic current  $I_g$ . The coupling is maintained for 90 days to maximize the mass loss on the rebar (and thus the accuracy of the measurement), as presented in the next section 3.4.1. Finally, the galvanic current values shown are obtained by doing the integral under the curve, divided by the total duration.

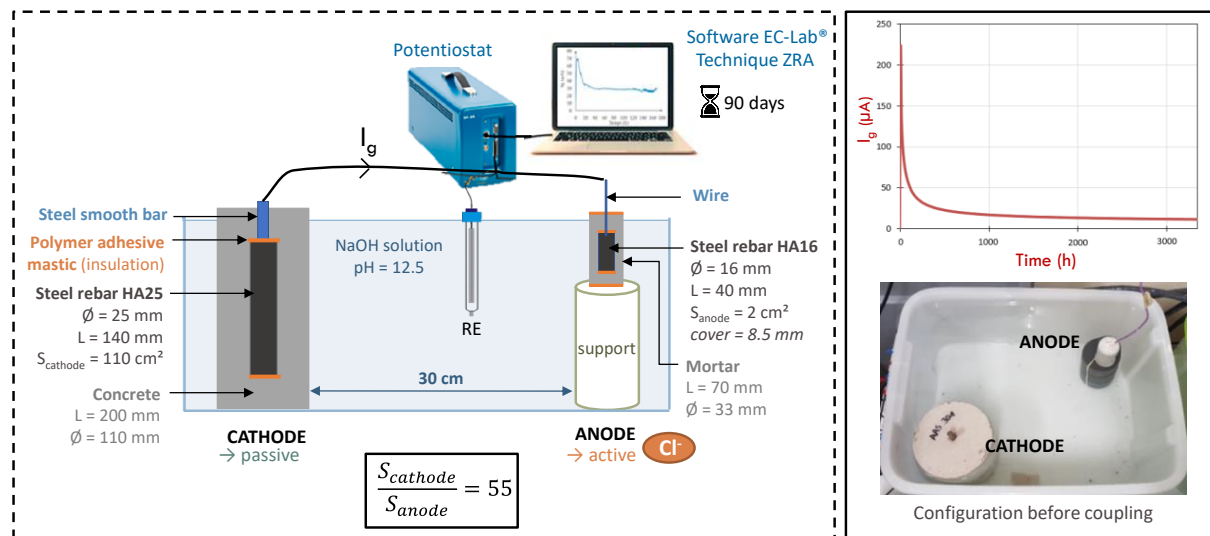


Figure 46: Detail of the set up used for the galvanic current ( $I_g$ ) measurement, inspired from (Chalhoub, François, and Carcasses 2019).

### 3.4 Autopsy of the anodes

#### 3.4.1 Mass loss

At the end of the coupling, the anodes are split in order to visually observe the presence of corrosion, then the corrosion products are quantified by a mass loss measurement following the ASTM G01-03 standard (ASTM International 2012). It is also important to visually control that there is no crevice corrosion on the extremities of the rebar that were insulated, to avoid distortion of the results. When it is the case (for some LCK anodes), the concerned samples and results are discarded.

The cleaning method consists of immersing the rebar in the cleaning solution (500 ml hydrochloric acid + 3.5 g hexamethylene tetramine + 500 ml distilled water), then brushing and weighing it. The cleaning cycles last 10 min and are repeated 4 to 6 times depending on the amount of corrosion products observed. The difference between the initial mass of steel (measured during the preparation of the steel) and the mass after cleaning, corresponds to the loss of mass which is associated to the amount of corrosion products.

Finally, it must be taken into account that rebars before casting are often covered with a layer of mill scale. The ideal cleaning procedure should remove only the corrosion products, but in reality it also removes the mill scale and even a small amount of metal. In order to quantify this part, three uncorroded control rebars ( $\text{Ø}16 \times 40 \text{ mm}$ ) were cleaned using the same procedure. The metal loss resulting from the cleaning (about 0.08% of the original mass of the rebar) can then be used to correct the mass loss on corroded rebars. In the rest of the paper, when there is no specification, the mass loss values presented have been corrected (mass loss due to the cleaning procedure and mill scale subtracted) and therefore correspond to corrosion products only.

### 3.4.2 Calculation of $I_{tot}$ from the mass loss

At the end of the galvanic coupling, the autopsy of the anodes allows to quantify the mass loss of each anode rebar, which corresponds to the quantity of corrosion products formed, as presented in the previous section (3.4.1). This mass loss  $m$  is proportional to the total current  $I_{tot}$  flowing through the steel concrete interface (SCI) during the coupling and these two variables are related to each other by Faraday's law (Equation (21)).

$$m = \frac{A \cdot I_{tot} \cdot t}{n \cdot F} \quad (21)$$

Where  $m$  is the mass loss (g),  $A$  is the molar mass of iron (55.84 g/mol),  $I_{tot}$  is the corrosion current (A),  $t$  is the duration of the coupling (s),  $n$  is the number of valence electrons (2 for Fe) and  $F$  is the Faraday's constant (96485 C/mol).

$I_{tot}$  can then be deduced from the known mass loss  $m$ , following Equation (21).  $I_{tot}$  being the sum of the galvanic current  $I_g$  flowing between the anode and the cathode and measured during the test and of local current  $I_{mi-anode}$  flowing at the anode scale (Equation (22)) as illustrated on Figure 47.

$$I_{tot} = I_g + I_{mi-anode} \quad (22)$$

$I_{mi-anode}$  is itself the sum of a local galvanic current flowing between the active and passive zones of the anode (called  $I_a$ ) and of a localized microcell current at the corrosion spot (called  $I_{mic}$ ), as illustrated on Figure 47. However, the repartition between  $I_a$  and  $I_{mic}$  cannot be determined.  $I_{mi-anode}$  can then be deduced from the known currents  $I_{tot}$  (determined using Equation (22)) and  $I_g$ .

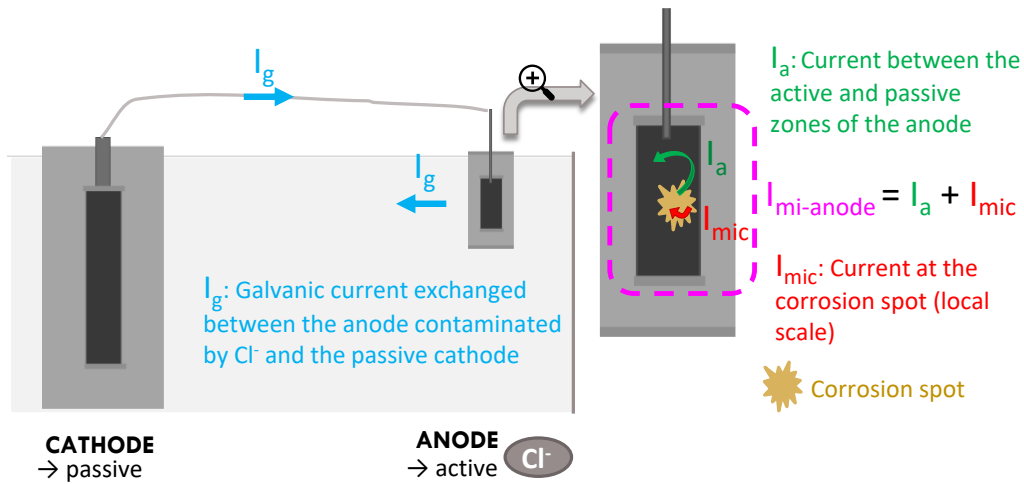


Figure 47: Details of the measurement and calculation of  $I_{\text{tot}}$  components.

### 3.4.3 Chloride concentration at the steel/concrete interface (SCI)

At the end of the autopsy, the mortar, previously split in half, is recovered and dry-sawn to keep only the 5 mm thickness around the rebar (Figure 48). The mortar is then crushed and sieved to 350  $\mu\text{m}$  for chemical analysis by precipitation with a silver nitrate solution. Total chloride contents per mass of mortar (as well as free chloride for LCK) are then determined following NF EN 14629 standard (AFNOR 2007) and the procedure recommended by GranDuBé (Hornain 2007) respectively, to relate the chloride level to the experimental corrosion current densities.

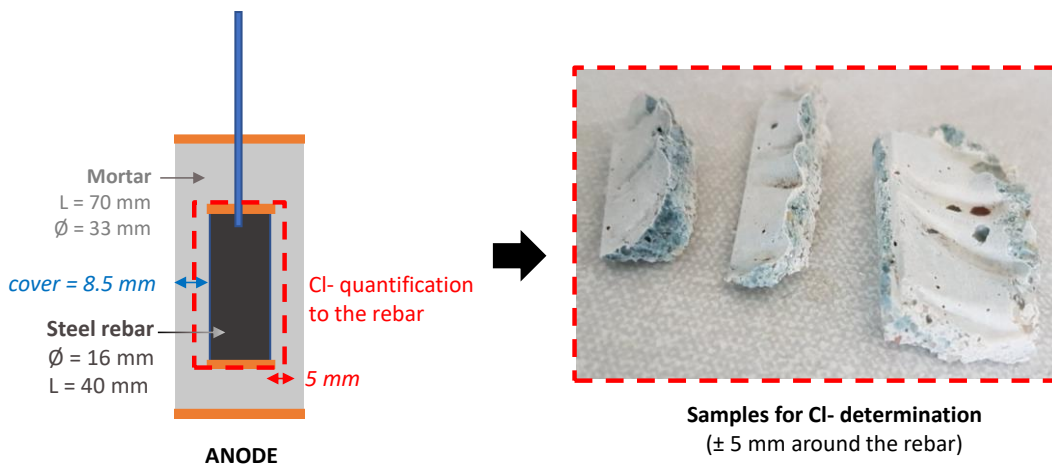


Figure 48: Determination of chloride content per mass of mortar at the SCI.

## 4 Results

The results are deliberately presented in a rather succinct manner and will be analysed more in details in the discussion section.

### 4.1 Classic electrochemical measurement

#### 4.1.1 Tafel curves

Each Tafel curve was performed on 2 to 3 samples per binder in order to ensure repeatability, except on one sample for active anodes contaminated at 300 g/L. Note that no Tafel test was performed on SSC anodes contaminated at 300g/L. Figure 49 shows the fitting curves obtained on the cathodes at passive state (after 28 days of cure), and also on active anodes contaminated by chlorides (after 90 days of galvanic coupling). All the replicates are not plotted for reasons of readability of the Figure. Similarly, passive anodes after 28 days of cure are not represented for reasons of readability.

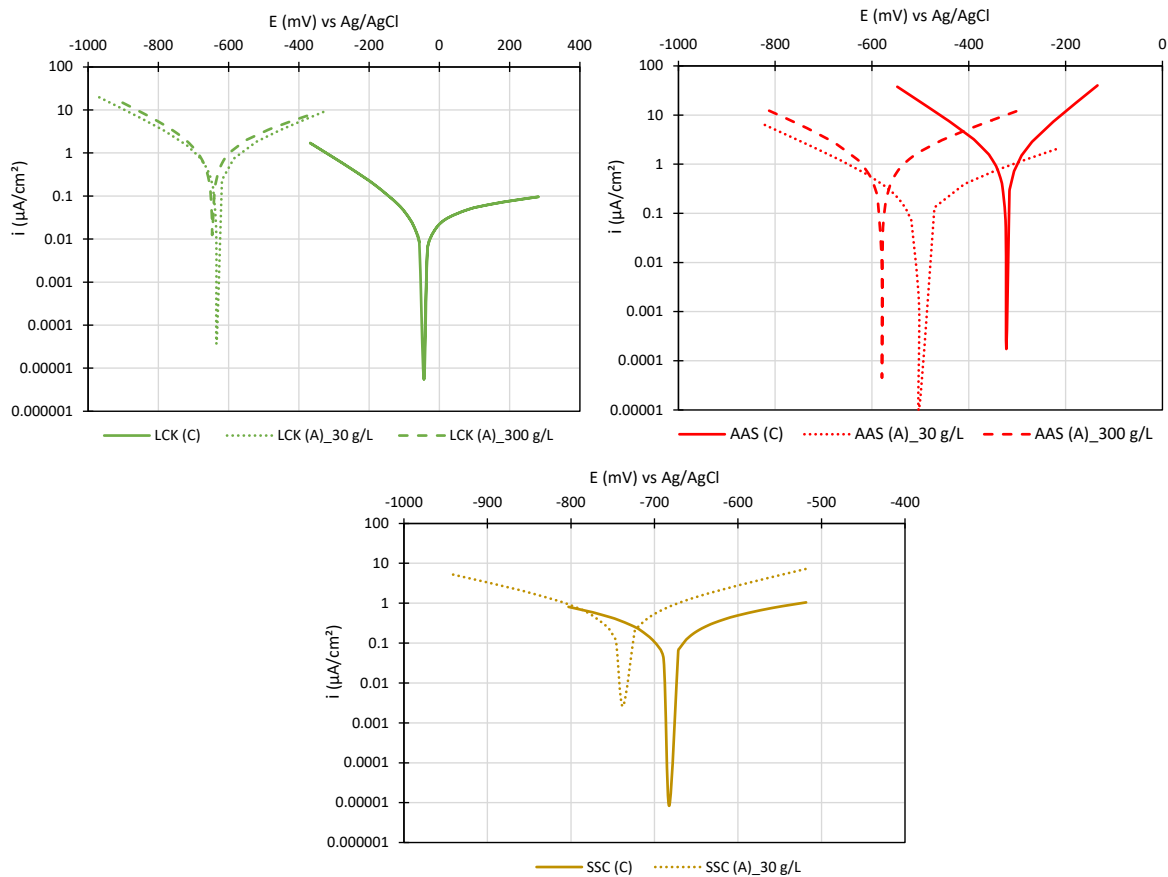


Figure 49: Tafel curves (fitting) obtained on passive cathodes after 28 days of cure (solid lines) and on active anodes after galvanic coupling, contaminated at 30 g/L (dotted lines) or at 300 g/L (dashed lines).

The values of the electrochemical parameters ( $\beta_a$ ,  $\beta_c$  and  $i_{mi-Tafel}$ ) obtained by fitting the Butler-Volmer equation (Equation (19)) to the experimental curves are summarized in Table 31 (average of the 2 or 3 samples each time, except 1 sample at 300 g/L). It should be noted that the values obtained on the cathode scale (concrete) cannot be directly compared to those



obtained on the anode scale (mortar), because the materials are different (mortar/concrete). The SCI will also be different between the two samples and it is therefore normal to find values that vary between passive anodes and cathodes.

$\beta_a$ , which is the anodic Tafel slope of the electrochemical system, expressing the oxidation of iron (and/or sulphur for slag-based binders, as explained in 4.1.2), is supposed to decrease with chloride contamination, as illustrated in (Chalhoub et al. 2020) (their Figures 2 and 17), which is confirmed by the values presented in Table 31 for the anodes of each binder.

$\beta_c$ , which is the cathodic Tafel slope of the electrochemical system, expressing the reduction reaction of oxygen, vary slightly with chloride contamination, while remaining in the same order of magnitude.

The apparent current density  $i_{mi-Tafel}$ , logically increases with the chloride contamination for the LCK samples, as this binder has a traditional behaviour similar to PC-based binders. This trend was not verified for slag-based samples (AAS and SSC), as explained in the next section 4.1.2.

The same observation applies for the corrosion potential  $E_{corr}$ , which strongly decreases due to chloride contamination for LCK, contrary to slag-based binders (Figure 49).

The Tafel test therefore seems less suitable for slag-based samples (small or no increase in  $i_{mi-Tafel}$  and small drop in  $E_{corr}$  with chloride contamination). These different behaviours between PC and slag-based binders are discussed more in details in the next section 4.1.2.

In the rest of the paper, the values of the **constant B** presented in Table 31 are used in the Stern-Geary equation to calculate  $i_{mi-Rp}$  (Equation (18)). As no Tafel test was performed on SSC anodes contaminated at 300 g/L, the value of B for this condition is taken equal to the one obtained at 30 g/L ( $B = 52$  mV). A significant scatter in this parameter is observed, which is not surprising because the test carried out gives information on the electrochemical state of the rebars at a given moment, whereas in reality the continuous electrochemical reactions which take place at the SCI induce a transient behaviour with variations over time (Angst et al. 2022). Commonly values of B used for PC-based materials in the literature are 52 mV for the passive state and 26 mV for the active state (C. Andrade and Alonso 1996; C. Andrade and González 1978), while the values presented in Table 31 are quite different as they are obtained on low-carbon concretes with specific binders. Similar values of B were measured on AAS-based mortars activated by chlorides ( $\approx 54$  mV) by (Runci, Provis, and Serdar 2023), but are different at passive state ( $\approx 25$  mV). Many parameters are likely to influence the values of Tafel slopes and B constant, such as the composition of the pore solution, pH, chloride concentration, relative humidity and availability in oxygen (Runci, Provis, and Serdar 2023).

Table 31: Anodic and cathodic Tafel slopes  $\beta_a$  and  $\beta_c$ , as well as apparent current density  $i_{mi-Tafel}$  obtained by fitting the polarization curve from Tafel test with the Butler-Volmer equation, for passive or active cathodes (C) and anodes (A). Values of constant  $B$  used in Stern-Geary relation, calculated from Equation (18), and associated to Tafel slopes  $\beta_a$  and  $\beta_c$ .

		Passive C	Passive A	Active A (30 g/L)	Active A (300 g/L)
LCK	$\beta_a$ (V/dec)	0.627	0.715	0.305	0.381
	$\beta_c$ (V/dec)	0.175	0.162	0.25	0.253
	$i_{mi-Tafel}$ ( $\mu\text{A}/\text{cm}^2$ )	0.03	0.17	0.91	1.46
	<b>B (mV)</b>	<b><math>58 \pm 20</math></b>	<b><math>57 \pm 5</math></b>	<b><math>61 \pm 1</math></b>	<b>66</b>
AAS	$\beta_a$ (V/dec)	0.34	0.669	0.411	0.284
	$\beta_c$ (V/dec)	0.219	0.197	0.244	0.235
	$i_{mi-Tafel}$ ( $\mu\text{A}/\text{cm}^2$ )	1.88	1.25	0.43	1.27
	<b>B (mV)</b>	<b><math>53 \pm 29</math></b>	<b><math>65 \pm 10</math></b>	<b><math>66 \pm 30</math></b>	<b>56</b>
SSC	$\beta_a$ (V/dec)	0.347	0.881	0.208	
	$\beta_c$ (V/dec)	0.341	0.369	0.288	
	$i_{mi-Tafel}$ ( $\mu\text{A}/\text{cm}^2$ )	0.42	5.61	0.87	
	<b>B (mV)</b>	<b><math>74 \pm 3</math></b>	<b><math>113 \pm 23</math></b>	<b><math>52 \pm 8</math></b>	

#### 4.1.2 Electrical resistivity ( $\rho$ ), corrosion potential ( $E_{corr}$ ), polarisation resistance ( $R_p$ ) and apparent current density ( $i_{mi-Rp}$ )

Figure 50 shows the evolution of different electrochemical parameters measured on the anodes before and after chloride contamination. Each value is an average realized on 7 to 13 samples at 0 g/L, 4 to 9 samples at 30 g/L and 2 to 3 samples at 300 g/L. For the interpretation of  $E_{corr}$  or  $i_{mi-Rp}$ , the values are associated respectively to a corrosion risk (with a probability  $P$ ) following ASTM C-876 (ASTM International 2022) or a corrosion level according to TC RILEM 154 recommendations (C. Andrade and Alonso 2004).

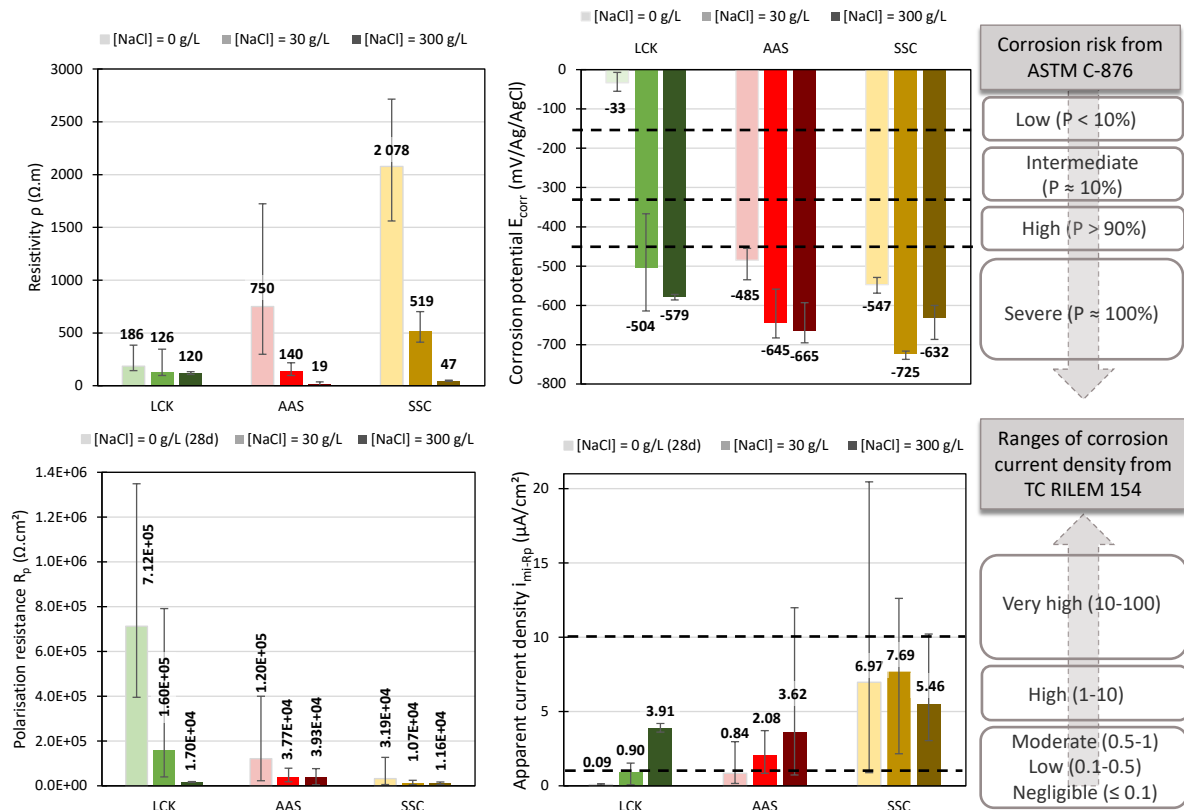


Figure 50: Classical electrochemical parameters ( $\rho$ ,  $E_{corr}$ ,  $R_p$  and  $i_{mi-Rp}$ ) measured on the anodes before and after chloride contamination (0 g/L, 30 g/L or 300 g/L, respectively from lightest to darkest on the histograms), in green for LCK, red for AAS and yellow for SSC.

### Results without chloride contamination

Before contamination (i.e. after 28 days of curing), the three binders have different initial parameters related to their composition.

A high resistivity  $\rho$ , as for SSC (2078  $\Omega \cdot m$  before chloride contamination), is a sign of a strong resistance to the passage of current and chlorides (Azarsa and Gupta 2017; Hornbostel, Larsen, and Geiker 2013) and come from a very low ionic concentration in its pore fluid solution (Article A), contrary to AAS (750  $\Omega \cdot m$ ) and LCK (186  $\Omega \cdot m$ ).

A high value of linear polarization resistance  $R_p$ , as for LCK before chloride contamination (contrary to AAS and SSC), is associated with a high capacity of the steel to resist polarisation and therefore to a low corrosion current density  $i_{mi-Rp}$  (inversely proportional relationship as shown in Equation (18)). Concerning the corrosion potential  $E_{corr}$ , the one of the LCK formula (-33 mV/Ag/AgCl) is logically associated with a low corrosion risk in the absence of chlorides and the low  $i_{mi-Rp}$  ( $< 0.1 \mu A/cm^2$ ) is considered negligible (Figure 50). The LCK matrix, which is based indeed on PC, is expected to have a classical behavior.

On the contrary, still in the absence of chlorides and in the case of passive rebars, for the AAS and SSC binders, the measured  $E_{corr}$  and  $i_{mi-Rp}$  are respectively associated with a severe corrosion risk (-485 to -547 mV/Ag/AgCl) and a moderate level of apparent current density for

AAS ( $0.84 \mu\text{A}/\text{cm}^2$ ) to high for SSC ( $6.97 \mu\text{A}/\text{cm}^2$ ). This is due to the presence of sulfur in slag which reacts with the oxygen in the pore solution and creates a very reducing environment, lowering the redox potential of the latter. The very electronegative  $E_{\text{corr}}$  and the high  $i_{\text{mi-Rp}}$  (also applies for the low  $R_p$ ) measured correspond to chemical reactions of the sulfur in the pore solution and not to an active state of corrosion in the rebar (Mundra, Bernal, et al. 2017; Criado et al. 2018; Mundra et al. 2023). It is confirmed by the study of (Mundra and Provis 2021), which observed a decrease of  $R_p$  with increasing  $\text{HS}^-$  concentration, measured on a steel in a synthetic pore solution simulating the one of an AAS.

Therefore, the values obtained ( $E_{\text{corr}}$ ,  $R_p$  and  $i_{\text{mi-Rp}}$ ) for AAS and SSC do not represent accurately an active state of corrosion of the rebars. It highlights that the criteria used for PC are not adapted and cannot be directly applied to binders with a high slag content, hence the use of the galvanic current measurement presented in the next section.

### Results with chloride contamination

Figure 50 illustrates that chloride contamination leads for the three formulas considered to a drop in the parameters  $\rho$ ,  $E_{\text{corr}}$  and  $R_p$ , as well as an increase in  $i_{\text{mi-Rp}}$ . This behavior is in agreement with the literature (Chalhoub 2020; Hornbostel, Larsen, and Geiker 2013). A strong decrease of the resistivity is observed for the three binders with chloride contamination.

For the **LCK**, after chloride contamination the corrosion potential  $E_{\text{corr}}$  is logically associated to a severe corrosion risk ( $< -500 \text{ mV}/\text{Ag}/\text{AgCl}$ ), while the corrosion current density  $i_{\text{mi-Rp}}$  corresponds to high corrosion rates ( $> 1 \mu\text{A}/\text{cm}^2$ ). It confirms that the anode samples were activated by the chloride contamination.

For **AAS** and **SSC**, the drop in  $E_{\text{corr}}$  is much lower than for the LCK, due to already very electronegative values at passive state. Similarly, mainly for the SSC, the  $i_{\text{mi-Rp}}$  are very high (associated to very low  $R_p$ ), due to the very reducing environment created by the presence of sulfur species in the pore solution (less pronounced for the AAS). They were already classified as high corrosion rates at passive state for the same reason. Therefore, it is difficult to know if the anodes have been activated based on these parameters ( $E_{\text{corr}}$ ,  $i_{\text{mi-Rp}}$ ).

It can be noted that for alkali-activated materials, (Runci, Provis, and Serdar 2023) recently proposed new conservative values (for corrosion potential, mortar resistance and constant B) for active and passive steel, associated with a corresponding risk of corrosion. These values could later be refined with additional experimental tests.

Finally, the drying step of the anodes to further accelerate their chloride contamination, may have led to a partial oxidation of the sulfur species present in the pore solution of AAS and SSC. However, this effect is limited because the mortar samples after autopsy still show a blue-green color characteristic of the presence of reduced sulfur species (Criado, Bernal, et al. 2018), but less pronounced than the blue-green color observed after wet curing (Figure 51). Therefore, despite the drying step, they still have the capacity to create a reducing environment by consuming oxygen during the contamination by chlorides, to block the cathodic corrosion

reaction or to maintain very electronegative potentials (low  $E_{\text{corr}}$  are still observed due to chloride contamination), as it is the case in real conditions. After contamination by chlorides, the LCK formula based on PC, for which the recommendations are effective, shows a  $E_{\text{corr}}$  associated with a high corrosion risk and a  $i_{\text{mi-Rp}}$  considered as high, which shows the anodes were well activated.



Figure 51: Mortar of a SSC anode after 90 days of galvanic coupling ( $[\text{NaCl}] = 30 \text{ g/L}$ ).

## 4.2 Galvanic coupling between anode and cathode

### 4.2.1 Galvanic current ( $I_g$ )

Figure 52 shows the galvanic current  $I_g$  measured between anode and cathode at the end of 90 days of coupling for each binder and chloride concentration. The  $I_g$  values at 30 g/L are the average of 4 to 8 couplings and those at 300 g/L of 2 to 3 couplings. The values associated with the concentration 0 g/L (only 1 coupling performed) are used as a reference and were obtained from a coupling with an anode not contaminated by chlorides, to verify that the galvanic current  $I_g$  is negligible. In this configuration, the anode and the cathode having similar corrosion potentials  $E_{\text{corr}}$  (because both are in the passive state), when  $E_{\text{corr,anode}} < E_{\text{corr,cathode}}$  the values of  $I_g$  measured are slightly positive and negative in the opposite case ( $E_{\text{corr,anode}} > E_{\text{corr,cathode}}$ ).

Then, the results obtained are of different orders of magnitude depending on the binder and chloride concentration considered, as discussed in detail in section 5.1. In absence of chloride contamination, no significant galvanic current is measured. For the **LCK**, the galvanic current  $I_g$  increases with the chloride concentration. For the **AAS**,  $I_g$  is negligible at 30 g/L and strongly increases at 300 g/L. For the **SSC**,  $I_g$  remains negligible for both chlorides concentrations.

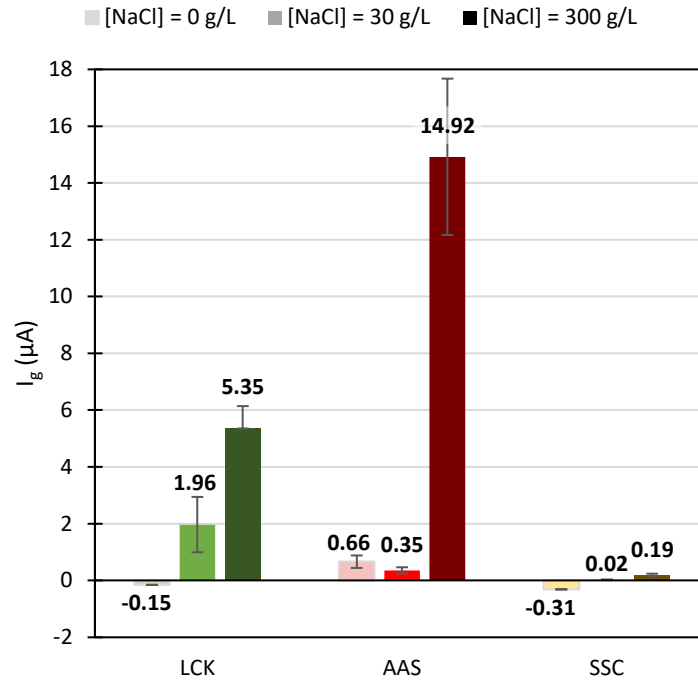


Figure 52: Galvanic current  $I_g$  after 90 days of coupling, depending on concrete type and chloride concentration.

#### 4.2.2 Total resistance ( $R_{tot}$ )

The total resistance  $R_{tot}$  between anode and cathode takes into account both the materials resistances  $R_e$  (from the classical measurement presented in section 3.2.1) and the polarization resistances  $R_p$  at the SCI, as described by Equation (23), where the solution resistance is negligible.

$$R_{tot} = R_{p,cathode} + R_{e,cathode} + R_{e,solution} + R_{e,anode} + R_{p,anode} \quad (23)$$

The table in Figure 53 presents the contribution of each variable in  $R_{tot}$ . In the passive state (0 g/L), the  $R_{tot}$  is mainly due to the  $R_{p,anode}$  component (67 to 93% depending on the binder). An increase in chloride concentration leads to a drop in  $R_{tot}$  (drop in  $R_{p,anode}$  and  $R_{e,anode}$ ), in agreement with what was observed in Figure 50. Nevertheless, for slag-based formulations (AAS and SSC), the  $R_{tot}$  parameter must be analysed carefully because it is based on the  $R_p$  values which are not representative of the corrosion state of the rebars, but rather of the sulphur oxidation reactions, as explained previously (4.1.2). The total resistance  $R_{tot}$  will influence the measured galvanic current value  $I_g$  (Revert et al. 2019; C. Andrade et al. 1992): for PC-based binders a low  $R_{tot}$  would favor a high  $I_g$  (more details are given in section 5).

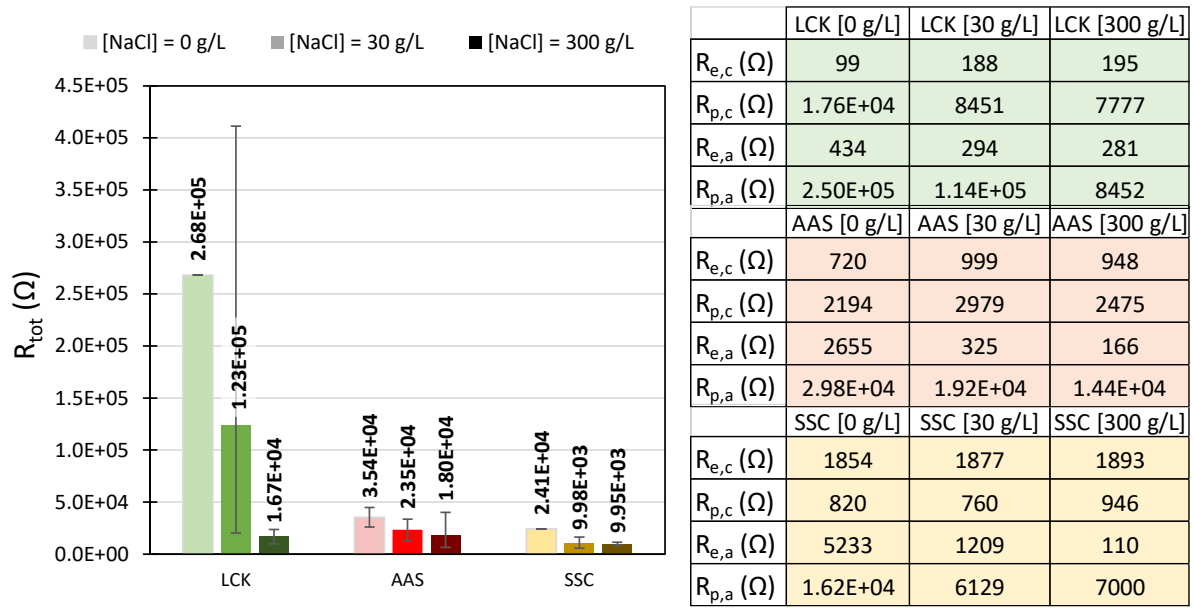


Figure 53: Total electrical resistance  $R_{tot}$  between reinforcement embedded in anode and cathode sample, before galvanic coupling. In the Table on the right side are detailed the different resistances (in ohm) forming  $R_{tot}$  (Equation (23)).

#### 4.2.3 Potential difference ( $\Delta E_{A-C}$ )

The potential difference ( $\Delta E_{A-C}$ ) between anode and cathode before galvanic coupling is shown in Figure 54, for each binder and chloride concentration.

In the case of coupling with an uncontaminated reference anode (0 g/L), the potential difference  $\Delta E_{A-C}$  between anode and cathode is negligible since both samples are passive (same electrochemical state). When the cathode has a more electronegative corrosion potential  $E_{corr}$  than the anode, the associated  $\Delta E_{A-C}$  is positive.

For PC-based binders (such as LCK), it is expected that the different electrochemical state between the active anode (electronegative corrosion potential  $E_{corr}$ ) and the passive cathode (less electronegative  $E_{corr}$ ), will generate an important potential difference  $\Delta E_{A-C}$  between the two (A. Nasser et al. 2010; Revert et al. 2019; C. Andrade et al. 1992). An increase in the chloride concentration, indeed, leads to a potential drop of the active anode and to an increase in the potential difference  $\Delta E_{A-C}$ . The measured  $\Delta E_{A-C}$  for anodes contaminated by chlorides is thus strong for LCK (-343 to -528 mV).

This potential difference  $\Delta E_{A-C}$  is less pronounced for the slag-based formulations, which already present a very electronegative  $E_{corr}$  at passive state, corresponding to chemical reactions of the sulfur in the pore solution as previously explained in section 4.1.2. The measured  $\Delta E_{A-C}$  for anodes contaminated by chlorides is weaker for AAS (-218 to -267 mV) and almost negligible for SSC (-21 to -26 mV). Therefore, a different behaviour of the LCK is expected.

Finally, the potential difference  $\Delta E_{A-C}$  would constitute the electromotive force generating the galvanic current  $I_g$ : a high  $\Delta E_{A-C}$  would thus favour a high  $I_g$  (Revert et al. 2019).

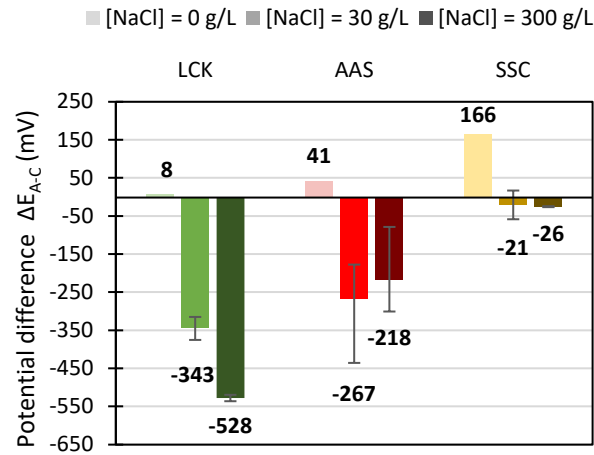


Figure 54: Potential difference  $\Delta E_{A-C}$  associated to each anode-cathode coupling, for the different binders and chloride concentrations considered.

### 4.3 Classic electrochemical measurement after galvanic coupling

In order to compare the corrosion rates measured with the galvanic current method and with the classic electrochemical methods at close time scales, a characterization of the active anodes by LPR measurement is performed after the galvanic coupling (once the samples are depolarized and have returned to their equilibrium state) and before the autopsies. In parallel to these LPR measurements, some active anodes are used to perform a Tafel test in order to obtain the parameters associated to the active state (results presented in section 4.1.1). Figure 55 shows a comparison of corrosion potentials  $E_{corr}$  and apparent current densities  $i_{mi-Rp}$ , obtained by LPR measurements, on active anodes before galvanic coupling (solid bars) or after galvanic coupling (hatched bars). The results on contaminated anodes before galvanic coupling are those of section 4.1.2.

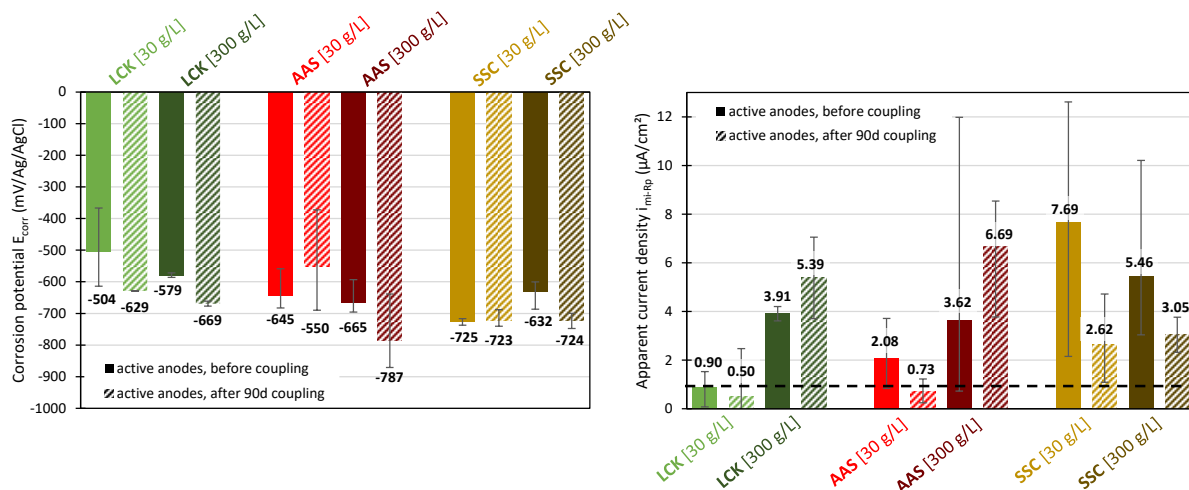


Figure 55: Corrosion potential  $E_{corr}$  and apparent current density  $i_{mi-Rp}$  measured on activated anodes (chloride contamination at 30 g/L or 300 g/L) by LPR measurement, before (solid bars) and after (hatched bars) galvanic coupling. The dotted black line indicates the threshold of 1  $\mu A/cm^2$ , associated with high levels of corrosion (see Figure 50).



Figure 55 shows there is little variation in  $E_{\text{corr}}$  before and after coupling (taking into account the error bars), which shows that when the galvanic coupling between anode and cathode is stopped, the anodes seem to return to their initial state (after depolarization). The more electronegative  $E_{\text{corr}}$  measured after coupling, possibly come from a more advanced and stable corrosion process.







On the other hand, the values of  $i_{\text{mi-Rp}}$  obtained on active anodes by LPR, have decreased after coupling at 30 g/L and increased after coupling at 300 g/L (except for SSC). The  $E_{\text{corr}}$  and  $i_{\text{mi-Rp}}$  parameters obtained by LPR measurement, give information on the corrosion state of the reinforcement at a given time (at the moment the measurement is made). However, it is known that corrosion reactions are a continuous and transient phenomenon. During the contamination by chloride ions, phenomena of depassivation-repassivation of the reinforcements are common, before a stable corrosion takes place (Angst et al. 2022). These two considerations can partially explain the differences in  $i_{\text{mi-Rp}}$  observed between the two time periods and chloride concentrations. Some repassivation could have occurred at 30 g/L compared to before coupling, explaining the lower  $i_{\text{mi-Rp}}$ . On the contrary, a more stable corrosion at 300 g/L after galvanic coupling (at later times), probably explains the higher  $i_{\text{mi-Rp}}$ , which is confirmed by the lower error bars after coupling (thus better reliability of the measured currents). Moreover, the galvanic coupling between the anode and the cathode could have influenced the corrosion current developing at the anode, as discussed in section 5.2.

#### **4.4 Autopsy of the anodes**

##### **4.4.1 Visual inspection**

In order to complete the electrochemical results obtained, the anodes are split in two and a visual inspection is performed in order to have a first estimation of the quantity of corrosion products. For each chloride concentration, one representative photo is displayed in Table 32. Localized corrosion spots, characteristic of pitting corrosion, as commonly observed with chloride contamination (D. Li et al. 2019; Y. Zhao et al. 2020), are visible for each binder and each chloride contamination after 90 days of galvanic coupling. A relatively small amount of corrosion products is observed on the rebar surface, except for AAS at 300 g/L.

Table 32: State of the rebars during autopsies after 90 days of galvanic coupling (1 representative sample per condition). The number of rebars without crevice corrosion analysed is specified below the image.

	[NaCl] = 30 g/L	[NaCl] = 300 g/L
LCK	 <p>2 samples without crevice corrosion</p>	 <p>1 sample without crevice corrosion</p>
AAS	 <p>6 samples without crevice corrosion</p>	 <p>1 sample without crevice corrosion</p>
SSC	 <p>2 samples without crevice corrosion</p>	 <p>2 samples without crevice corrosion</p>

#### 4.4.2 Mass loss

Figure 56 presents the mass loss measured on the anode rebars after galvanic coupling. The passive anodes used for the reference coupling (0 g/L) were not autopsied because it is assumed that they will not show any corrosion (no chloride contamination). For anodes contaminated at 30 g/L, the mass losses presented are the average of 2 (LCK and SSC) or 6 (AAS) samples, versus 1 (LCK and AAS) or 2 (SSC) samples for 300 g/L.

Figure 56 also differentiates the amount of mass loss due to the corrosion products themselves (solid bars) from that due to the cleaning process and mill scale (blank bars), as specified in section 3.4.1. It shows around 50 mg of the mass loss measured comes from the cleaning process. The amount of mass loss corresponding to corrosion products is much lower and represents only 18-32% of the total mass loss. Except for AAS anodes at 300 g/L, for which a significant amount of corrosion products was measured (47% of the total mass loss). These observations are in agreement with the visual inspections of section 4.4.1, where relatively small amounts of corrosion products were observed, except for AAS at 300 g/L.

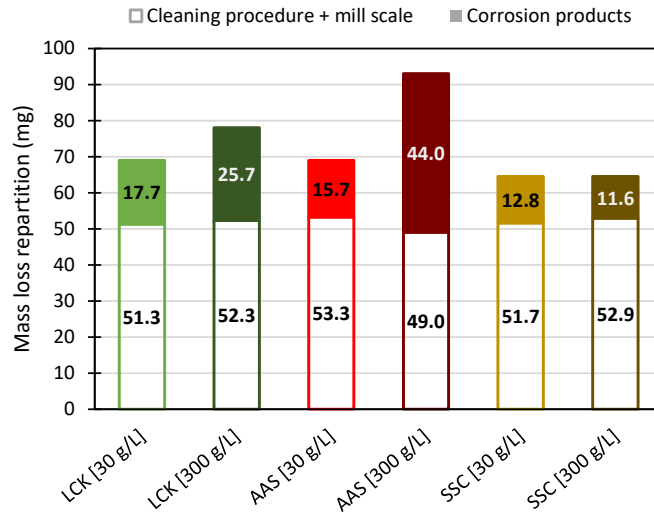


Figure 56: Mass loss measured on anode rebars, after 90 days of galvanic coupling. The numbers on the bars show the distribution in milligrams between the mass loss due to corrosion products and the mass loss due to the cleaning procedure and mill scale.

#### 4.4.3 Total current $I_{tot}$ calculated from the mass loss

The values of total current  $I_{tot}$  after 90 days of coupling, associated with the total mass losses measured previously and calculated according to Faraday's law (Equation (21)), are presented on Figure 57. As explained in section 3.4.2,  $I_{tot}$  corresponds to the sum of the currents flowing between the anode and the cathode ( $I_g$ ) but also at the local scale of the anode ( $I_{mi-anode}$ , being the sum of  $I_a$  and  $I_{mic}$ ). The total currents  $I_{tot}$  are logically proportional to the mass losses (corrosion products) in Figure 56 and vary according to the binders and the chloride concentrations. In general,  $I_{tot}$  is higher at 300 g/L than at 30 g/L, except for SSC where no significant difference is observed and for which the total currents are lower than for AAS and LCK. A more detailed analysis of these currents is proposed in section 5.2.

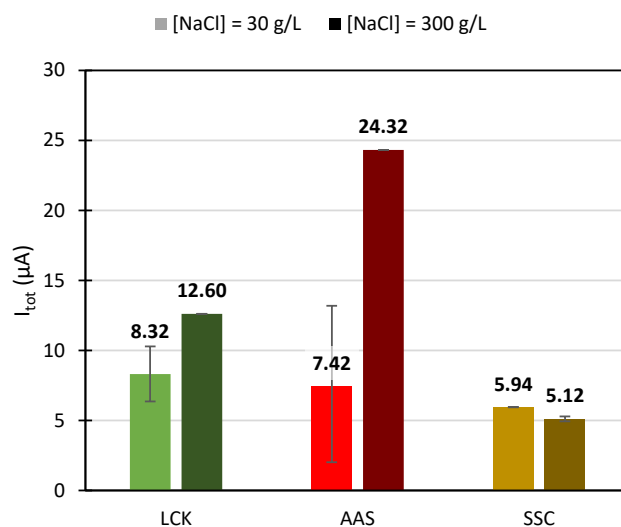


Figure 57: Total current  $I_{tot}$  after 90 days of coupling, calculated from mass loss.

4.4.4 Chloride concentration at the steel/concrete interface (SCI)

Figure 58 presents the total chlorides measured at the SCI of several anodes used for the galvanic coupling. The values presented are the average of 4 samples at 30 g/L and 2 samples at 300 g/L.

For LCK samples, analysis enables to quantify the proportion of free and bound chlorides, which is 80% free chlorides and 20% bound chlorides at 30 g/L, and 90% free versus 10% bound at 300 g/L. These results illustrate the limited ability of this binder to bind chlorides.

Figure 58 shows that the same total chloride concentrations at the SCI are measured for LCK and AAS at 30 g/L or 300 g/L, while they are much higher for SSC (factor 2 at 30 g/L and factor 4 at 300 g/L). The total chloride concentrations at the SCI are presented in percentage per mass of binder on Figure 58, which can be converted in percentage per mass of cement for LCK and SSC, considering the binder without the inert limestone filler (only CEM I for LCK and slag, anhydrite and CEM III/B for SSC). The total chloride concentrations at the SCI is thus 1.82% and 0.99% of chlorides per mass of cement at 30 g/L for LCK and SSC, respectively, and to 3.71% and 3.98% chlorides per mass of cement for LCK and SSC at 300 g/L.

In reality there are probably differences between the binders about the amount of free chlorides at the SCI available to initiate steel depassivation, depending on the repartition of free and bound chlorides, which is not quantified for the slag-based binders (Article A). Finally, when the chloride concentration of the solution used to contaminate the anodes is multiplied by 10, the total chloride concentration measured at SCI double. This behaviour was not expected and deeper investigations are required to explain this observation.

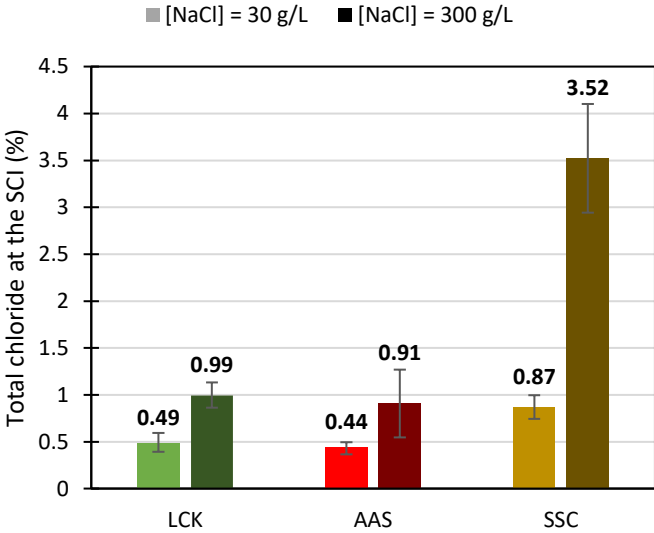


Figure 58: Total chloride concentration (% per mass of binder) measured on the anodes at the SCI.

## 5 Discussion

### 5.1 Galvanic current ( $I_g$ )

The galvanic current  $I_g$  obtained at the end of 90 days of coupling for each binder and each chloride concentration is shown in Figure 59, represented by circles whose diameter is proportional to  $I_g$ . For the Portland cement-based **LCK** samples,  $I_g$  increases as the potential difference  $\Delta E_{A-C}$  increases and  $R_{tot}$  decreases. This is because an increase in chloride concentration leads to a drop in  $R_{tot}$  (drop in  $R_{p,anode}$  and  $R_{e,anode}$ , section 4.2.2) and an increase in the potential difference  $\Delta E_{A-C}$  (section 4.2.3), thus promoting an increase in  $I_g$ . This behaviour was expected and corresponds to the literature findings for PC-based binders (Revert et al. 2019; Abdelkader Nasser and Castel 2014; T.-T. Nguyen et al. 2022).

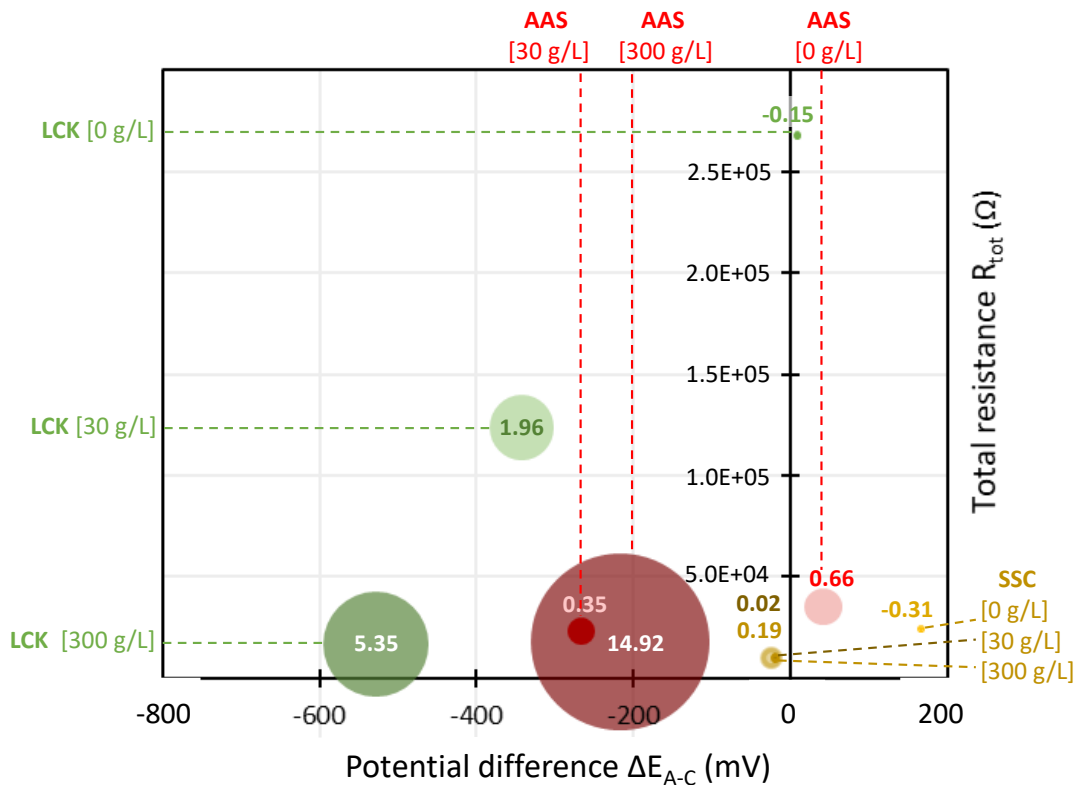


Figure 59: Relation of the measured galvanic current  $I_g$  with the total resistance  $R_{tot}$  associated to each anode-cathode pair and the potential difference ( $\Delta E_{A-C}$ ) measured between the two before coupling. The diameter of circles is proportional to  $I_g$  (in  $\mu A$ ).

For the AAS and SSC binders, this trend is not verified. This is partly due to the fact that the parameter  $R_{tot}$  cannot be used to interpret the different  $I_g$  values obtained, as it is based on the  $R_p$  values (Equation (23)), which are not representative of the corrosion state of the rebars, but rather of the sulphur oxidation reactions, as explained in section 4.1.2.

Concerning the **SSC**, the very low potential difference  $\Delta E_{A-C}$  (-21 mV at 30 g/L and -26 mV at 300 g/L) nevertheless explains the almost zero  $I_g$  values (0.02  $\mu A$  at 30 g/L and 0.19  $\mu A$  at 300 g/L) regardless of the chloride concentration, as there is no electromotive force to generate a galvanic current.

Finally, for the **AAS**, very different  $I_g$  values are measured at 30 g/L and 300 g/L (average of 0.35 and 14.92  $\mu\text{A}$ , respectively), despite similar potential difference  $\Delta E_{A-C}$  (average of -267 and -218 mV, respectively). Thus, it seems that another parameter is involved in this case, because the potential difference  $\Delta E_{A-C}$  is not sufficient to cause a high  $I_g$  in regard to the results at 30 g/L.

One hypothesis to explain the difference of  $I_g$  measured between 30 and 300 g/L is based on the critical chloride threshold. It corresponds to the critical chloride concentration required at the SCI to initiate the corrosion (U. M. Angst et al. 2022). This threshold could have been largely exceeded at 300 g/L, explaining the high  $I_g$ . On the contrary, at 30 g/L, it is possible that the threshold has not been exceeded, explaining the low  $I_g$ . The analysis of the chloride concentration at the SCI (Figure 58) seems to be in line with this assumption, as 0.44% of total chlorides per mass of binder were measured at the SCI for anodes contaminated at  $[\text{NaCl}] = 30$  g/L, against 0.91% for those contaminated at  $[\text{NaCl}] = 300$  g/L. The active state of the anodes cannot be verified by the  $R_p$  values for this binder, as explained in section 4.1.2. Finally, the amount of chlorides required to initiate corrosion pitting is not necessarily the same as that required to have stable pitting (depassivation/repassivation phenomena of the steel), as reported by (Mundra, Criado, et al. 2017). Thus, the concentration of 0.44% of total chlorides at the SCI may not be sufficient to cause stable corrosion, contrary to 0.91%. This hypothesis is discussed more in details in the next section 5.2.

Another hypothesis to explain the difference of  $I_g$  measured between 30 and 300 g/L is the presence of an interfacial defect (interfacial voids...) at the SCI. It was shown by (A. Nasser et al. 2010; Abdelkader Nasser and Castel 2014), that galvanic corrosion current densities twice as high can be measured in the presence of an interfacial defect. However, during the autopsy of the AAS anodes samples at 300 g/L no particular defect was observed on the rebar or at the SCI.

## **5.2 Total corrosion current ( $i_{tot}$ ): contributions of galvanic current between anode and cathode ( $i_g$ ) and local current at the anode ( $i_{mi-anode}$ )**

Figure 60 presents the apparent current densities on the active anodes by LPR measurement after coupling ( $i_{mi-Rp}$ ), and those that develops during 90 days of the anode-cathode coupling ( $i_{tot}$ ). The distribution between the two apparent current densities forming  $i_{tot}$ , the galvanic contribution between the anode and cathode ( $i_g$ ) and the local contribution at the anode scale ( $i_{mi-anode}$ ), is also specified. All values are apparent current densities for easier comparison. However, it is important to clarify a limitation of the results presented in this section. As observed in Table 32, the anodes are not entirely activated (meaning covered with corrosion spots). Therefore, the anodic surface considered is the one of the anode rebar, while the real active areas corresponding to corrosion pits are much lower. It results in apparent current densities which are lower than the real current densities (corresponding to the active zones of the anode).

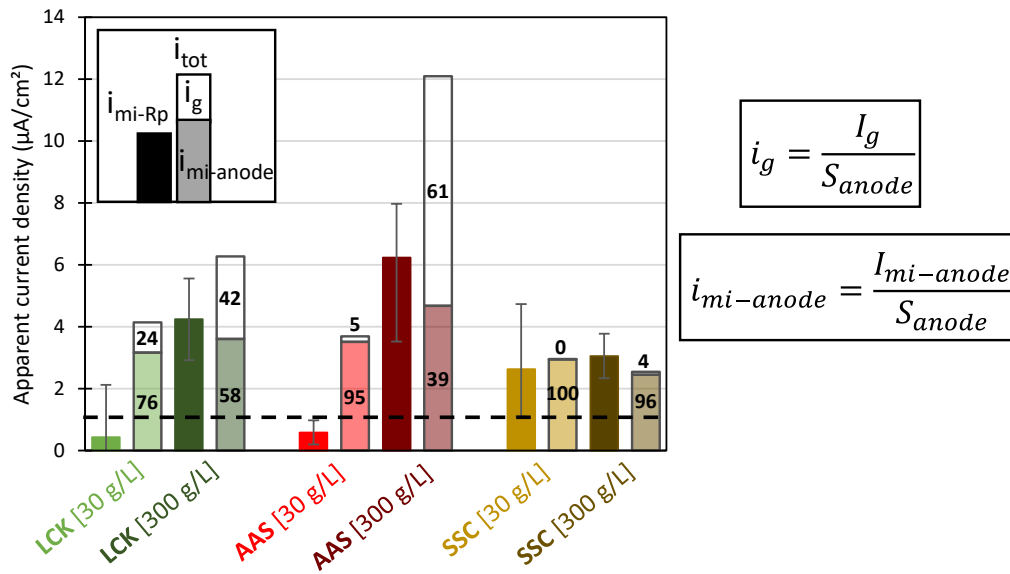


Figure 60: Comparison of the apparent current density measured on the active anodes after coupling ( $i_{mi-Rp}$ ) with that which develops during 90 days of anode-cathode coupling ( $i_{tot}$ ). The numbers on the bars show the distribution in percentage between the galvanic ( $i_g$ ) and local at the anode ( $i_{mi-anode}$ ) apparent current density. The dotted black line indicates the threshold of  $1 \mu A/cm^2$ , associated with high levels of corrosion (see Figure 50).

### 5.2.1 Focus on local corrosion current densities at the anode ( $i_{mi-anode}$ )

First of all, it appears that  $i_{mi-anode}$  is high ( $> 1 \mu A/cm^2$ ) for each condition, due to activation by chlorides. However, these high values correspond to ranges of corrosion rates available in the literature for CEM I-concretes. For chloride-induced corrosion ( $[NaCl] = 30 \text{ g/L}$ ), (C. Andrade et al. 1992; Carmen Andrade 2023) report and review ranges of apparent current densities from the literature generally between  $2$  to  $5 \mu A/cm^2$  on concrete CEM I. It makes LCK, AAS and SSC concretes competitive from the view point of corrosion rates.

Figure 60 also illustrates that  $i_{mi-anode}$  do not vary according to the type of binder. At  $30 \text{ g/L}$ , values of  $i_{mi-anode}$  are similar for the three low-carbon concretes. The same observation can be done at  $300 \text{ g/L}$ .

### 5.2.2 Composition of $i_{tot}$ : repartition between $i_g$ and $i_{mi-anode}$

First of all, it appears that  $i_{mi-anode}$  is not negligible ( $> 1 \mu A/cm^2$ ) for each condition, due to activation by chlorides, while in general  $i_g$  is low for contaminations at  $30 \text{ g/L}$  and increases at  $300 \text{ g/L}$  (not negligible compared to  $i_{mi-anode}$  for LCK and AAS).

The distribution between  $i_g$  and  $i_{mi-anode}$  is different for each binder and is dependent of the C/A ratio (fixed at 55 in this study). For example, (Lliso-Ferrando et al. 2022) finds a different repartition than in this paper, with a higher proportion of galvanic current than local current, on CEM I-concretes contaminated by chlorides. Other studies focusing on corrosion due to chlorides (Chalhoub, François, and Carcasses 2019; Warkus and Raupach 2010) or carbonation

(Revert et al. 2019; Angst et al. 2020), emphasize the influence of the C/A ratio (varying between 0.5 and 3000) either experimentally or numerically: higher C/A ratio promoting a higher galvanic current for CEM I-based samples.

For **LCK**, in addition to the high  $i_{mi-anode}$ , the high potential difference  $\Delta E_{A-C}$  between anode and cathode causes the development of a non-negligible  $i_g$ , which increases with chloride concentration (24% of  $i_{tot}$  at 30 g/L and 42% at 300g/L) and that is explained by a drop in  $R_{tot}$  and an increase in the potential difference  $\Delta E_{A-C}$ , as explained in section 5.1.

For **SSC**, the  $i_g$  remains zero due to the absence of significant potential difference  $\Delta E_{A-C}$ , but a high  $i_{mi-anode}$  is observed, favoured by a lower resistivity of the mortar with chloride contamination (Hornbostel, Larsen, and Geiker 2013) (519  $\Omega.m$  at 30 g/L and 47  $\Omega.m$  at 300 g/L, contrary to 2078  $\Omega.m$  in absence of chloride), in spite of a higher chloride concentration than in the other binders at the SCI (section 4.4.4). This suggests that another phenomenon must be involved to limit the corrosion.

Finally for **AAS**, the low resistivity of the anode in the presence of chlorides (140  $\Omega.m$  at 30 g/L and 19  $\Omega.m$  at 300 g/L, contrary to 750  $\Omega.m$  in absence of chloride) also favours a high  $i_{mi-anode}$ . It is associated with a negligible  $i_g$  at 30 g/L (only 5% of  $i_{tot}$ ) but which becomes predominant (61% of  $i_{tot}$ ) at 300 g/L. The behaviour observed at 300 g/L is probably due to the critical chloride threshold largely exceeded at the rebar, as discussed more in details in section 4.2.1.

### 5.2.3 Influence of galvanic coupling on $i_{mi-anode}$

The literature shows that when a galvanic coupling is realized, the electronic and ionic current generated between the active anode and the passive cathode, favours the migration of chloride ions (negative electrical charge) towards the anode rebar, which has positive electrical charge due to the anodic reaction (oxidation of steel producing electrons) (Lliso-Ferrando et al. 2022). (Lliso-Ferrando et al. 2022) also shows that compared to a configuration without galvanic coupling, it results in an earlier corrosion onset and an increase in the local corrosion rate due to a higher chloride concentration at the rebar, which maintains the activity of the active zone (decrease of resistivity and  $R_p$ , depassivation of steel). They measured a chloride content at the rebar (% per cement weight) between 80% and 600% higher when galvanic coupling is performed (Lliso-Ferrando et al. 2022).

For SSC almost no galvanic current is measured, thus this migration of chloride ions to the rebar is certainly negligible. However, the total chloride concentration at the rebar (section 4.4.4) is still higher than in other binders, while it does not result in higher currents. One hypothesis could be that there is a higher chloride concentration at the rebar which is not associated to a higher current because a lot of total chlorides are bound by this binder, which is known for its high chloride binding capacity (K. S. Nguyen et al. 2018; Divet and Le Roy 2013). Another explanation is that the migration of negative ionic species to the rebar also leads to the migration of  $OH^-$  ions in addition to  $Cl^-$  ions, which changes the critical concentration  $C_{crit}$  ( $C_{crit} = [Cl^-]/[OH^-]$ ) at the rebar. In general, the onset of corrosion by chlorides is associated with a



chloride "threshold" (called  $C_{crit}$ ) above which there is depassivation of the rebar. SSC contains less  $OH^-$  ions than in the other binders (Article A). (Mundra, Criado, et al. 2017) shows in their study that solutions with a high basicity (high  $[OH^-]$ ) have a higher degree of passivation. Therefore, the lower amount of  $OH^-$  ions in this binder could be associated to a higher  $C_{crit}$  needed to initiate corrosion.

### 5.3 Methodology: interest and perspectives of the galvanic current method

#### 5.3.1 Comparison between $i_{mi-Rp}$ and $i_{tot}$ and interest of the galvanic current method

First of all, Figure 60 shows that the apparent current densities  $i_{mi-Rp}$  and  $i_{tot}$  are all high (taking into account the error bars), according to TC RILEM 154 recommendations (C. Andrade and Alonso 2004), whatever the type of binder or the chloride concentration considered. For LCK and AAS the values of  $i_{tot}$  are higher than those of  $i_{mi-Rp}$ , while they are similar for SSC due to a negligible galvanic current and therefore a negligible migration of chloride ions towards the anode rebar. As explained in section 5.2, the galvanic coupling generates a migration of chloride ions towards the anode rebar. This side effect of the galvanic coupling, partly explains the higher local apparent current density  $i_{mi-anode}$  compared to  $i_{mi-Rp}$  (measured before coupling) for LCK and AAS.

The apparent current densities  $i_{tot}$  are dependent on the C/A ratio (fixed at 55 for this experimental campaign), as well as  $i_{mi-Rp}$  (no coupling) to a lesser extent due to non-uniform corrosion. It is also important to note that  $i_{mi-Rp}$  is a single time measurement (after chloride contamination and before galvanic coupling in this case). Therefore, it represents the electrochemical state of the rebar at a given time, whereas  $i_{tot}$  is an average value that considers the duration of the experimental campaign (as it is obtained from the mass loss generated by all the currents to which the rebar has been subjected since its contamination by chlorides). The disadvantage of the LPR measurement, which is otherwise convenient and rapid to perform, is that it provides information on the electrochemical state of the rebar at a given time, whereas corrosion of steel in concrete is a continuous and transient process (Angst et al. 2022). This explains partly the significant variations (symbolized by the error bars in Figure 60 or Figure 55) associated with the values of  $i_{mi-Rp}$ . The fact that the measurements are carried out on a large number of samples nevertheless makes it possible to identify reliable trends and behaviours specific to each binder. The  $i_{tot}$  value is in some ways more representative of reality, because it takes into account the total current to which the rebar has been subjected. However, it is calculated from the mass loss values, which are themselves subject to a certain inaccuracy due to the small quantities of corrosion products measured, related to the small duration of the galvanic coupling (90 days) compared to corrosion of real reinforced structures.

Finally, the comparison between  $i_{mi-Rp}$  measured on the active anodes after coupling (local contribution) and  $i_{tot}$  measured during coupling (local and galvanic contributions), highlights the interest of the galvanic current measurement to quantify the corrosion kinetics due to chlorides. On a real structure, indeed, the contamination by chlorides leads to the appearance of localized corrosion spots which are then coupled with the rest of the passive rebar network, producing a galvanic current in addition to the local current, as considered by the protocol of

this article. The interest of the proposed method is to take into account this galvanic contribution  $i_g$  in the value of  $i_{tot}$ . Figure 60 illustrates, indeed, that  $i_g$  is not negligible for the LCK and AAS binders at 300 g/L. However,  $i_g$  is not considered by the classical measurement, that only gives information on the current at the local scale and therefore potentially underestimate the corrosion rates that could occur in real structures. It highlights that the corrosion kinetics analyses have to include both local and galvanic processes to accurately fit with the experimental mass losses measured.

Moreover, this test is suitable for binders with high slag content (AAS and SSC), as galvanic current measurement and mass loss measurement are direct techniques, not influenced by the sulphur contained in slag. Therefore, it offers an interesting alternative to classical electrochemical measurements based on LPR, where  $i_{mi-Rp}$  overestimates the corrosion kinetics due to the sulphur contained in the slag, as explained in section 4.1.2.

### 5.3.2 Perspectives to improve the galvanic current method

Research gap of the experimental protocol are reported. Some perspectives of improvement and future research needs are finally proposed.

The anodes were not entirely activated (meaning covered with corrosion spots). Therefore, the anodic surface considered is the one of the anode rebar, while the real active areas corresponding to corrosion pits are much lower. It results in an apparent current density which is lower than the real current density (corresponding to the active zones of the anode), and could lead to a misinterpretation of the results.

- To improve the activation of anodes by chloride contamination and to obtain a sample more uniformly active (covered with several corrosion spots), it could be recommended to wait a longer time after chlorides have reached the rebar (one month for example). The literature reports, indeed, that there is a transition period before a stable corrosion is reached (several depassivation-repassivation steps are possible and can take a longer time). Therefore, a more active anode will generate higher corrosion currents, resulting in a more precise mass loss measurement.
- To calculate more precise corrosion current densities, the precise surface of the active anode could be quantified.

Then, as explained in section 4.1.2, the drying step of the anodes to further accelerate their chloride contamination, may have conducted to a partial oxidation of the sulfur species present in the pore solution of AAS and SSC, preventing them to create a very reducing environment by consuming oxygen during the contamination by chlorides and during galvanic coupling, to block the cathodic corrosion reaction or to maintain very electronegative potentials. This bias leads to a divergence from the real conditions and could potentially underestimates the performance of slag-based binders, but it is probably negligible as autopsies reveal indirectly the presence of reduced sulfur species by the blue-green color of slag-based anodes, despite the drying step.

Finally, further research is needed to explain the differences in measured galvanic currents for AAS between 30 and 300 g/L or to validate the proposed hypotheses.

#### 5.4 Assessment of the corrosion risk in the three low-carbon concretes considered

This experimental campaign has allowed to provide answers on the performance of the three low-carbon concretes studied with respect to corrosion in a marine environment ( $[\text{NaCl}] = 30$  g/L) or due to de-icing salts ( $[\text{NaCl}] = 300$  g/L), which is interesting because the information available in the literature remains limited or without consensus on the corrosion risk for these binders.

As explained by Tutti (Tuutti 1982), corrosion occurs in two stages with a transition period between the two (Angst et al. 2022): an initiation phase that will be conditioned by the time of arrival of chlorides to the rebar, quantified by the natural diffusion coefficient of chlorides  $D_{\text{nss}}$ , and a propagation period, quantified by the corrosion rates  $i_{\text{tot}}$ . Table 33 summarizes the resistance to chloride penetration of LCK, AAS and SSC (as a result of a chloride diffusion test performed according to EN 12390-11 (AFNOR 2015), on a concrete cured 90 days and measured in Article A), as well as the  $i_{\text{tot}}$  developed (section 4.4.3), which allows to conclude about their possible use in a chloride-rich environment.

Table 33: Performance of LCK, AAS and SSC concretes against chloride corrosion, considering the initiation and propagation phases of corrosion.

Concrete	Natural chloride diffusion test $D_{\text{nss}}$ ( $\times 10^{-12}$ m <sup>2</sup> /s) *	Resistance to Cl <sup>-</sup> penetration: (corrosion initiation)	$i_{\text{tot}}$ ( $\mu\text{A}/\text{cm}^2$ ) (corrosion propagation)		Recommendation for use in chloride-rich environment
			$[\text{NaCl}] = 30$ g/L (sea water)	$[\text{NaCl}] = 300$ g/L (de-icing salts)	
LCK	$50.78 \pm 12.06$	Very low (low CEM I content)	High (4.13)	High (6.27)	Not recommended
AAS	$0.19 \pm 0.01$	Strong (high chloride binding capacity of slag)	High (3.69)	Very high (12.09)	OK at 30 g/L Not recommended at 300 g/L
SSC	$0.58 \pm 0.21$		High (2.95)	High (2.54)	OK

\*Article A

About the corrosion initiation, Table 33 highlights strong differences to chloride diffusion resistance according to the type of binder studied, slag-based binders (AAS and SSC) being much more resistant to chloride diffusion than LCK made with CEM I. This trend is also observed by other authors (Divet et Le Roy 2013; Yeau et Kim 2005; Roy, Jiang, et Silsbee 2000; Türkmen, Gavgalı, et Gül 2003; Zhang et al. 2022).

- LCK has a high chloride diffusion coefficient  $D_{\text{nss}}$ , compared to the one of a traditional CEM I-concrete (without limestone fillers) of similar strength class:  $50.78 \times 10^{-12}$  m<sup>2</sup>/s

for LCK against an average of  $23.35 \times 10^{-12} \text{ m}^2/\text{s}$  for CEM I-concretes from PERFBUB database (IREX 2022), also observed by (L Bertolini, Lollini, and Redaelli 2007; Lollini, Redaelli, and Bertolini 2014; 2016; Elgalhud, Dhir, and Ghataora 2018; Carrinho 2018). This is mainly due to its low clinker content (27% of the binder), which is responsible for a lower chloride-binding capacity. Its high chloride diffusion coefficient  $D_{\text{nss}}$  combined with a low resistivity (section 4.1.2), makes it poorly resistant to chloride ions penetration.

- On the contrary to the LCK concrete, for **AAS** and **SSC** concretes a strong resistance to chloride diffusion is observed, with very low chloride diffusion coefficients  $D_{\text{nss}}$ , mainly due to the high chloride binding capacity of slag which slows down their ingress, as mentioned in the literature (K. S. Nguyen et al. 2018; G. Yang, Zhao, and Wang 2022; Jingxiao Zhang et al. 2022).

About the **corrosion propagation**, the values of  $i_{\text{tot}}$  vary according to the chloride concentration and the binder.

- For **LCK**, after 90 days of galvanic coupling, high corrosion rates are measured ( $i_{\text{tot}} > 1 \mu\text{A}/\text{cm}^2$ ), both at 30 g/L ( $4.13 \mu\text{A}/\text{cm}^2$ ) and 300 g/L ( $6.27 \mu\text{A}/\text{cm}^2$ ). Combined with its low resistance to chloride penetration, it makes it poorly resistant to corrosion initiation (rapid arrival of chlorides to the rebar) and to corrosion propagation (high corrosion rates), that is why its use in a chloride-rich environment is not recommended.
- For **AAS**, after 90 days of galvanic coupling, high corrosion rates are measured at 30 g/L ( $3.69 \mu\text{A}/\text{cm}^2$ ) and even very high ( $> 10 \mu\text{A}/\text{cm}^2$ ) at 300 g/L ( $12.06 \mu\text{A}/\text{cm}^2$ ). Considering that this binder is extremely resistant to chloride penetration, the corrosion initiation will occur after a very long time, therefore its use in a marine environment ( $[\text{NaCl}] = 30 \text{ g/L}$ ) is possible even if it generates high currents. Nevertheless, its use for higher chloride concentrations, such as 300 g/L for de-icing salts, is more dangerous for the concrete structures and not recommended as very high currents ( $> 10 \mu\text{A}/\text{cm}^2$ ) were measured after 90 days of coupling.
- Finally for **SSC**, after 90 days of galvanic coupling high corrosion rates are measured,  $i_{\text{tot}}$  being just above the threshold of  $1 \mu\text{A}/\text{cm}^2$ , both at 30 g/L ( $2.95 \mu\text{A}/\text{cm}^2$ ) and 300 g/L ( $2.54 \mu\text{A}/\text{cm}^2$ ). Its use in a chloride-rich environment is recommended, as it is very resistant to both corrosion initiation and to corrosion propagation, either at 30 g/L or 300 g/L.

The conclusions presented here apply for  $i_{\text{tot}}$  obtained in the case of saturated conditions (anode and cathode immersed during the galvanic coupling test), which is not necessarily the most unfavorable case in reality (a dry cathode coupled to a saturated anode could generate higher potential differences and potentially higher currents). Therefore, the corrosion rates obtained cannot be generalised to other conditions.

## 6 Conclusion

The corrosion rates due to chloride contamination were assessed in three low-carbon concretes of same strength class C25/30: LCK, Na<sub>2</sub>CO<sub>3</sub>-AAS and SSC concretes. An experimental campaign based on 3 months of galvanic current measurement, combined with mass loss on the rebar was proposed. A high cathode to anode surface ratio of 55 was chosen to simulate conditions that could take place in a real concrete structure, and the test was conducted in solution on saturated samples. A comparison with classical electrochemical measurements (corrosion potential  $E_{\text{corr}}$ , polarization resistance  $R_p$ ) was also presented. Finally, the influence of two chloride concentrations on the corrosion rates was investigated, to evaluate the performance of each binder under conditions similar to sea water ([NaCl] = 30 g/L) or in the presence of de-icing salts ([NaCl] = 300 g/L). The following conclusions, that apply only for saturated conditions for anode and cathode, can be drawn:

### Corrosion propagation

- The results show the values of the total current density ( $i_{\text{tot}}$ ) due to chlorides is high for the three binders, because the measured galvanic current ( $i_g$ ) is added to a high local current at the anode ( $i_{\text{mi-anode}}$ ).
- **LCK** is characterized by high corrosion rates both at 30 g/L (nearly 4  $\mu\text{A}/\text{cm}^2$ ) and 300 g/L (around 6  $\mu\text{A}/\text{cm}^2$ ). The galvanic current is not negligible in this binder (24 to 42% of  $i_{\text{tot}}$ ) and depends mainly on the potential difference and the total resistance of the materials between the anode and the cathode.
- **AAS** is characterized by high corrosion rates at 30 g/L (nearly 4  $\mu\text{A}/\text{cm}^2$ ) and even very high at 300 g/L (above 10  $\mu\text{A}/\text{cm}^2$ ). The galvanic current measured is negligible at 30 g/L (5% of  $i_{\text{tot}}$ ) and then becomes high at 300 g/L (61% of  $i_{\text{tot}}$ ).
- **SSC** is characterized by slightly lower corrosion rates (under 3  $\mu\text{A}/\text{cm}^2$ ) at 30 and 300 g/L, because the galvanic current remains negligible for both concentrations. This characteristic is interesting for a real structure because it results in lower  $i_{\text{tot}}$ .

### Methodology

- The comparison with classical electrochemical measurements (corrosion potential  $E_{\text{corr}}$ , polarization resistance  $R_p$ ) confirms the literature findings reporting the limitations of these methods to assess the corrosion resistance of slag-based binders, which justifies the proposed galvanic current protocol. The use of existing recommendations developed for PC for the interpretation of potential, polarization resistance or current values in slag-based binders, could lead to misleading interpretations, if applied without modifications.
- The experimental campaign conducted showed the interest of the galvanic current measurement to characterize the corrosion rates in concrete with high slag content, as it is a direct measurement which does not require an external polarization of the rebar, and therefore is not influenced by the presence of sulfur species in the pore solution. It is combined with mass loss, which is also a direct measurement.
- Galvanic current and mass loss measurements together enable to take into account the localized aspect of corrosion initiated by chlorides, which is not negligible in real structures and not often considered by laboratory tests. Galvanic currents due to coupling between active and passive reinforcement should thus be considered for service life predictions.

## 7 Supplementary data

### Related to section 3.2.2

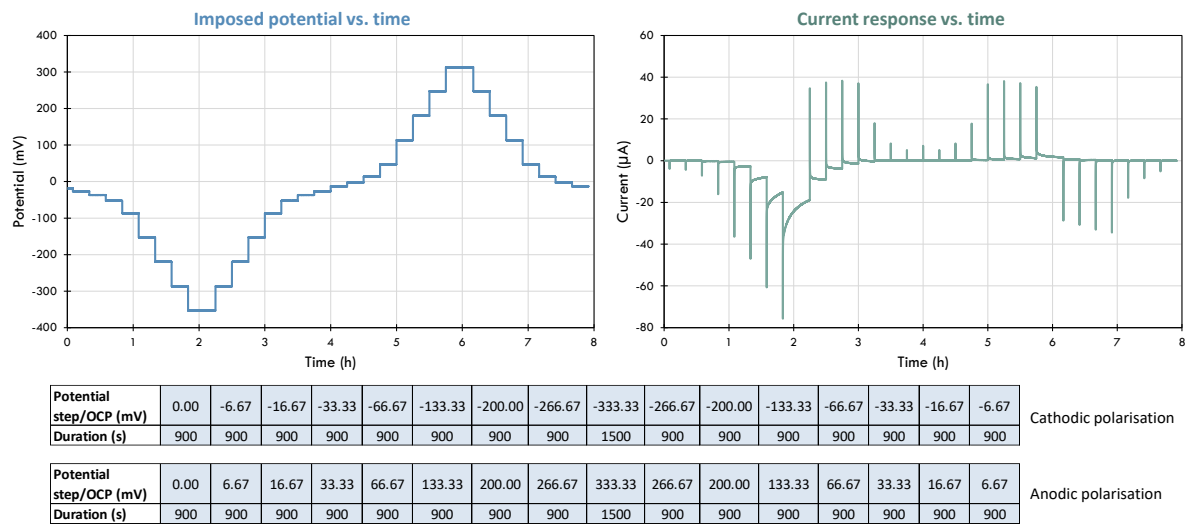


Figure 61: Example of Tafel test performed on an active anode LCK.

## 8 References

- AFNOR. 2007. ‘NF EN 14629 : Mesurage Du Taux de Chlorure d’un Béton Durci’.
- AFNOR. 2010. ‘NF EN 15743 : Ciment Sursulfaté - Composition, Spécifications et Critères de Conformité’.
- AFNOR. 2015. ‘EN 12390-11 : Détermination de La Résistance Du Béton à La Pénétration Des Chlorures, Diffusion Unidirectionnelle’.
- Alonso, C., and C. Andrade. 1987. ‘Effect of Cement Type and Cement Proportion in the Corrosion Rate of Rebars Embedded in Carbonated Mortar’. *Materiales de Construcción* 37 (205): 5–15. <https://doi.org/10.3989/mc.1987.v37.i205.874>.
- Andrade, C., and C. Alonso. 1996. ‘Corrosion Rate Monitoring in the Laboratory and On-Site’. *Construction and Building Materials, Durability of Reinforced Concrete Structures*, 10 (5): 315–28. [https://doi.org/10.1016/0950-0618\(95\)00044-5](https://doi.org/10.1016/0950-0618(95)00044-5).
- AFNOR. 2004. ‘Test Methods for On-Site Corrosion Rate Measurement of Steel Reinforcement in Concrete by Means of the Polarization Resistance Method’. *Materials and Structures* 37 (9): 623–43. <https://doi.org/10.1007/BF02483292>.
- Andrade, C., and J. A. González. 1978. ‘Quantitative Measurements of Corrosion Rate of Reinforcing Steels Embedded in Concrete Using Polarization Resistance Measurements’. *Materials and Corrosion* 29 (8): 515–19. <https://doi.org/10.1002/maco.19780290804>.
- Andrade, C., I.R. Maribona, S. Feliu, J.A. González, and S. Feliu. 1992. ‘The Effect of Macrocells between Active and Passive Areas of Steel Reinforcements’. *Corrosion Science* 33 (2): 237–49. [https://doi.org/10.1016/0010-938X\(92\)90148-V](https://doi.org/10.1016/0010-938X(92)90148-V).
- Andrade, Carmen. 2023. ‘Steel Corrosion Rates in Concrete in Contact to Sea Water’. *Cement and Concrete Research* 165 (March): 107085. <https://doi.org/10.1016/j.cemconres.2022.107085>.
- Angst, Fabrizio Moro, Mette Geiker, Sylvia Kessler, Hans Beushausen, Carmen Andrade, Jukka Lahdensivu, et al. 2020. ‘Corrosion of Steel in Carbonated Concrete: Mechanisms, Practical Experience, and Research Priorities – a Critical Review by RILEM TC 281-CCC’. *RILEM Technical Letters* 5 (December): 85–100. <https://doi.org/10.21809/rilemtechlett.2020.127>.
- Angst, U., and M. Büchler. 2015. ‘On the Applicability of the Stern–Geary Relationship to Determine Instantaneous Corrosion Rates in Macro-Cell Corrosion’. *Materials and Corrosion* 66 (10): 1017–28. <https://doi.org/10.1002/maco.201407997>.
- Angst, Ueli, Bernhard Elsener, Claus K. Larsen, and Øystein Vennesland. 2009. ‘Critical Chloride Content in Reinforced Concrete — A Review’. *Cement and Concrete Research* 39 (12): 1122–38. <https://doi.org/10.1016/j.cemconres.2009.08.006>.
- Angst, Ueli M., Carolina Boschmann, Matthias Wagner, and Bernhard Elsener. 2017. ‘Experimental Protocol to Determine the Chloride Threshold Value for Corrosion in Samples Taken from Reinforced Concrete Structures’. *Journal of Visualized Experiments : JoVE*, no. 126 (August): 56229. <https://doi.org/10.3791/56229>.
- Angst, Ueli M., O. Burkan Isgor, Carolyn M. Hansson, Alberto Sagüés, and Mette Rika Geiker. 2022. ‘Beyond the Chloride Threshold Concept for Predicting Corrosion of Steel in Concrete’. *Applied Physics Reviews* 9 (1): 011321. <https://doi.org/10.1063/5.0076320>.
- Aperador Chaparro, William, Jorge Hernando Bautista Ruiz, and Robinson De Jesús Torres Gómez. 2011. ‘Corrosion of Reinforcing Bars Embedded in Alkali-Activated Slag Concrete Subjected to Chloride Attack’. *Materials Research* 15 (1): 57–62. <https://doi.org/10.1590/S1516-14392011005000096>.
- ASTM International. 2012. ‘ASTM G01-03: Standard Practice for Preparing, Cleaning, and Evaluating Corrosion Test Specimens’.

- ASTM International. 2022. ‘ASTM C876-22b: Standard Test Method for Corrosion Potentials of Uncoated Reinforcing Steel in Concrete’.
- Azarsa, Pejman, and Rishi Gupta. 2017. ‘Electrical Resistivity of Concrete for Durability Evaluation: A Review’. *Advances in Materials Science and Engineering* 2017: 1–30. <https://doi.org/10.1155/2017/8453095>.
- Bertolini, L, F Lollini, and E Redaelli. 2007. ‘Influence of Concrete Composition on Parameters Related to the Durability of Reinforced Concrete Structures.’ In . Guimarães, Portugal.
- Bu, Yiwen, and Jason Weiss. 2014. ‘The Influence of Alkali Content on the Electrical Resistivity and Transport Properties of Cementitious Materials’. *Cement and Concrete Composites* 51 (August): 49–58. <https://doi.org/10.1016/j.cemconcomp.2014.02.008>.
- Bui, Huy Tang, Koichi Maekawa, and Kang Hai Tan. 2023. “Microcell and Macrocell Corrosion of Steel Bars in Reinforced Concrete Slabs under Different Corrosive Environments and Cathode/Anode Configurations.” *Cement and Concrete Composites* 138 (April): 104989. <https://doi.org/10.1016/j.cemconcomp.2023.104989>.
- Carrinho, Diogo José Scheepers. 2018. ‘Resistance to Chloride-Ion Penetration of Different Concrete Mixtures Subjected to Long-Term Immersion Tests’. *Materials Science*, 11.
- Chalhoub, Chantal. 2020. ‘Study of the Initiation and Propagation Phases of Chloride Induced Corrosion in Reinforced Concrete Structures’. Thesis, Toulouse: Université Toulouse 3 Paul Sabatier.
- Chalhoub, Chantal, Raoul François, and Myriam Carcasses. 2019. ‘Determination of Chloride Threshold Initiating Corrosion: A New Set-up Taking the Localized Aspect of Corrosion into Account’. *Cement and Concrete Research* 124 (October): 105825. <https://doi.org/10.1016/j.cemconres.2019.105825>.
- Chalhoub, Chantal, Raoul François, David Garcia, Stephane Laurens, and Myriam Carcasses. 2020. ‘Macrocell Corrosion of Steel in Concrete: Characterization of Anodic Behavior in Relation to the Chloride Content’. *Materials and Corrosion* 71 (9): 1424–41. <https://doi.org/10.1002/maco.201911398>.
- Criado, Bernal, Garcia-Triñanes, and Provis. 2018. ‘Influence of Slag Composition on the Stability of Steel in Alkali-Activated Cementitious Materials’. *Journal of Materials Science* 53 (7): 5016–35. <https://doi.org/10.1007/s10853-017-1919-3>.
- Criado, Mundra, Bernal, and Provis. 2018. ‘Influence of Sulfide on the Onset of Chloride-Induced Corrosion of Steel Reinforcement in Alkali-Activated Slags’. *Basheer, PAM, (Ed.) Durability of Concrete Structures - Sixth International Conference on the Durability of Concrete Structures, Leeds, UK*, 149–53.
- Criado, and Provis. 2018. ‘Alkali Activated Slag Mortars Provide High Resistance to Chloride-Induced Corrosion of Steel’. *Frontiers in Materials* 5 (June): 34. <https://doi.org/10.3389/fmats.2018.00034>.
- Diab, Ahmed M., Ali A. Aliabdo, and Ismail A. Mohamed. 2015. ‘Corrosion Behaviour of Reinforced Steel in Concrete with Ground Limestone Partial Cement Replacement’. *Magazine of Concrete Research* 67 (14): 747–61. <https://doi.org/10.1680/mac.14.00156>.
- Diab, Ahmed M., Ismail A. Mohamed, and Ali A. Aliabdo. 2016. ‘Impact of Organic Carbon on Hardened Properties and Durability of Limestone Cement Concrete’. *Construction and Building Materials* 102 (January): 688–98. <https://doi.org/10.1016/j.conbuildmat.2015.10.182>.
- Divet, Loïc, and Robert Le Roy. 2013. ‘Étude de La Durabilité Vis-à-Vis de La Corrosion Des Armatures Des Bétons Formulés Avec Des Ciments à Forte Teneur En Laitier de Haut Fourneau’. *BLPC*, no. 280–281 (November).
- Elgalhud, Abdurrahman A., Ravindra K. Dhir, and Gurmel Ghataora. 2018. ‘Chloride Ingress in Concrete: Limestone Addition Effects’. *Magazine of Concrete Research* 70 (6): 292–313. <https://doi.org/10.1680/jmacr.17.00177>.



- Gartner, Nina, Miha Hren, Tadeja Kosec, and Andraž Legat. 2021. 'Characterizing Steel Corrosion in Different Alkali-Activated Mortars'. *Materials* 14 (23): 7366. <https://doi.org/10.3390/ma14237366>.
- Habert, G., S. A. Miller, V. M. John, J. L. Provis, A. Favier, A. Horvath, and K. L. Scrivener. 2020. 'Environmental Impacts and Decarbonization Strategies in the Cement and Concrete Industries'. *Nature Reviews Earth & Environment* 1 (11): 559–73. <https://doi.org/10.1038/s43017-020-0093-3>.
- Hornain, H. 2007. 'GrandDuBé : Grandeurs Associées à La Durabilité Des Bétons'. *Presses Des Ponts*.
- Hornbostel, Karla, Claus K. Larsen, and Mette R. Geiker. 2013. 'Relationship between Concrete Resistivity and Corrosion Rate – A Literature Review'. *Cement and Concrete Composites* 39 (May): 60–72. <https://doi.org/10.1016/j.cemconcomp.2013.03.019>.
- IREX. 2022. 'Projet National PERFDUB'. 2022. <https://www.perfdub.fr/>.
- Ismail, Idawati, Susan A. Bernal, John L. Provis, Sinin Hamdan, and Jannie S. J. van Deventer. 2013. 'Drying-Induced Changes in the Structure of Alkali-Activated Pastes'. *Journal of Materials Science* 48 (9): 3566–77. <https://doi.org/10.1007/s10853-013-7152-9>.
- Jiang, Zhilu, Siyao Li, Chuanqing Fu, Zheng Dong, Xuefeng Zhang, Nanguo Jin, and Tian Xia. 2021. 'Macrocell Corrosion of Steel in Concrete under Carbonation, Internal Chloride Admixing and Accelerated Chloride Penetration Conditions'. *Materials* 14 (24): 7691. <https://doi.org/10.3390/ma14247691>.
- Laurens, S., P. Hénocq, N. Rouleau, F. Deby, E. Samson, J. Marchand, and B. Bissonnette. 2016. 'Steady-State Polarization Response of Chloride-Induced Macrocell Corrosion Systems in Steel Reinforced Concrete — Numerical and Experimental Investigations'. *Cement and Concrete Research* 79 (January): 272–90. <https://doi.org/10.1016/j.cemconres.2015.09.021>.
- Li, Dawang, Ren Wei, L. Li, Xiaotao Guan, and Xuming Mi. 2019. 'Pitting Corrosion of Reinforcing Steel Bars in Chloride Contaminated Concrete'. *Construction and Building Materials* 199 (February): 359–68. <https://doi.org/10.1016/j.conbuildmat.2018.12.003>.
- Lliso-Ferrando, J.R., I. Gasch, A. Martínez-Ibernón, and M. Valcuende. 2022. 'Effect of Macrocell Currents on Rebar Corrosion in Reinforced Concrete Structures Exposed to a Marine Environment'. *Ocean Engineering* 257 (August): 111680. <https://doi.org/10.1016/j.oceaneng.2022.111680>.
- Lollini, Federica, Elena Redaelli, and Luca Bertolini. 2014. 'Effects of Portland Cement Replacement with Limestone on the Properties of Hardened Concrete'. *Cement and Concrete Composites* 46 (February): 32–40. <https://doi.org/10.1016/j.cemconcomp.2013.10.016>.
- Lollini, Federica, Elena Redaelli, and Luca Bertolini. 2016. 'A Study on the Applicability of the Efficiency Factor of Supplementary Cementitious Materials to Durability Properties'. *Construction and Building Materials* 120 (September): 284–92. <https://doi.org/10.1016/j.conbuildmat.2016.05.031>.
- Ma, Qianmin, Sreejith V. Nanukuttan, P. A. Muhammed Basheer, Yun Bai, and Changhui Yang. 2016. 'Chloride Transport and the Resulting Corrosion of Steel Bars in Alkali Activated Slag Concretes'. *Materials and Structures* 49 (9): 3663–77. <https://doi.org/10.1617/s11527-015-0747-7>.
- Mangat, P. S., Olalekan O. Ojedokun, and Paul Lambert. 2021. 'Chloride-Initiated Corrosion in Alkali Activated Reinforced Concrete'. *Cement and Concrete Composites* 115 (January): 103823. <https://doi.org/10.1016/j.cemconcomp.2020.103823>.
- Masoudi, Rana. 2018. 'Examining Compositions, Hydration Mechanisms and Properties of Supersulfated Cement for Use in Concrete'. University of Toronto.

- Mundra, Shishir, Susan A. Bernal, Maria Criado, Petr Hlaváček, Gino Ebell, Steffi Reinemann, Gregor J.G. Gluth, and John L. Provis. 2017. ‘Steel Corrosion in Reinforced Alkali-Activated Materials’. *RILEM Technical Letters* 2 (December): 33–39. <https://doi.org/10.21809/rilemtechlett.2017.39>.
- Mundra, Shishir, Maria Criado, Susan A. Bernal, and John L. Provis. 2017. ‘Chloride-Induced Corrosion of Steel Rebars in Simulated Pore Solutions of Alkali-Activated Concretes’. *Cement and Concrete Research* 100 (October): 385–97. <https://doi.org/10.1016/j.cemconres.2017.08.006>.
- Mundra, Shishir, and John L. Provis. 2021. ‘Mechanisms of Passivation and Chloride-Induced Corrosion of Mild Steel in Sulfide-Containing Alkaline Solutions’. *Journal of Materials Science* 56 (26): 14783–802. <https://doi.org/10.1007/s10853-021-06237-x>.
- Mundra, Shishir, Gabriel Samson, Giulia Masi, Rebecca Achenbach, David M. Bastidas, Susan A. Bernal, Maria C. Bignozzi, et al. 2023. ‘Application of Electrochemical Methods for Studying Steel Corrosion in Alkali-activated Materials’. *Materials and Corrosion*, February, maco.202313743. <https://doi.org/10.1002/maco.202313743>.
- Nasser, A., A. Clément, S. Laurens, and A. Castel. 2010. ‘Influence of Steel–Concrete Interface Condition on Galvanic Corrosion Currents in Carbonated Concrete’. *Corrosion Science* 52 (9): 2878–90. <https://doi.org/10.1016/j.corsci.2010.04.037>.
- Nasser, Abdelkader, and Arnaud Castel. 2014. ‘Microcell versus Galvanic Corrosion Currents in Carbonated Concrete’. *Magazine of Concrete Research* 66 (July): 697–707. <https://doi.org/10.1680/macr.13.00214>.
- Nguyen, Khanh Son, Anh Toan Nguyen-Phung, Hong Thai Le, Thanh Tri Ho, Tri Huynh Nguyen-Ngoc, Soon Poh Yap, Nobuhiro Chijiwa, and Nobuaki Otsuki. 2018. ‘Chloride Binding Ability and Anti-Corrosion Properties of Supersulfated Cement in Seawater/Sand Mixing Concrete’. In *Proceedings of the 4th Congrès International de Géotechnique - Ouvrages -Structures*, edited by Hoang-Hung Tran-Nguyen, Henry Wong, Frederic Ragueneau, and Cuong Ha-Minh, 8:367–76. Singapore: Springer Singapore. [https://doi.org/10.1007/978-981-10-6713-6\\_36](https://doi.org/10.1007/978-981-10-6713-6_36).
- Nguyen, Thi-Thu, Raoul Francois, Tru Vu, and Myriam Carcasses. 2022. ‘A Comparison between Uniform and Galvanic Corrosion Rate in Carbonation Induced Corrosion of Reinforced Concrete’. *MATEC Web of Conferences* 364 (September). <https://doi.org/10.1051/mateconf/202236402025>.
- Noushini, Amin. 2018. ‘Durability of Geopolymer Concrete in Marine Environment’. Sydney, Australia: The University of New South Wales.
- Raupach, M. 1996. ‘Chloride-Induced Macrocell Corrosion of Steel in Concrete—Theoretical Background and Practical Consequences’. *Construction and Building Materials, Durability of Reinforced Concrete Structures*, 10 (5): 329–38. [https://doi.org/10.1016/0950-0618\(95\)00018-6](https://doi.org/10.1016/0950-0618(95)00018-6).
- Revert, Andres Belda, Karla Hornbostel, Klaartje De Weerd, and Mette Rica Geiker. 2019. ‘Macrocell Corrosion in Carbonated Portland and Portland-Fly Ash Concrete - Contribution and Mechanism’. *Cement and Concrete Research* 116 (February): 273–83. <https://doi.org/10.1016/j.cemconres.2018.12.005>.
- Rodrigues, Romain, Stéphane Gaboreau, Julien Gance, Ioannis Ignatiadis, and Stéphanie Betelu. 2020. ‘Corrosion of Carbon Steel in Concrete: Current Knowledge of Corrosion Mechanisms and Non-Destructive Testing of Corrosion Rates’.
- Roy, Della M, Weimin Jiang, and M. R Silsbee. 2000. ‘Chloride Diffusion in Ordinary, Blended, and Alkali-Activated Cement Pastes and Its Relation to Other Properties’. *Cement and Concrete Research, Papers presented at the Symposium on ‘Transport Properties and Microstructure of Cement-Based Systems’*, 30 (12): 1879–84. [https://doi.org/10.1016/S0008-8846\(00\)00406-3](https://doi.org/10.1016/S0008-8846(00)00406-3).

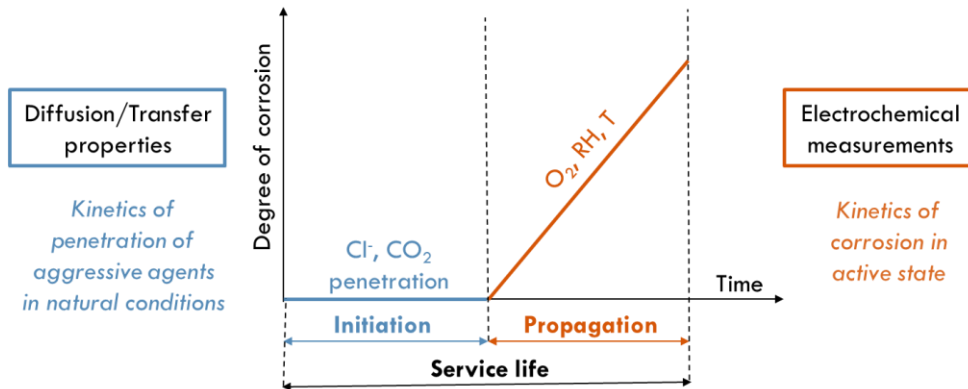
- Runci, Antonino, John L. Provis, and Marijana Serdar. 2023. 'Revealing Corrosion Parameters of Steel in Alkali-Activated Materials'. *Corrosion Science* 210 (January): 110849. <https://doi.org/10.1016/j.corsci.2022.110849>.
- Runci, Antonino, Marijana Serdar, and John Provis. 2019. 'Chloride-Induced Corrosion of Steel Embedded in Alkali-Activated Materials: State of the Art'. *5th Symposium on Doctoral Studies in Civil Engineering, Zagreb, Croatia*.
- Schwartzentruber, A, and C Catherine. 2000. 'Method of the Concrete Equivalent Mortar (CEM) - A New Tool to Design Concrete Containing Admixture'. *Materials and Structures*, October 2000, Vol. 33 edition.
- Scrivener, Karen L., Vanderley M. John, and Ellis M. Gartner. 2018. 'Eco-Efficient Cements: Potential Economically Viable Solutions for a Low-CO2 Cement-Based Materials Industry'. *Cement and Concrete Research* 114 (December): 2–26. <https://doi.org/10.1016/j.cemconres.2018.03.015>.
- Tahri, Walid, Xiang Hu, Caijun Shi, and Zuhua Zhang. 2021. 'Review on Corrosion of Steel Reinforcement in Alkali-Activated Concretes in Chloride-Containing Environments'. *Construction and Building Materials* 293 (July): 123484. <https://doi.org/10.1016/j.conbuildmat.2021.123484>.
- Türkmen, İbrahim, Mehmet Gavgalı, and Rüstem Gül. 2003. 'Influence of Mineral Admixtures on the Mechanical Properties and Corrosion of Steel Embedded in High Strength Concrete'. *Materials Letters* 57 (13): 2037–43. [https://doi.org/10.1016/S0167-577X\(02\)01136-9](https://doi.org/10.1016/S0167-577X(02)01136-9).
- Tuutti, K. 1982. 'Corrosion of Steel in Concrete'. Stockholm: Swedish Cement and Concrete Research Institute,.
- Wang, Wenrui, Huisu Chen, Xiangyu Li, and Zhigang Zhu. 2017. 'Corrosion Behavior of Steel Bars Immersed in Simulated Pore Solutions of Alkali-Activated Slag Mortar'. *Construction and Building Materials* 143 (July): 289–97. <https://doi.org/10.1016/j.conbuildmat.2017.03.132>.
- Warkus, J., and M. Raupach. 2010. 'Modelling of Reinforcement Corrosion – Geometrical Effects on Macrocell Corrosion'. *Materials and Corrosion* 61 (6): 494–504. <https://doi.org/10.1002/maco.200905437>.
- Yang, G., J. Zhao, and Y. Wang. 2022. 'Durability Properties of Sustainable Alkali-Activated Cementitious Materials as Marine Engineering Material: A Review'. *Materials Today Sustainability* 17 (March): 100099. <https://doi.org/10.1016/j.mtsust.2021.100099>.
- Yeau, Kyong Yun, and Eun Kyum Kim. 2005. 'An Experimental Study on Corrosion Resistance of Concrete with Ground Granulate Blast-Furnace Slag'. *Cement and Concrete Research* 35 (7): 1391–99. <https://doi.org/10.1016/j.cemconres.2004.11.010>.
- Zhang, Feng, Xun Xi, and Shangdong Yang. 2021. 'Research Progress in Corrosion Mechanism of Reinforced Alkali-Activated Concrete Structures'. *Corrosion and Materials Degradation* 2 (4): 641–56. <https://doi.org/10.3390/cmd2040034>.
- Zhang, Jingxiao, Yuwei Ma, Jie Hu, Hao Wang, and Zuhua Zhang. 2022. 'Review on Chloride Transport in Alkali-Activated Materials: Role of Precursors, Activators and Admixtures'. *Construction and Building Materials* 328 (April): 127081. <https://doi.org/10.1016/j.conbuildmat.2022.127081>.
- Zhao, Yuxi, Xiaoyi Xu, Yuzhou Wang, and Jianfeng Dong. 2020. 'Characteristics of Pitting Corrosion in an Existing Reinforced Concrete Beam Exposed to Marine Environment'. *Construction and Building Materials* 234 (February): 117392. <https://doi.org/10.1016/j.conbuildmat.2019.117392>.

La mise à jour automatique des citations est désactivée. Pour voir la bibliographie, cliquez sur Actualiser dans l'onglet Zotero.



## Durability of reinforcement in three low-carbon concretes

**Theoretical background:** presentation of binders + classical and galvanic corrosion mechanisms



### CORROSION INITIATION

**Objectives:** Estimate the time taken by the aggressive agents ( $\text{Cl}^-$  or  $\text{CO}_2$ ) to reach the reinforcement. Use reliable and representative test methods.

**Approach:** Characterisation of the general transfer properties, transport of  $\text{Cl}^-$  and  $\text{CO}_2$  on concrete.

#### Article A: General transfer properties and chloride penetration resistance

##### General transfer properties

- Tests:**
- Water porosity
  - Mercury intrusion porosity
  - Water permeability
  - Capillary absorption
  - Gas permeability
  - Resistivity

##### Transport of $\text{Cl}^-$

- Tests:**
- $\text{Cl}^-$  diffusion test
  - RCPT test

#### Article B: Resistance to carbonation

##### Transport of $\text{CO}_2$ and ability to maintain a high pH

- Tests:**
- Carbonation depth (natural, 1%  $\text{CO}_2$ , 3%  $\text{CO}_2$ )
  - pH measurements before and after carbonation of paste samples (natural, 1%  $\text{CO}_2$ )

### CORROSION PROPAGATION

**Objectives:** Evaluate the corrosion rates once the rebars have been depassivated. Use reliable and representative test methods.

**Approach:**

- Development of a methodology adapted to low-carbon binders and representative of real structures: galvanic current measurement + mass loss.
- Comparison with traditional electrochemical tests ( $E_{\text{corr}}$ ,  $\rho$ ,  $R_p$ ,  $i_{\text{corr}}$ , Tafel).

#### Article C: Chloride-induced corrosion

##### Experimental conditions:

- Different levels of chloride contamination:
- $[\text{NaCl}] = 30 \text{ g/L}$  (sea water)
  - $[\text{NaCl}] = 300 \text{ g/L}$  (de-icing salts)
- Saturated conditions

#### Article D: Carbonation-induced corrosion

##### Experimental conditions:

- Natural carbonation outdoor sheltered  
Samples with increased w/b ratio  
3 different moisture conditions tested

**Synthesis chapter:** discussion of articles A, B, C and D

## Transition to Article D

After the focus of corrosion propagation in chloride-rich environments, a similar investigation is performed for carbonation-induced corrosion in [Article D](#).

[Article B](#) already characterized the initiation period of LCK, AAS and SSC exposed to carbonation. The main results in natural conditions, showed the three binders are quite sensitive to carbonation, especially for short curing times, with different carbonation processes involved depending on their hydration products and pore solution chemistry.

In [Article D](#) it is now proposed to focus on the associated propagation period. The objective is to determine if carbonation leads to high corrosion rates in active state, damaging for the structure. The same method as for [Article C](#) is implemented, based on galvanic current measurement combined with mass loss on the rebar, and a comparison with classical electrochemical measurements (corrosion potential  $E_{\text{corr}}$ , polarization resistance  $R_p$ ) is also performed.



## Chapter 6 – Article D

# Carbonation-induced corrosion of steel in three low-carbon concretes studied by galvanic current measurements

## Table of contents

<b>1</b>	<b>Introduction .....</b>	<b>202</b>
<b>2</b>	<b>Materials.....</b>	<b>207</b>
2.1	Raw Materials.....	207
2.2	Mix design.....	207
2.3	Specimen characteristics and preparation: anode and cathode.....	209
<b>3</b>	<b>Test methods .....</b>	<b>214</b>
3.1	Overview of the experimental campaign.....	214
3.2	pH measurement.....	216
3.3	Carbonation front .....	217
3.4	Classic electrochemical measurements .....	217
3.5	Galvanic current measurement.....	221
3.6	Autopsy of the anodes .....	224
<b>4</b>	<b>Results.....</b>	<b>226</b>
4.1	pH measurement.....	226
4.2	Evolution of carbonation fronts.....	226
4.3	Classic electrochemical measurements .....	228
4.4	Galvanic coupling between anode and cathode.....	235
4.5	Classic electrochemical measurement after galvanic coupling .....	238
4.6	Autopsy of the anodes .....	239
<b>5</b>	<b>Discussion .....</b>	<b>243</b>
5.1	Influence of the galvanic coupling on corrosion .....	243
5.2	Total corrosion current (itot): contributions of galvanic current between anode and cathode (ig) and local current at the anode (imi-anode).....	245
5.3	Assessment of the corrosion risk in the three low-carbon concretes considered.....	250
<b>6</b>	<b>Conclusion .....</b>	<b>253</b>
<b>7</b>	<b>Supplementary data.....</b>	<b>254</b>
<b>8</b>	<b>References.....</b>	<b>255</b>





## **Carbonation-induced corrosion of steel in three low-carbon concretes, with different saturation conditions, studied by galvanic current measurements**

Lola Doussang<sup>1</sup>, Gabriel Samson<sup>1</sup>, Fabrice Deby<sup>1</sup>, Bruno Huet<sup>2</sup>, Emmanuel Guillon<sup>2</sup>, Martin Cyr<sup>1</sup>

<sup>1</sup> *Laboratoire des Matériaux et Durabilité des Constructions (LMDC), INSAT/UPS Génie Civil, 135 Avenue de Rangueil, 31077 Toulouse Cedex 04 France.*

<sup>2</sup> *Holcim Innovation Center, 95 rue du Montmurier, F-38070 Saint Quentin Fallavier, France*

### **Abstract**

The corrosion rates due to activation by natural carbonation were assessed in three low-carbon concretes (low clinker (LCK), alkali-activated slag (AAS) and supersulfated cement (SSC)), by both linear polarization resistance method and galvanic current measurement combined with mass loss on the rebar. The galvanic current method, not widely used in the literature, consists in measuring the galvanic current exchanged between an active anode and a passive cathode, spatially separated. Anodes samples with an increased w/b ratio were used to accelerate their corrosion initiation by natural carbonation. Three saturation conditions were tested for the anodes and cathodes, to evaluate an interval of possible corrosion rates due to carbonation: C<sub>w</sub>-A<sub>w</sub> (anode and cathode in water), C<sub>d</sub>-A<sub>d</sub> (dry anode and cathode) and C<sub>d</sub>-A<sub>w</sub> (dry cathode and anode in water). The results show the total corrosion current density due to carbonation is high for the three binders and the different saturation conditions tested. The galvanic current represents around 40 to 50% of the total current for LCK and AAS binders, while only 5 to 10% for SSC. The local current at the anode is high for all the conditions tested. The saturation conditions influence the total corrosion current density, with different behaviors observed for each binder. Higher total corrosion rates are measured for a dry cathode coupled with a saturated anode for LCK and AAS (C<sub>d</sub>-A<sub>w</sub>), this trend is not confirmed for SSC. Finally, LCK performs the best for permanently dry or wet conditions, and AAS for wet conditions. For SSC, lower corrosion rates are measured due to a negligible galvanic current, regardless of the saturation conditions.

### **Keywords**

Galvanic current, Carbonation-induced corrosion, Low-carbon concretes, Durability, Low clinker, Alkali-activated slag, Supersulfated cement

## 1 Introduction

### Context of the study

Carbonation occurs spontaneously in reinforced concrete structures exposed to atmospheric CO<sub>2</sub>. The dissolution of the CO<sub>2</sub> in the concrete pore solution leads to a series of carbonation reactions with the calcium-bearing phases of the cementitious matrix (von Greve-Dierfeld et al. 2020). These reactions are progressively accompanied by a decrease in the pH of the pore solution, which can lead to corrosion initiation when the carbonation front reaches the rebar (Pimienta et al. 2016). In the passive state, the high pH of the concrete favours the creation of a protective layer of iron oxides on the rebar, called the passive film. But for pH below 9, the passive film protecting the rebar becomes unstable and the latter is no longer protected. Corrosion can then occur, if sufficient water and oxygen are present at the steel-concrete interface (SCI).

Low-carbon concretes developed to reduce CO<sub>2</sub> emissions in the construction field have generally higher carbonation rates due to their lower amounts, or even absence, of portlandite to act as pH buffer (von Greve-Dierfeld et al. 2020). However, it was observed from many documented cases from engineering practice reviewed by (Angst et al. 2020), that a carbonated concrete or a reduced pH are not sufficient to lead to significant corrosion or observable damage at the structural level. Even if low-carbon concretes carbonate faster, the real challenge is to know if it leads to significant corrosion of the reinforcements, likely to cause damages for the structure. Until now, indeed, the great majority of the scientific literature focuses on concrete carbonation, and a limited number of studies addressed the associated corrosion rates (Angst et al. 2020). This is particularly true for low-carbon concretes, for which the lack of information related to corrosion of reinforcing still limit their use.

The present study focuses on three different low-carbon concretes, having a reduced carbon footprint, ranging from -40 to -75% (Article B), compared to that of a traditional concrete made only with CEM I: low clinker (LCK) concrete, alkali-activated slag with sodium carbonate (AAS) concrete and supersulfated cement (SSC) concrete. This article evaluates the corrosion kinetics associated to each binder, after complete carbonation in outdoor shelter environment. The initiation phase was investigated in Article B, based on the resistance to carbonation (carbonation rates and ability to maintain a high pH). Corrosion rates and mechanisms associated to carbonation-induced corrosion in CEM I-based concretes have been extensively studied in the literature as it is an important issue for the durability of structures, but little information is available for LCK, AAS and SSC binders.

### Summary of data available in the literature

#### Corrosion rates available for each binder

A summary of the corrosion rates measured in the literature, on the three low-carbon binders studied, is proposed hereafter. They characterize corrosion kinetics at a certain time, temperature, moisture conditions, and cannot be generalized to other exposure conditions. In reality, the corrosion rates will vary over time, according to the local weather (dry or wet conditions, rain, temperature...) (Köliö et al. 2017; Cid Andrade and Castillo 2003; Stefanoni, Angst, and Elsener 2020). Many studies highlight that wet conditions are required to measure

high corrosion rates on carbonated concretes and that the corrosion rates increase with its moisture (Cheng, Maruyama, and Ren 2021; Gonzalez, Algaba, and Andrade 1980; Stefanoni, Angst, and Elsener 2018; Glass, Page, and Short 1991; Dhir, Jones, and McCarthy 1992; Alonso, Andrade, and González 1988).

The **LCK** is a binder made of 27% CEM I and 73% limestone filler in the present study. (Elgalhud, Dhir, and Ghataora 2017) proposes an evaluation of carbonation-induced corrosion resistance of PC with limestone fillers. They reported that only 9 studies deal with the corrosion rates in carbonated concrete in this type of binder. The studies analysed only samples made with 0-25% filler, which is much lower than the substitution level considered in the present study (73%). The general trend observed is that corrosion rates of steel in carbonated concrete increase for an increasing level of cement replacement by fillers (up to a factor of 3 for 25% replacement). The review of corrosion rates in carbonated concretes by (Stefanoni, Angst, and Elsener 2018) reports different ranges of corrosion rates according to the exposure conditions: for PC with limestone fillers, between 0.002 and 0.015  $\mu\text{A}/\text{cm}^2$  for dry conditions (indoor) and between 0.5 and 3  $\mu\text{A}/\text{cm}^2$  at 100% RH, for example from (Moreno, Castro-Borges, and Cob-Sarabia 2004). Further research is nevertheless required to assess the corrosion kinetics in the LCK concrete of the current study (27% CEM I and 73% limestone filler, but a very low water-cement ratio (0.25)), to confirm these findings.

The **AAS** concrete in the current study is made with slag as calcium-aluminosilicate precursor, combined with a sodium carbonate ( $\text{Na}_2\text{CO}_3$ ) alkaline activator. The carbonation resistance of AAS materials has received much more attention in the literature than the corrosion rates of the rebars in these binders. The review of (F. Zhang, Xi, and Yang 2021) about research progress in corrosion mechanisms of reinforced alkali-activated concretes, concludes that there is a need for new experimental data and methods to measure corrosion rates in these binders to avoid controversial results. The study of (Aperador, Mejía de Gutiérrez, and Bastidas 2009) compared the corrosion rates obtained in carbonated AAS (activated by a mix of NaOH and NaSi) and ordinary Portland cement (OPC) concretes, exposed either to laboratory (0.03%  $\text{CO}_2$ , 65% RH) or accelerated (3%  $\text{CO}_2$ , 65% RH) conditions. Samples in laboratory conditions remained passive for the duration of the test, but high corrosion rates were measured on AAS concretes carbonated at 3%  $\text{CO}_2$ , compared to lower corrosion rates for OPC: 1.5  $\mu\text{A}/\text{cm}^2$  for AAS and less than 0.1  $\mu\text{A}/\text{cm}^2$  for OPC, after total carbonation. Similar conclusions were found on concrete samples by (K. Zhao et al. 2020) and by (Bakharev, Sanjayan, and Cheng 2001), with investigations done in simulated pore solutions. However, complementary investigations in natural conditions are necessary to confirm these conclusions. More studies focusing on  $\text{Na}_2\text{CO}_3$ -based activation are also required.

The composition of the **SSC** binder is defined by the European standard EN 15743 (AFNOR 2010). No information regarding the corrosion kinetics has been found in the literature for SSC, and more generally no electrochemical characterization, to the author's knowledge. The durability studies on SSC concretes highlight a lower resistance to carbonation in general, especially for short curing times, due to rapid carbonation rates and a low ability to maintain a high pH (Article B) (Ioannou 2012; Divet and Le Roy 2013). Nevertheless, further studies are

needed to determine if the corrosion initiation is associated with high corrosion kinetics in this binder.

#### Microcell and macrocell systems

Carbonation in reinforced concrete structures generally leads to an uniform depassivation of the first steel layer (modulo the offsets related to the heterogeneity of the concrete and spatial variation of the carbonation depth). It will then act both as an anode site for the oxidation of iron and cathode for the reduction of dissolved oxygen. This type of uniform corrosion caused by carbonation is also frequently called microcell corrosion. However, it would be abusive to assume only a uniform corrosion system because the active rebar (anode) is electrically connected to the rest of the passive rebar network (cathode). As the cathodic reaction is partly carried out at the passive sites spatially separated from the active sites, this leads to galvanic corrosion (also called macrocell corrosion), in addition to uniform corrosion (T.-T. Nguyen et al. 2022; Laurens et al. 2016). The concrete resistivity is an important parameter, because it strongly influences the galvanic ionic current exchanged (T.-T. Nguyen et al. 2022).

As reported by (Angst et al. 2020), studies available in the literature on Portland cement concretes show that galvanic currents can significantly increase the corrosion rates by a factor 2 or 3 (Revert et al. 2019; Menzel 1988; Fritz Hunkeler and von Greve-Dierfeld 2019). Similar conclusions were found by (Abdelkader Nasser and Castel 2014; A. Nasser et al. 2010; Castel and Nasser 2015). No data could be found on the influence of galvanic current in the three low-carbon concretes of the study. Further research is therefore needed, because due to their different chemical composition and pore structure, their resistivity and pore solution are different. It may influence the processes of corrosion and lead to differences in behaviour compared to Portland cement (especially for AAS and SSC).

#### Conclusion of the introduction and interest of the article

As summarized by (Angst et al. 2020), “the focus in research should shift from studying carbonation to studying corrosion of steel in carbonated concrete”, to promote the use of low-carbon concretes. That is why this article proposes a characterization of the corrosion kinetics in three low-carbon concretes (LCK, AAS and SSC), for which little information is available in the literature. The objective is to evaluate their performance in this environment, from the assessment of the durability of reinforcement. Complementary studies about the corrosion rates in LCK concrete are required, as the data available are limited and focus only on limestone filler replacement ranging from 0 to 25%. For AAS, no studies were performed on sodium carbonate activation and investigations in natural conditions are necessary, to avoid an overestimation of the corrosion kinetics. Finally, the absence of experimental data about corrosion rates in SSC carbonated concretes, justifies the study in this paper. Existing studies conducted on OPC-based binders, also reports the non-negligible increase of corrosion currents in carbonated reinforced structures, due to a galvanic corrosion between spatially separated active (steel in carbonated concrete) and passive (steel in sound concrete) rebars.

Therefore, the present study aims to fill this gap, by providing experimental data of corrosion rates in LCK, AAS and SSC carbonated concretes, considering both the local and galvanic

currents. For this purpose, an original approach based on both linear polarization resistance method and galvanic current measurement, associated to mass loss of the rebar, is proposed. Galvanic coupling is a method that allows to measure the galvanic current ( $I_g$ ) flowing between an anode (active reinforced mortar) and a cathode (passive reinforced concrete) spatially separated. This method, not widely used in the literature, has already been validated on PC-based binders (Revert et al. 2019; T.-T. Nguyen et al. 2022; A. Nasser et al. 2010; Sohail et al. 2015). The aim is to apply it to these three low-carbon concretes, for which no data is available.

Finally, one of the most important factor identified to influence the corrosion rates is the moisture state at the rebar. Therefore, three moisture conditions were tested for the anodes and cathodes, to evaluate an interval of possible corrosion rates due to carbonation:  $C_w-A_w$  (anode and cathode in water),  $C_d-A_d$  (dry anode and cathode) and  $C_d-A_w$  (dry cathode and anode in water).

## Nomenclature

### ABBREVIATIONS

**AAS** alkali-activated slag  
**C/A** cathode to anode surface ratio  
**CE** counter electrode  
**GGBS** ground granulated blast furnace slag  
**LCK** low clinker content  
**LPR** linear polarization resistance  
**OCP** open circuit potential  
**PC** Portland cement  
**RE** reference electrode  
**SCI** steel/concrete interface  
**SSC** supersulfated cement  
**w/b** water to binder ratio  
**WE** working electrode  
**ZRA** zero resistance ammeter

### SYMBOLS

**B** constant from Stern-Geary relation, calculated from Tafel test [V]  
 **$\beta_a$**  anodic Tafel slope [V/dec]  
 **$\beta_c$**  cathodic Tafel slope [V/dec]  
 **$E_{\text{corr}}$**  corrosion potential [mV/ref]  
 **$i_g$**  apparent galvanic current density [ $\mu\text{A}/\text{cm}^2$ ]  
 **$I_g$**  galvanic current [ $\mu\text{A}$ ]  
 **$i_{\text{mi-anode}}$**  apparent local current density at anode scale, calculated [ $\mu\text{A}/\text{cm}^2$ ]  
 **$i_{\text{mi-Rp}}$**  apparent current density obtained by LPR measurement [ $\mu\text{A}/\text{cm}^2$ ]  
 **$i_{\text{mi-Tafel}}$**  apparent current density obtained by fitting the polarization curve from Tafel test with the Butler-Volmer equation [ $\mu\text{A}/\text{cm}^2$ ]  
 **$i_{\text{tot}}$**  total current density [ $\mu\text{A}/\text{cm}^2$ ]  
 **$I_{\text{tot}}$**  total current [ $\mu\text{A}$ ]  
 **$R_e$**  electrolyte resistance [ $\Omega$ ]  
 **$R_p$**  value of linear polarization resistance [ $\Omega.\text{cm}^2$ ]  
 **$\Delta E_{\text{A-C}}$**  potential difference between anode (A) and cathode (C):  $E_A - E_C$  [mV]  
 **$\rho$**  resistivity [ $\Omega.\text{m}$ ]

## 2 Materials

### 2.1 Raw Materials

The chemical composition of raw materials used in low clinker content (LCK), alkali-activated slag (AAS) and supersulfated cement (SSC) concretes and mortars, determined by X-ray fluorescence (XRF), are given in Table 34. The Blaine specific surfaces of CEM I, GGBS and limestone filler are 3900, 5500 and 5490 cm<sup>2</sup>/g, respectively.

Table 34: Chemical composition of cements and slag (% in mass) used in LCK, AAS and SSC concretes and mortars, determined by XRF.

	Chemical composition (% in mass)								
	CaO	SiO <sub>2</sub>	Al <sub>2</sub> O <sub>3</sub>	MgO	Fe <sub>2</sub> O <sub>3</sub>	K <sub>2</sub> O	Na <sub>2</sub> O	SO <sub>3</sub>	TiO <sub>2</sub>
CEM I	64.7	20.4	3.9	0.8	5.0	0.6	0.1	2.8	0.2
CEM III/B	50.5	37.7	8.1	4.5	1.9	0.5	0.2	2.0	0.5
GGBS	42.9	37.7	10.3	6.5	0.3	0.4	0.2	1.6	0.7

For the concrete design, the semi-crushed alluvial mix of aggregates ranged from 0 to 20 mm for LCK and from 0 to 16 mm for AAS and SSC. As for the mortar design, a normalized sand CEN EN 196-1, ranging from 0 to 2 mm, was used for practical reasons.

### 2.2 Mix design

The three low-carbon concretes studied are designed to be C25/30 and also self-compacting (spread class SF1). Their respective compositions, as well as some properties at fresh and hardened state, are detailed in Table 35. The binder of the LCK is made with 27% CEM I and 73% limestone filler, while AAS and SSC are both slag-based binders activated either by sodium carbonate and quicklime or by anhydrite and CEM III/B, respectively. Water reducing agents are used to improve the workability at fresh state for all mixes. The three concretes studied are considered as « low-carbon » because they have a significant reduced carbon footprint (Table 35) compared to the one of a standard concrete made with CEM I of similar strength (C25/30) which is around 207 kg eq. CO<sub>2</sub>/m<sup>3</sup> (Article B). The compressive strengths given in Table 35 are obtained on cylindrical samples Φ110 mm x 220 mm for concrete and on 40 mm x 40 mm x 160 mm samples for mortar.



Table 35: Composition and characteristics at fresh and hardened state of LCK, AAS and SSC concretes and mortars.

	<b>Concrete</b>			<b>Mortar</b> <i>with increased w/b</i>		
	<b>LCK</b>	<b>AAS</b>	<b>SSC</b>	<b>LCK</b> w/b ↑40%	<b>AAS</b> w/b ↑20%	<b>SSC</b> w/b ↑20%
<b>Composition (kg)</b>						
<i>CEM I</i>	136.8			162.3		
<i>Limestone filler</i>	375.0		49.1	445.0		58.7
<i>GGBS</i>		481.7	329.3		560.7	393.9
<i>Na<sub>2</sub>CO<sub>3</sub></i>		20.3			23.6	
<i>Quicklime</i>		5.1			5.9	
<i>Anhydrite</i>			29.6			35.4
<i>CEM III/B</i>			11.1			13.3
<i>Water reducing agent</i>	6.02	11.15	5.1	7.1	13.0	6.1
<i>Normalized sand (0-2 mm)</i>				1520.4	1269.6	1407.8
<i>Sand (0-5 mm)</i>	678.5	686.5	739.7			
<i>Fine aggregates (5-10 mm)</i>	272.1	609.6	656.9			
<i>Coarse aggregates (&gt; 10 mm)</i>	827.1	229.6	247.4			
<i>Total water</i>	130.0	220.0	210.0	194.1	288.8	280.9
<b>Mixture parameters</b>						
<i>w/b ratio</i>	0.25	0.43	0.50	0.32	0.49	0.56
<i>w<sub>eff</sub>/b ratio</i>	0.22	0.40	0.46	0.31	0.48	0.55
<i>Theoretical specific gravity (kg/m<sup>3</sup>)</i>	2425.5	2263.8	2278.2	2336.1	2174.7	2202.2
<i>Paste volume (L/m<sup>3</sup>)</i>	318	407	360	417	506	461
<i>CO<sub>2</sub> footprint (eq. CO<sub>2</sub>/m<sup>3</sup>)</i>	122	104	50			
<b>Characteristics at fresh and hardened state</b>						
<i>Inversed cone flow rate (rheology) (seconds)</i>	9.7	1.7	2.0			
<i>Cone spread (mm)</i>	525	580	490			
<i>Air content (%)</i>	1.3	1.2	1.8			
<i>28 days compressive strength (MPa)</i>	33.0	33.3	32.0	23.7	23.7	19.2

For the needs of the experimental campaign, to achieve low material cover, the concrete compositions presented above were adapted to the mortar scale, using the concrete equivalent mortar method (Schwartzentruber and Catherine 2000). As they explained, “its principle is to design a mortar, deduced from the concrete composition and called concrete equivalent mortar”, for which the rheological properties are similar to those of concrete. It consists in keeping the specific surface of aggregates constant between the concrete and the mortar. In

return, the quantity of paste is increased during the change of scale (Table 35). In order to accelerate the arrival of the carbonation front (natural carbonation) at the reinforcement (and thus initiate the corrosion process), and thus to have an activation of the anodes in a reasonable time, it was chosen to increase the w/b ratios of each mortar. As detailed in section 3.1, it was chosen to work in natural carbonation rather than accelerated carbonation, to avoid the modification of carbonation products formed, leading to lower pH for AAS in accelerated conditions (S. A. Bernal et al. 2012). However, it may increase the corrosion process. The w/b ratio of the AAS and SSC mortars are increased by 20% compared to the concretes and that of LCK is increased by 40% due to the high compactness of this mixture (reduced transfer properties, as studied in Article A). A normalized sand CEN EN 196-1 (0-2 mm) is used to make the mortar, instead of the same sand used for the concrete, for practical reasons. To take into account the difference in water absorption between the aggregates, the water content of the mortar is corrected to match that of the concrete. Finally, compressive strength tests after 28 days of curing are carried out, to evaluate and compare the properties of the mortar with those of the initial concrete (Table 35). The results show lower compressive strengths on mortar samples, mainly due to the increase in the w/b ratio, as well as higher paste content and a different type of aggregates.

Finally, LCK, AAS and SSC pastes samples with unmodified w/b ratio (same as concrete) and with increased w/b (same as mortar), are also made to perform pH measurements, presented in more detail in section 3.2.

## ***2.3 Specimen characteristics and preparation: anode and cathode***

### ***2.3.1 Geometry***

Two types of samples are used for this experiment: anodes (reinforced mortar) and cathodes (reinforced concrete). The dimensions and geometries of each are presented in Figure 62. The anode is made of mortar to have a small sample size. The small cover (8.5 mm) allows to reduce the arrival time of the carbonation front to the rebar, while the small size rebar compared to the cathode (ratio of 55) allows to maximize the exchanged current values (Revert et al. 2019; Chalhoub, François, and Carcasses 2019; Andrade et al. 1992).

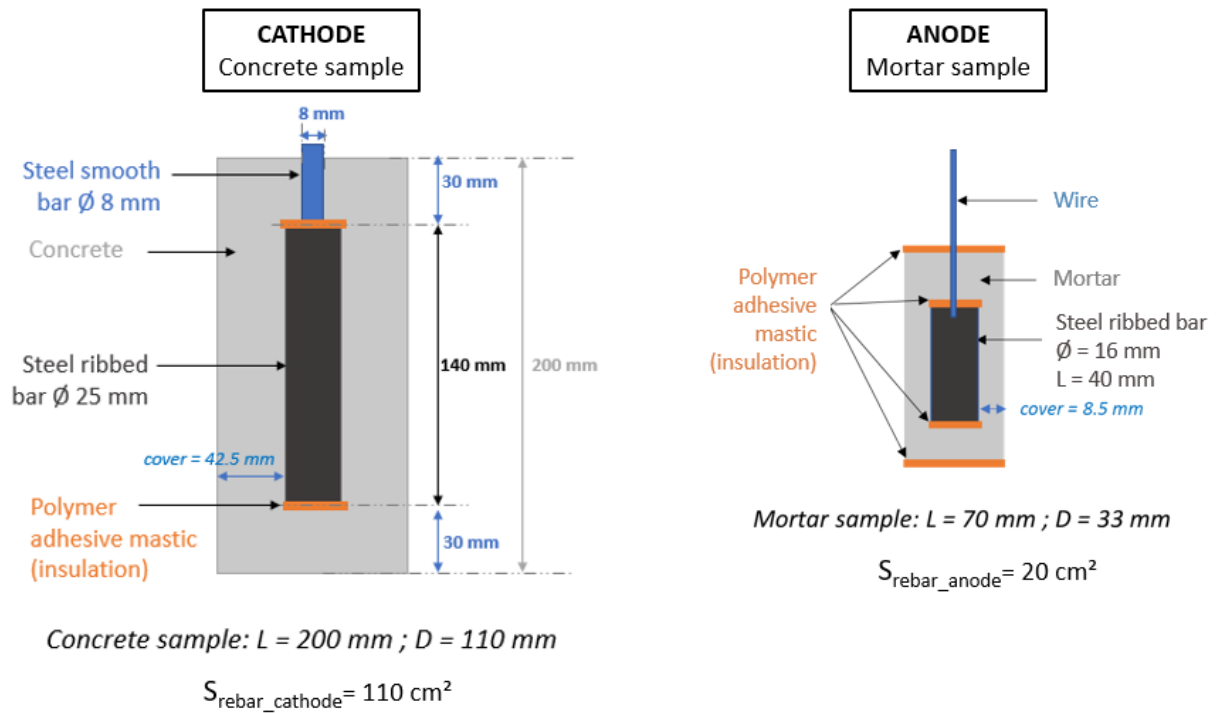


Figure 62: Geometry of the cathodes and anodes.

### 2.3.2 Preparation of steel rebars

Rebars (ribbed carbon steel) are selected without initial corrosion spots and used “as received”, with the mill scale. Deliberately no cleaning treatment is performed to eliminate the defects of the steel or to have a uniform steel surface, to stay representative of real conditions. Then, rebars are cut with a band saw, at the lengths specified in Figure 63, and one extremity is drilled with a drill machine, at 15 mm depth.

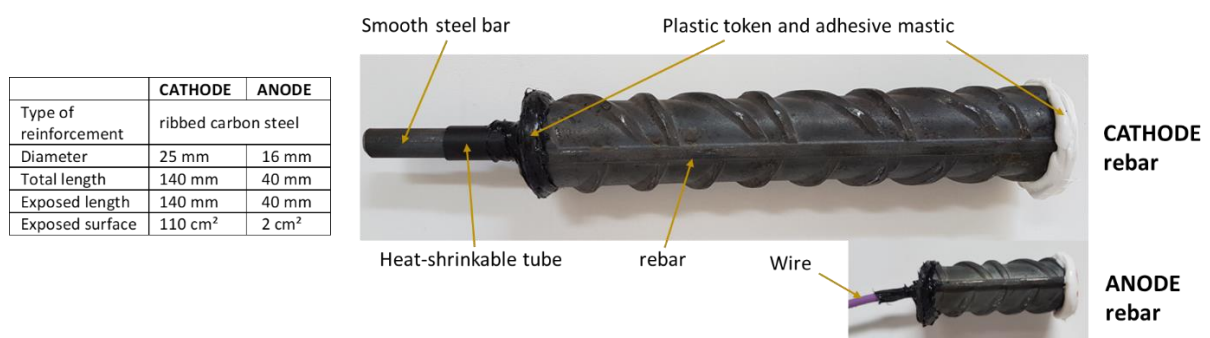


Figure 63: Rebar dimensions and preparation for cathode and anode samples.

The rebar is then cleaned with compressed air and precisely weighted (as initial mass). For cathode samples, a smooth steel bar of 8 mm diameter and 65 mm length (same steel as the rebar to avoid the creation of a galvanic current) is mechanically slotted into the previous drilled extremity of the rebar with a hammer. If needed, the smooth steel bar can be slightly sanded to fit easily with the hole. A good electrical contact between the two pieces of steel is checked with a multimeter. The purpose of this mechanical connection is to avoid the use of welding:

on one hand the tin used for the welding could generate a galvanic current with the rebar and on the other hand it is difficult to remove, which make it unsuitable to make a precise measurement of the loss of mass (section 3.6.1). The smooth steel bar is then covered with a heat-shrinkable tube to avoid polarization that will be applied on the rebar during the electrochemical tests.

The same steps are performed for the anodes, but with an electric wire instead of the smooth steel bar (no need of heat-shrinkable tube as the electrical wire is already protected). Therefore, the steel surfaces in contact with concrete are respectively 110 cm<sup>2</sup> for the cathode and 2 cm<sup>2</sup> for the anode. Finally, to insulate the cut surfaces of the rebar, a plastic token is stuck on each extremity with a polymer adhesive mastic (Bostik MSP 107) and let dry 24h (Figure 63). The goal is to avoid crevice corrosion or galvanic current that could appear between the cut surface and the side surface of the steel ribbed bar because of their different surface condition.

### 2.3.3 Casting

For **cathodes**, concrete samples are cast in a cylindrical cardboard mould (Ø110 x 220 mm) with a cover of 42.5 mm. A polyacetal disc (Ø110 x 20 mm) drilled (Ø 8.4 mm) in its centre, is placed in the bottom of the mould and used to centre the rebar by inserting the smooth steel bar in its hole (Figure 64 and Figure 65). Then, the mould is filled in 3 layers of concrete, each of them being vibrated approximately 30 s holding the rebar by hand. After casting, the surface of concrete specimen is covered with a plastic cover to avoid evaporation. The different steps of preparation for the cathodes are summarized on Figure 64.

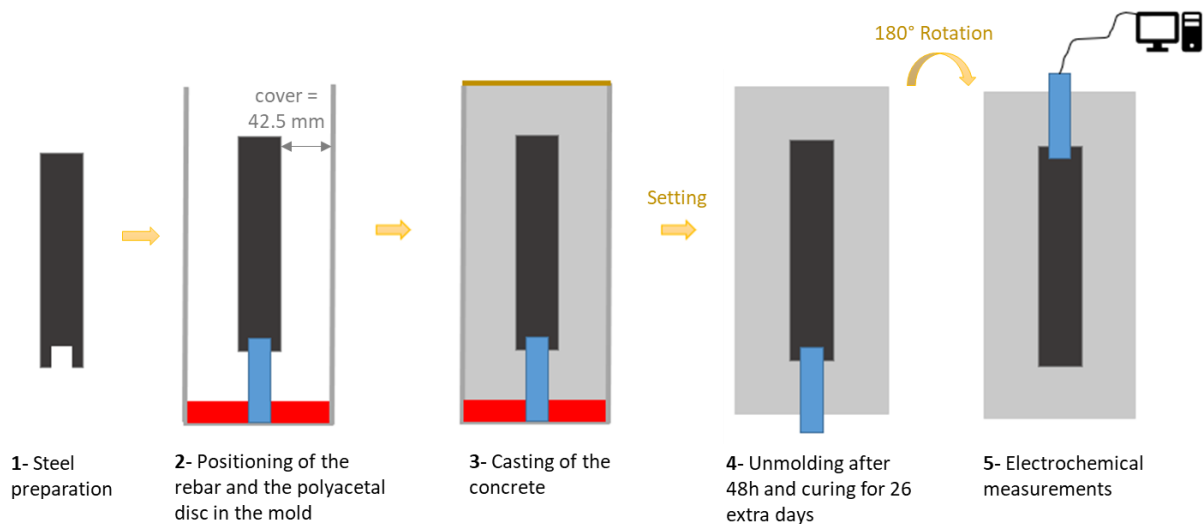


Figure 64: Steps for cathodes preparation.

For **anodes**, mortar samples are cast in a cylindrical plastic mould (Ø33 x 70 mm) with a cover of 8.5 mm. This time, a hole is made in the mould cover, allowing the wire to be adjusted to the desired position to centre the rebar, as illustrated on Figure 65.

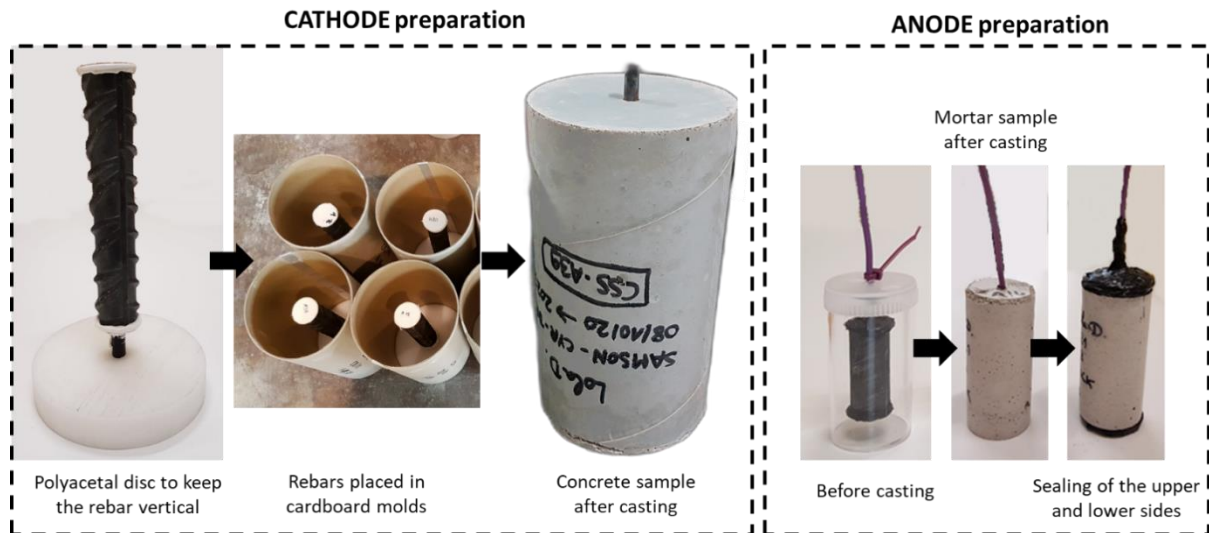


Figure 65: Focus on some main preparation steps for anode and cathode.

#### 2.3.4 Curing and exposure conditions

After the casting, the **cathodes** are placed in a wet curing room at 20 °C, with a relative humidity of approximately 95% and demoulded after 48h. After 14 days of wet curing, half of the cathodes are placed outdoor under shelter and the other half is kept in the wet curing room, as summarized in Table 36. The aim is to have cathodes with two different degrees of saturation for the experimental campaign presented in more detail in the following section 3.1. The cathodes placed outdoor will be mostly dried while those kept in the wet room will remain mostly saturated. The outer cathodes are subject to natural carbonation, but must remain passive for the test. Regular monitoring of the carbonation front on additional unreinforced samples is performed in parallel to ensure that this condition is respected.

After the casting, the **anodes** are placed in the wet curing room, demoulded after 48h and cured for 3 days more in the same room, before being placed in natural outdoor carbonation under shelter at the age of 5 days. During the curing period, the top and bottom surface of the anode are covered with adhesive mastic to ensure a unidirectional penetration of the carbon dioxide later on (Figure 65). The anodes are placed in natural carbonation at a young age for several reasons. On the one hand, 5 days of curing corresponds to the time after which 30 to 50% of the mechanical strength in compression at 28 days has been reached for the three formulas. On the other hand, this will contribute to a faster carbonation of the anodes in addition to the increased w/b, because at 5 days of cure the microstructure of the material is not yet fully developed and part of the water evaporated during the carbonation will not be used for hydration. In parallel, additional anodes are kept in the wet room (no carbonation), as references, throughout the experimental campaign, as summarized in Table 36.

Table 36: Summary of the number of anodes and cathodes and their storage conditions

	Exposure conditions			
	Outdoor under shelter, after...		Wet curing room (95% RH)	
	5 days of curing	14 days of curing		
	Active anodes (100% carbonated)	Passive cathodes (mostly dried)	Passive anodes (references without carbonation)	Passive cathodes (mostly saturated)
<b>LCK</b>	12 samples (w/b ↑40%)	6 samples	4 samples (w/b ↑40%)	6 samples
<b>AAS</b>	12 samples (w/b ↑20%)	6 samples	4 samples (w/b ↑20%)	6 samples
<b>SSC</b>	12 samples (w/b ↑20%)	6 samples	4 samples (w/b ↑20%)	6 samples

### 3 Test methods

#### 3.1 Overview of the experimental campaign

The galvanic current measurement is performed between a cathode (reinforced concrete) and an anode (reinforced mortar) of same formulation, keeping in mind that the anode has an increased w/b ratio compared to the cathode (20% increase for AAS and SSC and 40% increase for LCK, as detailed in 2.2), in order to accelerate its complete carbonation. It was chosen to work in natural carbonation rather than accelerated carbonation, to preserve as much as possible the hydrates and reactions observed in natural conditions and thus to assess the corrosion rates in conditions as close as possible to reality (Article B). Different preparation steps are performed in parallel on anodes and cathodes, as illustrated in Figure 66. The middle boxes summarize the tests performed and the blank ones correspond to the results presented in this paper. The galvanic current measurements used in this study is inspired by the literature (Chalhoub, François, and Carcasses 2019; Revert et al. 2019; T.-T. Nguyen et al. 2022).

The cathodes and anodes are cast and cured, before being characterized a first time after 5 days or 14 days of cure (passive state) for the anodes and cathodes respectively, by classic electrochemical tests presented in section 3.4. Then, as previously detailed in section 2.3.4, half of the cathodes are placed outdoor under shelter and the other half is kept in the wet curing room, to have samples with two different degrees of saturation (mainly dry or mainly saturated) for the galvanic coupling. The cathodes stored outdoor under shelter must remain passive for the coupling, that is why regular monitoring of the evolution of the carbonation front (section 3.3) and the electrochemical parameters (corrosion potential  $E_{\text{corr}}$ , resistivity  $\rho$ , value of linear polarisation resistance  $R_p$ , apparent current density  $i_{\text{mi-Rp}}$ ) is carried out. It was chosen not to dry the cathodes in temperature because of the important volume of samples and because it was observed in a previous study that the preconditioning in temperature is not necessarily adapted to these low-carbon concretes (Article A). Before galvanic coupling, one mainly dry cathode (outdoor under shelter) and one mainly saturated cathode (wet curing room) per formula is discarded to perform a Tafel test (which can change slightly the electrochemical state of the specimen due to high polarization). Then, a splitting and a visual observation of the rebar, allows to attest the absence of corrosion for the cathodes.

In parallel, after 5 days of curing the anodes are placed in natural outdoor carbonation under shelter for one year, which has been determined to be a sufficient time for the carbonation front to reach the rebar and to initiate corrosion, considering the increased w/b ratio, the carbonation exposure at young age and the low mortar cover. To follow the evolution of the carbonation front over time, it is regularly measured on additional unreinforced samples cast at the same time as the anodes (section 3.3). The electrochemical parameters of the reinforced anodes are also measured (corrosion potential  $E_{\text{corr}}$ , resistivity  $\rho$ , linear polarisation resistance  $R_p$ ) as the carbonation progresses (passive then active state). Apparent current density  $i_{\text{mi-Rp}}$  is calculated from  $R_p$ , using the Stern-Geary equation and the B coefficient determined with the Tafel tests (presented after). In parallel, additional anodes are kept exclusively in the wet room (no

carbonation), as references, throughout the experimental campaign. Regular electrochemical measurements are made on these references, at the same times as for the anodes in carbonation.

Finally, galvanic coupling is performed by coupling a passive cathode with an active anode of same formulation, spatially separated, as explained in section 3.5. Since the active steel of the anode has a different corrosion potential  $E_{\text{corr}}$  than the passive steel of the cathode, it generates a galvanic current  $I_g$  between the two, which is recorded for 90 days using a potentiostat. To test the influence of the saturation degree of the anodes and cathodes on the galvanic current, three coupling conditions are tested: (1)  $C_w-A_w$  (anode and cathode in water), (2)  $C_d-A_d$  (dry anode and cathode) and (3)  $C_d-A_w$  (dry cathode and saturated anode). These conditions are presented more in details in section 3.5. The anodes and cathodes used for the measurements in water are immersed one week before the coupling, so that an hydric equilibrium can be created and the electrochemical parameters stabilized in these new conditions before the coupling. In parallel to the three galvanic coupling conditions tested, one anode per formula is kept in natural carbonation (no coupling), in order to compare the current levels measured with and without coupling.

At the end of the coupling, a last electrochemical characterization is performed on anode samples ( $E_{\text{corr}}$ ,  $\rho$ ,  $R_p$ ,  $i_{\text{mi-Rp}}$ ), as well as a Tafel test on passive (references kept in wet room) and active anodes (section 3.4.2). Finally, the anodes not used for the Tafel test, are split to visually observe the presence of corrosion, and then the corrosion products are quantified by a mass loss measurement (section 3.6.1) following ASTM G01-03 (ASTM International 2012). The mass loss obtained is used to calculate the associated total current  $I_{\text{tot}}$  using Faraday's law (section 3.6.2).



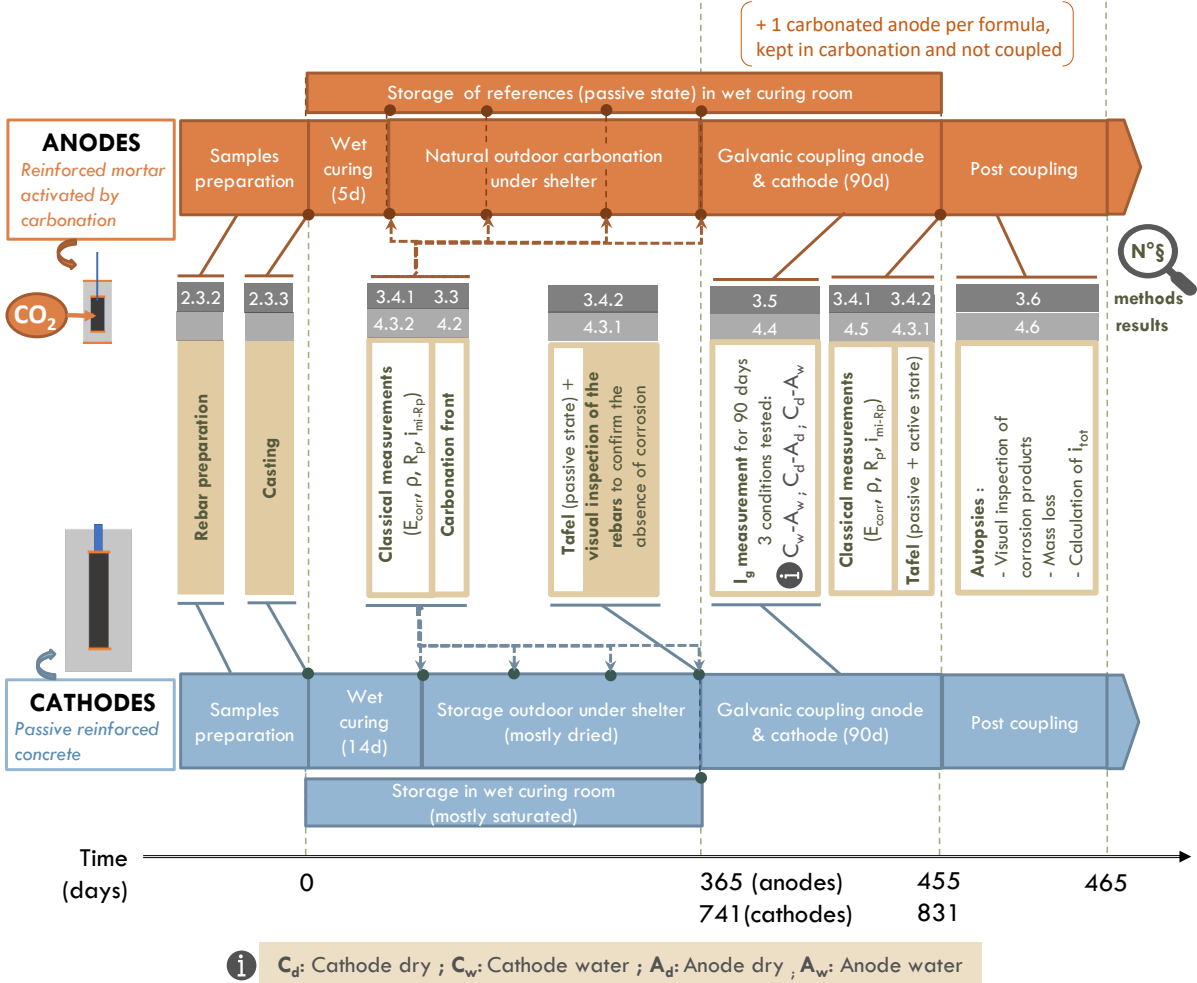


Figure 66: Overview of the experimental campaign associated with the classical measurements and the galvanic current measurement. The blank boxes correspond to the measurements presented in this article. In grey, the paragraph number of the article (methods and results), to which each step refers.

### 3.2 pH measurement

The initial pH of the material is among the important parameters that will condition the initiation of corrosion. The w/b ratio of the anodes having been increased to accelerate the carbonation of the samples, the objective is to check that the pH is not affected by the change of w/b. Therefore, a pH measurement after 38 days of curing (before carbonation) is performed on paste with a w/b ratio identical to that of the concrete (0.25 ; 0.43 and 0.50 for LCK, AAS and SSC, respectively) and compared to the pH measured on paste with an increased w/b ratio as for the anodes (0.32 ; 0.49 and 0.56 for LCK, AAS and SSC, respectively).

For this purpose, pastes were cast in plastic molds Ø33 mm x 70 mm and kept in endogenous cure for 38 days. The "suspension" pH measurement method (W.-C. Wang et al. 2021) is used, because it has been shown in Article B that it is a good compromise between quick measurement and accuracy. Moreover, the results obtained are similar to those obtained by extraction of pore solution (variation lower than 0.2 pH unit). It consists of grinding the sample on which the pH measurement is to be performed into a powder, in less than 15 min (machine RETSCH – RS

100 used for grinding in this study), sieving it with a 80  $\mu\text{m}$  sieve, and then preparing a suspension to be used for the pH measurement by mixing 10 g of powder with 10 mL of demineralized water. This suspension is then mixed for 5 min with a magnetic bar on a magnetic stirring plate (speed of 400 rpm), and the pH measurement is performed immediately after, with a previously calibrated pH-meter.

### 3.3 Carbonation front

The advancement of the carbonation front of mortar ( $\text{Ø}33 \times 70 \text{ mm}$ ) and concrete ( $\text{Ø}110 \times 220 \text{ mm}$ ) samples placed in natural outdoor carbonation under shelter is evaluated according to the standard EN 12390-10 (AFNOR 2018), using both phenolphthalein and rainbow as color indicators. Mortar samples are exposed to natural carbonation after 5 days of curing and the associated carbonation front measured after 46, 60, 90, 107, 144, 182 and 352 days of exposure. Concrete samples are exposed to natural carbonation after 14 days of curing and the associated carbonation front measured after 90, 180, 365 and 748 days of exposure.

### 3.4 Classic electrochemical measurements

#### 3.4.1 Linear polarisation resistance

To measure the classical electrochemical properties of passive and active steel, polarization tests were performed on cathode and anode samples. The linear polarisation resistance (LPR) measurement summarized in Figure 68, allows to obtain different parameters: the resistivity  $\rho$  and the polarization resistance  $R_p$ , and to estimate the apparent current density  $i_{\text{mi-Rp}}$ . The measurement is performed using a BioLogic SP-50 potentiostat. Two different experimental set up are used depending on whether the test is performed on a sample saturated in water or on a dry sample.

When the LPR measurement is carried out on a reinforced sample immersed **in water**, a classic three-electrode set-up is performed, with the reinforcement as working electrode (WE), a reference electrode (RE) Ag/AgCl and a titanium mesh as counter electrode (CE), as illustrated in Figure 67. The sample is immersed in water and not in a NaOH solution (at  $\text{pH} = 12.5$ ), as it was the case for the experimental campaign with chloride contamination, to avoid a re-alkalisation of the carbonated material in the NaOH solution.

When the LPR measurement is carried out on a **dry** sample, the classic three-electrode set up was modified to avoid immersing the dry sample in water and changing too much its hydric equilibrium. It has been highlighted in the literature, indeed, that the degree of saturation of the material has a strong influence on the availability of oxygen to the rebar and on the electrochemical parameters measured: saturated materials are generally characterized by a more electronegative  $E_{\text{corr}}$ , a lower resistivity  $\rho$ , a lower polarization resistance  $R_p$  and a higher corrosion current density  $i_{\text{mi-Rp}}$ , compared to dry materials (Cheng, Maruyama, and Ren 2021; Gonzalez, Algaba, and Andrade 1980; Stefanoni, Angst, and Elsener 2018; Glass, Page, and Short 1991; Dhir, Jones, and McCarthy 1992; Alonso, Andrade, and González 1988). The immersion of a dry sample in water to make a LPR measurement, would therefore lead to

electrochemical parameters not representative of its corrosion state in conditions of natural carbonation (dry sample).

Therefore, to perform the LPR measurement for dry samples, the specimen is wrapped in a soaked and thin sponge (soaked with water). The goal is to have a good electrolytic contact between the sponge and the concrete (or mortar) to realize the polarization measurement without immersing it in water, which could strongly destabilize its internal hydric conditions and therefore the associated electrochemical parameters ( $E_{\text{corr}}$ ,  $\rho$ ,  $R_p$ ,  $i_{\text{mi-Rp}}$ ). The sponge is maintained around the sample by three elastic bands. Sponge electrical resistivity is negligible compared to sample resistivity and it has been verified that its resistance is zero at any point of the sample, which ensures a uniform potential on sponge surface. This modified three-electrode set up considers the reinforcement as working electrode (WE), a reference electrode (RE) Ag/AgCl and the soaked sponge as counter electrode (CE), as illustrated in Figure 67. As the sponge is soaked and covers the whole surface of the sample, it is considered it could replace the classical counter electrode made with titanium mesh, as it guarantees a uniform distribution of the current along the sample. The reference electrode is maintained in contact with the sponge using a clamp attached to a vertical chemistry stand.

Finally, the comparison of both set-up (classical and modified) to apply the LPR measurement on a saturated concrete sample, showed comparable results, as illustrated on Figure 86 in supplementary data.

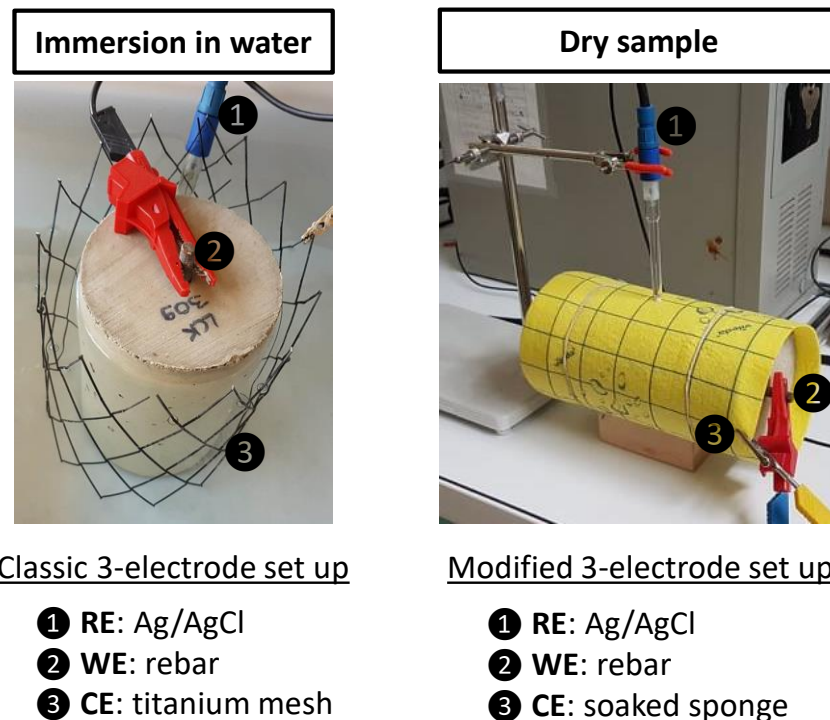


Figure 67: Classic and modified 3-electrode set up used for the LPR measurement, in the case of a sample immersed in water (saturated) or for a dry sample, respectively.

The LPR technique is based on the one described in (Laurens et al. 2016) with some adaptations. First, the corrosion potential  $E_{\text{corr}}$ , also frequently called open circuit potential (OCP) in other studies (Mundra et al. 2023), is recorded and the LPR test is run only when a stable value is measured (variation  $< \pm 1$  mV/5 min). For dry samples, wrapped in a soaked sponge, this condition may take some time to be reached, while a hydric equilibrium is established between the surface of the sample wetted by the sponge and the core of the dry sample. For cathodes that have a significant concrete thickness (42.5 mm of cover), it takes about two to three hours of stabilization after wrapping in the sponge for this criterion to be reached.

Then, the protocol consists in applying five successive potential drops of -15, -7.5, 0, +7.5 and +15 mV, chosen to generate a reversible polarization within a range of  $\pm 15$  mV, with respect to the OCP (Figure 68). Each potential drop lasts 600 s (duration chosen to reach a steady current response) and the data are acquired with a sample period of 0.1 s.

For each potential drop, a current response composed by an instantaneous part and an asymptotic part, is recorded (Figure 68 - right). Based on Ohm law, the instantaneous response for each step enables to determine the electrolyte resistance  $R_e$  that can be converted into resistivity  $\rho$  by multiplying it by a geometric factor  $k$  obtained from a numerical model on the COMSOL Multiphysics<sup>®</sup> finite elements software ( $k = 0.717$  m for cathodes and  $k = 0.428$  m for anodes) (Chalhoub 2020).

The asymptotic response quantified the polarization behavior of the steel by the polarization resistance  $R_p$  parameter. As the reference electrode is located at the concrete surface, an ohmic drop correction between WE and RE is applied using Ohm law, to take into account the concrete resistance (Laurens et al. 2016). For that, at each potentiostatic step  $\Delta E$  (n°x) applied, the concrete/mortar resistance  $R_{e,x}$  needs to be determined from the instantaneous part of the current response  $I_0$  (Equation (24)).  $R_e$  being the average of the five different  $R_{e,x}$  (for drop n°x,  $x = 1 \rightarrow 5$ ).

$$R_{e,x} = \frac{\Delta E}{I_0} \quad (24)$$

Then, based on Ohm law, the potential response of steel can be deduced subtracting at each step of the protocol the concrete/mortar resistance multiplied by the value of the asymptotic current to the potential value at the concrete surface.

Finally, the apparent current density  $i_{mi-Rp}$  (in  $\mu\text{A}/\text{cm}^2$ ), can be deduced by the Stern-Geary equation (Equation (25)).

$$i_{mi-Rp} = \frac{B}{R_p} \quad (25)$$

Where  $i_{mi-Rp}$  ( $\mu\text{A}/\text{cm}^2$ ) is the apparent current density,  $R_p$  is the value of linear polarisation resistance ( $\Omega.\text{cm}^2$ ) and  $B$  (V) is a constant determined by a Tafel test (section 3.4.2).

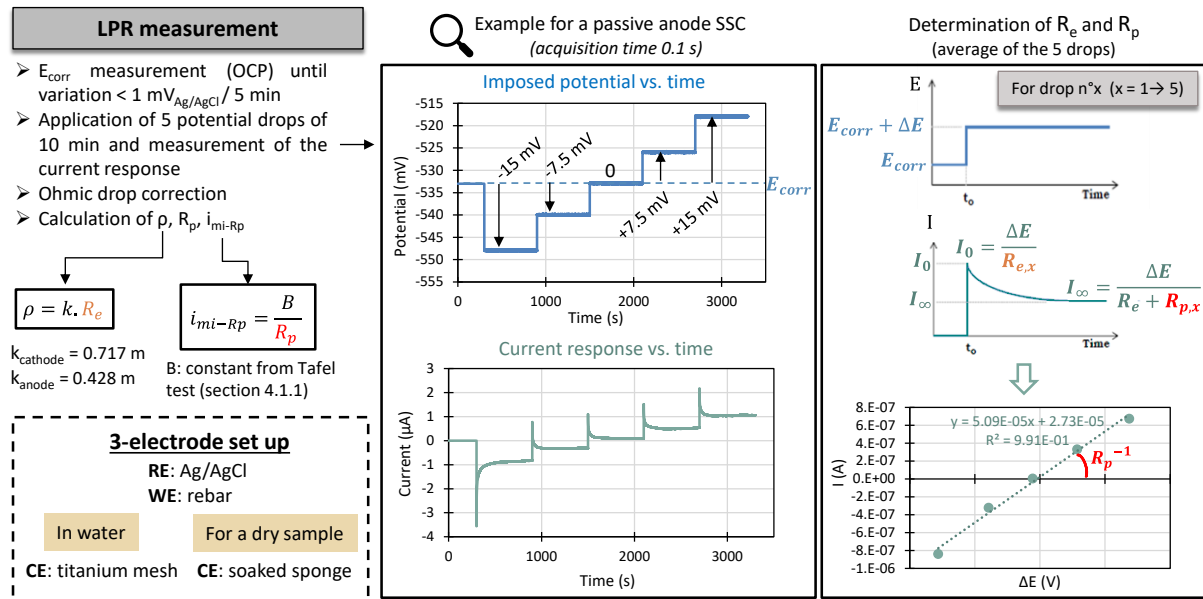


Figure 68: Details of LPR test to obtain the following parameters  $E_{corr}$ ,  $\rho$ ,  $R_p$ ,  $i_{mi-Rp}$ .

The equation of Stern-Geary is normally applicable only for uniform corrosion, that is why apparent current densities are presented in the rest of the study (the autopsies of the section 4.6 show that the corrosion is not perfectly uniform). The current density is called apparent, because the surface considered in active state is that of the rebar whereas the latter is not uniformly active in reality.

### 3.4.2 Tafel

A Tafel test was performed on active and passive anodes of each formula, at the end of the galvanic coupling (Figure 66). Active anodes were carbonated anodes used for the galvanic coupling (after waiting for their complete depolarization, around 10 to 15 days), while passive anodes were the anodes of reference store in the wet curing room (not activated) in parallel, for the whole experimental campaign. Therefore, active and passive anodes have the same age when the Tafel test is realised. For each condition (passive or active) and for each formulation, one anode is used to perform a Tafel test using the classic 3-electrode set up and one anode using the modified 3-electrode set up (Figure 67), to have an electrochemical characterisation corresponding either to saturated or dry sample.

Similarly, a Tafel test is performed on passive cathodes before the galvanic coupling, considering for each concrete formulation a saturated sample (sample stored in the wet curing room and immersed in water for the test) and a dry sample (sample stored outdoor under shelter and wrapped in a soaked sponge for the test).

The Tafel test is an intrusive test, because the strong polarization of the rebar moves it away from its equilibrium potential ( $E_{corr}$ ) in an irreversible way, and therefore the samples used are removed from the experimental campaign afterwards. The test is performed here by polarizing the rebar first cathodically and then anodically, by successive potential steps, until reaching  $\pm 333$  mV with respect to OCP (details in Figure 87 in supplementary data). Each step lasts 1800

s, except for both steps at  $\pm 333$  mV that last 2700 s. This is the same method as for the LPR measurement, for which the test principle is described in (Laurens et al. 2016), but for a larger polarization range in order to obtain the full polarization curve of the rebar. Finally, a correction of the ohmic drop is performed. The advantage of this method compared to a constant scan rate is that for high levels of polarization the stabilization time of the current response can be long. The polarization from OCP to the anodic branch then back to OCP (same thing for the cathodic branch), allows to approximate the value of the stabilized current for each step, by averaging the ascendant asymptotic response with the descendant one, as illustrated in Figure 19 in (Laurens et al. 2016). Finally, the Tafel test allows to obtain different electrochemical parameters ( $\beta_a$ ,  $\beta_c$ ,  $i_{mi-Tafel}$ ) by fitting the curve obtained with the equation of the Butler-Volmer model (Equation (26)).

$$i = i_{mi-Tafel} \left( \exp \left( \ln(10) \frac{E - E_{corr}}{\beta_a} \right) - \exp \left( \ln(10) \frac{E - E_{corr}}{\beta_c} \right) \right) \quad (26)$$

Where  $E_{corr}$  is the OCP ( $V_{ref}$ ) of the uniform corrosion system at equilibrium,  $i$  is the net current density ( $A/m^2$ ) flowing through the metal-electrolyte interface of the uniform system forced at potential  $E$  (involving a polarization with respect to the equilibrium potential  $E_{corr}$ ),  $i_{mi-Tafel}$  is the corrosion current density ( $A/m^2$ ), corresponding to the exchange current density of the uniform corrosion system,  $\beta_a$  and  $\beta_c$  are anodic and cathodic Tafel slopes (V/dec) of the electrochemical system, respectively.

The constant  $B$ , used in the Stern-Geary equation (Equation (25)) is calculated according to Equation (27), from anodic and cathodic Tafel slopes  $\beta_a$  and  $\beta_c$ .

$$B = \frac{\beta_a \cdot \beta_c}{\ln(10)(\beta_a + \beta_c)} \quad (27)$$

### 3.5 Galvanic current measurement

A galvanic coupling is performed for 90 days by connecting a passive cathode and an active anode (fully carbonated in natural conditions), as shown in Figure 69. It was chosen to study the influence of the degree of saturation of the samples (anodes and cathodes) on the galvanic current developed, as it is known this parameter can strongly influence the results obtained (section 3.4.1). Limited information is available on the influence of the degree of saturation of the samples on the galvanic current developed in the literature. Moreover, this study allows to estimate an interval of possible currents generated, in favourable or unfavourable conditions, that can be encountered in reality.

To simplify, it was decided to consider two extreme cases of saturation of the anodes (A) and cathodes (C): saturated (called “w” for water) or dry (called “d”). Four combinations for the galvanic coupling were then possible (Table 37), but only three were selected for the experimental campaign, because they were considered most representative of real conditions that could frequently occur on site.

Table 37: Different possible galvanic couplings taking into account two possible saturation conditions for anodes (A) and cathodes (C): saturated (“w” for water) or dry (“d”).

	Anode   dry (A <sub>d</sub> )	Anode   water (A <sub>w</sub> )
Cathode   dry (C <sub>d</sub> )	C <sub>d</sub> -A <sub>d</sub>	C <sub>d</sub> -A <sub>w</sub>
Cathode   water (C <sub>w</sub> )	C <sub>w</sub> -A <sub>d</sub>	C <sub>w</sub> -A <sub>w</sub>

The following conditions of galvanic coupling could happen on site when the carbonation has led to a uniform depassivation of the first reinforcement layer (anode), the other layers remaining passive (cathode):

- **C<sub>d</sub>-A<sub>d</sub>**: The structure considered in this example is exposed to aerated conditions (dry anode and cathode in absence of precipitation).
- **C<sub>w</sub>-A<sub>w</sub>**: The structure considered in this example could be a concrete slab, saturated during periods of rainfall (saturated anode and cathode).
- **C<sub>d</sub>-A<sub>w</sub>**: The structure considered in this example could be a concrete wall, the upper part of which is protected by a canopy (dry), while the lower part remains saturated during rainfall (saturated anode and dry cathode).
- **C<sub>w</sub>-A<sub>d</sub>**: This condition (dry anode and saturated cathode) has been identified as unlikely to occur in reality, compared to the previous ones, and is not retained for the rest of the experimental campaign. This could correspond to a problem of capillarity, with the lower part of the structure saturated by capillary rise and the upper part carbonated.

In practice, three different experimental setups of galvanic current must be set up, depending on the degree of saturation of the anodes and cathodes (C<sub>w</sub>-A<sub>w</sub> ; C<sub>d</sub>-A<sub>d</sub> ; C<sub>d</sub>-A<sub>w</sub>). Each of them is detailed on Figure 69.

- For the condition **C<sub>w</sub>-A<sub>w</sub>**, the same set up as for the campaign with chloride contaminated anodes is used (Article C), and is represented on Figure 69. The test is carried out in a sealed tank, where the active anode and passive cathode are immersed in water and spatially separated. The saturated cathode used for this condition is one that was kept in the wet curing room (Figure 66). After one year of natural carbonation, the active anode (dry sample) was immersed in water one week before to perform the galvanic coupling, to be totally saturated and so that an hydric equilibrium can be created and the electrochemical parameters stabilized in these new conditions. The samples are immersed in water and not in a NaOH solution (at pH = 12.5), as it was the case for the experimental campaign with chloride contamination, to avoid a re-alkalisation of the carbonated material in the NaOH solution.
- For the condition **C<sub>d</sub>-A<sub>d</sub>**, galvanic coupling cannot be performed by immersing the samples in water, in order to preserve their hydrous state (dry). The alternative that has been chosen is to wrap them in soaked sponges maintained by elastic bands (same principle as for the LPR measurement presented in section 3.4.1), as illustrated on Figure 69. In order to obtain a sufficient electrolytic contact between anode and cathode, the two samples, each one being wrapped in a soaked sponge, are kept in contact on

their lateral surface by elastic bands. To maximize the time during which the sponges remain moist, the galvanic coupling is performed in a hermetic box. The bottom of the box contains a saturated solution of  $\text{KNO}_3$  salts, which allow to maintain a relative humidity of 93% inside the box and thus to keep the sponges moist. The anode and the cathode are placed in a horizontal position on a support to be elevated, so that they are not in contact with the  $\text{KNO}_3$  solution (Figure 69). In order to guarantee the humidity of the sponges, in addition to the salts used in the box, the galvanic coupling is paused every 15 days in order to rewet the sponges of the anodes and cathodes. The dry cathodes used for this condition are those stored outdoor under shelter (Figure 66). After one year of natural carbonation, the active anodes are also considered as dry.

*This condition is called “dry” because the samples are in a drier state compared to the previous condition with immersion in water. The cathodes are large samples and will remain mostly dry being wrapped with sponges. The anodes are small samples with a low cover depth (8.5 mm). Therefore, they will probably be more wet than dry in this condition (but still not as saturated as when immersed in water).*

- For the condition  $\text{C}_d\text{-A}_w$ , the same experimental set up as for the condition  $\text{C}_d\text{-A}_d$  is performed. The dry cathodes used for this condition are those stored outdoor under shelter (Figure 66). The only difference is that after one year of natural carbonation, the active anodes (dry samples) were immersed in water one week before to perform the galvanic coupling, to be totally saturated and so that an hydric equilibrium can be created and the electrochemical parameters stabilized in these new conditions.

The galvanic current  $I_g$  exchanged between anode and cathode is recorded over time (90 days) using the ZRA mode of a BioLogic SP-50 potentiostat. It consists in applying zero resistance between both samples and then measuring the current  $I_g$  exchanged. An example of a galvanic current  $I_g$  versus time curve that is recorded is presented on Figure 69. There is first a transient behaviour and then quickly a stabilization of the galvanic current  $I_g$ . The fact that the anode and cathode are spatially separated allows to not only focus on the corrosion kinetics at the local scale of the anode, but also to quantify the current exchanged at a larger scale, as is the case in a real structure where a localized part of the reinforcement network is activated and is coupled to the rest of the passive steel. The coupling is maintained for 90 days to maximize the mass loss on the rebar (and thus the accuracy of the measurement), as presented in the next section 3.6.1. Finally, the galvanic current values shown are obtained by doing the integral under the curve, divided by the total duration of the coupling.



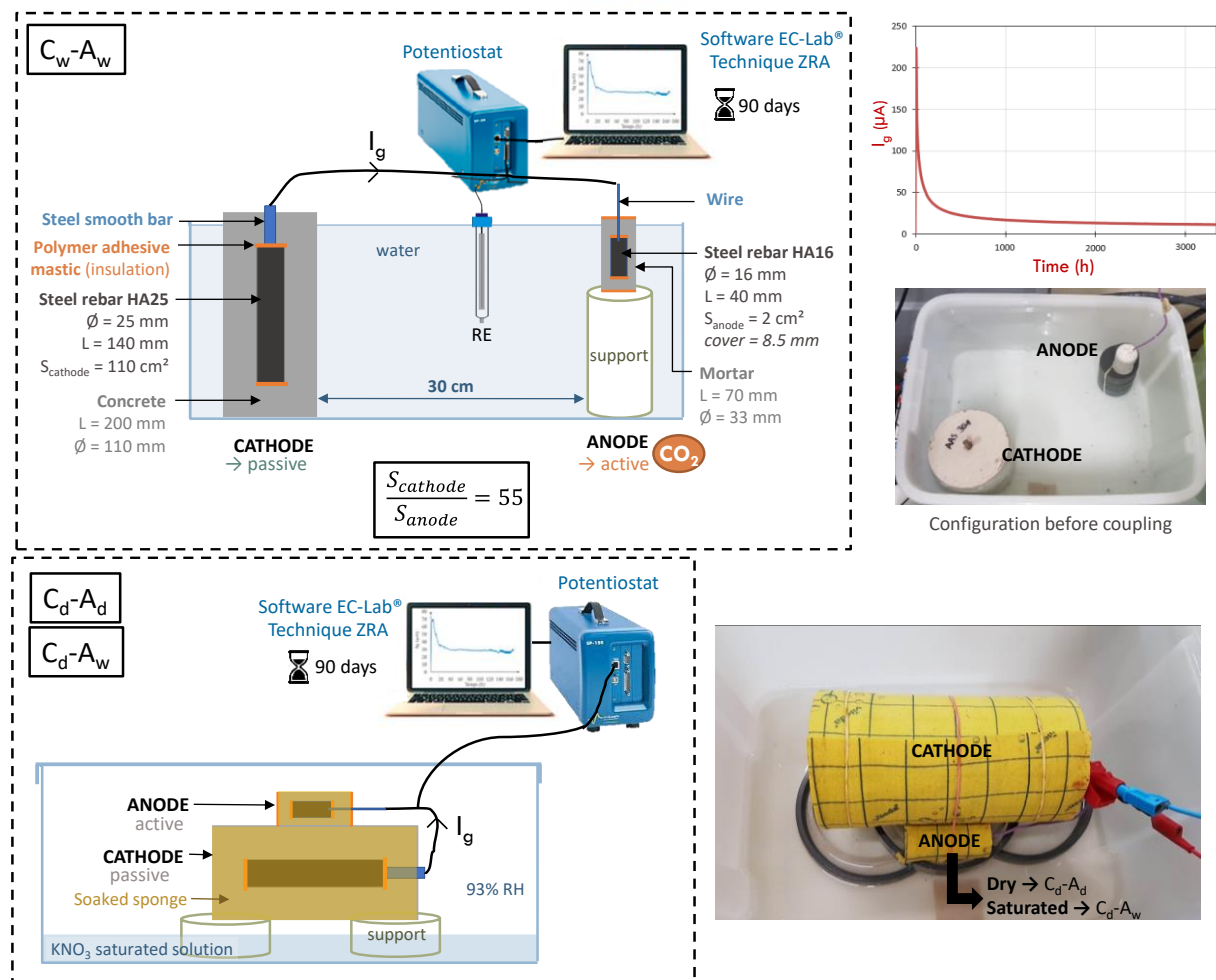


Figure 69: Detail of the set up used for the galvanic current ( $I_g$ ) measurement, depending on the saturation degree considered for the anodes and cathodes: C<sub>w</sub>-A<sub>w</sub> (anode and cathode in water), C<sub>d</sub>-A<sub>d</sub> (dry anode and cathode) and C<sub>d</sub>-A<sub>w</sub> (dry cathode and saturated anode).

### 3.6 Autopsy of the anodes

#### 3.6.1 Mass loss

At the end of the coupling, the anodes are split in order to visually observe the presence of corrosion, then the corrosion products are quantified by a mass loss measurement following the ASTM G01-03 standard (ASTM International 2012). It is also important to visually control that there is no crevice corrosion on the extremities of the rebar that were insulated, to avoid distortion of the results. When it is the case (not for this experimental campaign), the concerned samples and results have to be discarded.

The cleaning method consists of immersing the rebar in the cleaning solution (500 ml hydrochloric acid + 3.5 g hexamethylene tetramine + 500 ml distilled water), then brushing and weighing it. The cleaning cycles last 10 min and are repeated 4 to 6 times depending on the amount of corrosion products observed. The difference between the initial mass of steel (measured during the preparation of the steel) and the mass after cleaning, corresponds to the loss of mass which is associated to the amount of corrosion products.

Finally, it must be taken into account that rebars before casting are often covered with a layer of mill scale. The ideal cleaning procedure should remove only the corrosion products, but in reality it also removes the mill scale and even a small amount of metal. In order to quantify this part, three uncorroded control rebars ( $\text{Ø}16 \times 40 \text{ mm}$ ) were cleaned using the same procedure. The metal loss resulting from the cleaning (about 0.08% of the original mass of the rebar) can then be used to correct the mass loss on corroded rebars. In the rest of the paper, when there is no specification, the mass loss values presented have been corrected (mass loss due to the cleaning procedure and mill scale subtracted) and therefore correspond to corrosion products only.

### 3.6.2 Calculation of $I_{tot}$ from the mass loss

At the end of the galvanic coupling, the autopsy of the anodes allows to quantify the mass loss of each anode rebar, which corresponds to the quantity of corrosion products formed, as presented in the previous section (3.6.1). This mass loss  $m$  is proportional to the total current  $I_{tot}$  flowing through the steel concrete interface (SCI) during the coupling and these two variables are related to each other by Faraday's law (Equation (28)).

$$m = \frac{A \cdot I_{tot} \cdot t}{n \cdot F} \quad (28)$$

Where  $m$  is the mass loss (g),  $A$  is the molar mass of iron (55.84 g/mol),  $I_{tot}$  is the corrosion current (A),  $t$  is the duration of the coupling (s),  $n$  is the number of valence electrons (2 for Fe) and  $F$  is the Faraday's constant (96485 C/mol).

$I_{tot}$  can then be deduced from the known mass loss  $m$ , following Equation (28).  $I_{tot}$  being the sum of the galvanic current  $I_g$  flowing between the anode and the cathode and measured during the test and of local current  $I_{mi-anode}$  flowing at the anode scale (Equation (29)) as illustrated on Figure 70.

$$I_{tot} = I_g + I_{mi-anode} \quad (29)$$

$I_{mi-anode}$  is itself the sum of a local galvanic current flowing between the active and passive zones of the anode (called  $I_a$ ) and of a localized microcell current at the corrosion spot (called  $I_{mic}$ ), as illustrated on Figure 70. However, the repartition between  $I_a$  and  $I_{mic}$  cannot be determined.  $I_{mi-anode}$  can then be deduced from the known currents  $I_{tot}$  (determined using Equation (29)) and  $I_g$ .

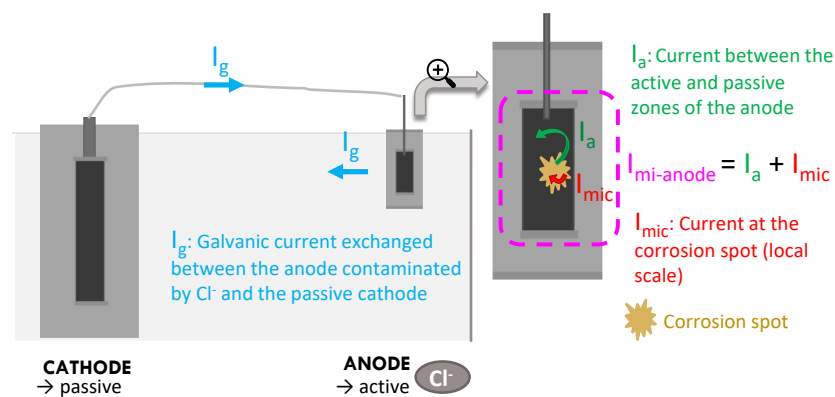


Figure 70: Details of the measurement and calculation of  $I_{tot}$  components.

## 4 Results

An in-depth analysis of the results obtained by classical methods is proposed in section 4.3. Other results are deliberately presented in a rather succinct manner and will be analysed more in details in the discussion section, which focuses on the galvanic coupling.

### 4.1 pH measurement

Table 38 presents the pH of the pore solution measured on LCK, AAS and SSC pastes, using the suspension method presented in section 3.2. Similar pH are measured for each formula, on pastes with a w/b ratio identical to that of the concrete (0.25 ; 0.43 and 0.50 for LCK, AAS and SSC, respectively) and on paste with an increased w/b ratio as for the mortar (0.32, 0.49 and 0.56 for LCK, AAS and SSC, respectively). Considering the precision of the pH-meter is 0.1 pH unit, the change of the w/b ratio does not impact at all the pH.

Table 38: pH of the pore solution of LCK, AAS and SSC pastes (with two different w/b ratios presented in part 2.2), measured by the suspension method, after 38 days of endogenous curing.

	LCK	AAS	SSC
w/b similar to concrete samples	13.0	13.0	12.0
w/b increased, similar to mortar samples	13.0	13.1	12.1

### 4.2 Evolution of carbonation fronts

Figure 71 presents the evolution of the carbonation depth measured on mortar samples (similar geometry as anode samples without reinforcement) with increased w/b ratio (0.32 ; 0.49 and 0.56 for LCK, AAS and SSC, respectively), exposed to natural outdoor carbonation under shelter after 5 days of curing. It shows that the carbonation front reaches the reinforcement (8.5 mm cover) at about 6 months for each formula. The anodes are nevertheless kept up to 1 year in natural carbonation so that corrosion has time to initiate and to obtain the most uniformly active reinforcement possible for the galvanic coupling. However, it should be kept in mind that a corrosion current has already developed during this period, before the galvanic coupling is performed.

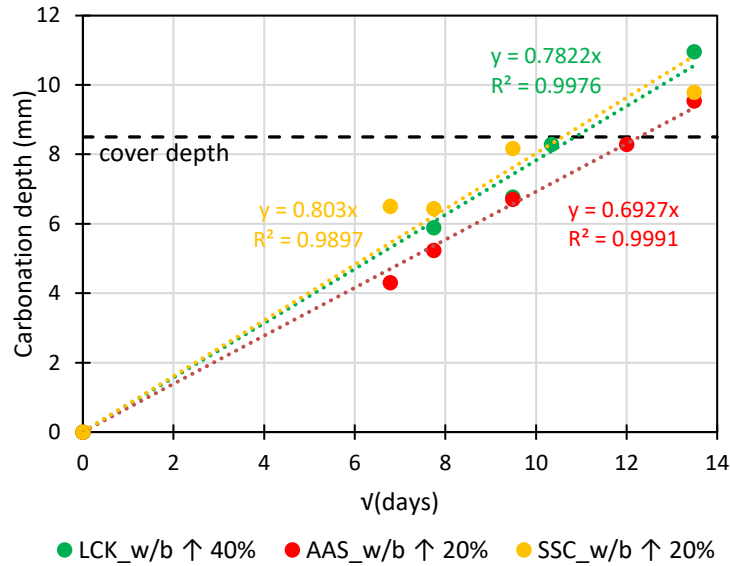


Figure 71: Carbonation depth measured on mortar samples with increased w/b ratio, exposed to natural outdoor carbonation under shelter after 5 days of curing.

The evolution of the carbonation front was also measured on concrete samples (similar geometry as cathode samples without reinforcement), exposed to natural outdoor carbonation under shelter after 14 days of curing, as illustrated on Figure 72.

The objective of these measurements is to ensure that the carbonation front has not reached the rebar (42.5 mm of cover) after the two years of natural carbonation, in order to keep passive cathodes for the galvanic coupling.

Figure 72 confirms that the carbonation front did not reach the rebar after two years of exposure. At this time, one cathode per formula is split to confirm by visual observation that they are still passive (absence of corrosion products at the rebar), as illustrated on Figure 72.

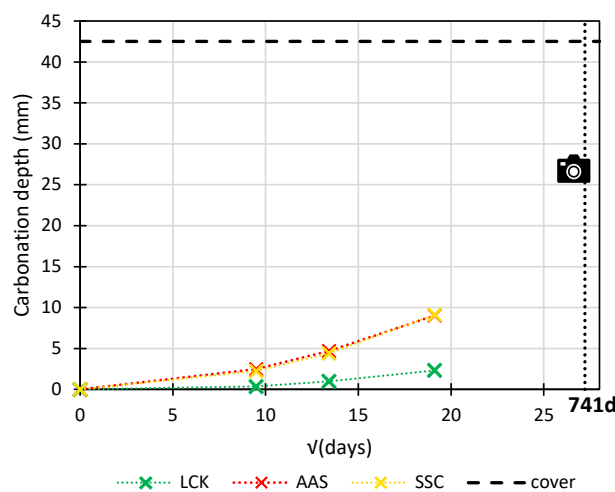


Figure 72: Carbonation depth measured on concrete samples, exposed to natural outdoor carbonation under shelter after 14 days of curing. The camera representing the visual inspection of the reinforcement at 741 days of carbonation.

### 4.3 Classic electrochemical measurements

#### 4.3.1 Tafel curves

Each Tafel curve was performed on 1 sample per condition (formula, anode/cathode, passive/active, water/dry), except for the passive cathode in water where an average of 3 samples is proposed. Figure 73 shows the fitting curves obtained on passive cathodes and on active anodes, either dry or in water, as previously explained in section 3.4.2. Passive anodes are not plotted for reasons of readability, but were also characterized.

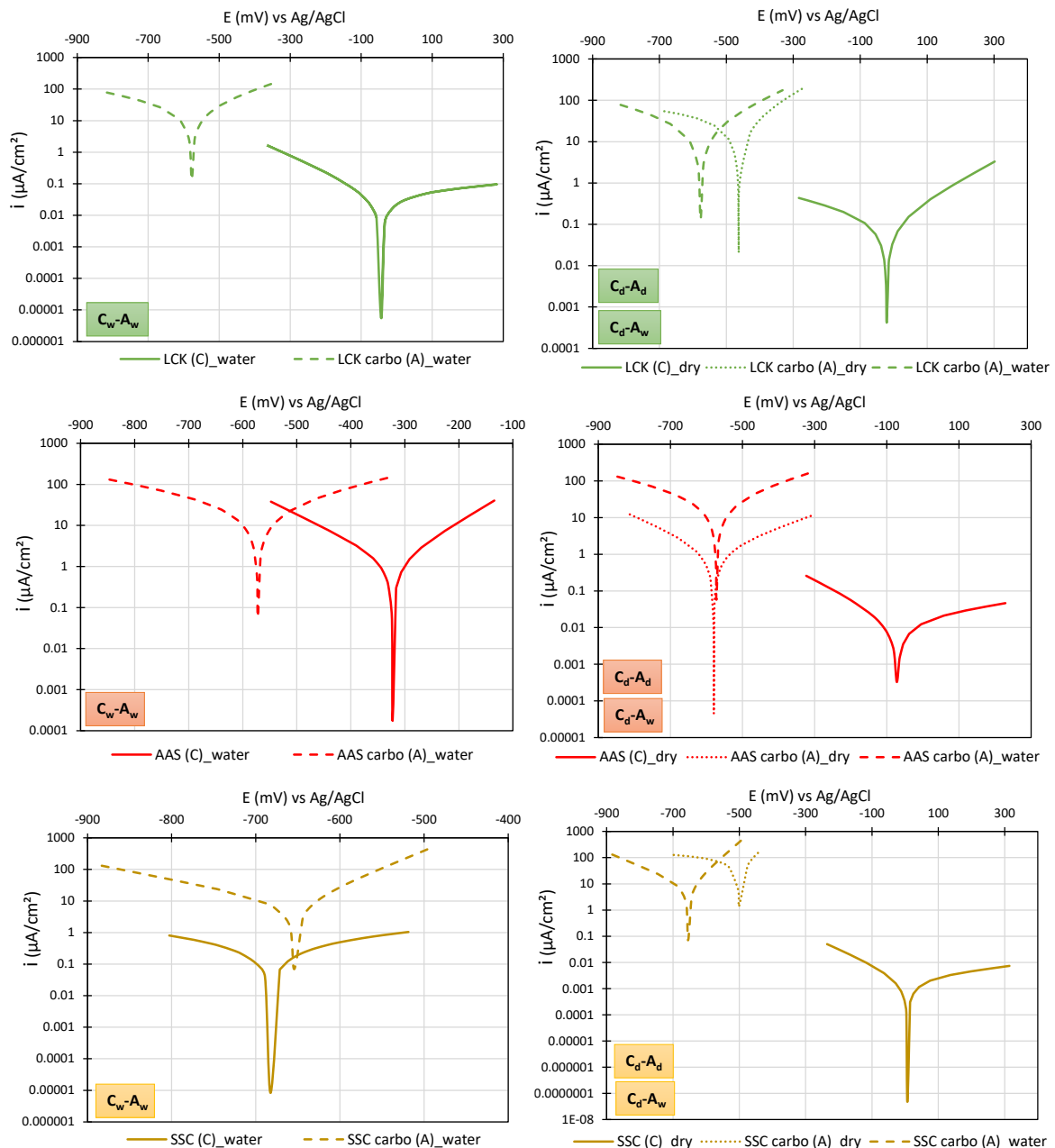


Figure 73: Tafel curves (fitting) obtained on passive cathodes (solid lines) and on active anodes either dry (dotted lines) or in water (dashed lines).

The values of the electrochemical parameters ( $\beta_a$ ,  $\beta_c$  and  $i_{mi-Tafel}$ ) obtained by fitting the Butler-Volmer equation (Equation (26)) to the experimental curves are summarized in Table 39. It should be noted that the values obtained on the cathode scale (concrete) cannot be directly compared to those obtained on the anode scale (mortar), because the materials are different (mortar/concrete, different w/b). The SCI will also be different between the two samples and it is therefore normal to find values that vary between passive anodes and cathodes.

$\beta_a$  is the anodic Tafel slope of the electrochemical system, expressing the oxidation of iron (and/or sulphur for slag-based binders, as explained in 4.3.2). It is supposed to decrease with the activation by carbonation (Revert et al. 2019), which is mostly confirmed by the values presented in Table 39 for the anodes of each binder.

$\beta_c$  is the cathodic Tafel slope of the electrochemical system, expressing the reduction reaction of oxygen. It varies depending on the conditions tested.

About the apparent current density  $i_{mi-Tafel}$ , it logically increases with the activation by carbonation for the three formulas.

For the LCK, having a traditional behaviour similar to PC-based binders, the corrosion potential  $E_{corr}$  strongly decreases due to the activation by carbonation. This trend is not verified for slag-based samples (AAS and SSC), due to their electronegative corrosion potential  $E_{corr}$ , even at passive state, as explained in the next section 4.3.2.

Concerning the degree of saturation of the samples (dry or in water), it seems that saturated materials are characterized in most cases by a more electronegative  $E_{corr}$  and a higher corrosion current density  $i_{mi-Tafel}$ , compared to dry materials, as observed in the literature (Vennesland, Raupach, et Andrade 2007; Cheng, Maruyama, et Ren 2021; Gonzalez, Algaba, et Andrade 1980; Stefanoni, Angst, et Elsener 2018a; Glass, Page, et Short 1991; Dhir, Jones, et McCarthy 1992; Alonso, Andrade, et González 1988).

In the rest of the paper, the values of the **constant B** presented in Table 39 are used in the Stern-Geary equation to calculate  $i_{mi-Rp}$  (Equation (25)). Good confidence is attributed to the measurements made, but these B values would still need to be confirmed on a larger number of samples. Commonly values of B used for PC-based materials in the literature are 52 mV for the passive state and 26 mV for the active state (C. Andrade and Alonso 1996; C. Andrade and González 1978), while the values presented in Table 39 are quite different as they are obtained on low-carbon concretes with specific binders. Many parameters are likely to influence the values of Tafel slopes and B constant, such as the composition of the pore solution, pH, relative humidity and availability in oxygen (Runci, Provis, and Serdar 2023).

Table 39: Anodic and cathodic Tafel slopes  $\beta_a$  and  $\beta_c$ , as well as apparent current density  $i_{mi-Tafel}$  obtained by fitting the polarization curve from Tafel test with the Butler-Volmer equation, for passive cathodes (C) and passive or active anodes (A), either in water or dry. Values of constant B used in Stern-Geary relation, calculated from Equation (27), and associated to Tafel slopes  $\beta_a$  and  $\beta_c$ .

		Passive C water <sup>(1)</sup>	Passive C dry <sup>(1)</sup>	Passive A water <sup>(2)</sup>	Passive A dry <sup>(2)</sup>	Active A water <sup>(2)</sup>	Active A dry <sup>(2)</sup>
LCK	$\beta_a$ (V/dec)	0.63	0.23	0.74	0.16	0.28	0.25
	$\beta_c$ (V/dec)	0.18	0.48	0.16	0.09	0.45	1.13
	$i_{mi-Tafel}$ ( $\mu A/cm^2$ )	0.03	0.12	0.004	0.01	23.46	37.73
	<b>B (mV)</b>	<b>58 ± 20</b>	<b>67</b>	<b>58</b>	<b>25</b>	<b>74</b>	<b>89</b>
AAS	$\beta_a$ (V/dec)	0.34	0.61	0.84	0.32	0.33	0.25
	$\beta_c$ (V/dec)	0.22	0.20	0.28	0.27	0.41	1.62
	$i_{mi-Tafel}$ ( $\mu A/cm^2$ )	1.88	0.02	1.34	0.47	28.78	65.80
	<b>B (mV)</b>	<b>53 ± 29</b>	<b>67</b>	<b>91</b>	<b>63</b>	<b>80</b>	<b>107</b>
SSC	$\beta_a$ (V/dec)	0.35	0.60	0.27	0.45	0.09	0.14
	$\beta_c$ (V/dec)	0.34	0.18	0.44	0.34	0.19	1.27
	$i_{mi-Tafel}$ ( $\mu A/cm^2$ )	0.42	0.002	0.63	2.96	7.96	90.59
	<b>B (mV)</b>	<b>74 ± 3</b>	<b>60</b>	<b>73</b>	<b>85</b>	<b>27</b>	<b>54</b>

<sup>(1)</sup> After 2 years of natural carbonation and before galvanic coupling for “dry” or conservation in parallel in wet curing room for “water” (same age).

<sup>(2)</sup> After 90 days of galvanic coupling for “active” or conservation in parallel in wet curing room for “passive” (same age).

#### 4.3.2 Electrical resistivity ( $\rho$ ), corrosion potential ( $E_{corr}$ ), polarisation resistance ( $R_p$ ) and apparent current density ( $i_{mi-Rp}$ )

All results presented in this section were obtained with LPR measurement protocol for dry sample (set up with soaked sponge presented in section 3.4.1).

##### Electrochemical parameters of cathodes

Figure 74 shows the evolution of different electrochemical parameters ( $\rho$ ,  $E_{corr}$ ,  $R_p$  and  $i_{mi-Rp}$ ) measured on the cathodes exposed to natural outdoor carbonation under shelter (after 14 days of curing) for two years. Each value is an average realized on 6 samples, which are placed in a room at 20 °C 24 hours before making the LPR measurement, so that they have time to return to this reference temperature as they are quite “massive” samples. For the interpretation of  $E_{corr}$  or  $i_{mi-Rp}$ , the values are associated respectively to a corrosion risk following ASTM C-876 (ASTM International 2022) or a corrosion level according to TC RILEM 154 recommendations (C. Andrade and Alonso 2004).

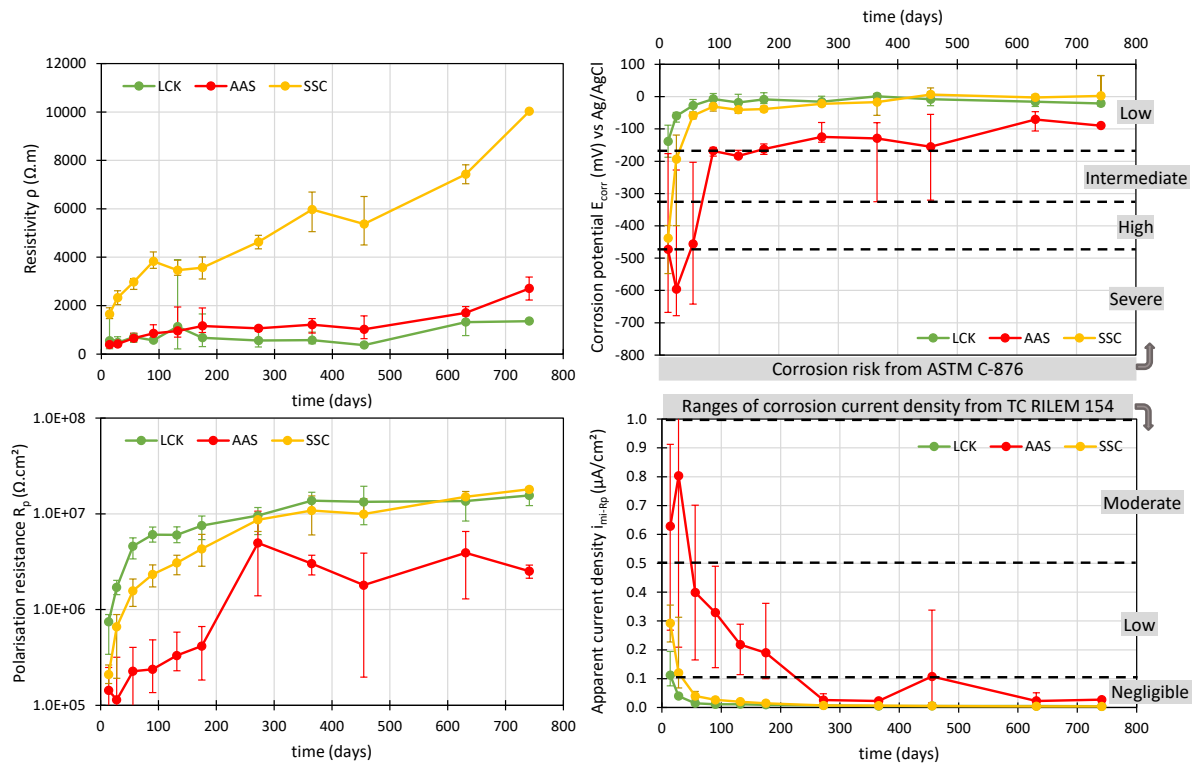


Figure 74: Classical electrochemical parameters ( $\rho$ ,  $E_{corr}$ ,  $R_p$  and  $i_{mi-Rp}$ ) measured on the cathodes exposed to natural outdoor carbonation under shelter (after 14 days of curing) for two years.

At the end of the wet curing (first measurement at 14 days on Figure 74), the three binders have different initial parameters related to their composition.

A high resistivity  $\rho$ , as for SSC (1650  $\Omega \cdot m$  before carbonation), is a sign of a strong resistance to the passage of current (Azarsa and Gupta 2017; Hornbostel, Larsen, and Geiker 2013) and come from a very low ionic concentration in its pore fluid solution (Article A), contrary to LCK (546  $\Omega \cdot m$ ) and AAS (390  $\Omega \cdot m$ ).

A high value of linear polarization resistance  $R_p$ , as for LCK before carbonation ( $8 \times 10^5$   $\Omega \cdot cm^2$ ) (contrary to AAS and SSC), is associated with a high capacity of the steel to resist polarisation and therefore to a low corrosion current density  $i_{mi-Rp}$  (0.11  $\mu A/cm^2$ ), due to the inversely proportional relationship between these two parameters, as shown in Equation (25). On the contrary, slag-based binders show a different behaviour with a lower  $R_p$  ( $1 \times 10^5$   $\Omega \cdot cm^2$  for AAS and  $2 \times 10^5$   $\Omega \cdot cm^2$  for SSC) and a higher  $i_{mi-Rp}$  (0.63  $\mu A/cm^2$  for AAS and 0.29  $\mu A/cm^2$  for SSC).

Concerning the corrosion potential  $E_{corr}$ , the one of the LCK (-139 mV/Ag/AgCl) is very different from slag-based formulations for which much more electronegative values are measured (-473 mV/Ag/AgCl for AAS and -438 mV/Ag/AgCl for SSC). These differences are explained in more detail in the following paragraph about the case of anodes.



As the samples are exposed outdoors under shelter, Figure 74 shows an evolution of the electrochemical parameters, compared to the end of cure, that tend to stabilize. The drying of the cathodes (also leading to a renewal of the oxygen facilitated at the rebar and thus consumption of sulfides) results in an increase of the resistivity  $\rho$ , the corrosion potential  $E_{\text{corr}}$  and the polarisation resistance  $R_p$  and in a decrease of the apparent current density  $i_{\text{mi-Rp}}$ , as commonly reported in the literature (Cheng, Maruyama, and Ren 2021; Gonzalez, Algaba, and Andrade 1980; Stefanoni, Angst, and Elsener 2018; Glass, Page, and Short 1991; Dhir, Jones, and McCarthy 1992; Alonso, Andrade, and González 1988).

Finally, after two years of exposure to natural carbonation, the cathodes are still in the passive state because the carbonation front has not reached the rebar (section 4.2), which is in agreement with the interpretation of  $E_{\text{corr}}$  and  $i_{\text{mi-Rp}}$  values measured, indicating a low risk of corrosion associated with  $E_{\text{corr}}$  (ASTM International 2022) and negligible corrosion rates associated with  $i_{\text{mi-Rp}}$  (C. Andrade and Alonso 2004) for each binder.

#### Electrochemical parameters of anodes

Figure 75 shows the evolution of different electrochemical parameters ( $\rho$ ,  $E_{\text{corr}}$ ,  $R_p$  and  $i_{\text{mi-Rp}}$ ) measured on the anodes exposed to natural outdoor carbonation under shelter (after 5 days of curing) for one year, and also on the reference anodes stored in parallel in the wet curing room. Each value is an average realized on 5 samples for the dry anodes and on 2 to 3 samples for the reference anodes. The same interpretation of  $E_{\text{corr}}$  or  $i_{\text{mi-Rp}}$  values as for the cathodes is proposed, based on the thresholds proposed by ASTM C-876 (ASTM International 2022) or TC RILEM 154 recommendations (C. Andrade and Alonso 2004), respectively.

As several phenomena, having opposite effects on the measured electrochemical parameters ( $\rho$ ,  $E_{\text{corr}}$ ,  $R_p$  and  $i_{\text{mi-Rp}}$ ), take place at the same time on the anodes placed in natural outdoor carbonation (drying and activation of the anodes due to carbonation), it was chosen to follow these same parameters on passive reference anodes kept in a wet curing room, in order to better understand the obtained results. In a first step, the analysis focuses on the parameters measured on the reference anodes.

#### Reference anodes stored in a wet curing room

Similar to what was observed on the cathodes after their wet cure, the reference anodes are characterized by different resistivities according to the composition of their binder (Article A). It stabilizes between 50 and 100 days when the hydration of the material is complete.

Concerning the corrosion potential  $E_{\text{corr}}$ , the one of the **LCK** anodes (-133 to -54 mV/Ag/AgCl) remains stable over the time and is logically associated with a low corrosion risk at passive state (ASTM International 2022). Its polarization resistance  $R_p$  stabilizes at high values and corresponds to a low apparent current density  $i_{\text{mi-Rp}}$  ( $\approx 0.1 \mu\text{A}/\text{cm}^2$ ). The LCK matrix, which is based indeed on PC, is expected to have a classical behavior.

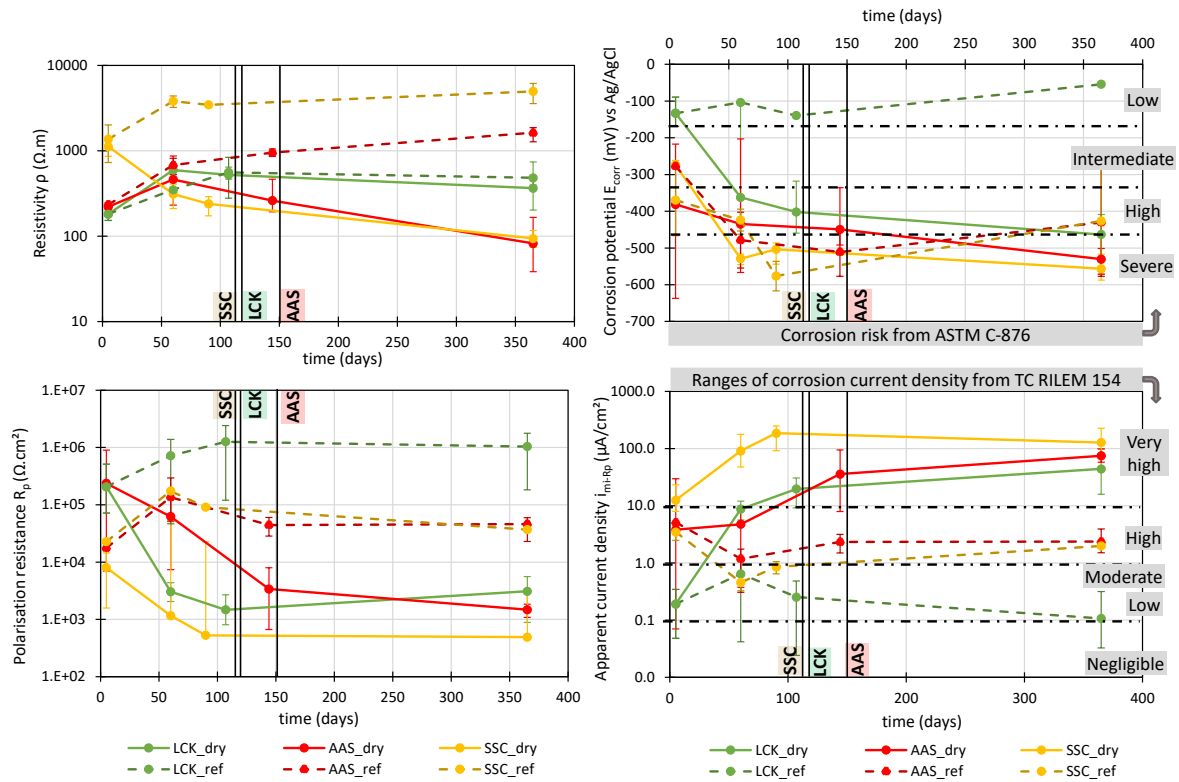


Figure 75: Classical electrochemical parameters ( $\rho$ ,  $E_{corr}$ ,  $R_p$  and  $i_{mi-Rp}$ ) measured on the dry anodes exposed to natural outdoor carbonation under shelter (after 5 days of curing) for one year (solid lines), and on the reference anodes stored in parallel in the wet curing room (dashed lines). The vertical black lines represent the arrival of the carbonation front at the rebar for each formula.

On the contrary, still in the case of passive rebars, for the **AAS** and **SSC** binders, the measured  $E_{corr}$  and  $i_{mi-Rp}$  are respectively associated after one year with a high corrosion risk ( $-430$  mV/Ag/AgCl) and a high level of apparent current density ( $2 \mu\text{A}/\text{cm}^2$ ). This is due to the presence of sulfur in slag which reacts with the oxygen in the pore solution and creates a very reducing environment, lowering the redox potential of the latter. The very electronegative  $E_{corr}$  and the high  $i_{mi-Rp}$  (also applies for the low  $R_p$ ) measured correspond to chemical reactions of the sulfur in the pore solution and not to an active state of corrosion in the rebar (Mundra, Bernal, et al. 2017; Criado et al. 2018; Mundra et al. 2023). It is confirmed by (Mundra and Provis 2021), who observed a decrease of  $R_p$  with increasing  $\text{HS}^-$  concentration, measured on a steel in a synthetic pore solution simulating the one of an AAS.

Therefore, the values obtained ( $E_{corr}$ ,  $R_p$  and  $i_{mi-Rp}$ ) for AAS and SSC do not represent accurately an active state of corrosion of the rebars. It highlights that the criteria used for PC are not adapted and cannot be directly applied to saturated binders with a high slag content, hence the use of the galvanic current measurement presented in the next section. It can be noted that for alkali-activated materials, (Runci, Provis, and Serdar 2023) recently proposed new conservative values (for corrosion potential, mortar resistance and constant B) for active and passive steel,

associated with a corresponding risk of corrosion. These values could later be refined with additional experimental tests.

#### Anodes exposed to natural outdoor carbonation

The analysis now focuses on the parameters measured on the anodes exposed to natural outdoor carbonation after 5 days of curing. The interpretation of the parameters obtained is more complex, because several phenomena, having opposite effects on the measured electrochemical parameters ( $\rho$ ,  $E_{\text{corr}}$ ,  $R_p$  and  $i_{\text{mi-Rp}}$ ), take place at the same time, such as the drying and the activation of the anodes due to carbonation. The corrosion initiation, generally associated to the arrival of the carbonation front at the rebar (transition from passive to active state), is represented on the Figure 75 by the vertical black lines for each formula.

The drying of the samples, as observed previously in Figure 74, commonly results in an increase of the resistivity  $\rho$ , the corrosion potential  $E_{\text{corr}}$  and the polarisation resistance  $R_p$  and in a decrease of the apparent current density  $i_{\text{mi-Rp}}$  (Cheng, Maruyama, and Ren 2021; Gonzalez, Algaba, and Andrade 1980; Stefanoni, Angst, and Elsener 2018; Glass, Page, and Short 1991; Dhir, Jones, and McCarthy 1992; Alonso, Andrade, and González 1988). Moreover, it may lead to a partial oxidation of the sulfur species present in the pore solution of AAS and SSC, therefore limiting their capacity to create a reducing environment by consuming oxygen (as it is the case in saturated conditions where oxygen is renewed less easily), to block the cathodic corrosion reaction or to maintain very electronegative potentials.

It is observed on Figure 74 indeed, that the values of  $E_{\text{corr}}$  become similar to those of the LCK after drying. On the contrary, the literature reports the corrosion initiation causes a potential drop and an increase of  $i_{\text{mi-Rp}}$  (ASTM International 2022; C. Andrade and Alonso 2004). For this reason, it is difficult to observe a sharp variation of the electrochemical parameters in Figure 75, indicating an initiation of corrosion. Their evolution is rather progressive, but at the end of the two years of carbonation, the measured  $E_{\text{corr}}$  and  $i_{\text{mi-Rp}}$  are respectively associated with a severe corrosion risk and a very high level of apparent current density, showing the anodes were well activated.

The  $i_{\text{mi-Rp}}$  values obtained are particularly high. It is partly due to their calculation (Equation (25)) from experimental values of the Tafel constant B (section 4.3.1). It results in higher corrosion current densities than with values of constant B commonly used for Portland cements (52 mV for the passive state and 26 mV for the active state (C. Andrade and Alonso 1996; C. Andrade and González 1978)). In addition, the apparent current densities  $i_{\text{mi-Rp}}$  are overestimated, considering they are obtained on anodes for which an increased w/b ratio has been used and that consequently have a lower resistivity. A relationship between resistivity and corrosion rate has precisely been demonstrated in the literature (Hornbostel, Larsen, and Geiker 2013), lower resistivities leading to higher corrosion rates.

#### 4.4 Galvanic coupling between anode and cathode

##### 4.4.1 Galvanic current ( $I_g$ )

Figure 76 shows the galvanic current  $I_g$  measured between anode and cathode at the end of 90 days of coupling for the three different types of galvanic coupling tested ( $C_w-A_w$ ,  $C_d-A_d$ ,  $C_d-A_w$ ), considering various saturation conditions for anodes (A) and cathodes (C): saturated (“w” for water) or dry (“d”). The  $I_g$  values for the  $C_w-A_w$  and  $C_d-A_d$  conditions are the average of 2 couplings and those for  $C_d-A_w$  are obtained from only one coupling.

The results obtained are of different orders of magnitude depending on the binder and saturation conditions considered. The galvanic currents  $I_g$  measured for the SSC binder are much lower than for the LCK or AAS.

The saturation conditions have a different influence on the galvanic current generated between anode and cathode, depending on the type of binder considered. For the LCK, the  $C_d-A_d$  condition generates a lower  $I_g$  than for the two other conditions. For the AAS, the three conditions result in three different orders of magnitude for  $I_g$ . On the contrary for SSC, the same galvanic current is measured whatever the saturation conditions tested. Thus, it seems that different mechanisms are involved depending on the binder considered, as discussed in more detail in the section 5.2.

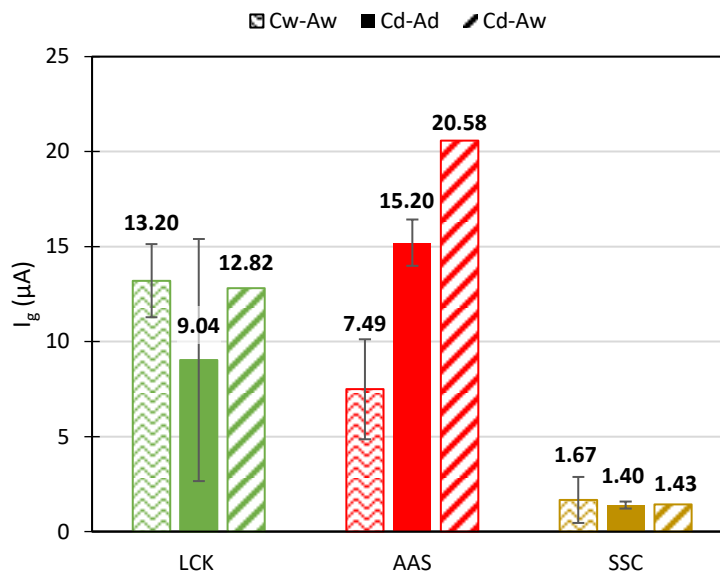


Figure 76: Galvanic current  $I_g$  after 90 days of coupling, depending on the saturation conditions of cathode and anode:  $C_w-A_w$  (anode and cathode in water),  $C_d-A_d$  (dry anode and cathode) and  $C_d-A_w$  (dry cathode and anode in water).

#### 4.4.2 Total resistance ( $R_{tot}$ )

The total resistance  $R_{tot}$  between anode and cathode takes into account both the materials resistances  $R_e$  (from the classical measurement presented in section 3.4.1) and the polarization resistances  $R_p$  at the SCI, as described by Equation (30), where the solution or sponge resistance is negligible.

$$R_{tot} = R_{p,cathode} + R_{e,cathode} + R_{e,solution\ or\ sponge} + R_{e,anode} + R_{p,anode} \quad (30)$$

Figure 77 illustrates the measured  $R_{tot}$  depends mainly on the saturation conditions considered for anode and cathode. For all three formulas, the  $R_{tot}$  associated with the  $C_w-A_w$  condition is lower than the other two conditions ( $C_d-A_d$  and  $C_d-A_w$ ). It seems logical, given that the resistance of the electrolyte  $R_e$  and the polarization resistance  $R_p$  are lower on saturated samples compared to dry samples, as observed in Figure 74 where these parameters increase during drying.

The table in Figure 77 presents the contribution of each variable in  $R_{tot}$ . For the  $C_w-A_w$  condition, the  $R_{tot}$  is mainly due to the  $R_{p,cathode}$  component (70 to 84% depending on the binder), except for the SSC for which it is the  $R_{e,cathode}$  component due to its high resistivity. For the two others conditions ( $C_d-A_d$  and  $C_d-A_w$ ) it is mainly due to the  $R_{p,cathode}$  (around 90%). Nevertheless, for slag-based formulations (AAS and SSC), especially for saturated conditions, the  $R_{tot}$  parameter must be analysed carefully because it is based on the  $R_p$  values. As explained previously (4.3.2), these  $R_p$  values are not representative of the corrosion state of the rebars, but rather of the sulphur oxidation reactions. Finally, the total resistance  $R_{tot}$  will influence the measured galvanic current value  $I_g$  (Revert et al. 2019; C. Andrade et al. 1992): a low  $R_{tot}$  would favor a high  $I_g$  (more details are given in section 5).

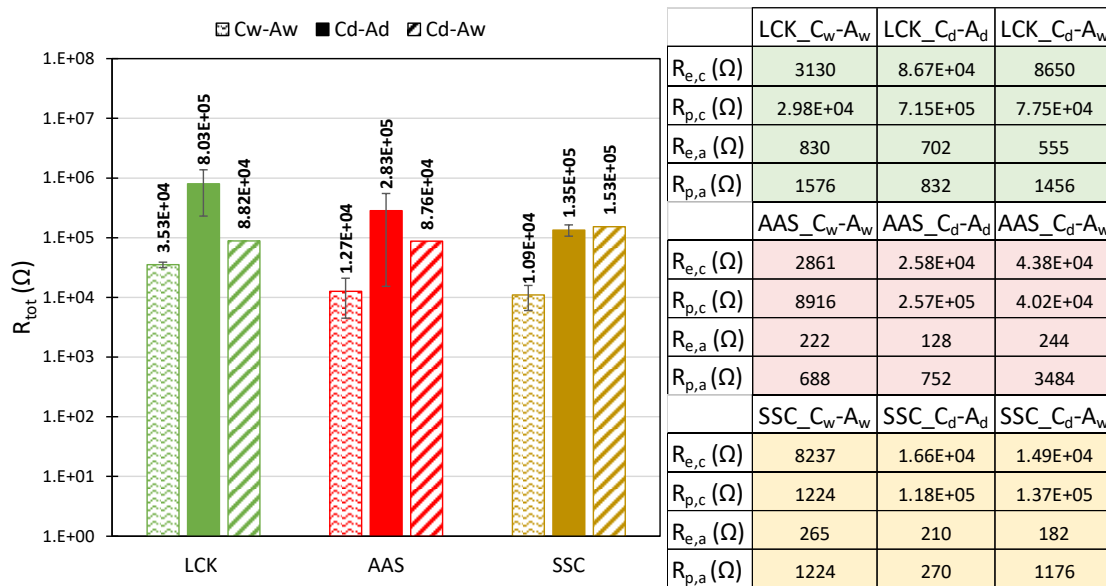


Figure 77: Total electrical resistance  $R_{tot}$  between reinforcement embedded in anode and cathode sample, before galvanic coupling. In the Table on the right side are detailed the different resistances (in ohm) forming  $R_{tot}$  (Equation (30)).

#### 4.4.3 Potential difference ( $\Delta E_{A-C}$ )

The potential difference ( $\Delta E_{A-C}$ ) between anode and cathode before galvanic coupling is shown in Figure 78, for each binder and the three different types of galvanic coupling tested ( $C_w-A_w$ ,  $C_d-A_d$ ,  $C_d-A_w$ ). Corrosion potential  $E_{\text{corr}}$  measured for anodes and cathodes, mainly depends on the saturation (saturated or dry) and the electrochemical state (passive or active) of the sample: saturated and/or active samples result in more electronegative  $E_{\text{corr}}$  than those dry and/or passive (section 4.3.2). For the galvanic coupling performed in this experimental campaign, cathodes are passive while anodes are active, and different conditions of saturation were tested for both samples, resulting in different  $\Delta E_{A-C}$ . For each condition tested, the anode has a more electronegative corrosion potential  $E_{\text{corr}}$  than the cathode, resulting in a negative  $\Delta E_{A-C}$ .

Figure 78 illustrates similar behaviours for slag-based binders depending on the saturation conditions, different from the LCK. Contrary to the LCK, slag-based binders already present a very electronegative  $E_{\text{corr}}$  at passive state in saturated conditions, corresponding to chemical reactions of the sulfur in the pore solution. Therefore it will lead to different  $\Delta E_{A-C}$  from those of the LCK depending on the conditions considered, as discussed more in detail in section 5.2. Finally, the potential difference  $\Delta E_{A-C}$  would constitute the electromotive force generating the galvanic current  $I_g$ : a high  $\Delta E_{A-C}$  would thus favour a high  $I_g$  (Revert et al. 2019; Abdelkader Nasser and Castel 2014; A. Nasser et al. 2010).

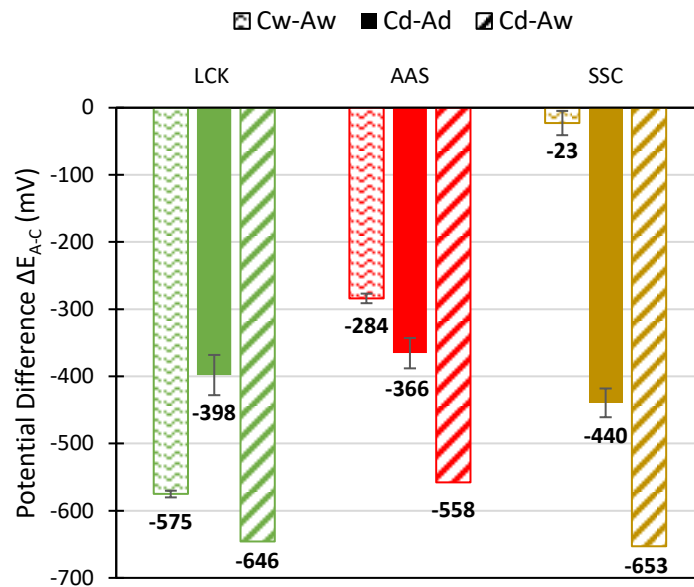


Figure 78: Potential difference  $\Delta E_{A-C}$  associated to each anode-cathode coupling, for the different saturation conditions of cathode and anode:  $C_w-A_w$  (anode and cathode in water),  $C_d-A_d$  (dry anode and cathode) and  $C_d-A_w$  (dry cathode and anode in water).

#### 4.5 Classic electrochemical measurement after galvanic coupling

To evaluate the influence of the galvanic coupling on the electrochemical parameters of the active anodes, a new characterization by LPR measurement is performed after the galvanic coupling (once the samples are depolarized and have returned to their equilibrium state) and before the autopsies (Figure 66).

Figure 79 and Figure 80 show a comparison of corrosion potential  $E_{\text{corr}}$  and apparent current densities  $i_{\text{mi-Rp}}$ , respectively, obtained by LPR measurement, on active anodes before galvanic coupling or after galvanic coupling. The results on activated anodes before galvanic coupling are those of section 4.3.2 (after 365 days of natural carbonation, Figure 75). After the galvanic coupling, Figure 79 illustrates more electronegative  $E_{\text{corr}}$  measured, for almost all binders and conditions tested. It possibly comes from a more advanced and stable corrosion process, because during coupling the  $E_{\text{corr}}$  of the active anodes had been shifted to less electronegative values, due to the creation of an equilibrium potential with the passive cathodes (more electropositive  $E_{\text{corr}}$ ). At the same time, it is observed on Figure 80 a strong influence of galvanic coupling on the apparent current densities  $i_{\text{mi-Rp}}$  (strong evolution before and after coupling). For the three binders and for all the conditions tested, indeed, Figure 80 shows a decrease in  $i_{\text{mi-Rp}}$  after coupling, which is probably a consequence of the 90 days of galvanic coupling. This hypothesis is confirmed by the study conducted by (Bui, Maekawa, and Tan 2023), showing that the galvanic coupling influences also the local apparent current density. Qualitatively, they observe that for a concrete with a quite low resistivity (saturated conditions for example), a high increase in galvanic current results in a slight decrease in the local apparent current. These results are analysed and interpreted in more detail in section 5.2 of the discussion.

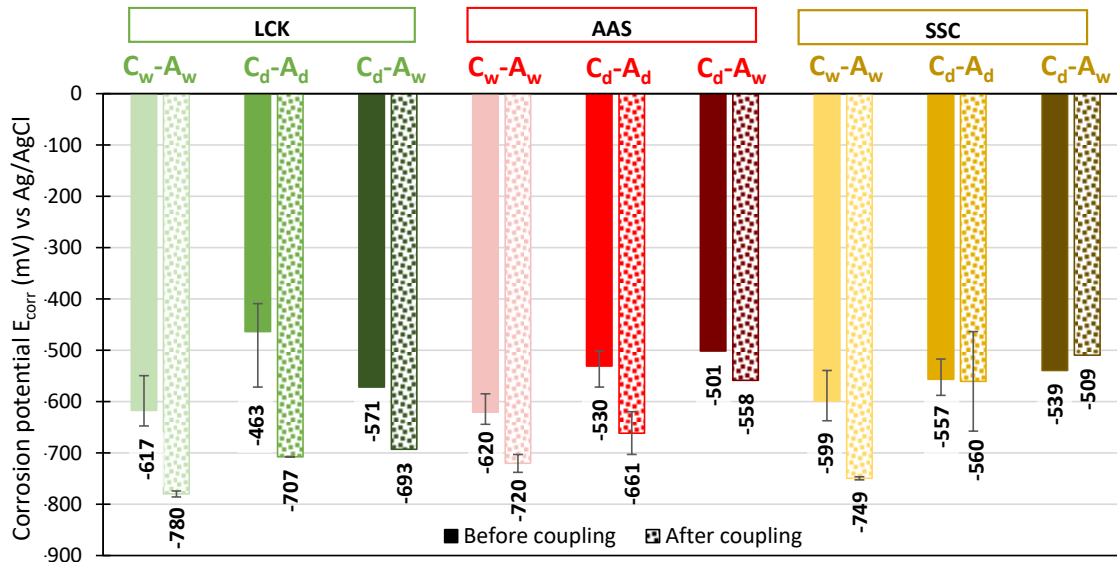


Figure 79: Corrosion potential  $E_{\text{corr}}$  measured on activated anodes by LPR measurement, before (solid bars) and after (bars filled with dots) galvanic coupling.

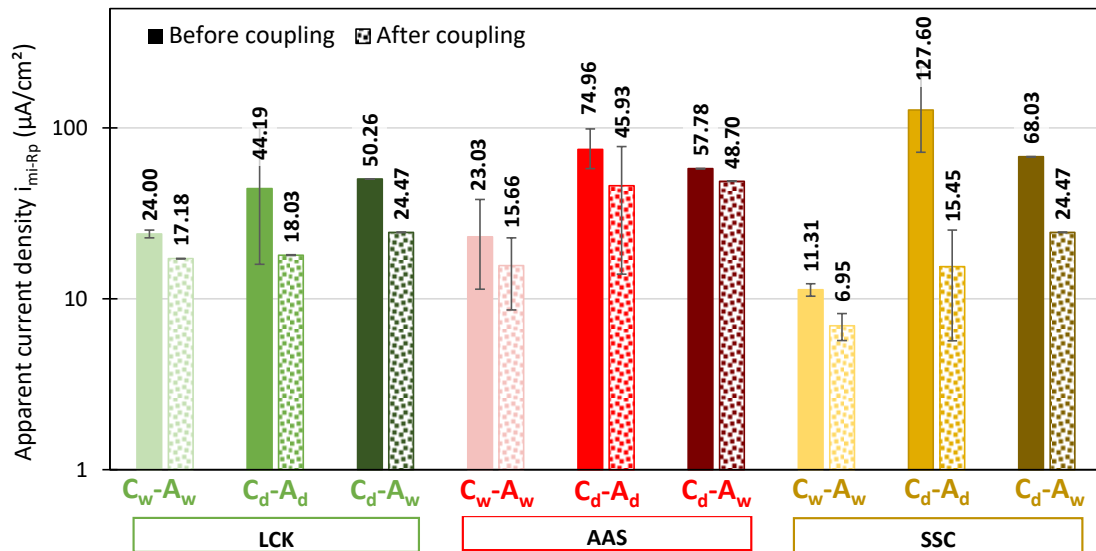


Figure 80: Apparent current density  $i_{mi-Rp}$  measured on activated anodes by LPR measurement, before (solid bars) and after (bars filled with dots) galvanic coupling.













## 4.6 Autopsy of the anodes

### 4.6.1 Visual inspection

In order to complete the electrochemical results obtained, the anodes are split in two and a visual inspection is performed in order to have a first estimation of the quantity of corrosion products. For each condition tested (C<sub>w</sub>-A<sub>w</sub>, C<sub>d</sub>-A<sub>d</sub>, C<sub>d</sub>-A<sub>w</sub>), one representative photo is displayed in Table 40. Different areas covered with corrosion products (more or less large) are present on the surface of the rebar. Black corrosion products are sometimes more easily observed on the mortar than on the steel. In addition to the autopsies on the anodes used to perform the different galvanic couplings, one carbonated anode per formula kept in carbonation and not coupled (called “carbonated without coupling”) was autopsied for comparison by the same deadline (Figure 66). Finally, autopsies have verified the absence of crevice corrosion near the electrical connexions, for all the anodes.



Table 40: State of the rebars during autopsies after 90 days of galvanic coupling (1 representative sample per condition), or for carbonated anodes without coupling.

	LCK	AAS	SSC
C <sub>w</sub> -A <sub>w</sub>			
C <sub>d</sub> -A <sub>d</sub>			
C <sub>d</sub> -A <sub>w</sub>			
Carbonated without coupling			

#### 4.6.2 Mass loss

The mass loss measured on the anode rebars after galvanic coupling is shown in Figure 81. The mass losses presented are the average of 2 samples, except for the condition C<sub>d</sub>-A<sub>w</sub> and for the carbonated anode without coupling LCK, for those only one measurement was performed.

As explained in section 3.6.1, it is important to note that in addition to the amount of mass loss due to the corrosion products themselves (Figure 81), about 50 mg of mass loss due to the cleaning process and mill scale was measured for each condition (not represented on Figure 81 for reasons of readability). The corrosion products are therefore present in large enough quantities to have an acceptable accuracy of measurement (except for the carbonated anodes without coupling for which the corrosion products represent only 5 to 10% of the total mass loss).

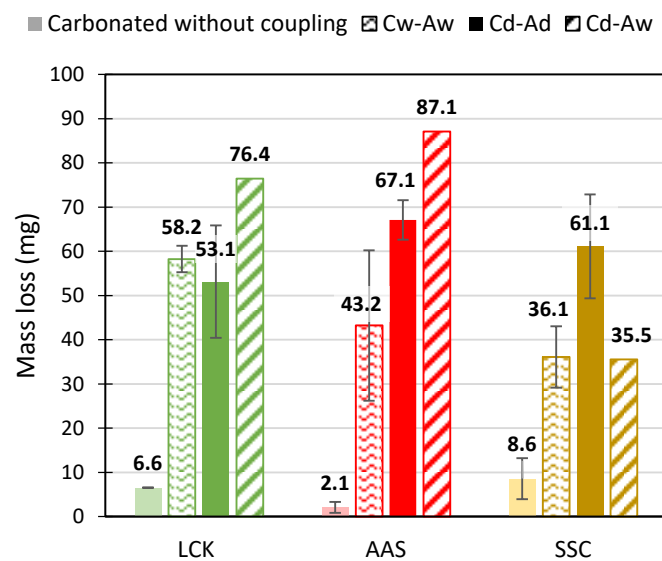


Figure 81: Mass loss associated to corrosion products, measured on anode rebars after 90 days of galvanic coupling or for carbonated anodes without coupling.

#### 4.6.3 Total current $I_{tot}$ calculated from the mass loss

The values of total current  $I_{tot}$  after 90 days of coupling, associated with the total mass losses measured previously and calculated according to Faraday's law (Equation (28)), are presented on Figure 82. As explained in section 3.6.2,  $I_{tot}$  corresponds to the sum of the currents flowing between the anode and the cathode ( $I_g$ ) but also at the local scale of the anode ( $I_{mi-anode}$ , being the sum of  $I_a$  and  $I_{mic}$ ).

It is important to specify here, that a non-negligible  $I_{mi-anode}$  current surely have developed before the galvanic coupling, during the natural carbonation of the anodes, as highlighted on Figure 81 by the mass loss of carbonated samples without coupling. It has been observed in Figure 71 indeed, that the carbonation front reaches the rebar after about 6 months of exposure for the three formulas. However, the samples are kept in carbonation for another 6 months (1 year in total), which leaves time for a corrosion current to develop at the anode before the galvanic coupling. Further analysis is included in sections 5.1 and 5.2 of the discussion.

The total currents  $I_{tot}$  are logically proportional to the mass losses (corrosion products) in Figure 81 and vary according to the binders and the saturation conditions tested. A more detailed analysis of these currents is also proposed in section 5.2.

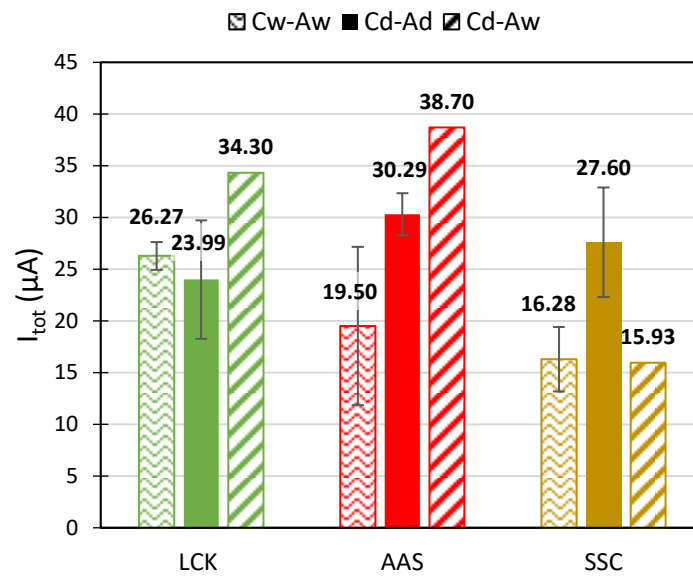


Figure 82: Total current  $I_{tot}$  after 90 days of coupling, calculated from mass loss.

5 Discussion

5.1 Influence of the galvanic coupling on corrosion

Figure 83 presents the total apparent current densities ( $i_{tot}$ ) calculated from the mass losses (section 3.6.2), associated to carbonated anodes without coupling (references) and those associated to the 90 days of anode-cathode coupling for the different conditions of saturation tested. The lifetime of these two types of samples is summarized in Figure 66.

Values of  $i_{tot}$  are apparent current densities, obtained by dividing the currents  $I_{tot}$  (presented in section 4.6.3 for the anodes used for the galvanic coupling) by the surface of the anode rebar. In this case, the total apparent current density  $i_{tot}$  is the sum of the galvanic current ( $i_g$ ) flowing between the anode and the cathode during the  $i_{tot}$  coupling and of the local current at the anode scale ( $i_{mi-anode}$ ) (Equation (29)), as detailed in the next section 5.2.

For the carbonated anodes without coupling, the mass loss comes only from the current that developed at the anode scale after the activation by carbonation ( $i_{mi-anode}$ ), since they were not used for galvanic coupling (no  $i_g$ ). It should be noted that the mass loss measurements were performed on samples of the same age.

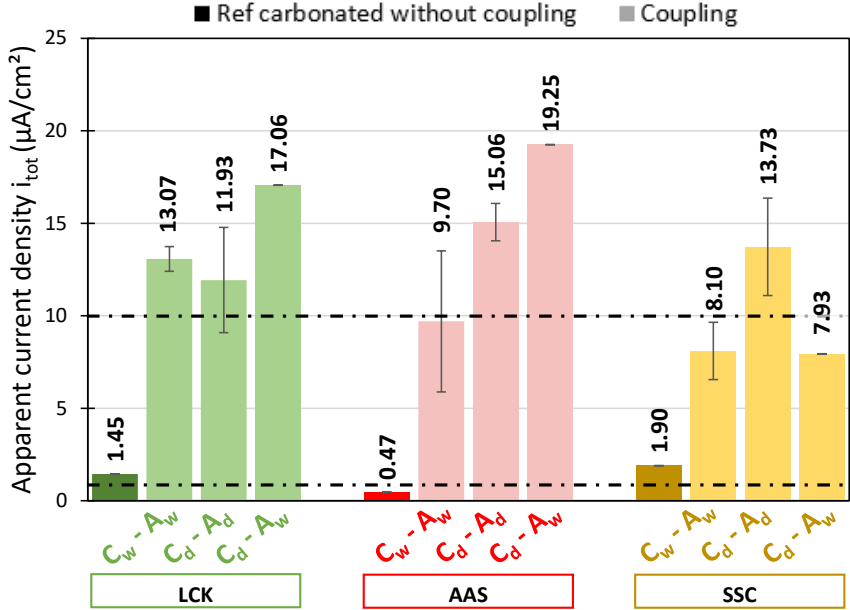


Figure 83: Comparison of the total apparent current density ( $i_{tot}$ ) which develops during 90 days of anode-cathode coupling for the different conditions of saturation tested (light bars), with the one measured on carbonated anodes without coupling (dark bars), at the same deadline. The dotted black line indicates the thresholds of 1 or 10  $\mu A/cm^2$ , associated with high or very high levels of corrosion, respectively.

First of all, it appears that the total apparent current densities ( $i_{tot}$ ), developed during 90 days of anode-cathode coupling for the different conditions of saturation tested, are all high ( $>1 \mu A/cm^2$ ) and even very high ( $>10 \mu A/cm^2$ ) for LCK, AAS and the C<sub>d</sub>-A<sub>d</sub> condition for SSC. These interpretations are based on TC RILEM 154 recommendations (C. Andrade and Alonso

2004). However, it is important to clarify a limitation of the results presented in this section, since these values of  $i_{tot}$  are surely overestimated, due to the parameters chosen for the experimental set up. Several aggressive conditions were chosen for the anodes of this study (low cover depth of 8.5 mm, increased w/b ratio, humidity), in order to activate samples by natural carbonation in a reasonable time and also to maximize the developed currents and thus the associated mass loss. The objective was to maximize the accuracy of these measurements and then to highlight behaviours according to the formulas. Moreover, a high C/A ratio equal to 55 was chosen for the experimental set up (Figure 69), also to maximise the galvanic current exchanged between anode and cathode, while it is generally taken between 1 and 16 in other experimental studies (Revert et al. 2019; T.-T. Nguyen et al. 2022; Abdelkader Nasser and Castel 2014; Sohail et al. 2015). It will therefore be associated with higher currents, because these same studies show that  $I_g$  (and thus  $i_{tot}$ ) increases with the C/A ratio. In reality, the C/A ratio will tend to decrease as the carbonation front progresses (increase of the anodic surface). A last parameter that can explain these high currents  $i_{tot}$ , is the small distance between anode and cathode (Figure 69) compared to reality, where the resistance of the electrolyte (concrete) will be higher, thus leading to an increase in the parameter  $R_{tot}$  and a decrease in  $I_g$  (and thus  $i_{tot}$ ).

Thus, the  $i_{tot}$  presented on Figure 83 are surely overestimated, considering they are obtained on anodes with an increased w/b ratio (+20% for AAS and SSC and +40% for LCK) and consequently with a lower resistivity. A relationship between resistivity and corrosion rate has precisely been demonstrated in the literature (Hornbostel, Larsen, and Geiker 2013), lower resistivities leading to higher corrosion rates. Moreover, to a lesser extent, the anodic surface considered is the one of the anode rebar, while the real active areas are much lower according to the autopsies (Table 40). It results in an apparent current density slightly lower than the real one (corresponding to the active zones of the anode), and counterbalances the previous remarks. Even if the  $i_{tot}$  values presented on Figure 83 are overestimated, they can be used to make comparisons and to identify behaviours according to the saturation condition tested. Then, for the reference anodes carbonated without coupling, the total apparent current densities ( $i_{tot}$ ) are high for LCK and SSC ( $> 1 \mu\text{A}/\text{cm}^2$ ), while they are low for AAS (0.1 to 0.5  $\mu\text{A}/\text{cm}^2$ ).

But in general, it can be observed on Figure 83 that the  $i_{tot}$  values are much lower on the reference anodes without coupling (dark bars), compared to those used for galvanic coupling (light bars): factor 8 to 11 between the two for LCK, factor 21 to 40 for AAS and factor 4 to 7 for SSC. This is partly explained by the fact that the  $i_{tot}$  developed on the anodes used for the coupling, is the sum of the galvanic current  $i_g$  between the active anode and the passive cathode, and of the local current at the anode scale  $i_{mi-anode}$  ( $i_{mi-anode}$  being partly developed during the natural carbonation before the coupling (same order of magnitude as  $i_{tot}$  for the reference anodes), and partly during the coupling). On the contrary, for the reference anodes not coupled,  $i_g$  is zero, meaning that  $i_{tot}$  is equal to  $i_{mi-anode}$  (Equation (29)). The galvanic coupling thus intensified the corrosion phenomena at the anode, as illustrated in Figure 79 where the  $E_{corr}$  becomes more electronegative on the anodes after coupling, or in Figure 81 where the mass losses measured (proportional to  $i_{tot}$ ) are largely higher on the anodes used for galvanic coupling than on the reference anodes kept only in carbonation.

Finally, Figure 83 highlights the interest of the galvanic current measurement to quantify the corrosion kinetics due to carbonation in low-carbon concretes, as the proposed method takes into account both the galvanic contribution  $i_g$  and the local contribution  $i_{mi-anode}$ , in the value of  $i_{tot}$ . The values of  $i_{tot}$  obtained by galvanic current measurement indeed, are much higher than those obtained without coupling. Not taking into account the galvanic contribution can therefore lead to a strong underestimation of the corrosion kinetics. Yet, the galvanic coupling is a phenomena that occurs on real structures (multi-layers reinforcement), where carbonation leads to a uniform depassivation of the first reinforcement layer, which is coupled with the rest of the passive network. It is not often taken into account by laboratory experiments, while its contribution can be not negligible and should be considered to assess the durability of reinforcement, as recommended by other authors (Revert et al. 2019; Sohail et al. 2015; Castel and Nasser 2015; 2015).

**5.2 Total corrosion current ( $i_{tot}$ ): contributions of galvanic current between anode and cathode ( $i_g$ ) and local current at the anode ( $i_{mi-anode}$ )**

**5.2.1 Composition of  $i_{tot}$ : repartition between  $i_g$  and  $i_{mi-anode}$**

Figure 84 presents the distribution between the two apparent current densities forming  $i_{tot}$ , that is to say the galvanic contribution between the anode and cathode ( $i_g$ ) and the local contribution at the anode scale ( $i_{mi-anode}$ ). Their proportion in percentage is also specified. All values are apparent current densities for easier comparison.

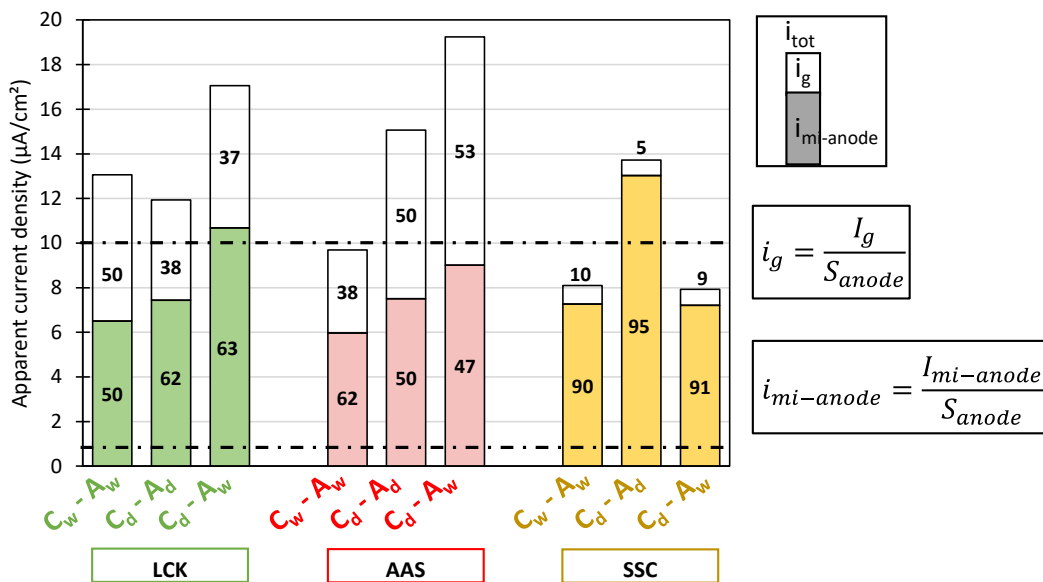


Figure 84: Distribution between the galvanic ( $i_g$ ) and local at the anode ( $i_{mi-anode}$ ) apparent current density, which develops during 90 days of anode-cathode coupling. The sum of  $i_g$  and  $i_{mi-anode}$  gives  $i_{tot}$ . The numbers on the bars corresponds to percentages. The dotted black line indicates the thresholds of 1 and 10  $\mu A/cm^2$ , associated with high and very high levels of corrosion, respectively.

First of all, it appears that the distribution between  $i_g$  and  $i_{mi-anode}$  is different for all binders and all saturation conditions tested.  $i_{mi-anode}$  is high ( $> 1 \mu A/cm^2$ ) for each condition, due to activation by carbonation.

For each condition, more than 50% of  $i_{tot}$  is attributed to  $i_{mi-anode}$ . The saturation conditions tested have the same influence on the apparent current densities  $i_{mi-anode}$  of LCK and AAS binders.  $i_{mi-anode}$  increases following the conditions  $C_w-A_w < C_d-A_d < C_d-A_w$ . For SSC, the  $i_{mi-anode}$  obtained with the conditions  $C_w-A_w$  is similar, while the one obtained with  $C_d-A_d$  is higher. A more detailed analysis and explanation of the  $i_{mi-anode}$  values is given in the next paragraph "Focus on local current at the anode ( $i_{mi-anode}$ )".

Similarly,  $i_g$  is non negligible for LCK and AAS no matter what saturation conditions are considered, while it remains low for SSC. It represents between 37 to 53% of  $i_{tot}$  for LCK and AAS, against only 5 to 10% for SSC. A more detailed analysis and explanation of the  $i_g$  values is given in the following paragraph "Focus on galvanic current ( $i_g$ )".

For different experimental set up, different C/A and PC-based concretes, higher proportions of galvanic currents were measured experimentally or calculated by numerical simulations, compared to local currents in the literature : 68 % of galvanic current for C/A equal to 5 (A. Nasser et al. 2010), 54% for C/A equal to 0.5 to 90% of galvanic current for C/A equal to 50 (Revert et al. 2019), each time for quasi-saturated conditions. (Abdelkader Nasser and Castel 2014) also confirms that galvanic corrosion seems to be the predominant corrosion activity in a carbonated CEM I-concrete, contrary to what is observed in this study. Finally, (T.-T. Nguyen et al. 2022) reports a lower galvanic current measured on concrete containing slag (CEM III cement compared to CEM I cement), attributed to a higher resistivity of the CEM III concrete. The same behaviour could be expected for the SSC binder because it has a high resistivity, as illustrated in Figure 74.

### 5.2.2 Focus on galvanic current ( $I_g$ )

The galvanic current  $I_g$  obtained at the end of 90 days of coupling for each binder and each saturation condition tested is shown in Figure 85, represented by circles whose diameter is proportional to  $I_g$ . These values of galvanic current  $I_g$  can be correlated with the total resistance  $R_{tot}$  (summarized in Figure 77) and the potential difference  $\Delta E_{A-C}$  (summarized in Figure 78), between anode and cathode before coupling.

For the Portland cement-based **LCK** samples, it was expected an increase of  $I_g$ , increasing the potential difference  $\Delta E_{A-C}$  and decreasing  $R_{tot}$  (Revert et al. 2019; C. Andrade et al. 1992). This is verified when analysing each condition one after the other. In general, corrosion potential  $E_{corr}$ , mainly depends on the saturation (saturated or dry) and the electrochemical state (passive or active) of the sample: saturated and/or active samples result in more electronegative  $E_{corr}$  than those dry and/or passive.

- For the **C<sub>d</sub>-A<sub>d</sub>** (cathode and anode dry) condition, the saturation conditions are similar for both samples. The different electrochemical state between the active anode (electronegative corrosion potential  $E_{corr}$  around -352 mV/Ag/AgCl) and the passive

cathode (less electronegative  $E_{\text{corr}}$  around +47 mV/Ag/AgCl), will generate a quite high potential difference  $\Delta E_{\text{A-C}}$  between the two (-398 mV/Ag/AgCl). The dry state of the sample will also lead to a higher total resistance  $R_{\text{tot}}$  (higher material resistance and polarisation resistance on dry materials compared to those immersed in water). A quite high galvanic current of 9.04  $\mu\text{A}$  is recorded for the  $\text{C}_d\text{-A}_d$  condition.

- Then, for the  $\text{C}_w\text{-A}_w$  (cathode and anode in water) condition, both samples have again the same saturation conditions. However, this time, their initial corrosion potential  $E_{\text{corr}}$  will be more electronegative for the active anode and the passive cathode in a saturated state (in water), compared to a dry state. Thus a potential difference  $\Delta E_{\text{A-C}}$  of -575 mV is measured (-639 mV/Ag/AgCl for the anodes and -64 mV/Ag/AgCl for the cathodes as initial  $E_{\text{corr}}$  before coupling), which is higher than the previous condition  $\text{C}_d\text{-A}_d$ . The total resistance  $R_{\text{tot}}$  for  $\text{C}_w\text{-A}_w$  is low, due to lower material resistance and polarisation resistance on materials immersed in water compared to those dry. Therefore a higher galvanic current of 13.20  $\mu\text{A}$  is recorded for the  $\text{C}_w\text{-A}_w$  condition, due to a higher  $\Delta E_{\text{A-C}}$  (electromotive force to generate  $I_g$ ) and a lower  $R_{\text{tot}}$ .
- For the last condition  $\text{C}_d\text{-A}_w$  (cathode dry and anode in water), this time anode and cathode have both different electrochemical state (active/passive) and saturation condition (dry/in water). Therefore, a higher  $\Delta E_{\text{A-C}}$  of -646 mV is recorded, as it corresponds to the most extreme condition with one active/in water sample and the other passive/dry (-681 mV/Ag/AgCl for the anode and -35 mV/Ag/AgCl for the cathode). An intermediate  $R_{\text{tot}}$  is associated to this condition ( $\text{C}_d\text{-A}_w$ ), due to an intermediate saturation condition combining a saturated anode and dry cathode, compared to  $\text{C}_d\text{-A}_d$  or  $\text{C}_w\text{-A}_w$ . An intermediate galvanic current of 12.82  $\mu\text{A}$  is recorded for the  $\text{C}_d\text{-A}_w$  condition, as the higher potential difference  $\Delta E_{\text{A-C}}$  is balanced by the higher total resistance  $R_{\text{tot}}$  compared to  $\text{C}_w\text{-A}_w$ .

The behaviour observed for slag based-binders is slightly different, for two main reasons. As explained in the section 4.3.2, the presence of sulfur in slag generates more electronegative corrosion potentials  $E_{\text{corr}}$  in passive state and saturated conditions. Therefore, the potential difference  $\Delta E_{\text{A-C}}$  varies differently from the one of the LCK for the saturation conditions  $\text{C}_w\text{-A}_w$  and  $\text{C}_d\text{-A}_w$ . Then, as also explained in the section 4.3.2, the  $R_p$  values measured for AAS and SSC samples in water, are not always representative of the corrosion state of the rebars, but rather of the sulfur oxidation reactions. Therefore, the  $R_{\text{tot}}$  based on  $R_p$  values (Equation (30)), have to be analysed carefully.

For AAS:

- The same interpretation as for LCK applies for the  $\text{C}_d\text{-A}_d$  condition, as the sulfur oxidation no longer creates a highly reducing environment. Therefore, a quite high potential difference  $\Delta E_{\text{A-C}}$  of -366 mV is measured between active dry anode and passive dry cathode (-444 mV/Ag/AgCl for the anodes and -78 mV/Ag/AgCl for the cathode). It is also associated to a high  $R_{\text{tot}}$  compared to the other saturation conditions tested for AAS. These parameters correspond to a  $I_g$  of 15.20  $\mu\text{A}$ .



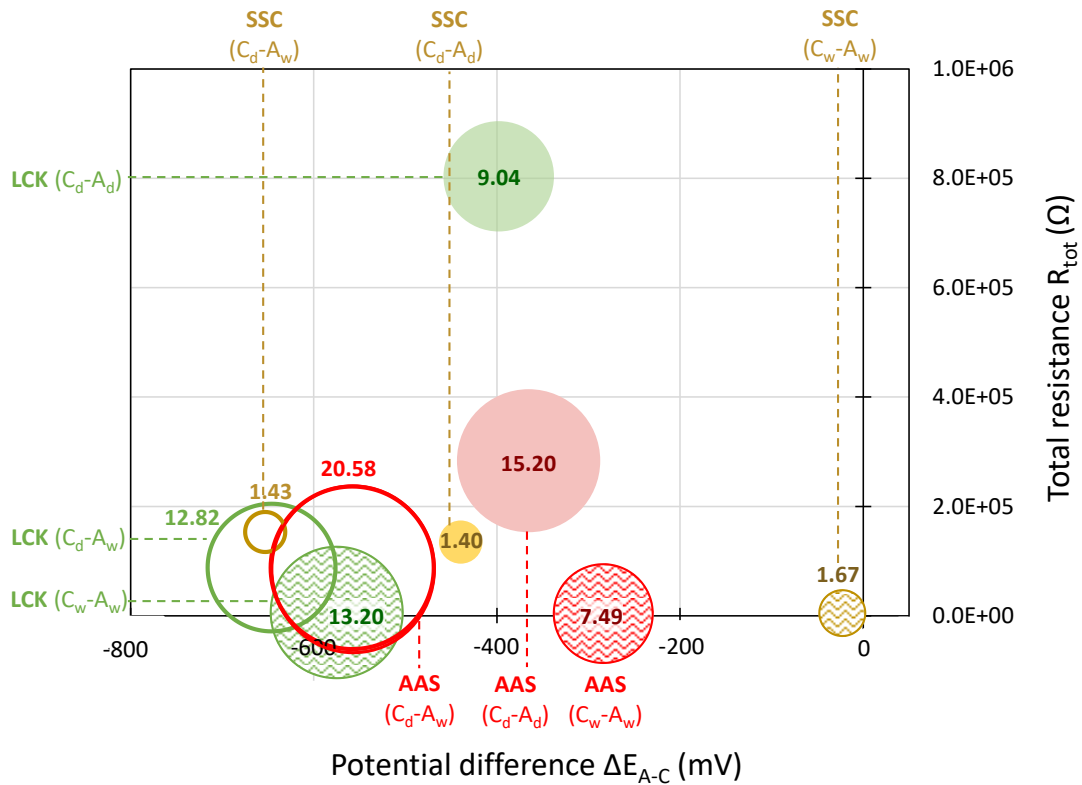


Figure 85: Relation of the measured galvanic current  $I_g$  with the total resistance  $R_{tot}$  associated to each anode-cathode pair and the potential difference ( $\Delta E_{A-C}$ ) measured between the two before coupling. The diameter of circles is proportional to  $I_g$  (in  $\mu A$ ).

- For the  $C_w-A_w$  condition, this time a lower  $\Delta E_{A-C}$  of -284 mV is measured (-601 mV/Ag/AgCl for the anodes and -317 mV/Ag/AgCl for the cathodes). As explained previously, the passive cathode still have an electronegative potential due to the reducing environment created by the presence of sulfur species from slag in its pore solution. It is also associated to a low  $R_{tot}$  compared to the other saturation conditions tested for AAS. These parameters correspond to a  $I_g$  of 7.49  $\mu A$ , lower than the  $C_d-A_d$  condition (15.20  $\mu A$ ) due to a lower  $\Delta E_{A-C}$  which compensates for the lower  $R_{tot}$ .
- The last condition  $C_d-A_w$  gives the higher  $\Delta E_{A-C}$  with -558 mV (-651 mV/Ag/AgCl for the anode and -93 mV/Ag/AgCl for the cathode) and an intermediate  $R_{tot}$ . It is associated to the highest  $I_g$  for AAS of 20.58  $\mu A$ , explained by the highest  $\Delta E_{A-C}$  that compensates for the intermediate  $R_{tot}$ . It seems for this binder, that the potential difference  $\Delta E_{A-C}$  has a greater influence than  $R_{tot}$  on the galvanic current.

Finally, the galvanic currents  $I_g$  measured on SSC remains low regardless of the saturation conditions tested.

- For the  $C_w-A_w$  condition, the negligible potential difference  $\Delta E_{A-C}$  of -23 mV explains the very low  $I_g$  of 1.67  $\mu A$ . As previously explained, passive cathodes have a very electronegative  $E_{corr}$  (-634 mV/Ag/AgCl) due to the presence of sulphur in slag, similar to the one of the anode (-657 mV/Ag/AgCl). This  $C_w-A_w$  condition is also associated to a low  $R_{tot}$ .

- For the **C<sub>d</sub>-A<sub>a</sub>** condition, a quite high  $\Delta E_{A-C}$  of -440 mV is measured (-453 mV/Ag/AgCl for the anodes and -14 mV/Ag/AgCl for the cathodes) and is associated with a higher  $R_{tot}$ , corresponding to a low  $I_g$  of 1.40  $\mu A$ . It seems the higher  $R_{tot}$  compensates for the higher  $\Delta E_{A-C}$ , as a lower  $I_g$  is measured compared to the **C<sub>w</sub>-A<sub>w</sub>** condition.
- Finally, the last condition **C<sub>d</sub>-A<sub>w</sub>** also leads to the highest  $\Delta E_{A-C}$  of -653 mV for this binder (-665 mV/Ag/AgCl for the anode and -12 mV/Ag/AgCl for the cathode), combined with a high  $R_{tot}$  (whereas an intermediate value would have been expected as for AAS and LCK). Despite the highest  $\Delta E_{A-C}$ , the  $I_g$  of 1.43  $\mu A$  measured for the condition **C<sub>d</sub>-A<sub>w</sub>**, is slightly higher than for the **C<sub>d</sub>-A<sub>d</sub>** condition, but still lower than the one for the **C<sub>w</sub>-A<sub>w</sub>** condition. Therefore, it seems the galvanic currents of SSC have a low dependency on  $\Delta E_{A-C}$  and seem more influenced by  $R_{tot}$ .

### 5.2.3 Focus on local current at the anode ( $i_{mi-anode}$ )

The local current at the anode scale  $i_{mi-anode}$  partly developed during the natural carbonation before the coupling (same order of magnitude as  $i_{tot}$  for the reference anodes carbonated but not coupled in Figure 83), and partly during the coupling. It is confirmed by Figure 79, where the corrosion potential  $E_{corr}$  becomes more electronegative on the anodes after coupling than before. During the galvanic coupling indeed, the  $E_{corr}$  of the active anodes had been shifted to less electronegative values, due to the creation of an equilibrium potential with the passive cathodes (more electropositive  $E_{corr}$ ) and cannot explain these results. Therefore, it can certainly be attributed to a more stable and advanced corrosion process at the anode scale due to the coupling. The corrosion potential  $E_{corr}$  becomes more electronegative on the anodes after coupling, except for the SSC binder where no significant evolution of  $E_{corr}$  is visible. It seems logical according to the previous analysis of Figure 85, showing very low values of galvanic currents measured on the SSC binder. Therefore, the negligible galvanic contribution (Figure 84) has not contributed to a more advanced corrosion process, that remained similar to before the coupling.

However, at the same time, Figure 80 shows a decrease of the apparent current densities  $i_{mi-Rp}$  measured at the anode scale with the LPR measurement, after the galvanic coupling. Therefore, it seems that with the galvanic coupling, some of the electrons that previously flowed between the active and passive areas of the anode, now flow between the active anode and the spatially separated cathode. Consequently, the corrosion kinetics at the local scale of the anode were slowed down.

The different saturation conditions tested also influence the  $i_{mi-anode}$  values for each binder. The **C<sub>w</sub>-A<sub>w</sub>** condition generates the lowest  $i_{mi-anode}$ . One hypothesis could be that during the galvanic coupling in water particularly, the hydroxide ions tend to migrate toward the anode rebar and thus to increase the pH. Therefore, it would have a protective effect and would contribute to slow down the corrosion kinetics. With the electronic and ionic current generated between anode and cathode coupling, indeed, negative electrical charge tend to move towards the anode rebar having positive electrical charge due to the anodic reaction (oxidation of steel producing electrons) (Lliso-Ferrando et al. 2022). Moreover in these conditions (**C<sub>w</sub>-A<sub>w</sub>**) the renewal of

oxygen, necessary for the cathodic corrosion reaction, is more difficult. For the  $C_d-A_w$  condition, the slightly higher  $i_{mi-anode}$  measured on LCK compared to AAS or SSC, could be attributed to its coarser porosity (Figure 12 and Figure 13 in Article A), which facilitates the renewal of oxygen at the rebar.

Concerning the higher values of  $i_{mi-anode}$  obtained on SSC for the  $C_d-A_d$  condition, this result was not expected as it is widely recognized that the corrosion kinetics are higher for high humidity in carbonated concretes (Stefanoni, Angst, and Elsener 2018). A repeat of the galvanic coupling in this condition would be beneficial to confirm this result. No particular cracks or other defects on the anodes concerned were observed, to explain these high values of  $i_{mi-anode}$ . Neither initial defects on the steel rebars used for this condition. However, it can be observed from Figure 77, that the anodes used for the  $C_d-A_d$  condition had a much lower  $R_{p,a}$  value (270  $\Omega$ ) compared to the two others conditions (1224  $\Omega$  for  $C_w-A_w$ , and 1176  $\Omega$  for  $C_w-A_w$ ) in favour of a high local current  $i_{mi-anode}$ .

Finally, the local corrosion current densities at the anode ( $i_{mi-anode}$ ), measured for the three binders (on mortar), are high but are nevertheless similar to the ranges available in the literature for CEM I (concretes). For carbonation-induced corrosion, the review of (Angst et al. 2020) reports ranges of corrosion currents on CEM I-concrete, around 1  $\mu A/cm^2$  in wet conditions (80-100% RH), and until 9  $\mu A/cm^2$  for very unfavourable conditions similar to those of this study (rebar in contact with liquid water, low cover dept and poor quality concrete).

### 5.3 Assessment of the corrosion risk in the three low-carbon concretes considered

This experimental campaign has allowed to provide answers on the performance of the three low-carbon concretes studied with respect to corrosion due to carbonation. The influence of different saturation conditions for anode and cathodes on the corrosion rates, was also evaluated. Table 41 summarizes the resistance to carbonation rates of LCK, AAS and SSC cured 1 to 14 days, as well as the  $i_{tot}$  developed. It allows to conclude about their possible use in an environment exposed to carbonation.

About the **corrosion initiation**, the previous results obtained in Article B, to assess the carbonation resistance of the three low-carbon concretes, were reported in Table 41. Their carbonation rates for different curing periods (1 to 14 days) are considered and compared to those of a CEM III/A reference from (Huy Vu et al. 2019). Their ability to maintain a high pH after carbonation, to delay the rupture of the passive film and the corrosion initiation, is also considered. The investigations conducted in Article B, allow to conclude that LCK has a moderate resistance to corrosion initiation considering relatively slow carbonation rates and a limited ability to maintain a high pH (reduced quantity of CEM I in its binder leads to a reduced amount of portlandite to buffer the pH). AAS also has a moderate resistance to corrosion initiation considering its rather rapid carbonation, balanced by a strong ability to maintain a high pH (due to different hydrates and mechanisms involved than in PC-binders). Finally, SSC has a lower resistance to corrosion initiation considering its rapid carbonation, especially for short curing times, and a low ability to maintain a high pH (no portlandite to buffer the pH).

Table 41: Performance of LCK, AAS and SSC concretes against corrosion due to carbonation, considering the initiation and propagation phases of corrosion.

Concrete	Natural carbonation rate on concrete after 1d to 14d curing <sup>(1)</sup> (mm/(years <sup>1/2</sup> ))	Resistance to carbonation assessed by comparison with a CEM III/A concrete of same strength class <sup>(2)</sup> (corrosion initiation)	pH measured after 18 months in natural carbonation <sup>(1)</sup> (corrosion initiation)	$i_{tot}$ ( $\mu\text{A}/\text{cm}^2$ ) for anodes with an increased w/b ratio <sup>(3)</sup> (corrosion propagation)	Recommendation for exposition to carbonation
LCK	11.3 to 2.2	+16%	8.9	Very high (11.93 to 17.06)	Ok
AAS	12.4 to 8.8	+17%	11.0	Very high (9.70 to 19.25)	Ok for specific curing and saturation conditions
SSC	21.7 to 8.8	+30%	8.6	High to very high (7.93 to 13.73)	Ok for specific curing and saturation conditions

<sup>(1)</sup> For natural carbonation outdoor sheltered (Article B).

<sup>(2)</sup> For 1 day of curing and for natural carbonation outdoor sheltered.

<sup>(3)</sup> w/b ratio increased by 20% for AAS and SSC and by 40% for LCK, meaning  $i_{tot}$  corresponds to overestimated corrosion kinetics.

About the **corrosion propagation**, the values of  $i_{tot}$  are used to evaluate the level of corrosion kinetics. Due to the extreme experimental parameters chosen, the  $i_{tot}$  values obtained on mortar anodes (increased w/b ratio and low cover) cannot be generalized to real reinforced concrete structures. Nevertheless, in order to conclude on the durability of the rebars in each binder, a coefficient is calculated for each formula, as the ratio between concrete resistivity and mortar resistivity (with increased w/b ratio). The resistivities of saturated concrete cathodes are 2244, 2052 and 9394  $\Omega\cdot\text{m}$  for LCK, AAS and SSC, respectively. The resistivities of the saturated mortar anodes (with increased w/b ratio) are: 483, 1627 and 3076  $\Omega\cdot\text{m}$  for LCK, AAS and SSC. The associated coefficients are therefore 4.65, 1.26, 3.05 for LCK, AAS and SSC. For the rest of the discussion, an estimation of the corrosion kinetics on concrete is proposed by dividing the  $i_{tot}$  values obtained on mortar by the coefficient calculated previously. A relationship between resistivity (depending on the w/b ratio) and corrosion rate has been confirmed in the literature in the case of carbonate samples (Hornbostel, Larsen, and Geiker 2013), but the high scattering observed in the results (very different corrosion rates measured according to the method and experimental design chosen) does not allow to identify a general relationship (with also variations due to the binder type). These corrosion kinetics on concrete should be considered with caution, as they represent only a rough estimation to conclude the discussion. The approximated  $i_{tot}$  after 90 days of galvanic coupling are finally high ( $>1 \mu\text{A}/\text{cm}^2$ ) for the three binders: 2.57 to 3.67  $\mu\text{A}/\text{cm}^2$  for LCK, 7.69 to 15.27  $\mu\text{A}/\text{cm}^2$  for AAS and 2.60 to 4.50  $\mu\text{A}/\text{cm}^2$  for SSC. These values probably remains still overestimated, for the other reasons discussed in section 5.1. Moreover, in real structures these high corrosion currents will be

encountered for a short duration, as the humidity conditions and the associated corrosion rates vary over time.

Finally, a conclusion about the use of each low-carbon concrete in environments exposed to carbonation is proposed, based on the results obtained to characterize both corrosion initiation and propagation.

- For **LCK**, the moderate resistance to corrosion initiation is combined with high corrosion rates. The carbonation rates are similar to those of a classical CEM III/A for short curing times and even much lower for long curing times. Its resistance to corrosion initiation is therefore acceptable and could be even be improved by favouring longer curing times, to delay the corrosion activation and the associated high currents (also probably overestimated in this experimental campaign as the 40% w/b increase strongly modified its transport properties). Its use for environments exposed to carbonation is therefore possible, rather for permanently dry or wet conditions (higher  $i_{tot}$  measured for  $C_d-A_w$  condition).
- For **AAS**, its moderate resistance to corrosion initiation (quite rapid carbonation but strong ability to maintain a high pH) is combined with higher corrosion rates than LCK and SSC. Its use for exposition to carbonation is however possible, preferentially for longer curing times or a reduced w/b ratio to slow down the corrosion initiation. Permanently wet expositions should be favoured (lower  $i_{tot}$  measured for  $C_w-A_w$  condition).
- Finally for **SSC**, its low resistance to corrosion initiation is combined with high corrosion rates. Therefore, its use for carbonation exposition is not recommended but could be possible for long curing times and a reduced w/b ratio, in order to slow down the corrosion initiation. The higher  $i_{tot}$  measured for  $C_d-A_d$  condition, need to be confirmed by further investigations. The special characteristic of this binder is that low galvanic currents have been measured regardless of the exposure conditions tested. Its use when strong galvanic couplings are likely to occur, could therefore be recommended.

## 6 Conclusion

The corrosion rates due to activation by natural carbonation were assessed in three low-carbon concretes of same strength class C25/30: LCK, Na<sub>2</sub>CO<sub>3</sub>-AAS and SSC concretes. An experimental campaign based on 3 months of galvanic current measurement, combined with mass loss on the rebar was proposed. Anodes samples with an increased w/b ratio were used to accelerate their corrosion initiation and a high cathode to anode surface ratio of 55 was chosen to maximize the corrosion currents. Classical electrochemical measurements (corrosion potential  $E_{\text{corr}}$ , polarization resistance  $R_p$ ) are also used to follow the electrochemical parameters of samples during their exposition to carbonation. Finally, three saturation conditions were tested for the anodes and cathodes, to evaluate an interval of possible corrosion rates due to carbonation. The following conclusions can be drawn:

- The results show that the total corrosion current density due to carbonation is high for the three binders and the different saturation conditions tested. These corrosion rates are nevertheless overestimated, as they are obtained on anodes with an increased w/b ratio.
- The galvanic current represents 38 to 53% of the total current for LCK and AAS binders. Its contribution is non-negligible and should be considered for the assessment of the durability of reinforcement, as this phenomenon takes place in real structures. The SSC binder presents a different behaviour with almost no galvanic current (5 to 10%) for all the condition tested.
- The measured galvanic current is added to a high local current at the anode, for the three binders and the different saturation conditions tested.
- The saturation conditions influence the total corrosion current density, with different behaviors observed for each binder. Higher corrosion rates are measured for the C<sub>d</sub>-A<sub>w</sub> (dry cathode and saturated anode) condition for LCK and AAS, while this trend is not confirmed for SSC. LCK performs the best for permanently dry or wet conditions, and AAS for wet conditions. For SSC, lower corrosion rates are measured due to a negligible galvanic current, regardless of the saturation conditions.
- The galvanic current is mainly driven by the potential difference and the total resistance of the materials between the anode and the cathode for LCK. For AAS is seems principally driven by the potential difference, while it depends essentially on the total resistance for SSC.
- As high corrosion rates are measured on these three binders, precautions must be taken to slow down their carbonation rates and delay the corrosion initiation as much as possible, in order to be used with exposure to carbonation.

## 7 Supplementary data

### Related to section 3.4.1

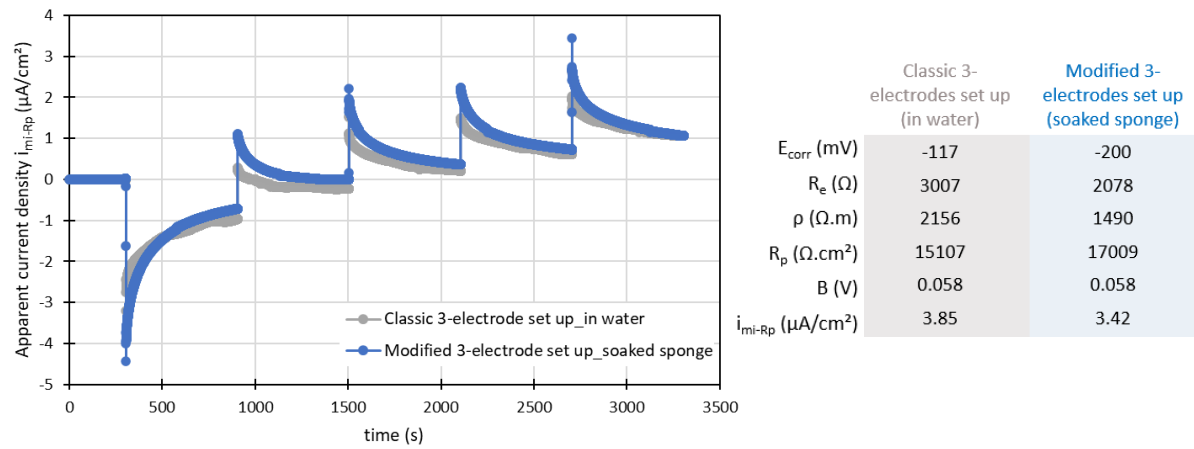


Figure 86: Comparison of current response and electrochemical parameters obtained with classical and modified 3-electrode set-up to apply the LPR measurement.

### Related to section 3.4.2

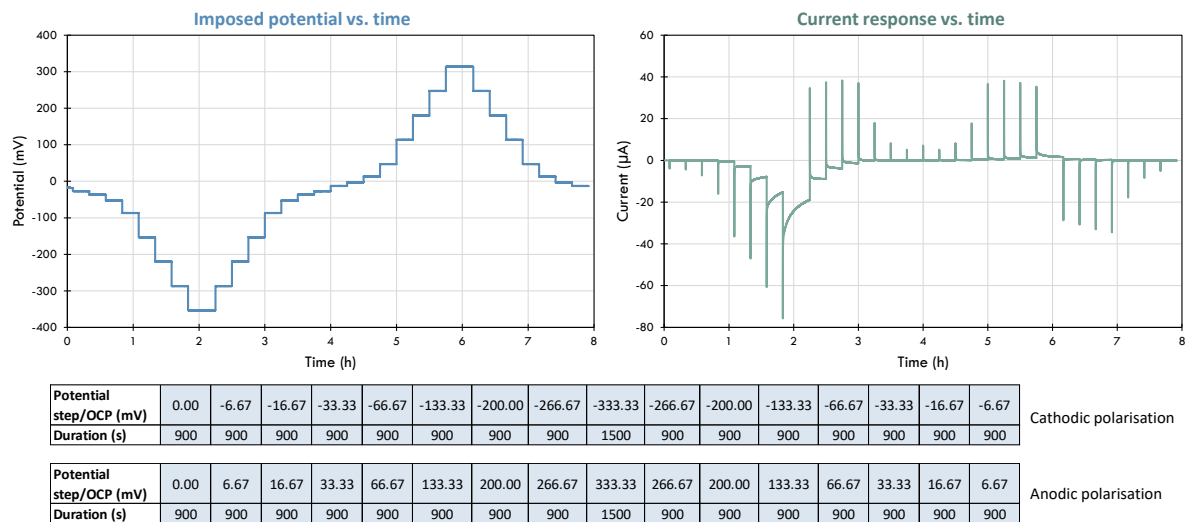


Figure 87: Example of Tafel test performed on an active anode LCK.

## 8 References

- AFNOR. 2010. “NF EN 15743 : Ciment Sursulfaté - Composition, Spécifications et Critères de Conformité.”
- AFNOR. 2018. “EN 12390-10 : Détermination de La Résistance à La Carbonatation Du Béton à Des Niveaux Atmosphériques de Dioxyde de Carbone.”
- Alonso, C., C. Andrade, and J. A. González. 1988. “Relation between Resistivity and Corrosion Rate of Reinforcements in Carbonated Mortar Made with Several Cement Types.” *Cement and Concrete Research* 18 (5): 687–98. [https://doi.org/10.1016/0008-8846\(88\)90091-9](https://doi.org/10.1016/0008-8846(88)90091-9).
- Andrade, C., and C. Alonso. 1996. “Corrosion Rate Monitoring in the Laboratory and On-Site.” *Construction and Building Materials, Durability of Reinforced Concrete Structures*, 10 (5): 315–28. [https://doi.org/10.1016/0950-0618\(95\)00044-5](https://doi.org/10.1016/0950-0618(95)00044-5).
- Andrade, C., and C. Alonso. 2004. “Test Methods for On-Site Corrosion Rate Measurement of Steel Reinforcement in Concrete by Means of the Polarization Resistance Method.” *Materials and Structures* 37 (9): 623–43. <https://doi.org/10.1007/BF02483292>.
- Andrade, C., and J. A. González. 1978. “Quantitative Measurements of Corrosion Rate of Reinforcing Steels Embedded in Concrete Using Polarization Resistance Measurements.” *Materials and Corrosion* 29 (8): 515–19. <https://doi.org/10.1002/maco.19780290804>.
- Andrade, C., I.R. Maribona, S. Feliu, J.A. González, and S. Feliu. 1992. “The Effect of Macrocells between Active and Passive Areas of Steel Reinforcements.” *Corrosion Science* 33 (2): 237–49. [https://doi.org/10.1016/0010-938X\(92\)90148-V](https://doi.org/10.1016/0010-938X(92)90148-V).
- Andrade, Cid, and Angel Castillo. 2003. “Evolution of Reinforcement Corrosion Due to Climatic Variations.” *Materials and Corrosion* 54 (June): 379–86. <https://doi.org/10.1002/maco.200390087>.
- Angst, Fabrizio Moro, Mette Geiker, Sylvia Kessler, Hans Beushausen, Carmen Andrade, Jukka Lahdensivu, et al. 2020. “Corrosion of Steel in Carbonated Concrete: Mechanisms, Practical Experience, and Research Priorities – a Critical Review by RILEM TC 281-CCC.” *RILEM Technical Letters* 5 (December): 85–100. <https://doi.org/10.21809/rilemtechlett.2020.127>.
- Aperador, W., R. Mejía de Gutiérrez, and D.M. Bastidas. 2009. “Steel Corrosion Behaviour in Carbonated Alkali-Activated Slag Concrete.” *Corrosion Science* 51 (9): 2027–33. <https://doi.org/10.1016/j.corsci.2009.05.033>.
- ASTM International. 2012. “ASTM G01-03: Standard Practice for Preparing, Cleaning, and Evaluating Corrosion Test Specimens.”
- ASTM International. 2022. “ASTM C876-22b: Standard Test Method for Corrosion Potentials of Uncoated Reinforcing Steel in Concrete.”
- Azarsa, Pejman, and Rishi Gupta. 2017. “Electrical Resistivity of Concrete for Durability Evaluation: A Review.” *Advances in Materials Science and Engineering* 2017: 1–30. <https://doi.org/10.1155/2017/8453095>.
- Bakharev, T, J.G Sanjayan, and Y.-B Cheng. 2001. “Resistance of Alkali-Activated Slag Concrete to Carbonation.” *Cement and Concrete Research* 31 (9): 1277–83. [https://doi.org/10.1016/S0008-8846\(01\)00574-9](https://doi.org/10.1016/S0008-8846(01)00574-9).
- Bernal, Susan A., John L. Provis, David G. Brice, Adam Kilcullen, Peter Duxson, and Jannie S.J. van Deventer. 2012. “Accelerated Carbonation Testing of Alkali-Activated Binders Significantly Underestimates Service Life: The Role of Pore Solution Chemistry.” *Cement and Concrete Research* 42 (10): 1317–26. <https://doi.org/10.1016/j.cemconres.2012.07.002>.
- Bui, Huy Tang, Koichi Maekawa, and Kang Hai Tan. 2023. “Microcell and Macrocell Corrosion of Steel Bars in Reinforced Concrete Slabs under Different Corrosive Environments and Cathode/Anode Configurations.” *Cement and Concrete Composites* 138 (April): 104989. <https://doi.org/10.1016/j.cemconcomp.2023.104989>.
- Castel, A., and A. Nasser. 2015. “Influence of Pre-Existing Oxides Layer and Interface Condition with Carbonated Concrete on Active Reinforcing Steel Corrosion: Influence of Pre-Existing Oxides Layer and Interface Condition.” *Materials and Corrosion* 66 (3): 206–14. <https://doi.org/10.1002/maco.201307195>.



- Chalhoub, Chantal. 2020. “Study of the Initiation and Propagation Phases of Chloride Induced Corrosion in Reinforced Concrete Structures.” Thesis, Toulouse: Université Toulouse 3 Paul Sabatier.
- Chalhoub, Chantal, Raoul François, and Myriam Carcasses. 2019. “Determination of Chloride Threshold Initiating Corrosion: A New Set-up Taking the Localized Aspect of Corrosion into Account.” *Cement and Concrete Research* 124 (October): 105825. <https://doi.org/10.1016/j.cemconres.2019.105825>.
- Cheng, Luge, Ippei Maruyama, and Yuqi Ren. 2021. “Novel Accelerated Test Method for RH Dependency of Steel Corrosion in Carbonated Mortar.” *Journal of Advanced Concrete Technology* 19 (3): 207–15. <https://doi.org/10.3151/jact.19.207>.
- Criado, Mundra, Bernal, and Provis. 2018. “Influence of Sulfide on the Onset of Chloride-Induced Corrosion of Steel Reinforcement in Alkali-Activated Slags.” *Basheer, PAM, (Ed.) Durability of Concrete Structures - Sixth International Conference on the Durability of Concrete Structures, Leeds, UK*, 149–53.
- Dhir, R. K., M. R. Jones, and M. J. McCarthy. 1992. “Pulverized-Fuel Ash Concrete: Carbonation-Induced Reinforcement Corrosion Rates.” *Proceedings of the ICE: Structures and Buildings* 94 (3): 335–42. <https://doi.org/10.1680/istbu.1992.20293>.
- Divet, Loïc, and Robert Le Roy. 2013. “Étude de La Durabilité Vis-à-Vis de La Corrosion Des Armatures Des Bétons Formulés Avec Des Ciments à Forte Teneur En Laitier de Haut Fourneau.” *BLPC*, no. 280–281 (November).
- Elgalhud, Abdurrahman A., Ravindra K. Dhir, and Gurmel S. Ghataora. 2017. “Carbonation Resistance of Concrete: Limestone Addition Effect.” *Magazine of Concrete Research* 69 (2): 84–106. <https://doi.org/10.1680/jmacr.16.00371>.
- Glass, G. K., C. L. Page, and N. R. Short. 1991. “Factors Affecting the Corrosion Rate of Steel in Carbonated Mortars.” *Corrosion Science* 32 (12): 1283–94. [https://doi.org/10.1016/0010-938X\(91\)90048-T](https://doi.org/10.1016/0010-938X(91)90048-T).
- Gonzalez, J. A., J. S. Algaba, and C. Andrade. 1980. “Corrosion of Reinforcing Bars in Carbonated Concrete.” *British Corrosion Journal* 15 (3): 135–39. <https://doi.org/10.1179/bcj.1980.15.3.135>.
- Greve-Dierfeld, Stefanie von, Barbara Lothenbach, Anya Vollpracht, Bei Wu, Bruno Huet, Carmen Andrade, César Medina, et al. 2020. “Understanding the Carbonation of Concrete with Supplementary Cementitious Materials: A Critical Review by RILEM TC 281-CCC.” *Materials and Structures* 53 (6): 136. <https://doi.org/10.1617/s11527-020-01558-w>.
- Hornbostel, Karla, Claus K. Larsen, and Mette R. Geiker. 2013. “Relationship between Concrete Resistivity and Corrosion Rate – A Literature Review.” *Cement and Concrete Composites* 39 (May): 60–72. <https://doi.org/10.1016/j.cemconcomp.2013.03.019>.
- Hunkeler, Fritz, and Stefanie von Greve-Dierfeld. 2019. “Karbonatisierung von Beton Und Korrosionsgeschwindigkeit Der Bewehrung Im Karbonatisierten Beton.” ASTRA/VSS Report no. 696. Berne, Switzerland: Bundesamt für Strassen.
- Huy Vu, Quoc, Gabriel Pham, Alain Chonier, Eric Brouard, Sundar Rathnarajan, Radhakrishna Pillai, Ravindra Gettu, et al. 2019. “Impact of Different Climates on the Resistance of Concrete to Natural Carbonation.” *Construction and Building Materials* 216 (August): 450–67. <https://doi.org/10.1016/j.conbuildmat.2019.04.263>.
- Ioannou, Socrates. 2012. “An Assessment of the Performance of Calcium Sulfoaluminate and Supersulfated Cements for Use in Concrete.” PhD, UK: University of Bath.
- Köliö, Arto, Toni A. Pakkala, Harri Hohti, Anssi Laukkarinen, Jukka Lahdensivu, Jussi Mattila, and Matti Pentti. 2017. “The Corrosion Rate in Reinforced Concrete Facades Exposed to Outdoor Environment.” *Materials and Structures* 50 (23). <https://doi.org/10.1617/s11527-016-0920-7>.
- Laurens, S., P. Hénocq, N. Rouleau, F. Deby, E. Samson, J. Marchand, and B. Bissonnette. 2016. “Steady-State Polarization Response of Chloride-Induced Macrocell Corrosion Systems in Steel Reinforced Concrete — Numerical and Experimental Investigations.” *Cement and Concrete Research* 79 (January): 272–90. <https://doi.org/10.1016/j.cemconres.2015.09.021>.
- Lliso-Ferrando, J.R., I. Gasch, A. Martínez-Ibernón, and M. Valcuende. 2022. “Effect of Macrocell Currents on Rebar Corrosion in Reinforced Concrete Structures Exposed to a Marine

- Environment.” *Ocean Engineering* 257 (August): 111680. <https://doi.org/10.1016/j.oceaneng.2022.111680>.
- Menzel, Klaus. 1988. “Karbonatisierungszellen – Ein Beitrag zur Korrosion von Stahl in karbonatisiertem Beton.” *Materials and Corrosion* 39 (3): 123–29. <https://doi.org/10.1002/maco.19880390303>.
- Moreno, Eric, Pedro Castro-Borges, and Enrique Cob-Sarabia. 2004. “Corrosion Rates from Carbonated Concrete Specimens,” January.
- Mundra, Shishir, Susan A. Bernal, Maria Criado, Petr Hlaváček, Gino Ebell, Steffi Reinemann, Gregor J.G. Gluth, and John L. Provis. 2017. “Steel Corrosion in Reinforced Alkali-Activated Materials.” *RILEM Technical Letters* 2 (December): 33–39. <https://doi.org/10.21809/rilemtechlett.2017.39>.
- Mundra, Shishir, and John L. Provis. 2021. “Mechanisms of Passivation and Chloride-Induced Corrosion of Mild Steel in Sulfide-Containing Alkaline Solutions.” *Journal of Materials Science* 56 (26): 14783–802. <https://doi.org/10.1007/s10853-021-06237-x>.
- Mundra, Shishir, Gabriel Samson, Giulia Masi, Rebecca Achenbach, David M. Bastidas, Susan A. Bernal, Maria C. Bignozzi, et al. 2023. “Application of Electrochemical Methods for Studying Steel Corrosion in Alkali-activated Materials.” *Materials and Corrosion*, February, maco.202313743. <https://doi.org/10.1002/maco.202313743>.
- Nasser, A., A. Clément, S. Laurens, and A. Castel. 2010. “Influence of Steel–Concrete Interface Condition on Galvanic Corrosion Currents in Carbonated Concrete.” *Corrosion Science* 52 (9): 2878–90. <https://doi.org/10.1016/j.corsci.2010.04.037>.
- Nasser, Abdelkader, and Arnaud Castel. 2014. “Microcell versus Galvanic Corrosion Currents in Carbonated Concrete.” *Magazine of Concrete Research* 66 (July): 697–707. <https://doi.org/10.1680/mac.13.00214>.
- Nguyen, Thi-Thu, Raoul Francois, Tru Vu, and Myriam Carcasses. 2022. “A Comparison between Uniform and Galvanic Corrosion Rate in Carbonation Induced Corrosion of Reinforced Concrete.” *MATEC Web of Conferences* 364 (September). <https://doi.org/10.1051/mateconf/202236402025>.
- Pimienta, Pierre, Blandine Albert, Bruno Huet, Michael Dierkens, Philippe Fransisco, and Patrick Rougeau. 2016. “Durability Performance Assessment of Non-Standard Cementitious Materials for Buildings: A General Method Applied to the French Context.” *RILEM Technical Letters* 1 (December): 102. <https://doi.org/10.21809/rilemtechlett.2016.17>.
- Revert, Andres Belda, Karla Hornbostel, Klaartje De Weerd, and Mette Rica Geiker. 2019. “Macrocell Corrosion in Carbonated Portland and Portland-Fly Ash Concrete - Contribution and Mechanism.” *Cement and Concrete Research* 116 (February): 273–83. <https://doi.org/10.1016/j.cemconres.2018.12.005>.
- Runci, Antonino, John L. Provis, and Marijana Serdar. 2023. “Revealing Corrosion Parameters of Steel in Alkali-Activated Materials.” *Corrosion Science* 210 (January): 110849. <https://doi.org/10.1016/j.corsci.2022.110849>.
- Schwartzentruber, A, and C Catherine. 2000. “Method of the Concrete Equivalent Mortar (CEM) - A New Tool to Design Concrete Containing Admixture.” *Materials and Structures*, October 2000, Vol. 33 edition.
- Sohail, M. G., S. Laurens, F. Deby, and J. P. Balayssac. 2015. “Significance of Macrocell Corrosion of Reinforcing Steel in Partially Carbonated Concrete: Numerical and Experimental Investigation.” *Materials and Structures* 48 (1–2): 217–33. <https://doi.org/10.1617/s11527-013-0178-2>.
- Stefanoni, Angst, and Elsener. 2018. “Corrosion Rate of Carbon Steel in Carbonated Concrete – A Critical Review.” *Cement and Concrete Research* 103 (January): 35–48. <https://doi.org/10.1016/j.cemconres.2017.10.007>.
- Stefanoni, Angst, and Elsener. 2020. “The Mechanism Controlling Corrosion of Steel in Carbonated Cementitious Materials in Wetting and Drying Exposure.” *Cement and Concrete Composites* 113 (October): 103717. <https://doi.org/10.1016/j.cemconcomp.2020.103717>.
- Vennesland, Ø., M. Raupach, and C. Andrade. 2007. “Recommendation of Rilem TC 154-EMC: ‘Electrochemical Techniques for Measuring Corrosion in Concrete’—Measurements with

- Embedded Probes.” *Materials and Structures* 40 (8): 745–58. <https://doi.org/10.1617/s11527-006-9219-4>.
- Wang, Wei-Chien, Wei-Hsing Huang, Ming-Yu Lee, Hoang Trung Hieu Duong, and Ya-Hui Chang. 2021. “Standardized Procedure of Measuring the PH Value of Cement Matrix Material by Ex-Situ Leaching Method (ESL).” *Crystals* 11 (4): 436. <https://doi.org/10.3390/cryst11040436>.
- Zhang, Feng, Xun Xi, and Shangtong Yang. 2021. “Research Progress in Corrosion Mechanism of Reinforced Alkali-Activated Concrete Structures.” *Corrosion and Materials Degradation* 2 (4): 641–56. <https://doi.org/10.3390/cmd2040034>.
- Zhao, Kai, Yongning Liang, Tao Ji, Yue Lu, and Xujian Lin. 2020. “Effect of Activator Types and Concentration of CO<sub>2</sub> on the Steel Corrosion in the Carbonated Alkali-Activated Slag Concrete.” *Construction and Building Materials* 262 (November): 120044. <https://doi.org/10.1016/j.conbuildmat.2020.120044>.





Chapter 7

# Synthesis Chapter

## Table of contents

<b>1</b>	<b>Corrosion initiation: comparison of chloride diffusion rates and carbonation rates .....</b>	<b>263</b>
1.1	General comments .....	263
1.2	Resistance to chloride penetration.....	264
1.3	Resistance to carbonation .....	265
<b>2</b>	<b>Corrosion propagation: comparison of corrosion rates obtained for chloride and carbonation exposure .....</b>	<b>265</b>
2.1	Comparison between low-carbon concretes .....	266
2.2	Comparison with conventional concretes.....	268
<b>3</b>	<b>Behaviour of low-carbon concretes compared to conventional concretes, and classifications</b>	<b>269</b>
<b>4</b>	<b>Conclusions and recommendations for the use of each low-carbon concrete .....</b>	<b>270</b>
4.1	Low clinker content (LCK) .....	270
4.2	Alkali-activated slag (AAS) .....	271
4.3	Supersulfated cement (SSC).....	272
<b>5</b>	<b>References.....</b>	<b>273</b>



## SYNTHESIS CHAPTER: Durability of reinforcement in the three low-carbon concretes exposed to chlorides or carbonation

The objective of this chapter is to compare and discuss in a synthetic way the results obtained in the 4 articles, and finally conclude on the durability of reinforcement in each low-carbon concrete.

First (section 1), the transport properties of chlorides ([Article A](#)) and CO<sub>2</sub> ([Article B](#)), both conditioning the corrosion initiation, are compared for the three low-carbon concretes. Similarly, in section 2, the corrosion rates measured in the case of contamination by chlorides ([Article C](#)) or after carbonation ([Article D](#)) are compared. Then, in section 3, a brief discussion about the behaviour of the low-carbon concretes compared to the conventional concretes is proposed. Finally, in section 4, the initiation and propagation phase for each exposure condition are considered together ([Articles A](#) and [C](#) for chlorides, [Articles B](#) and [D](#) for carbonation), to conclude for the use of each binder.

### 1 Corrosion initiation: comparison of chloride diffusion rates and carbonation rates

#### 1.1 General comments

Figure 88 summarizes the previous results of natural chloride diffusion coefficient ( $D_{\text{nss}}$ ) and natural carbonation rates ( $k_{\text{nat}}$ ), obtained in the [Articles A](#) and [B](#) respectively. For the natural carbonation outside sheltered, 1 day, 3 days and 14 days of curing are considered. A comparison with the corresponding values measured on CEM III/A (Huy Vu et al. 2019) or CEM I (IREX 2022) concretes is also proposed. The CEM III/A, of slightly higher strength class C35/45 instead of C25/30, was chosen as reference because it is also a low-carbon concrete, with a carbon footprint similar to that of the LCK. The values obtained on CEM I-concretes C20/25, C25/30 or C30/37 are from the database of the national project PERFDUB (IREX 2022).

The objective of this section is to evaluate and compare the transport of chlorides and CO<sub>2</sub>, conditioning the corrosion initiation for the three low-carbon concretes of same strength class C25/30. The transport of chlorides is characterized by the natural diffusion coefficient ( $D_{\text{nss}}$ ), while the transport of CO<sub>2</sub> is characterized by the natural carbonation rates ( $k_{\text{nat}}$ ).

Figure 88 illustrates different behaviours and performances according to the type of binder, for the two exposure conditions. For the chloride diffusion, slag-based binders are much more efficient to limit the transport of chloride ions compared to the LCK or to the reference CEM III/A. The LCK concrete is very permeable to chlorides, because it has an apparent chloride diffusion coefficient 2 times higher than the reference CEM I ( $23.35 \times 10^{-12} \text{ m}^2/\text{s}$ ) and 20 times higher than the reference CEM III/A ( $2.4 \times 10^{-12} \text{ m}^2/\text{s}$ ). On the contrary, for the carbonation exposure after 1 or 3 days of curing, the LCK and AAS have similar carbonation rates than the reference CEM III/A ( $9 \text{ mm}/\text{years}^{0.5}$ ), and are more resistant to carbonation exposure than the SSC. After 14 days of curing, the carbonation rates measured are much lower than for short



curing times and become similar or lower than the reference CEM III/A. It shows the influence of the curing period on the initiation phase for low-carbon binders.

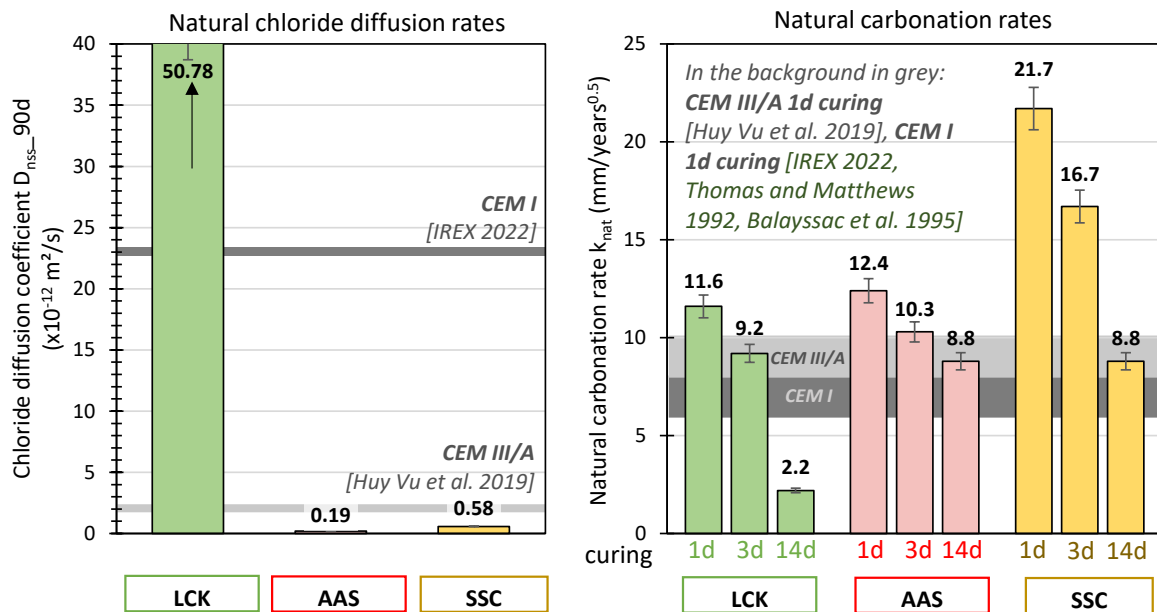


Figure 88: Natural chloride diffusion rates (left hand side) and natural carbonation rates (right hand side) measured on LCK, AAS and SSC concretes, of same strength class C25/30. The corresponding parameters measured on a CEM III/A (C35/45) are from (Huy Vu et al. 2019), and those measured on CEM I (C20/25 to C30/37) are from the national project PERFDUB (IREX 2022) and from (Thomas and Matthews 1992; Balayssac et al. 1995).

## 1.2 Resistance to chloride penetration

The **LCK** concrete is characterized by a high chloride permeability, despite having “excellent” transfer properties (low water porosity, gas permeability, water permeability and capillary absorption) due to a low w/b ratio. This was partly explained by its low clinker content ( $137 \text{ kg}/\text{m}^3$  or 27% of the binder), which is responsible on the one hand for a lower chloride-binding capacity, and on the other hand for a high conductivity (thus a low resistivity) because there are less hydrates to trap chloride ions. Its majority of capillary pores ( $>10 \text{ nm}$ ) also promotes the mobility of chloride ions. With a chloride diffusion coefficient twice higher than a CEM I and 20 times higher than the reference CEM III/A, the corrosion initiation is likely to occur after a short time. Therefore, the possibility of using this binder in a chloride-rich environment should be limited, or the formula should be adapted to minimize capillary pores, increase its resistivity or its chloride binding capacity, to achieve the same performance.

On the contrary, the **AAS** and **SSC** concretes are both extremely resistant to chloride penetration. For AAS, the more important diffusion mechanisms and its low resistivity, seem to be balanced by a stronger chloride binding capacity. For SSC, the lower diffusive transport and the very low amount of ions in its pore solution leads to a high resistivity, in favour of a reduced chloride mobility. Both concretes enable to strongly delay the arrival of chlorides at the rebar and therefore the corrosion initiation, compared to the reference CEM III/A.

### 1.3 Resistance to carbonation

The **LCK** has a carbonation resistance comparable to that of the CEM III/A reference (slightly higher but same order of magnitude) for short curing times. It has a low w/b ratio, resulting in a low porosity, which acts as an efficient physical barrier to slow down the CO<sub>2</sub> diffusion. However, its low clinker content is responsible for a limited amount of calcium bearing hydrates, such as portlandite, to act as a pH buffer. It is possible to strongly reduce the carbonation rates of the LCK concrete, and therefore to delay the corrosion initiation, by increasing the curing time.

The **AAS** also has a carbonation resistance comparable to that of the CEM III/A reference. It carbonates quickly, but has a strong ability to maintain a high pH (pH > 9 after 11 months at 1% CO<sub>2</sub> or 18 months in natural carbonation), governed by the amount of alkali ions in its pore solution.

The **SSC** has a low carbonation resistance, with twice the carbonation rate as the CEM III/A concrete for short curing times (e.g. 1 day). It is characterized by a rapid carbonation, resulting in an increase in porosity, combined with a low ability to maintain a high pH. By increasing the curing time of the SSC from 1 to 14 days, it is possible to divide by two the obtained carbonation rates.

Finally, Figure 88 clearly highlights the importance of respecting the curing times for low-carbon concretes for which construction practices (demoulding at 16 or 24 hours) do not ensure sufficient curing. It shows the emergency to change the practices and habits on site to develop their use while maintaining an acceptable durability. Moreover, the performances of AAS and SSC can also be improved, to delay the corrosion initiation, by reducing their w/b ratio to improve their physical barrier against CO<sub>2</sub> diffusion.

## 2 Corrosion propagation: comparison of corrosion rates obtained for chloride and carbonation exposure

Figure 89 summarizes the previous results of total apparent current density ( $i_{\text{tot}}$ ), developed during 90 days of anode-cathode coupling, either for chloride-induced corrosion (left) or carbonation-induced corrosion (right). For each condition, the proportion of galvanic current density ( $i_g$ ) and local current density at the anode ( $i_{\text{mi-anode}}$ ) is specified. For chloride contamination, two concentrations representative of sea water ([NaCl] = 30 g/L) or de-icing salts ([NaCl] = 300 g/L) were tested. For carbonation-induced corrosion, three different saturation conditions were investigated ( $C_w\text{-}A_w$ ,  $C_d\text{-}A_d$ ,  $C_d\text{-}A_w$ ).

A comparison with ranges of  $i_g$  and  $i_{\text{mi-anode}}$  generally measured on CEM I-concretes in the literature, is also proposed and discussed in the next section 2.2.

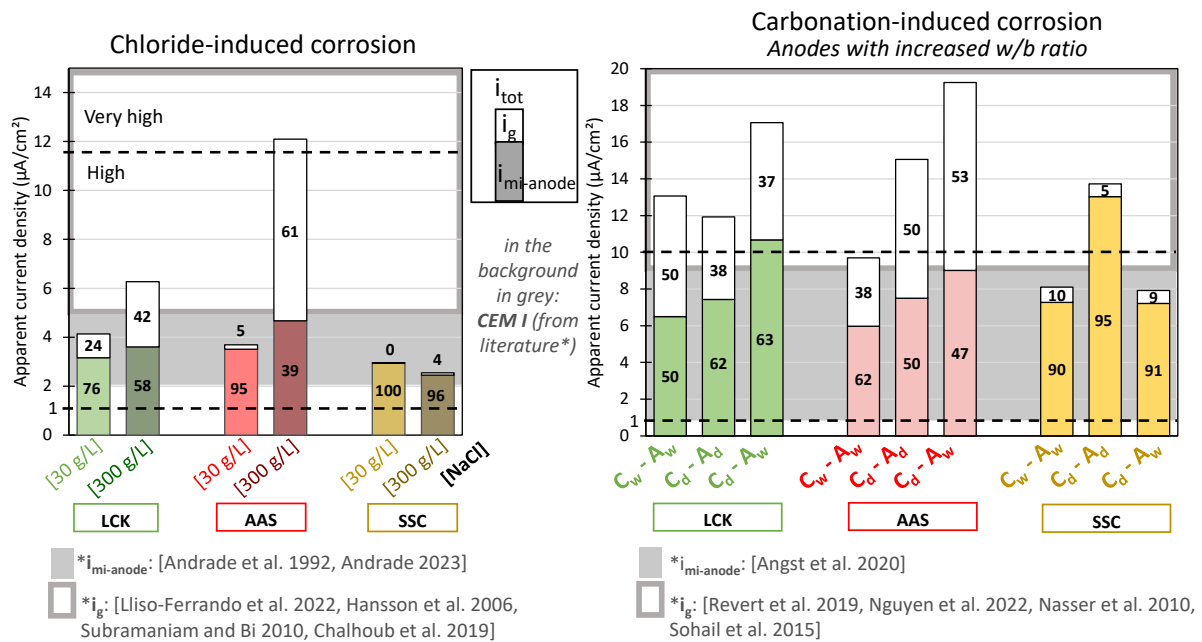


Figure 89: Total apparent current density  $i_{tot}$  developed during 90 days of anode-cathode coupling, either for chloride-induced corrosion (left hand side) or carbonation-induced corrosion (right hand side). The proportion (in %) between the galvanic ( $i_g$ ) and local at the anode ( $i_{mi-anode}$ ) apparent current densities, forming part of  $i_{tot}$ , is specified. The dotted black line indicates the threshold associated with high ( $>1 \mu\text{A}/\text{cm}^2$ ) and very high ( $>10 \mu\text{A}/\text{cm}^2$ ) levels of corrosion. The ranges of  $i_{mi-anode}$  generally measured on CEM I-concretes are from (C. Andrade et al. 1992; Carmen Andrade 2023; Angst et al. 2020). The ranges of  $i_g$  are from (Lliso-Ferrando et al. 2022; Hansson, Poursaee, and Laurent 2006; Subramaniam and Bi 2010; Chalhoub, François, and Carcasses 2019; Revert et al. 2019; T.-T. Nguyen et al. 2022; A. Nasser et al. 2010; Sohail et al. 2015).

## 2.1 Comparison between low-carbon concretes

The objective of this section is to evaluate and compare the corrosion rates measured by the galvanic current protocol in the case of contamination by chlorides or after carbonation of the samples, for each binder.

First of all, Figure 89 illustrates that the ranges of  $i_{mi-anode}$  obtained are similar for all types of binders for a same condition. On the contrary,  $i_g$  seems to be dependant of the type of binder:

- For **LCK** in all tested conditions, the galvanic current represents 25 to 50% of additional current density. It is driven by the potential difference between anode and cathode and the total resistance between both samples.

For AAS and SSC, the relation between  $i_g$  and these two parameters (potential difference and total resistance between anode) is less obvious to identify. Additional influencing parameters

seem to be involved. Complementary studies are necessary to understand the mechanisms driving  $i_g$  in these binders.

- For **AAS**, the same trend as for LCK is observed in carbonation, because the oxidation of sulfides during the carbonation process leads to electrochemical parameters close to those of the LCK. In the presence of chlorides, the tests were performed under saturated conditions. Therefore, the majority of sulfides in the AAS were not oxidized, resulting in very different electrochemical parameters and behaviour than the LCK. At 30 g/L, the small potential difference generated limits the galvanic current exchanged. At 300 g/L on the other hand, the corrosion rates increase strongly. Further research is needed to explain this behaviour and to determine if it is related to the chloride threshold necessary to initiate corrosion.
- Finally, for **SSC**, low galvanic currents are measured regardless of the exposure conditions tested. The high resistivity of this binder contributes to limit the galvanic current exchanged. In the presence of chlorides (in saturated conditions) this is also explained by the absence of potential difference between anode and cathode (as for AAS at 30 g/L). Further studies are necessary to better understand the mechanisms involved.

Figure 89 also illustrates that, either for chloride contamination or for carbonation, the contribution of galvanic current ( $i_g$ ) is non-negligible in the total current ( $i_{tot}$ ), for LCK and AAS binders (except for AAS contaminated with  $[NaCl] = 30$  g/L). It should therefore be considered, when predicting the lifetime of the structures. For chloride-induced corrosion, the autopsies of the anodes in Article C, revealed little corroded surfaces at the end of the 90 days experimental campaign. The galvanic current density  $i_g$  could have been more important, if a longer time had been waited for the anode to be in a more stable corrosion state before being coupled (as observed in other studies (Lliso-Ferrando et al. 2022)). The consideration of  $i_g$  is important because it allows distinguishing differences between the formulas, not visible by considering only  $i_{mi-anode}$ .

Therefore, considering  $i_{tot}$  (the sum of  $i_g$  and  $i_{mi-anode}$ ) it can be concluded that:

- In chloride-rich environments, LCK has a higher  $i_{tot}$  (due to a non-negligible  $i_g$ ) compared to AAS and SSC (negligible  $i_g$ ). AAS at 300 g/L is a special case, for which very high current levels were measured.
- For carbonation exposure, the  $i_{tot}$  developed for LCK and AAS are similar. For the SSC, on the contrary, the  $i_{tot}$  developed are relatively lower, due a negligible galvanic current in the different expositions tested (the high  $i_{tot}$  obtained for the  $C_d-A_d$  condition would require verification).

Then, it seems that the total apparent current densities  $i_{tot}$  are higher for carbonation-induced corrosion than those for chloride-induced corrosion. Moreover, the autopsies and the mass loss revealed a less developed corrosion in the case of contamination by chlorides. In the case of carbonation, the values of  $i_{tot}$  are also overestimated, because the anodes were formulated with an increased w/b ratio of 20% for AAS and SSC and 40% for LCK (to reduce the corrosion

initiation times). As a consequence, samples with a lower resistivity and less resistant to corrosion are obtained, making the comparison more difficult. Even if the comparison between both conditions is not recommended to avoid misinterpretations, these experimental campaigns provide information on the order of magnitude of the corrosion kinetics likely to develop in these binders (either exposed to chlorides or carbonation).

Finally, the different saturation conditions, tested for the case of carbonation, highlight the influence of this parameter (variable over time on site depending on the weather) on the measured total apparent current density  $i_{tot}$ . For LCK and AAS, the  $C_d-A_w$  condition is the most unfavorable (associated to the highest  $i_{tot}$ ), as the anode and cathode have at the same time a different state (active/passive) and different saturation conditions (in water/dry), leading to very different electrochemical parameters. This suggests that the same conclusions could be expected for chlorides, where only one saturation condition was tested (equivalent of  $C_w-A_w$ ). In the unfavourable  $C_d-A_w$  condition (corresponding for example in the reality, to a partially immersed structure), larger  $i_{tot}$  currents would probably be expected, due to a higher potential difference between anode and cathode.

The corrosion rate of  $1 \mu A/cm^2$  is about  $10 \mu m/year$  of steel section loss and 3 to 4 times more iron oxides. Fib considers that 50 to  $100 \mu m$  of steel loss can lead to cracking (Torres-Acosta and Sagues 2004). **In the end, despite some differences, the measured corrosion rates remain high for all binders and all conditions tested and could generate cracking. Thus, it seems that it is the initiation phase more than the propagation phase, which conditions the durability of the rebars in these low-carbon concretes of strength class C25/30.**

## 2.2 Comparison with conventional concretes

Figure 89 also proposes a comparison with ranges of apparent current densities generally measured on CEM I-concretes in the literature, in absence of galvanic coupling ( $i_{mi-anode}$ ). These values give an order of magnitude of the corrosion currents generally measured on CEM I. They are used to situate the values measured on the low-carbon concretes, and not in an absolute sense, assuming certain variations with the results of this study (concrete samples, classical measurements).

### $i_{mi-anode}$

For chloride-induced corrosion ( $[NaCl] = 30 \text{ g/L}$ ), (C. Andrade et al. 1992; Carmen Andrade 2023) report and review ranges of apparent current densities from the literature generally between  $2$  to  $5 \mu A/cm^2$  on concrete CEM I. Figure 89 shows that similar order of magnitude were found for the low-carbon concretes. Some authors have measured higher corrosion rates, up to  $25 \mu A/cm^2$ , in exposed areas known to be more aggressive (splash zone) (Valipour, Shekarchi, and Ghods 2014).

For carbonation-induced corrosion, the review of (Angst et al. 2020) reports ranges of corrosion currents on CEM I-concrete, around  $1 \mu A/cm^2$  in wet conditions (80-100% RH), and up to  $9 \mu A/cm^2$  for very unfavourable conditions. Very unfavourable conditions refer to a rebar in

contact with liquid water, low cover depth and poor quality concrete (coarse pore structure after carbonation). These conditions are similar to those of this study, where anodes are mortar samples with a low cover depth and an increased w/b ratio. As for chlorides, similar apparent current densities ( $i_{mi-anode}$ ) were measured for the low-carbon binders as for CEM I.

$i_g$

It is more complicated to compare the galvanic current values obtained in the literature on CEM I, with those obtained on the low-carbon concretes of the study. The differences between the experimental protocols used (C/A ratio, exposure conditions, duration of the coupling, geometry of the samples or experimental set up to perform the measurements) can strongly influence the galvanic current measured and make the comparison complicated. Therefore, a large interval of  $i_g$  was found, depending on the condition used. However, the authors report non-negligible galvanic currents in CEM I-based concretes for high C/A ratios and severe exposure conditions (Lliso-Ferrando et al. 2022; Revert et al. 2019; Sohail et al. 2015; Abdelkader Nasser and Castel 2014).

For chloride-induced corrosion ( $[NaCl] = 30$  g/L), (Lliso-Ferrando et al. 2022; Hansson, Poursaee, and Laurent 2006; Subramaniam and Bi 2010; Chalhoub, François, and Carcasses 2019) report ranges of  $i_g$  between 2 to 10  $\mu A/cm^2$ , for C/A ratios between 2 and 19. Figure 89 shows that similar order of magnitude was found for the low-carbon concretes. For very severe conditions, (Lliso-Ferrando et al. 2022) even measured values around 50  $\mu A/cm^2$  (not considered on Figure 89).

For carbonation-induced corrosion, (Revert et al. 2019; T.-T. Nguyen et al. 2022; A. Nasser et al. 2010; Sohail et al. 2015) report ranges of  $i_g$  on CEM I between 1 to 12  $\mu A/cm^2$  (for C/A ratios varying between 1 and 16), comparable to those obtained on low-carbon concrete. For carbonation-induced corrosion, for a given C/A ratio of 16, (T.-T. Nguyen et al. 2022) reports significant lower galvanic current densities on CEM III cement (around 0.5  $\mu A/cm^2$ ), compared to CEM I (around 15.5  $\mu A/cm^2$ ), confirming an influence of the binder (high resistivity of CEM III in this case) on the galvanic current, as observed in this study for the SSC.

**Finally, similar corrosion rates were measured on low-carbon concretes compared to CEM I. Therefore, in addition to their reduced carbon footprint, it makes LCK, AAS and SSC concretes competitive and attractive, from the view point of corrosion rates.**

### **3 Behaviour of low-carbon concretes compared to conventional concretes, and classifications**

The exposure classes, defined by the EN 206 standard (AFNOR 2022b), allow to take into account the durability of concrete. For the classes of interest in this study, XD (risk of corrosion induced by chlorides having a non-marine origin, de-icing salts for example) and XS (risk of corrosion induced by the chlorides present in the sea water) for chlorides and XC (corrosion induced by carbonation) for carbonation, different levels of severity are defined according to the degree of saturation.

Then, in practice, if a concrete is exposed to both carbonation and chlorides, it is the chloride exposure that is considered the most unfavourable for conventional binders, according to the design of structures by Eurocode 2 (AFNOR 2005). However, it has been shown through this study that it is not necessarily the case for the three low-carbon binders considered. Particularly for slag-based binders exposed to sea water ( $[\text{NaCl}] = 30 \text{ g/L}$ ), which have a high resistance to chloride penetration (Article A) and lower  $i_{\text{tot}}$  compared to carbonation exposure (considering an increased w/b ratio for carbonation). Further research would be required to validate this assumption. Thus, the determination of the rebar cover according to the procedures used for conventional binders, will not necessarily be optimized for these slag-based binders and might be based on carbonation phase during the initiation.

#### 4 Conclusions and recommendations for the use of each low-carbon concrete

Finally, the initiation (section 1) and propagation (section 2) phases for each exposure condition (chlorides, carbonation) are considered together, to conclude for the use of each binder. For this purpose, Table 42 summarizes the performance of each binder, for corrosion initiation and propagation, for the two exposure conditions considered.

*Table 42: Summary of the performances of each binder, considering corrosion initiation and propagation, in the case of chlorides or carbonation exposure. A green colour corresponds to a better performance than the reference, a yellow colour to an equivalent performance and a red colour to a worse performance (from comparisons made in sections 1 and 2).*

	CORROSION INITIATION		CORROSION PROPAGATION	
	Chlorides (Article A)	Carbonation (Article B)	Chlorides (Article C)	Carbonation (Article D)
<b>LCK</b>				
<b>AAS</b>			30 g/L	300 g/L
<b>SSC</b>				

##### 4.1 Low clinker content (LCK)

The LCK concrete has better transfer properties (lower water porosity, capillary absorption and gas permeability and higher resistivity) than reference concretes of similar strength (CEM I, CEM II/A, CEM III/A) due to its very low w/b ratio. This is positive for its durability, but it also results in a higher viscosity at fresh state.

##### Chlorides

The LCK concrete is very permeable to chlorides during the initiation phase, even compared to traditional concretes ( $D_{\text{nss}}$  twice higher than CEM I reference), mainly due to its reduced clinker content.

After 90 days of galvanic coupling, the propagation phase is characterized by high corrosion rates, comparable to those found on a CEM I-concrete. It is mainly explained by a galvanic current not negligible in this binder (24 to 42% of  $i_{\text{tot}}$ ), which is driven by the potential difference and the total resistance of the materials between the anode and the cathode.

- ⇒ Combined with its low resistance to chloride penetration, it makes it poorly resistant to corrosion initiation (rapid arrival of chlorides to the rebar) and to corrosion propagation (high corrosion rates), that is why its use in a chloride-rich environment is not recommended.

### Carbonation

The LCK concrete has an acceptable carbonation resistance during the initiation phase, comparable to that of a CEM III/A. Its low porosity acts as an efficient physical barrier to slow down the CO<sub>2</sub> diffusion, but its low clinker content is associated to a limited amount of portlandite to buffer the pH.

The propagation phase is characterized by very high corrosion rates ( $i_{\text{tot}} > 10 \mu\text{A}/\text{cm}^2$ ), but it should be reminded that they were associated to severe conditions in this study compared to real conditions. It also corresponds to ranges of currents found for CEM I binders in severe conditions. The galvanic current was not negligible (37 to 50% of  $i_{\text{tot}}$ ).

- ⇒ Its use for environments exposed to carbonation is therefore possible, rather for permanently dry (XC1) or wet conditions (XC2) (higher  $i_{\text{tot}}$  measured for C<sub>d</sub>-A<sub>w</sub> condition). Its resistance to corrosion initiation could even be improved by favouring longer curing times, to delay the corrosion activation and the associated high currents.

## **4.2 Alkali-activated slag (AAS)**

### Chlorides

The AAS concrete is extremely resistant to chloride penetration during the initiation phase, due to a strong chloride binding capacity.

In the propagation phase after 90 days of galvanic coupling, high corrosion rates  $i_{\text{tot}}$  are measured at 30 g/L (nearly 4  $\mu\text{A}/\text{cm}^2$ ), in the lower part of the values measured on CEM I. These relatively low values are explained by a negligible galvanic current (5% of  $i_{\text{tot}}$ ). Very high corrosion rates  $i_{\text{tot}}$  are measured at 300 g/L (above 10  $\mu\text{A}/\text{cm}^2$ ), in the upper part of the values measured on CEM I. These relatively high values are explained by a non-negligible galvanic current (61% of  $i_{\text{tot}}$ ).

- ⇒ Considering that this binder is extremely resistant to chloride penetration, the corrosion initiation will occur after a very long time, therefore its use in a marine environment ([NaCl] = 30 g/L) is possible, even if it generates high currents. Nevertheless, its use for higher chloride concentrations, such as 300 g/L for de-icing salts, is possible only if the initiation phase can be controlled and sufficiently delayed.

### Carbonation

The AAS concrete has a medium carbonation resistance during the initiation phase, comparable to that of a CEM III/A. It also has a strong ability to maintain a high pH (pH > 9 after 11 months at 1% CO<sub>2</sub> or 18 months in natural carbonation) governed by the amount of alkali ions in its



pore solution. However it is not sufficient to prevent corrosion to initiate, as active corrosion was obtained on anodes exposed to natural carbonation, during the galvanic current protocol.

The propagation phase is characterized by very high corrosion rates ( $i_{\text{tot}} > 10 \mu\text{A}/\text{cm}^2$ ), but it should be reminded that they were associated to severe conditions in this study compared to real conditions. It also corresponds to ranges of currents found for CEM I binders in severe conditions. The galvanic current was not negligible (38 to 53% of  $i_{\text{tot}}$ ).

- ⇒ Similarly to the LCK, its use for exposition to carbonation is however possible, preferentially for longer curing times or a reduced w/b ratio to slow down the corrosion initiation, which will be combined with its ability to maintain a high pH. Permanently wet expositions should be favoured (lower  $i_{\text{tot}}$  measured for  $C_w\text{-}A_w$  condition).

### 4.3 *Supersulfated cement (SSC)*

#### Chlorides

The SSC concrete is extremely resistant to chloride penetration during the initiation phase, mainly due to a high resistivity.

In the propagation phase after 90 days of galvanic coupling, high corrosion rates are measured,  $i_{\text{tot}}$  being just above the threshold of  $1 \mu\text{A}/\text{cm}^2$ , both at 30 and 300 g/L (under  $3 \mu\text{A}/\text{cm}^2$ ). However, it corresponds to the lower part of the values measured on CEM I, because almost no galvanic current ( $i_g$  remains negligible for both chloride concentrations) is added to the local current at the anode scale. This absence of galvanic current, not reported for CEM I, is interesting for a real structure, as it limits the total current.

- ⇒ Therefore a use in a chloride-rich environment is recommended, as the SSC is very resistant to both corrosion initiation and to corrosion propagation, either at 30 g/L or 300 g/L.

#### Carbonation

The SSC concrete has a low carbonation resistance. It is characterized by a rapid carbonation during the initiation phase, resulting in an increase in porosity, combined with a low ability to maintain a high pH.


This low resistance to corrosion initiation is combined with high corrosion rates in the propagation phase, but corresponding to the lower part of the values measured on CEM I. It is explained by the negligible galvanic current measured for this binder (5 to 10% of  $i_{\text{tot}}$ ).

- ⇒ Therefore, its use for carbonation exposition is not recommended for high w/b ratios, but could be possible for long curing times and a reduced water contents, in order to slow down the corrosion initiation. If the carbonation front reaches the rebar, the benefit of this binder is the limited contribution of the galvanic current to the total current.

## 5 References

- AFNOR. 2005. ‘NF EN 1992 : Eurocode 2 - Calcul Des Structures En Béton - Partie 1-1 : Règles Générales et Règles Pour Les Bâtiments’.
- AFNOR. 2022. ‘NF EN 206/CN’.
- Andrade, C., I.R. Maribona, S. Feliu, J.A. González, and S. Feliu. 1992. ‘The Effect of Macrocells between Active and Passive Areas of Steel Reinforcements’. *Corrosion Science* 33 (2): 237–49. [https://doi.org/10.1016/0010-938X\(92\)90148-V](https://doi.org/10.1016/0010-938X(92)90148-V).
- Andrade, Carmen. 2023. ‘Steel Corrosion Rates in Concrete in Contact to Sea Water’. *Cement and Concrete Research* 165 (March): 107085. <https://doi.org/10.1016/j.cemconres.2022.107085>.
- Angst, Fabrizio Moro, Mette Geiker, Sylvia Kessler, Hans Beushausen, Carmen Andrade, Jukka Lahdensivu, et al. 2020. ‘Corrosion of Steel in Carbonated Concrete: Mechanisms, Practical Experience, and Research Priorities – a Critical Review by RILEM TC 281-CCC’. *RILEM Technical Letters* 5 (December): 85–100. <https://doi.org/10.21809/rilemtechlett.2020.127>.
- Chalhoub, Chantal, Raoul François, and Myriam Carcasses. 2019. ‘Determination of Chloride Threshold Initiating Corrosion: A New Set-up Taking the Localized Aspect of Corrosion into Account’. *Cement and Concrete Research* 124 (October): 105825. <https://doi.org/10.1016/j.cemconres.2019.105825>.
- Hansson, C. M., A. Poursaei, and A. Laurent. 2006. ‘Macrocell and Microcell Corrosion of Steel in Ordinary Portland Cement and High Performance Concretes’. *Cement and Concrete Research* 36 (11): 2098–2102. <https://doi.org/10.1016/j.cemconres.2006.07.005>.
- Huy Vu, Quoc, Gabriel Pham, Alain Chonier, Eric Brouard, Sundar Rathnarajan, Radhakrishna Pillai, Ravindra Gettu, et al. 2019. ‘Impact of Different Climates on the Resistance of Concrete to Natural Carbonation’. *Construction and Building Materials* 216 (August): 450–67. <https://doi.org/10.1016/j.conbuildmat.2019.04.263>.
- IREX. 2022. ‘Projet National PERFDUB’. 2022. <https://www.perfdub.fr/>.
- Lliso-Ferrando, J.R., I. Gasch, A. Martínez-Ibernón, and M. Valcuende. 2022. ‘Effect of Macrocell Currents on Rebar Corrosion in Reinforced Concrete Structures Exposed to a Marine Environment’. *Ocean Engineering* 257 (August): 111680. <https://doi.org/10.1016/j.oceaneng.2022.111680>.
- Nasser, A., A. Clément, S. Laurens, and A. Castel. 2010. ‘Influence of Steel–Concrete Interface Condition on Galvanic Corrosion Currents in Carbonated Concrete’. *Corrosion Science* 52 (9): 2878–90. <https://doi.org/10.1016/j.corsci.2010.04.037>.
- Nasser, Abdelkader, and Arnaud Castel. 2014. ‘Microcell versus Galvanic Corrosion Currents in Carbonated Concrete’. *Magazine of Concrete Research* 66 (July): 697–707. <https://doi.org/10.1680/mac.13.00214>.
- Nguyen, Thi-Thu, Raoul Francois, Tru Vu, and Myriam Carcasses. 2022. ‘A Comparison between Uniform and Galvanic Corrosion Rate in Carbonation Induced Corrosion of Reinforced Concrete’. *MATEC Web of Conferences* 364 (September). <https://doi.org/10.1051/mateconf/202236402025>.
- Revert, Andres Belda, Karla Hornbostel, Klaartje De Weerd, and Mette Rica Geiker. 2019. ‘Macrocell Corrosion in Carbonated Portland and Portland-Fly Ash Concrete - Contribution and Mechanism’. *Cement and Concrete Research* 116 (February): 273–83. <https://doi.org/10.1016/j.cemconres.2018.12.005>.
- Sohail, M. G., S. Laurens, F. Deby, and J. P. Balayssac. 2015. ‘Significance of Macrocell Corrosion of Reinforcing Steel in Partially Carbonated Concrete: Numerical and Experimental Investigation’. *Materials and Structures* 48 (1–2): 217–33. <https://doi.org/10.1617/s11527-013-0178-2>.
- Subramaniam, Kolluru V., and Mingdong Bi. 2010. ‘Investigation of Steel Corrosion in Cracked Concrete: Evaluation of Macrocell and Microcell Rates Using Tafel Polarization Response’. *Corrosion Science* 52 (8): 2725–35. <https://doi.org/10.1016/j.corsci.2010.04.030>.
- Valipour, Mahdi, Mohammad Shekarchi, and Pouria Ghods. 2014. ‘Comparative Studies of Experimental and Numerical Techniques in Measurement of Corrosion Rate and Time-to-Corrosion-Initiation of Rebar in Concrete in Marine Environments’. *Cement and Concrete Composites* 48 (April): 98–107. <https://doi.org/10.1016/j.cemconcomp.2013.11.001>.





Chapter 8

# **General Conclusion and Perspectives**



## CONCLUSION

The need to reduce CO<sub>2</sub> emissions in the construction field, by the development of more sustainable concretes, is widely recognized. To face this environmental challenge, different binder technologies have been developed, without Portland cement or with a reduced quantity. As these low-carbon concretes are quite recent, the lack of information regarding their durability and particularly their compatibility with rebars and the associated risk of corrosion, still limits their use. The characterization of their behaviour against corrosion due to chlorides or due to carbonation, which is among the main causes of structural degradation, becomes crucial to achieve sustainable constructions. The focus in research is now starting to shift from the study of the time necessary to initiate corrosion to the study of rebar corrosion, which offers a greater opportunity for the use of low-carbon concretes.

Thus, the main objective of this thesis was to assess the durability of reinforcement in three very different low-carbon concretes, exposed either to chlorides or to carbonation. The concretes considered are a low clinker (LCK) concrete, an alkali-activated slag with sodium carbonate (AAS) concrete and a supersulfated cement (SSC) concrete. The strategy chosen for studying the durability of reinforcement, was to separate the study of corrosion initiation and propagation, and in each case to consider independently chloride exposure and carbonation exposure. The objective associated to the initiation period was to determine the time taken by the aggressive agents (chlorides or CO<sub>2</sub>) to reach the rebar. The objective associated to the propagation period was to evaluate the corrosion rates once the corrosion is initiated, as a literature analysis showed a lack of knowledge on this subject. Therefore, an experimental campaign divided into four parts was carried out, associated to the four articles of this thesis. This approach led to several conclusions.

A second objective related to the previous one, was to use reliable and representative test methods, to characterize the low-carbon concretes, due to their particular compositions and chemistry compared to Portland cement. For the study of corrosion initiation and the evaluation of their general transfer properties, traditional protocols for durability tests need to be questioned before being applied to alternative low-carbon binders (accelerated conditions exposure, preconditioning with drying), to avoid misinterpretations of the results. For the study of corrosion propagation, the onset of corrosion needs to be accelerated to study active corrosion over the duration of the thesis. The literature also reports difficulties with classical methods (corrosion potential and polarisation resistance measurement) for slag-based binders. The strategy adopted to answer this second objective, was to use experimental tests remaining as representative as possible of real conditions, whether for the initiation or propagation phase. Each time, the proposed alternatives were compared to classical measurements.

Thus a complete study of the durability of reinforcement was proposed, considering both the initiation and propagation of corrosion, exposure to chlorides and carbonation, evaluated by classical and alternative methods.

### **Durability of reinforcement**

The same experimental protocols were used to characterize the corrosion initiation and propagation of three low-carbon concretes of same strength class C25/30.

For the two exposure conditions tested (chlorides and carbonation), after studying the initiation and propagation phases of corrosion, **it seems that the durability of reinforcement is mainly governed by the corrosion initiation phase** (for strength class C25/30).

- Chlorides diffuse twice as fast in LCK concrete as in equivalent CEM I-concrete. The slag-based concretes, AAS and SSC, are extremely resistant to chloride penetration, even better than the conventional concretes.
- The three binders are quite sensitive to carbonation for short curing times, while they achieve similar or lower carbonation rates than an equivalent CEM III/A concrete for longer curing times.
- The importance of curing on low-carbon concretes is clear, which shows the emergency to change the practices and habits on site to develop their use while maintaining an acceptable durability.
- For the AAS, despite its high ability to maintain a pH higher than 9 in natural carbonation, a corrosion initiation was observed. This criteria on its own is therefore not sufficient to avoid corrosion to occur.
- If the chlorides or the carbonation front reach the rebar, high total corrosion rates are measured ( $> 1\mu\text{A}/\text{cm}^2$ ), with orders of magnitude similar to those of CEM I-based concretes.
- It is important to evaluate the order of magnitude of the galvanic current, because it governs the propagation of the corrosion. The local corrosion rates at the anode are similar for all types of binders for a same exposure condition. On the contrary, the galvanic current is dependant of the type of binder and allows distinguishing differences between the formulas, not visible by considering only the local current.
- The advantage of the SSC binder for the corrosion propagation is that it has negligible galvanic currents for all exposure conditions. The total measured currents are therefore lower than for the other binders, because there is no galvanic current added to the local current at the anode. This is mainly due to its high resistivity and the sulfur contained in its pore solution under saturated conditions.
- Otherwise, the galvanic current is not negligible: it can represent up to 50% of the total current densities. This has been observed mainly for carbonation, but would surely also have been the case for chlorides if more aggressive experimental conditions had been used.
- The results show that the initiation of corrosion conditions the durability of the reinforcement (for strength class C25/30), special precautions must be taken to delay this initiation (low w/b ratio, increase of the curing times, increase of the strength class of concrete).

## Recommendations

The three concrete technologies studied have confirmed that they can be competitive and promising low-carbon solutions, if used in the suitable environments and by adapting the current mix design and on-site practices to achieve desired durability performance.

- For **chloride exposure**, the slag-based binders (AAS and SSC) are recommended. They are much more resistant to the corrosion initiation (low permeability to chlorides) and have a negligible galvanic current (except for AAS at 300 g/L), to limit the total corrosion rates during the corrosion propagation phase. Nevertheless the LCK formulation could be adapted to achieve smaller pore sizes, higher resistivity or a higher chloride binding capacity. One option could be to add a small amount of slag or calcined clay for example.
- For **carbonation exposure**, the LCK is recommended because it more resistant to corrosion initiation (lower carbonation rates). Nevertheless, the use of the AAS and the SSC is also possible if the initiation phase can be controlled and sufficiently delayed. Several levers are already known, such as the decrease of the w/b ratio, the increase of the curing time or the increase of the concrete strength class for a given exposure. During the propagation phase, high total corrosion rates, comparable to those of CEM I binders, are measured for the LCK and the AAS. They are lower for the SSC (negligible galvanic contribution), but this binder is more vulnerable to corrosion initiation.

## Methodology

The tests performed to characterize the corrosion initiation and the durability of concretes made with alternative binders require adaptations:

- For the water porosity and gas permeability, a drying temperature of 50 °C instead of 105 °C, combined with a reduction of the sample thickness, is recommended for the preconditioning of slag-based samples.
- When possible, it remains preferable to favour direct tests on a pathology without prior thermal preconditioning (RCPT, migration or diffusion tests to assess the performance of concrete against chloride penetration for example) for greater reliability and representativity of the real conditions.
- For carbonation, if needed, it is recommended to perform accelerated tests at 1% CO<sub>2</sub> rather than at 3% CO<sub>2</sub> or higher CO<sub>2</sub> concentration, to preserve as much as possible the hydrates and reactions observed in natural conditions. The tests carried out within the scope of this study, showed that the accelerated tests at 1% CO<sub>2</sub> seemed to be representative of the natural conditions and could be used at least for the purpose of comparison between samples, if not in an absolute sense. Similar relative performance rankings and same hierarchy between the mixtures are found for the carbonation rates and pH.

An original method was proposed to study the corrosion propagation and to assess the corrosion kinetics, adapted to low-carbon binders, for chloride or carbonation-induced corrosion.



- The method is based on galvanic current measurement combined with mass loss on the rebar, which are both adapted to all types of binders.
- The method is representative of real structures, as it considers the local and also the galvanic corrosion, the latter being not often taken into account in laboratory tests. The results show the contribution of the galvanic current is important and should be considered for the assessment of the durability of reinforcement.
- The proposed method considers the fact that corrosion is a continuous phenomenon, by proposing corrosion current densities averaged over 90 days of testing. This method is however more complex to perform than the classical tests, which propose a faster single measurement, but giving information on the state of corrosion at a given time in particular conditions of humidity and temperature.
- A comparison with classical electrochemical measurements (corrosion potential  $E_{\text{corr}}$ , polarization resistance  $R_p$ ), confirmed that these measurements are not suitable for binders with a high slag content under saturated conditions because of sulfur contribution.
- The kinetics obtained for both exposure conditions are slightly overestimated compared to reality, considering that the anodes are mortar samples with a low resistivity and that the tests are carried out in a solution with negligible resistivity, which is not the case of the concrete material.

## PERSPECTIVES

This thesis work allowed to bring answers regarding the industrial/scientific objectives and methodology issues defined. Nevertheless, the following perspectives are suggested:

### Methodological perspectives

- The methodology proposed to evaluate the corrosion kinetics (due to  $\text{Cl}^-/\text{CO}_2$ ), based on galvanic current measurement coupled with mass loss of the rebar, could be applicable for new low-carbon concrete technologies (based on calcined clays, fly ash...).

### Corrosion initiation/propagation

- The new insight provided by this work based on the evaluation of the durability of reinforcement in LCK, AAS and SSC concretes, could be used in practice to improve the mix design of each concrete when exposed to  $\text{Cl}^-/\text{CO}_2$  and to increase their use in different environments.
- The experimental data about transport properties and corrosion kinetics in the three low-carbon concretes studied, could be used as input data to develop models for service life prediction.

To complete this research work complementary investigations are proposed:

- A new determination of free and bound chlorides using ionic chromatography should be conducted, to obtain this information for slag-based binders and better quantify the

transport of chlorides in this binder, by separating the phenomenon of pure diffusion and chemical bonding.

- An analysis of the hydrates and species in solution, obtained before and after natural and accelerated carbonation, could be performed to better understand the measured pH values.
- The measurement of the carbonation depth on concrete should be continued over several years to assess whether or not carbonation rates are constant over time for these binders (important for the extrapolation of the results).
- The amount of sulfur in the pore solution of AAS and SSC concretes could be quantified, to better understand their influence on the properties of these concretes on the corrosion initiation and propagation phase.
- To test the influence of different experimental conditions (saturation, C/A, chloride concentration) on the corrosion rates developed and to convert the currents obtained on mortar anodes to the concrete scale, the obtained experimental data could be coupled to a numerical study.
- The Tafel tests for the different conditions tested should be repeated to validate the value of the constant B. Thus, it would allow calculating more accurate values of corrosion current densities using the Stern-Geary equation.
- This study is a first step to characterize the corrosion kinetics on these alternative binders. Given the small number of samples used for some conditions of the galvanic coupling, this work needs to be supported by further studies.
- Deeper investigations should be carried out to better understand the parameters influencing the galvanic current for AAS and SSC binders.

Finally, some additional investigations were initiated during this PhD and should be continued:

- The laboratory results obtained regarding the chloride diffusion and corrosion rates due to chlorides, should be confirmed by measurements on site, on concrete slabs casted with the same low-carbon concretes as those investigated for the thesis, exposed in a tidal zone (rebars not activated during the thesis period).
- The laboratory results obtained regarding the carbonation rates and the associated corrosion rates, should be confirmed by measurements on a real structure build at Holcim Innovation centre with the same low-carbon concretes as those investigated for the thesis (rebars not activated during the thesis period).
- The reaction of the three binders with O<sub>2</sub> and CO<sub>2</sub>, as well as the diffusion of O<sub>2</sub> and CO<sub>2</sub> in the three concretes could be investigated in more details to better understand the associated mechanisms. A special device, inspired from research works in the literature, was designed for this purpose.